Strathclyde Institute of Pharmacy and Biomedical Science (SIPBS)

Exploration of novel Proteinase Activated receptor-4 (PAR4) interacting proteins for identification of new pathways for regulating receptor activity

Ryan Liam Shearer CEP BSc MSc MIBMS

A thesis submitted in fulfilment of the requirements for the degree of Doctor of Philosophy

2024

I. Declaration

This thesis is the result of the author's original research. It has been composed by the author and has not been previously submitted for examination which has led to the award of a degree.

Signed: R SHEARER

Date: 14/06/2024

II. SARS-COV2 Impact Statement

The SARS-COV2 pandemic resulted in significant delays in data generation due to no laboratory access for 5 months during my first year of PGR study (March-August 2020). This was subsequently followed by restricted access to labs between August 2020-July 2021) upon reopening due to social distancing which impacted the wet laboratory experimental studies carried out in Chapter 4 of this thesis. As no extension to funding was provided by the University of Strathclyde, it was not possible to delay submission of this thesis due to the PGR maximum study period.

One of the aims of the original PhD project was to screen novel Proteinase-activated receptor-4 (PAR-4) small molecules designed by Atomwise Atomnet technology. This was a major area of the thesis that was not fulfilled due to global impact of SARS-COV2. There was a significant delay in the receipt of a compound library from US collaborators which led to the redesign of the intended project.

Student Signature: Mr R. Shearer Supervisor Signature: Dr M. Cunningham

Date: 13/06/2024 Date: 13/06/2024

III. Acknowledgements

I declare that the work presented in this thesis, unless otherwise indicated, is my own, and that any work carried out by others (published or unpublished) has been acknowledged.

I am particularly grateful to my Principal Investigator and supervisor Dr. Margaret Rose Cunningham for one giving me the opportunity to study in her lab and for making me feel so welcome, but more importantly for her brilliant supervision, training and advice since the beginning of my PhD. I am incredibly grateful to have had the ability to learn from and work alongside you, you have made my PhD experience one to remember. Your creativity, drive and support are an inspiration to me and all the students you support, so thank you again for everything.

I would also like to extend my gratitude to the rest of the lab group Mohammad Safar, Callum McMullen, and Marco Bonfanti for their assistance, advice and support during the beginning of my PhD. I would in particular like to thank my evening and weekend lab colleague and partner in crime Zainab Bosakhar. You made the many late nights and weekend working enjoyable and a laugh. I have made a friend for life and thank you for making the experience so enjoyable, I am grateful to have had the pleasure of meeting and working alongside you. Finally, I would like to thank my second supervisor Prof Robin Plevin for giving me the opportunity to return to SIPBS to undertake my PhD and allowing me the chance to begin my research career.

I would like to give a special mention to the students of Gail McConnells group; in particular Jordan Murray, Mollie McFarlane, Shannon Foylan, Eliana Battistella and Katrina Wesencraft. For someone who struggles to fit in and make new friends they were always willing to include me in their group. They gave me many happy memories and I have made friends for life. Thank you for making my time in my PhD a joy, I am so grateful to have met you all.

Finally, and most importantly, I thank my family. There amazing support was pivotal to the success of my masters, which without it wouldn’t have allowed me the opportunity to be offered this PhD position. Their support gave me the confidence to push myself and without them this would not be possible. Thank you all.

IV. Abstract

The role of Proteinase Activated Receptor-4 (PAR4) in eliciting platelet shape change upon stimulation with thrombin is well established, however functional characterisation of the pathways involved in coordinating this change is not. In particular proteins which sever actin allowing for the formation of new filamentous actin hasn't been shown in the context of PARs. The present study aimed at experimentally identifying and validating novel interacting proteins downstream of PAR4. Proteomic analysis revealed actin remodelling and dynamic regulation proteins as standout pathways close to the PAR4 receptor, with the actin severing protein Cofilin emerging as a high-confidence hit. MEG-01 cells were used as a cell model expressing physiological levels of both PAR1 and PAR4 in order to validate the findings of the proteomic data. Results of western blotting revealed that stimulation of MEG-01 cells with thrombin or PAR4-AP (AYPGKF) lead to significant increases in the levels of Cofilin phosphorylation reaching a peak at 15 mins post stimulation. It was also shown that phosphorylation of Cofilin showed dose dependency with all concentrations used showing significant changes in Cofilins phosphorylation state. This was also confirmed using immunofluorescent analysis. Stimulation of just PAR1 with TFLRRN showed no significant increase in Cofilin phosphorylation through western blot analysis, however significance was shown through IF analysis but non-comparable to the changes seen in PAR4 stimulated MEG-01 cells. Stimulation of PAR4 showed significant activity regulation of Cofilin pathway proteins, including regulators of phosphorylation (ROCK1, LIMK2 and TESK1) and Cofilin phosphatases (SSHL1 and PDXP). In addition, MEG-01 cells were shown to contain the Cofilin-2 isoform and stimulation with thrombin showed dose dependant variation in both total Cofilin-2 and Cofilin-2 phosphorylation showing distinct regulatory signalling dynamics compared to Cofilin-1

The study identified a novel potential interacting protein with PAR4 and functionally validated this interaction within a physiologically relevant cell model.

V. Table of Contents

Table of Contents

VI. List of Figures

VII. List of Tables

VIII. ABBREVIATIONS

$5HT_{2A}$	5-Hydroxytryptamine receptor 2A
A4P	Adenosine tetraphosphate
AA	Arachidonic Acid
AC	Adenylyl cyclase
ACS	Acute Coronary Syndrome
ACSL1	Long-chain-fatty-acid—CoA ligase 1
ADP	Actin depolymerising factor
ADP	Adenosine diphosphate
AI	Artificial Intelligence
AKT	Protein kinase B
ANO6	Anoctamin 6
APS	Ammonium persulphate
Arp2/3	Actin related protein 2/3 complex
ATCC	American Type Culture Collection
ATP	Adenosine triphosphate
BCA	Bicinchoninic Acid
BMS	Bristol Meyers Squibb
BPNT1	3'(2'),5'-bisphosphate nucleotidase 1
BSA	Bovine serum albumin
c-Mpl	Myeloproliferative leukaemia protein (Thrombopoietin receptor)
Ca^{2+}	Calcium
CAD	Coronary artery disease
CalDAG-GEF1	Ca^{2+}- and diacylglycerol-regulated guanine nucleotide-exchange factor 1
cAMP	cyclic Adenosine monophosphate
CDC42	Cell division control protein 42 homolog
CFL1	Cofilin-1
CFL2	Cofilin-2
CFP	Cyan fluorescent protein

cGMP	cyclic Guanosine monophosphate
CHD	Coronary Heart Disease
CIN	Chronophin
CKAP4	Cytoskeleton-associated protein 4
CLEC-2	C-type lectin-like type II
CMV	Cytomegalovirus
Co-IP	Co-immunoprecipitation
COX1	Cyclooxygenase-1
$cPLA_2$	Cytosolic phospholipase. A_2
CVD	Cardiovascular disease
CYP450	Cytochrome P450
Daam	Dishevelled-associated activator of morphogenesis 1
DAPI	4' ,6-diamidion-2-phenylindole
DCNN	Deep convolutional neural network
DMEM	Dulbecco's Modified Eagle Medium
DMSO	Dimethyl sulfoxide
DNA	Deoxyribonucleic acid
DNAJA2	DnaJ homolog subfamily A member 2
Dpi	Dots per inch
DSP	dual specific phosphatases
EC NOS	Endothelial cell nitric oxide synthase
EC50	Effective concentration 50%
ECL	Enhanced chemiluminescence
ECL2	Extracellular loop-2
ECL3	Extracellular loop 3
ECT2	Epithelial cell transforming 2
EDTA	Ethylenediaminetetraacetic acid
ER	Endoplasmic Reticulum
EXOSC8	Exosome complex component RRP43
F-actin	filamentous actin
Fab	Antibody fragment
FBS	Fetal Bovine Serum

FcRγ	Fc receptor γ-chain
FCS	Foetal Calf Serum
FDR	False Discovery Rate
FLI1	Friend leukaemia integration 1 transcription factor
FRAP	Fluorescence recovery after photobleaching
FRET	Fluorescence resonance energy transfer
G-actin	globular actin
GATA1	GATA-binding factor 1 (Erythroid transcription factor)
GC	Guanylate cyclase
GDP	Guanosine diphosphate
GEF	Guanosine exchange factor
GEF-H1	Guanine nucleotide exchange factor H1
GFP	Green fluorescent protein
GI	Gastrointestinal
GPCR	G-protein coupled receptor
GPIb	Glycoprotein Ib
GPIb-IX-V	Glycoprotein Ib-IX-V
GPIb/IX	Glycoprotein Ib/IX
GPVI	Glycoprotein VI
GTF2I	General transcription factor IIi isoform D
GTP	Guanosine triphosphate
GTPase	Guanosine triphosphate -ase
H/D	Hydrogen/Deuterium
H_2O_2	Hydrogen peroxide
HEK293	Human embryonal kidney-293
HL	Heavy/Light
HNRNPF	Heterogeneous nuclear ribonucleoprotein F
HRP	Horse radish peroxidase
HSD17B11	Estradiol 17-beta-dehyrogenase 11
Hsp70	Heat shock protein 70
Hsp90	Heat shock protein 90
IC50	Inhibitory concentration 50%

ICL2	Intracellular loop-2
ICL3	Intracellular loop-3
IFNg	Interferon gamma
IgG1	Immunoglobulin G1
INNOVATE-PCI	INtraveNous and Oral administration of elinogrel to eVAluate Tolerability and Efficacy in nonurgent PCI patients
INVENT	International Network of Venous Thromboembolism Clinical Research Networks
IP	Inositol phosphate
IP3	Inositol triphosphate
IPA	Inhibition of platelet aggregation
ITAM	Immunoreceptor tyrosine-based activation motif
JACoP	Just Another Colocalization Plugin
KIF5B	Kinesin-1 heavy chain
KTN1	Kinectin
LC MS/MS	Liquid Chromatography with tandem Mass Spectrometry
LDS	Lithium dodecyl sulfate
LIM	LIN-11 ISI1 MEC3
LIMK1	LIM kinase 1
LIMK2	LIM kinase 2
LRRC59	Leucine-rich repeat-containing protein 59
M-CSF	Monocyte-colony stimulating factor
MAPK	Mitogen activated protein kinase
MARCKS	Myristoylated alanine rich C-kinase substrate
MCCC2	Methylcrotonoyl-CoA carboxylase beta chain, mitochondrial
mDia	mammalian Diaphanous-related
MEG-01	Human Megakaryoblastic leukaemia cell line – 01
MEM	Minimum Essential Medium
MH	Medium/Heavy
MI	Myocardial infarction
ML	Medium/Light

MPN	Myeloproliferative neoplasm
MPO	Myeloperoxidase
mRNA	messenger Ribonucleic acid
MRPS9	28S ribosomal protein S9
MS	Mass Spectrometry
Mut	mutant
NaCl	Sodium chloride
NDUFA4	Cytochrome c oxidase subunit NDUFA4
NESK	Nik-like embryo-specific kinase
NFE2	Nuclear factor, Erythroid 2
NIK	Nik-related protein kinase
NM	Nemaline myopathy
NO	Nitric oxide
NOC4L	Nucleolar complex protein 4 homolog
NSAID	Non-steroidal anti-inflammatory drugs
NSTEMI	Non-ST elevated myocardial infarction
NT	No treatment
P/S	Penicillin/Streptomycin
PAK	p21-activated kinase
PAK4	p21-activated kinase-4
PANTHER	Protein Analysis Through Evolutionary Relationships
PAR1	Protease activated receptor-1
PAR2	Protease activated receptor-2
PAR3	Protease activated receptor-3
PAR4	Protease activated receptor-4
PAR4-AP	Protease activated receptor 4-activating peptide
PBS	Phosphate buffered saline
PCAM-1	Platelet endothelial cell adhesion molecule-1
PCI	Percutaneous coronary intervention
PDCD4	Programmed cell death protein 4
PDE2	Phosphodiesterase E2
PDE3	Phosphodiesterase E3

PDE5	Phosphodiesterase E5
PDXP	pyridoxal-5-phosphate phosphatases
PEI	Polyethyleneimine
PGE_2	Prostaglandin E_2
PGG_2	Prostaglandin G_2
PGH_2	Prostaglandin H_2
PGI_2	Prostaglandin I_2
pH	Properties of Hydrogen
PI3K	Phosphoinositide 3-kinase
PIP_3	Phosphatidylinositol 3,4,5-triphosphate
PK/PD	Pharmacokinetics/Pharmacodynamics
PKA	Protein kinase A
PKCα	protein kinase-C α
PKCa	Protein kinase Ca
PKCb	Protein kinase Cb
PKC_ε	Protein kinase C epsilon
PKD	Protein kinase D
PKD1	Protein kinase D1
PKD2	Protein kinase D2
PKD3	Protein kinase D3
PKG	Protein kinase G
PLA_2	Phospholipase A_2
PLCb	Phospholipase Cb
PLCg	Phospholipase Cg
PLCγ	Phospholipase C gamma
$PLC_{\gamma 2}$	phospholipase-$C_{\gamma 2}$
PMA	Phorbol 12-myristate 13-acetate
PPA1	Inorganic pyrophosphatase
PPI	Polyphosphoinositides
PPO	Platelet Peroxidase
PPP6C	Serine/threonine-protein phosphatase 6 catalytic subunit
PRPS1	Ribose-phosphate pyrophosphokinase 1

PtdSer	Phosphatidylserine
RAC1	Ras-related C3 botulinum toxin substrate 1
RDX	Radixin
RFP	Red fluorescent protein
Rho	G-protein signalling GTPase
RhoA	Ras homolog family member A
ROCK	Rho-associated protein kinase
ROCK1	Rho-associated protein kinase 1
ROCK2	Rho-associated protein kinase 2
ROI	Region of interest
RPL3	60S ribosomal protein L3
RPMI	Rosewell Park Memorial Institute
RPS23	40S ribosomal protein S23
RPS24	40S ribosomal protein S24
RPS6	40S ribosomal protein S6
Rt-PA	Tissue plasminogen activator
RUNX1	Runt-related transcription factor-1
SD	standard deviation
SDS	Sodium dodecyl sulfate
SEQUEST	Tandem Mass Spectrometry data analysis program
Ser3	Serine 3
SFK	Src family kinases
SGR	Small G-protein regulators
SiGN	Stroke Genetics Network
SILAC	Stable isotope labelling using amino acids in cell culture
SLC25A5	Mitochondrial phosphate carrier protein
SLC25A6	ADP/ATP translocase 3
Snaclec	snake C-type lectin
SNARE	SNAP receptor
SNP	Single nucleotide polymorphism
SRC	Proto-oncogene tyrosine-protein kinase Src
SSH	Slingshot homolog

SSH1	Slingshot homolog 1
SSH2	Slingshot homolog 2
SSH3	Slingshot homolog 3
SSHL1	Slingshot homolog long 1
SSHL2	Slingshot homolog long 2
SSHL3	Slingshot homolog long 3
STEMI	ST-elevated myocardial infarction
STK	Serine/threonine-protein kinases
SYK	Tyrosine-protein Kinase SYK (Spleen tyrosine kinase)
T2DM	Type 2 diabetes mellitus
TAL1	T-cell acute lymphocytic leukaemia protein-1
TBS-T	Tris buffered saline – tween 20
TEMED	N,N,N′,N′-Tetramethylethane-1,2-diamine
TESK1	Testicular associated actin remodelling kinase 1
TESK2	Testicular associated actin remodelling kinase 2
TF	Tissue factor
TGF-β	Transforming growth factor – beta
TM2	Transmembrane 2
TM3	Transmembrane 3
TM6	Transmembrane 6
TM7	Transmembrane 7
TNF-a	Tumour necrosis factor alpha
TP	Thromboxane receptor
TRAP	Thrombin receptor-activating peptides
tRNA	transfer ribonucleic acid
TTP	Thrombotic thrombocytopenia purpura
TxA_2	Thromboxane A_2
UK	United Kingdom
v/v	Volume by volume
VHR	VH1-related phosphatase
VTE	Venous thromboembolism
vWF	von Willebrand factor

w/v	Weight by volume
WASP	Wiskott-Aldrich syndrome protein
WAVE	WASP-family verprolin-homologous protein
WDR82	WD repeat-containing protein 82
Wt	wild type
YD-3	1-benzyl-3(ethoxycarbonylphenyl)-indazole
YFP	Yellow fluorescent protein

Chapter One:

Introduction

1 Introduction

1.1 Overview

Acute coronary syndromes (ACS) encompass both myocardial infarction and ischemic stroke and are commonly lethal manifestations of cardiovascular disease (CVD). CVD is comprised of coronary heart disease (CHD) and hypertension and was concluded in a 25-year global study to result in the number one cause of death globally collectively (Roth et al., 2017). In the year 2015, >17 million people died as a result of CVD, representing 31% of all global deaths for that year (Stewart et al., 2017; Libby et al., 2019). However, the majority of global deaths which occur as a result of ACS are in low- and middle-income countries where patients suffering from CVD have limited access to healthcare services, detection and intervention are made late in the disease where the risk from ACS complications are much higher (Collins et al., 2017). In contrast, a high-income country such as the UK has seen a steep decline in CVD mortality from the 1950s to the 2010s (22% vs. 6%) due to risk reduction strategies and early intervention (Herrington et al., 2016). However, deaths associated with CVD remain a significant problem in the UK and saw their first rise in half a century from 41042 in 2014 to 42384 in 2017. In addition, CVD is one of the leading causes of death in Scotland and accounts for ~22% of all premature deaths, around 4600 a year. ACS is primarily caused by the rupture of atherosclerotic plaques and subsequent platelet aggregation, leading to thrombus formation.

The development of new antiplatelet agents has been significantly advanced by a deeper understanding of platelet surface receptors, such as protease-activated receptor 4 (PAR4), which is the target of interest in this thesis. PAR4, which plays a crucial role in platelet activation and aggregation, has become a focal point for research, enabling the creation of targeted therapies that can more effectively inhibit platelet function and reduce the risk of thrombotic events in ACS patients. Specifically targeting PAR4, these novel agents aim

to provide a therapeutic benefit with potentially fewer side effects than traditional antiplatelet drugs. PAR4 is integral to platelet activation and aggregation, yet its precise mechanisms and functions are less understood, necessitating further research.

In this thesis, quantitative proteomics was carried out to advance the knowledge of the PAR4 interactome. Whilst proteomics was conducted in recombinantly expressed fluorescent tagged cell lines, efforts were made to translate key interacting protein pathways in a cell line with megakaryocytic characteristics, namely MEG-01 (Ogura M et al., 1985; Nunthanasup et al., 2023). These cells represent a valuable tool in haematology and thrombosis research, offering insights into the receptor activity of PAR4 expressed in megakaryocytes and platelets.

1.2 Megakaryocytes and platelet formation

Platelets are anucleated cell fragments (2-4μm in diameter) which circulate in the blood for 7-10 days in humans or 4-5 days in mice before being cleared by the liver and spleen (Cohen and Leeksma, 1956; Odell and Macdonald, 1961). Megakaryocytes are the cells responsible for the generation of platelets. They are responsible for maintaining a physiologically stable platelet count of 150-400x10^9 platelets per litre of human whole blood. They achieve this by producing and clearing platelets at a rate of 10^{11} per day. Megakaryocytes are huge cells which are generated from haematopoietic stem cells via a variety of key transcription factors, such as Friend leukaemia integration one transcription factor (FLI1), Runt-related transcription factor-1 (RUNX1), GATA-binding factor 1 (GATA1), T-cell acute lymphocytic leukaemia protein-1 (TAL1), and Nuclear factor, Erythroid 2 (NFE2) (Tijssen et al., 2011; Bianchi et al., 2016). Megakaryocytes sequester in the bone marrow and are unique cells in that they undergo numerous endomitotic cell cycles without division (2n – 256n), resulting in a large, polyploid, multilobulated nucleus (Machlus and Italiano, 2013).

The formation of platelets can be divided into two main developmental stages; the first is megakaryocyte development and maturation, which can take days to complete (Ebbe and Stohlman, 1965; Odell and Jackson, 1968) during this phase under the control of megakaryocyte specific growth factors (mainly thrombopoietin and its megakaryocyte receptor c-Mpl) results in massive nuclear proliferation, enlargement of the cytoplasm, development of platelet specific granules (dense and α), and sufficient membrane for platelet production. The second phase is more rapid, taking only hours, where megakaryocytes generate platelets by extruding elongations into the sinusoidal spaces of the bone marrow vascular niche (Machlus and Italiano, 2013). This process is controlled partially by the motor protein dynein, which allows for the shuttling of granules, organelles, and vesicular structures from the cell body into the newly forming platelet. These pro-platelets are sheared off by hemodynamic forces, forming bar bell-shaped pre-platelets, which then undergo further fission to produce two discoid-shaped mature platelets. A megakaryocyte can produce 10^4 platelets per cell, leading to the complete usage of the cell membrane, resulting in the nucleus being extruded and the cell's death. Therefore, although platelets do not contain a nucleus, they receive all the cellular components and machinery necessary for sufficient signalling and activation to maintain physiological haemostasis (Bender et al., 2015; van der Meijden and Heemskerk, 2019).

1.3 Platelet activation and signalling

Platelets are maintained within an inactive state by the vascular endothelium via a variety of mechanisms, mainly the release of prostacyclin (PGI_2), ectonucleotidases (degrade ADP and ATP), thrombomodulin (inactivates thrombin) and nitric oxide production. Nitric oxide and PGI_2 effectively suppress most platelet activation processes, such as procoagulant activity, adhesion, aggregation, pseudopod formation and secretion (Bye et al., 2016; van der Meijden and Heemskerk, 2019). Studies have shown that type I and type III collagens present in the arterial intima and media are the most potent

activators of platelets (De Witt et al., 2014). In addition, tissue factor, which is highly expressed in endothelial smooth muscle cells and macrophages, activates thrombin, another potent activator of platelets (Kaikita et al., 1997; Schecter et al., 1997). These opposing processes provide the central dogma of platelet function; during normal haemostasis, intact endothelium keeps platelets in a quiescent state; however, when damaged, expose platelets to potent activators to rapidly plug the damaged vessel and maintain haemostasis. Conversely, in the pathological sense, when an atherosclerotic plaque ruptures, huge quantities of these collagens and TF:thrombin complex are exposed and leak into the vessel, explaining why atherosclerotic plaque rupture leads to full occlusive thrombus due to mass activation of platelets (van der Meijden and Heemskerk, 2019).

Platelets are initially activated through the binding of platelet integrins to adhesive proteins exposed at sites of vascular injury. Integrins are a family of widely expressed heterodimeric transmembrane receptors composed of non-covalently linked α- and β-subunits. The large extracellular domain forms a globular head with a single transmembrane domain and a short cytoplasmic tail (Bennett et al., 2009). Platelets express five different integrins which bind to their respective ligands: $\alpha_2\beta_1$ (collagen), $\alpha_5\beta_1$ (fibronectin), $\alpha_6\beta_1$ (laminin), $\alpha_{IIb}\beta_3$ (collagen, fibrinogen, von Willebrand factor, fibronectin and vitronectin), and $\alpha_v\beta_3$ (vitronectin) (Nieswandt et al., 2009). The importance of platelet integrins in platelet activation and adhesion was demonstrated in the genetic disorder of integrin $\alpha_{IIb}\beta_3$ (Glanzmann's thrombasthenia), resulting in a severe bleeding phenotype in patients (Nurden, 2006).

Soluble agonists released during vessel damage (ADP), produced from the coagulation cascade (thrombin) or inflammation (platelet-activating factor), play critical roles in platelet activation and thrombus formation (Offermanns, 2006). In addition, platelets also release these soluble agonists (ADP, serotonin and thromboxane A_2 (TXA_2)) from their granular contents, which can further activate platelets in a paracrine and autocrine fashion as well as lead

to further recruitment of platelets to the site of tissue injury (Joo., 2012). These soluble agonists work by activating platelets and stimulating a class of receptors known as G-protein coupled receptors (GPCRs), which are a family of seven-transmembrane domain receptors which signal through the recruitment of heterotrimeric G-proteins to the intracellular domain (Li et al., 2010) (Figure 1.1).

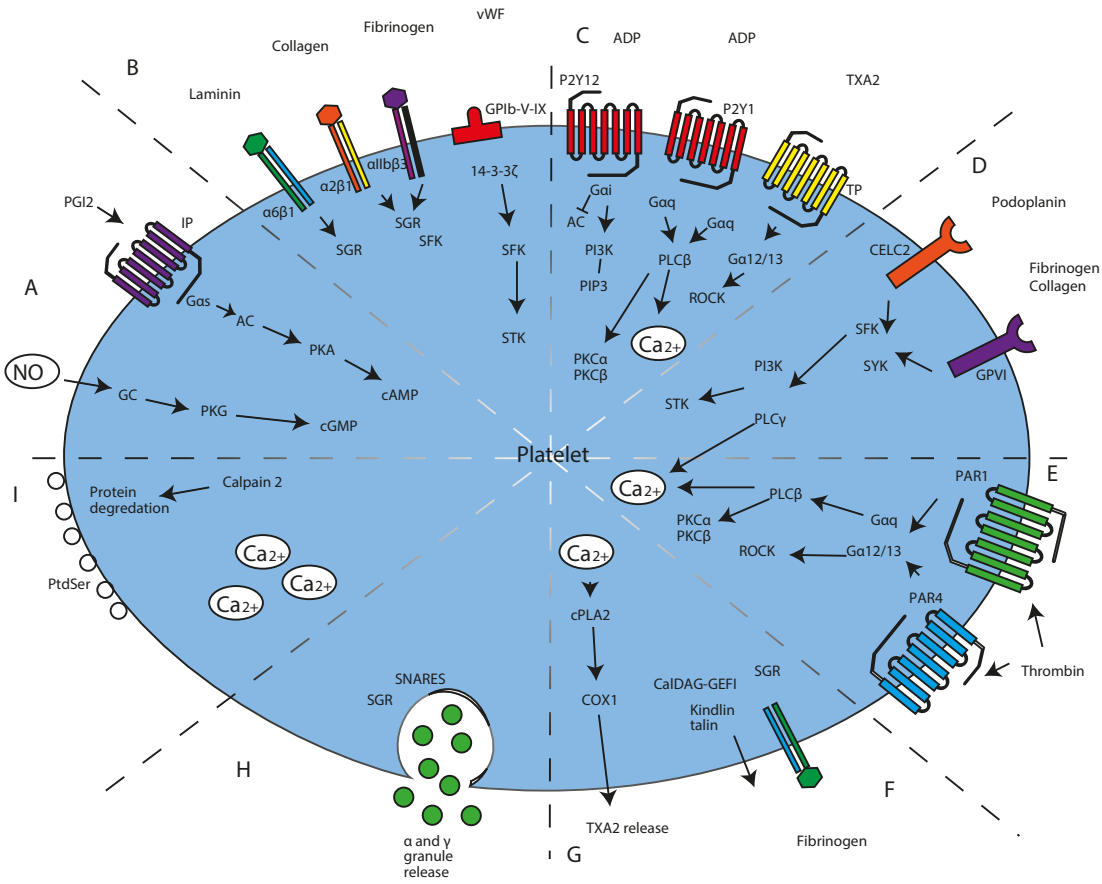

Figure 1.1 The major signalling responses and events during platelet activation. Platelet activation events are ordered clockwise from A-I. A) Platelet inhibition and maintenance with in an inactive state is controlled by nitric oxide and PGI_2 and works by signalling the production of cAMP and cGMP. B) Activation of platelets are initiated via interaction of integrins with their respective ligands and results in signalling through SRC kinases and serine/threonine kinases (STK). C) The release of soluble agonists from dense granules results in the activation of GPCRs ($P2Y_1$, $P2Y_{12}$ and Thromboxane A_2 receptor. D) Amplification of the activation process involves GPVI and C-type lectin-like receptor 2 (CLEC2) resulting in strong tyrosine kinase signalling. E) The strongest platelet agonist thrombin activates PAR1 and PAR4 by proteolytic cleavage. F) Conformational change of integrin αIIbβ3 from a low affinity to high affinity state. G) The release of TXA_2 via the activation of COX-1. H) Release of platelet granular contents which further activates platelets in an autocrine and paracrine fashion. I) Membrane ballooning and exposure of phosphatidylserine on the platelet surface.

Heterotrimeric G-proteins are made up of three subunits α,β, and γ, which bind to GPCR in an α/β/γ complex. Upon receptor engagement, the α -subunit is converted from a GDP-bound form to a GTP-bound form. This then dissociates from the β/γ complex to initiate the signalling of downstream targets (Offermanns, 2006). Based on alpha subunit homology, G-proteins can be divided into four classes: Gq/G11, G12/G13, Gi/Go/Gz and Gs, each coupled to their specific receptor and downstream effectors (Simon et al., 1991; McCudden et al., 2005). G12/13, Gq, Gi/Gz and Gs are expressed in platelets, all except Gs, and are coupled to receptors which stimulate platelet activation and aggregation; Gs couples mainly to NO and PGI_2 and mediates inhibitory signals by stimulating cAMP synthesis (Offermanns, 2006). ADP induces platelet activation via $P2Y_1$ (Gq coupled) and $P2Y_{12}$ (Gi-coupled), TXA_2 activates platelets via its receptor TP (Gq and G13 coupled), serotonin activates platelets via the receptor 5HT2A (Gq coupled), epinephrine via its receptor a2 (Gz), and finally, protease-activated receptors (PARs), PAR1 and PAR4 in humans (PAR3 and PAR4 in mice) are activated by thrombin and couple to Gi, Gq and G12/13 (Offermanns, 2006; Li et al., 2010).

1.4 Protease Activated Receptors

The PAR family comprises four members: PAR1, PAR2, PAR3 and PAR4. They are unique from other GPCRs in that they undergo proteolytic cleavage of the N-terminal domain to reveal a tethered ligand that interacts with and activates the receptor within the extracellular loop-2 of the PAR (Vu et al., 1991a). This proteolytic cleavage is mediated by a class of enzymes that contain serine within their active site and are termed serine proteases. Thrombin is the main protease that activates PAR1, PAR3, and PAR4, whereas trypsin is the main serine protease that activates PAR2 (Cunningham et al., 2016). The PARs are encoded on chromosome 5q13, F2R (PAR1), F2RL1 (PAR2) and F2RL2 (PAR3), and chromosome 19p12, F2RL3 (PAR4). Human platelets express PAR1 and PAR4 (Heuberger and Schuepbach, 2019).

PAR1 was the first of the PAR family to be discovered in 1991 in an attempt to identify the GPCR that mediates the thrombin signalling pathway (Vu et al., 1991a). In addition to platelets, PAR1 is also expressed in various cell types, including all blood cells, neurons, astrocytes, and epithelial and endothelial cells. PAR1 is recognised as a high-affinity thrombin receptor due to the presence of a high-affinity thrombin hirudin-like domain within the N-terminal sequence (Vu et al., 1991b). It is, therefore, activated by low thrombin concentration (0.2 nM PAR1 and 5 nM PAR4) (Liu et al., 1991; Xu et al., 1998; French et al., 2016). Proteolytic activation occurs at the carboxyl side of R^{41} to reveal the tethered ligand S^{42}FLLRN, which binds to ECL2, activating the receptor and initiating signalling (Macfarlane et al., 2001) (Figure 1.2).

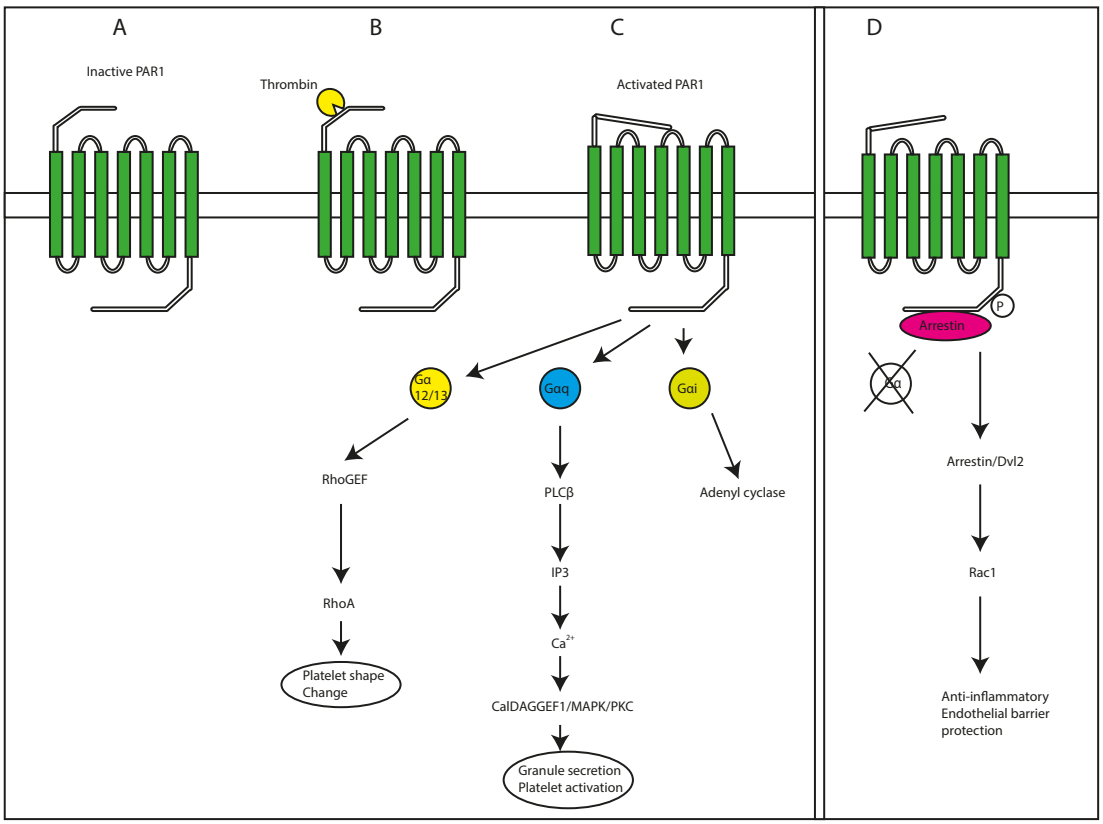

Figure 1.2 A schematic showing the mechanism of PAR1 receptor activation and the G-proteins which it can couple to and subsequent signalling cascades. A) PAR1 is expressed on the platelet surface in an inactive state. B) PAR1 contains a high-affinity thrombin hirudin-like domain within its N-terminal sequence, therefore is activated by low concentrations of thrombin. Thrombin proteolytically cleaves the N-terminal sequence on the carboxyl side of R^{41}. C) Cleavage reveals a tethered ligand sequence S^{42}FLLRN which binds to ECL2 activating the receptor. Activated PAR1 in platelets couples to three main G-protein partners; Gα 12/13, Gαq and Gαi. Coupling to Gα 12/13 signals through RhoGEF and RhoA to initiate platelet shape change. Coupling to Gαq signals through PLCβ and IP3 to mobilise intracellular calcium resulting in platelet activation and granule secretion. Coupling to Gαl signals through adenyl cyclase to promote platelet aggregation. D) PAR1 arrestin signalling does not occur in platelets, but in other cell types such as endothelial cells. It signals through RAC1 to promote anti-inflammatory responses such as endothelial barrier protection.

1.5 PAR4

The PAR4 receptor is a seven-transmembrane GPCR made up of 385 amino acids and is now recognised as a key thrombin receptor in platelet activation and aggregation. It was initially cloned in 1998 (Xu et al., 1998). PAR4 differs from the high-affinity thrombin receptor PAR1 (and PAR3), lacking the hirudin-like binding domain. The PAR4 receptor contains several structural domains which aid in its function and include the thrombin cleavage site, the tethered ligand sequence, the tethered ligand binding sequence on ECL2, an anionic region which interacts with exosite-I of thrombin, and a C-terminal sequence (RAGLFQRS) which regulates calcium signalling (Rudinga et al., 2018). Figure 1.3 (below) shows the structure and position of all 385 amino acid residues, including some of the important sites within the receptor (highlighted).

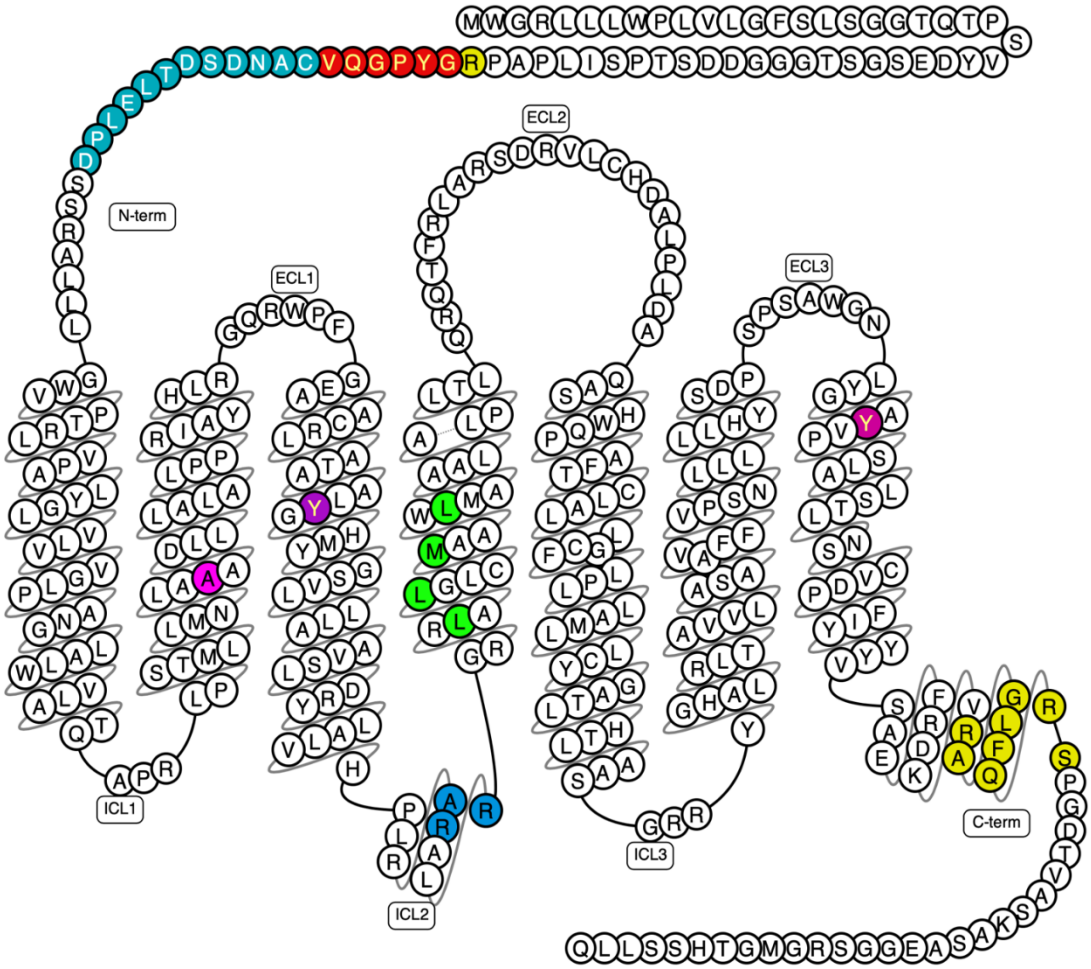

Figure 1.3 The structure of PAR4 showing all 385 amino acid residues. Thrombin cleavage site is shown between yellow (R47) and red (G48). Tethered ligand sequence is shown in red (GYPGQV). Turquoise sequence shows target of PAR4 function blocking antibody by Mumaw et al., 2014. Sequence (yellow) in the C-terminal tail has been shown to be responsible for regulating calcium signalling. Pink (A) shows site of $Ala^{120}Thr$ mutant. Purple (Y) shows site of Y157C mutant along with its proposed hydrogen bonding partner dark pink (Y) at Y322. $R^{183}AR$ shown in blue at ICL2 is arginine based RXR endoplasmic reticulum retention motif. L192 – L202 shown in green is the proposed leucine-rich zipper motif that was mapped by De La Fuente et al., 2012 and proposed to be important in PAR4 homodimerisation.

Once cleaved and activated, PAR4 tends to couple to two different G-proteins (Gq and G12/13) (Dorsam et al., 2002; Offermanns, 2006). Coupling of activated PAR4 with G-protein Gq results in calcium mobilisation and elevation and platelet shape change through the activation of PLCβ. PLCβ results in the hydrolysis of phosphoinositide to inositol triphosphate and diacylglycerol, which stimulates the endoplasmic reticulum to mobilise calcium and activate protein kinase C (PKC). This pathway ultimately results in platelet shape change, aggregation, adhesion and procoagulant activity (Coughlin, 2000; Dorsam et al., 2002). However, when activated PAR4 couples to G-protein G12/13, it activates RhoGEF, causing the activation of Rho, which activates RhoKinase and PLC to promote platelet shape change (French and Hamilton, 2016) (Figure 1.4).

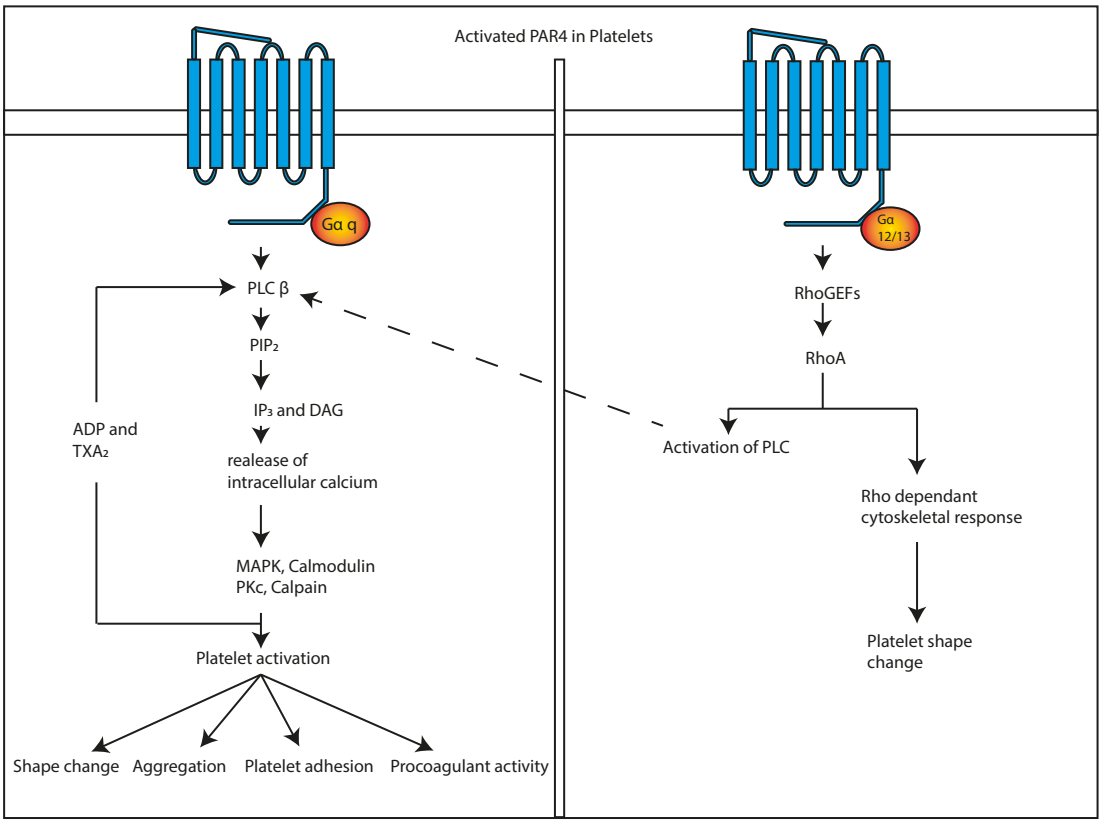

Figure 1.4 Signalling pathways in PAR4. Following PAR4 cleavage and activation, PAR4 signals via coupling to either G12/13 or Gq members. Signalling via Gq involves PLCβ hydrolysis of phosphoinositide and mobilization of calcium. This results in promotion of calcium mediated kinases mainly; MAPK, PKC, PLA_2 and calpain. These underlie PAR4 platelet activation and vascular remodelling. Signalling downstream of G12/13 is via RhoGEF and activation of Rho resulting in cytoskeletal responses and platelet shape change.

Receptor trafficking of PAR4 is a key regulator of signalling mechanisms and is of particular importance in PARs due to the irreversible cleavage and activation of the receptor (Smith et al., 2016). An important distinction between the receptor desensitisation of PAR4 and PAR1/2 is that PAR1/2 are rapidly desensitised via phosphorylation of the C-terminus and rapidly internalised. However, PAR4 contains a much shorter C-terminus than PAR1/2 and doesn't contain many phosphorylation sites compared to PAR1/2 – 8 for PAR4 and 13 for PAR1. As a result, receptor phosphorylation and receptor internalisation are much slower in PAR4, which was shown in a study where there was an 80% reduction in surface expression of PAR1 after 1 hour when stimulated with SFLLRN in comparison with PAR4, which showed only a 35% reduction in surface expression when stimulated with AYPGKF. Therefore, this results in a much more prolonged and sustained signal for PAR4 (Shapiro et al., 2000). Once internalised PAR4 is sorted into either lysosome (degradation) or endosomes (recycling), however, unlike PAR1 internalisation, which is dependent on the C-terminal tail, agonist-based internalisation of activated PAR4 receptors was shown to contain a tyrosine-based sorting motif in the intracellular loop-3 (ICL3), and tend to be mainly sorted to lysosomes for signal termination and degradation. In addition, inactivated PAR4 can be recycled tonically between endosomes and the cell surface to ensure continued agonist sensitivity without *de novo* receptor synthesis (Smith et al., 2016).

PAR4 is trafficked efficiently to the cell surface from the endoplasmic reticulum via Golgi after posttranscriptional modification via glycosylation (Hoxie et al., 1993). However, a recent study showed that PAR4 contains an arginine endoplasmic reticulum retention motif within the ICL2, which may regulate its expression on the surface. It was found that co-expression of PAR2 appeared to interfere with this endoplasmic retention motif on PAR4, enhancing PAR4 expression on the surface in a keratinocyte cell model and providing some context on regulating surface PAR4 expression (Cunningham et al., 2012).

PAR4 has also been shown to form dimers with other GPCRs, including homodimers and heterodimers. PAR4 has been shown to form stable heterodimers with PAR1. A Study shows that preventing this association impaired downstream signalling of either receptor and effectively prevented artery occlusion in an in vivo thrombosis mouse model (Leger et al., 2006). There has been no evidence thus far that PAR4 forms heterodimers with PAR3; however, given that mouse platelets express PAR3/4, it has been postulated that PAR3 serves as a co-factor for the efficient activation of PAR4 (Hakanishi-Matsui et al., 2000). In addition, PAR4 has been shown to form stable homodimers with the interaction mapped to transmembrane helix 4 of the receptor (De La Fuente et al., 2012). PAR4 homodimers were shown to be important for normal signalling after a study which mutated several regions in the transmembrane helix four region, preventing homodimer formation in transfected HEK293 cells reduced PAR4-mediated calcium signalling.

PAR4 has also been shown to form heterodimers with other GPCRs, including the $P2Y_{12}$ receptor, a_{2A}-adrenoreceptor and the B_2 bradykinin receptor. PAR4 has been shown to work in synergy with $P2Y_{12}$ to contribute to platelet activation and aggregation through TXA_2 synthesis and release of ADP, with work showing that PAR4 interacts directly with $P2Y_{12}$ (Khan et al., 2014). PAR4 has also been shown to interact with a_{2A}-adrenoreceptor, overcoming the inhibitory effect of aspirin in platelet activation through the activation of P2X1 ATP-gated calcium channels, negating the therapeutic effects of aspirin (French and Hamilton, 2016) (Figure 1.5).

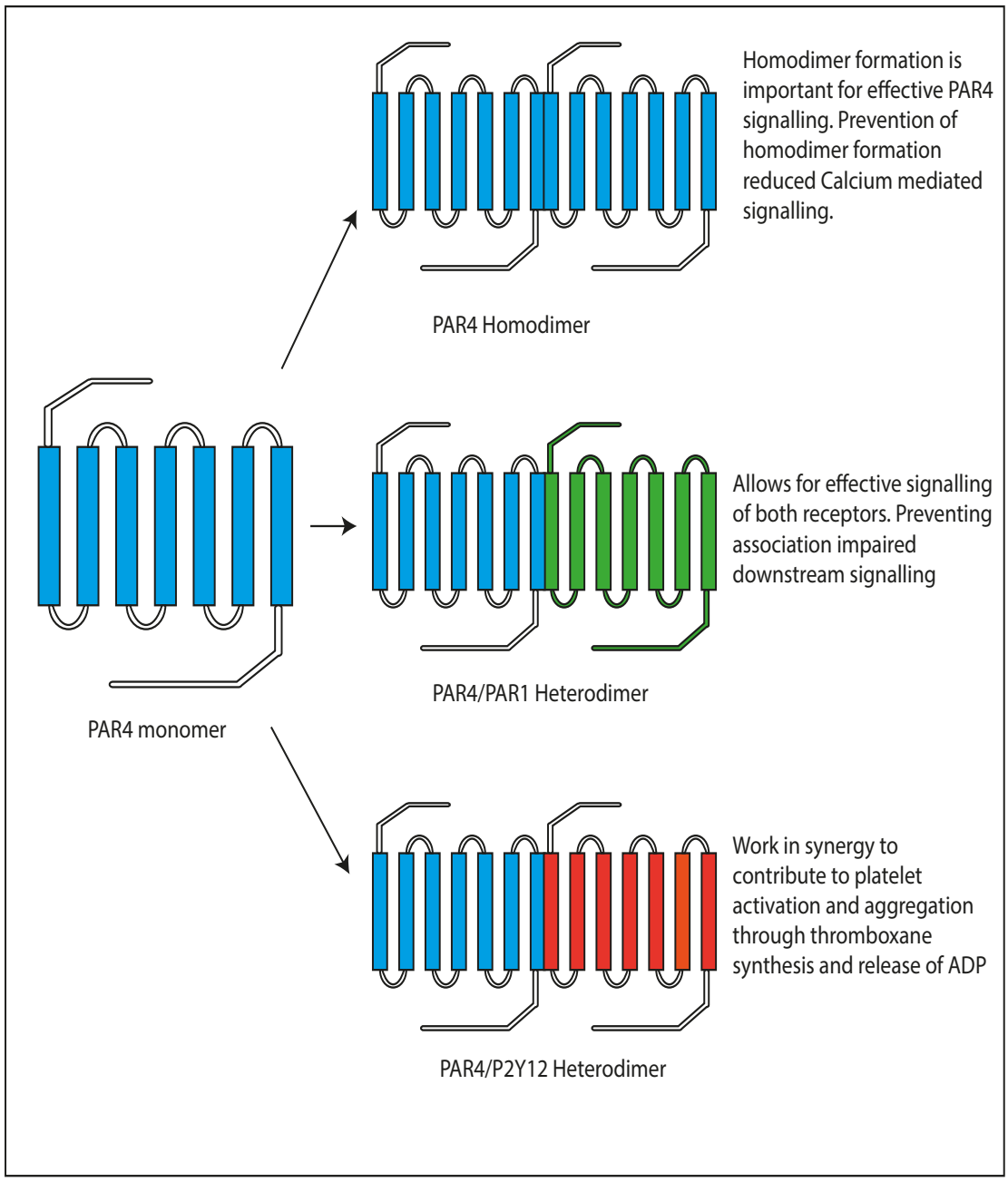

Figure 1.5 Dimerization partners of PAR4. PAR4 is believed to form homodimers which is important in normal intracellular signalling. It also forms heterodimers with PAR1 which enhances its cleavage via thrombin resulting in more efficient platelet activation. Dimerization with $P2Y_{12}$ results in synergy with the two receptors contributing to TXA_2 generation and ADP release. PAR4 is also believed to form heterodimers with Bradykinin B_2 with implication in inflammation.

1.6 Prevention of ACS

The key therapeutics in the prevention of ACS are a class of medications known as antiplatelet therapies. They also treat stable coronary artery disease and those undergoing revascularisation procedures. Four classes of drugs are currently approved for treating ACS, and each targets distinct pathways to prevent platelet activation (McFadyen et al., 2018).

1.6.1 Aspirin

Aspirin was a first-in-class non-steroidal anti-inflammatory drug (NSAID) initially synthesised by Felix Hoffman in 1897 and has been in commercial use since 1901. It works by blocking the metabolism of arachidonic acid (AA) and ubiquitous ω-6 polyunsaturated fatty acid released from phospholipid membranes in most cells in response to various stimuli. AA is a precursor to several biologically active molecules, including Thromboxane A_2 (TXA_2), Prostaglandin E_2 (PGE_2) and prostacyclin (PGI_2), all of which are crucial in the regulation of platelet activation (Gresele P, Deckmyn H, Nenci GG, 1991; Vezza et al., 1993). Aspirin exerts its pharmacological effect as an antiplatelet drug through the irreversible acetylation of cyclooxygenase-1 (COX-1), which cannot exert its effect on AA. This prevents COX-1 from converting AA into Prostaglandin G_2 (PGG_2) and Prostaglandin H_2 (PGH_2), which are the direct precursors of TXA_2 (C. Patrono., 1994).

Despite its short half-life in human circulation (Approx. 20mins), its effect on COX-1 is persistent and long-lasting in both circulating mature platelets and the bone,-marrow-derived megakaryocytic niche. This leads to a profound and long-acting inhibition of TXA_2 biosynthesis, which allows for a once-per-day dosing regimen of aspirin in most cases (Pedersen AK, 1984; Patrignani and Patrono, 2018). Despite its age, aspirin is still recommended as a first-line antiplatelet therapy requiring lifelong use in the majority of guidelines for the secondary prevention of recurrent cardiac events where it reduces the risk of

MI by ~25% in patients considered at high risk of secondary events, and reduces mortality by ~23% after an ACS episode. However, despite its success, aspirin suffers from the main pitfall of all subsequent anti-platelet drugs, which is the increased risk of bleeding; in particular, aspirin is associated with an increased risk of gastrointestinal (GI) bleeding. In addition, aspirin use in some patients results in incomplete inhibition of COX-1, non-responders, In particular patients with myeloproliferative neoplasms (MPNs), Obesity and type-2 diabetes (T2DM) (Gresele, 2013; Rodríguez et al., 2016; Patrono and Rocca, 2017).

1.6.2 $P2Y_{12}$ antagonists

ADP activates the P2Y12 receptor and has an important role in sustaining the activation of the major platelet integrin αIIbβ3. Antagonists of $P2Y_{12}$ work by inhibiting the amplification of platelet activation agonist ADP and exerting a potent antithrombotic effect (McFadyen et al., 2018). Inhibitors of $P2Y_{12}$ are comprised of two classes of drugs: thienopyridines (clopidogrel, ticlopidine and prasugrel) and nucleoside-nucleotide derivatives (cangrelor and ticagrelor) (Figure 1.6). The thienopyridines are all orally available prodrugs converted to active metabolites by CYP450 enzymes in the liver and irreversibly inhibit $P2Y_{12}$. Prasugrel is a second-generation thienopyridine with greater bioavailability, less interpatient variability and a more significant antithrombotic effect than first-generation clopidogrel (Wallentin et al., 2008). The other class of $P2Y_{12}$ inhibitors do not require metabolic activation by CYP450 and are direct-acting inhibitors. Ticagrelor is an orally available and irreversible inhibitor of $P2Y_{12}$. It achieves a faster, more predictable and more potent antiplatelet effect than clopidogrel, with peak inhibition of platelet aggregation (IPA) achieved at around 2 hours compared to clopidogrel, which can take up to 8 days to achieve full IPA (Husted et al., 2006). In contrast, Cangrelor is a reversible direct-acting inhibitor of $P2Y_{12}$; it has a rapid onset of action and a very short half-life of only 3-6minutes; this allows for a fast recovery of platelet

function and is a good candidate for patients undergoing revascularisation procedures (McFadyen et al., 2018).

Despite the success of achieving five P2Y12 antagonists reaching the market there is still invested interest in the development of novel agents in targeting the P2Y12 receptor. One such drug, Elinogrel (PRT-060128), is a reversible P2Y12 antagonist developed for oral or intravenous administration. It was shown in preclinical studies to display antithrombotic activity without the off-target effects on haemostasis, which is thought to contribute to bleeding, as in clopidogrel (Andre et al., 2011). Elinogrel was shown to induce rapid and potent inhibition of ADP-mediated platelet activation in a phase 1 clinical trial; this included patients who suffered from coronary artery disease (CAD) and who were non-responsive to previous treatment with clopidogrel (Andre et al., 2011). The study results showed that the drug was well tolerated and had no serious adverse effects, resulting in progression to a phase 2 trial.

The INNOVATE-PCI trial aimed to compare the efficacy of Elinogrel compared to clopidogrel in patients undergoing percutaneous coronary intervention (PCI). This trial showed that Elinogrel results in similar adverse events when compared to clopidogrel; however, with increased liver enzymes, dyspnoea and more adverse bleeding events in the Elinogrel arm were observed, requiring medical intervention. In addition, it was shown that there was no difference in the prevention of ischemic events compared to clopidogrel, which resulted in the termination of this drug in 2012 (Welsh et al., 2012).

One disadvantage of the current P2Y12 inhibitors is that in the event of MI, orally administered doses are poorly absorbed and take hours to reach maximal plasma concentrations. A novel 2-phenylpyrimidine-4-carbxamide drug, Selatogrel, was developed, which can be administered by subcutaneous injection and allows for easier self-dosing. The attractiveness of this drug is that it can be administered in unconscious patients or patients at the peak of an MI and provides rapid and potent reversible inhibition of P2Y12 (Storey et

al., 2020). Selatogrel has successfully passed preclinical, phase 1 and phase 2 clinical trials and has been shown to have an acceptable safety profile, with only minor bleeding and dyspnoea being reported (Sinnaeve et al., 2020). Following the success of phase I and phase II clinical studies of Selatogrel, fast-track status was granted by the FDA in March 2024 with the initiation of a large-scalephase III clinical trial (SOS-AMI) in active recruitment (NCT04957719:SOS-AMI). In addition, it was shown that there was no adverse reaction with current P2Y12-inhibiting drugs, meaning that transition to selatogrel for rapid intervention is possible. Selatorgel is currently undergoing a large-scale phase 3 clinical trial in patients with prior MI for self-injection for new acute onset chest pain (NCT04957719) (Schilling J, et al., 2021).

1.6.3 P2Y1 antagonists

Platelets express ADP receptors P2Y12 and P2Y1, and while there has been success in developing P2Y12 antagonists, it partially explains how platelet activation can still occur in non-responders via P2Y1. The demonstration that inhibition of P2Y1 can have antithrombotic responses in vivo using mouse models was demonstrated using a candidate antagonist, MRS-2179 (Léon et al., 2001). Subsequent further studies were performed using the candidate drug MRS-2500, an adenine nucleotide-based drug that was demonstrated to inhibit ADP-induced platelet aggregation both in vitro and in vivo. In mouse models, MRS-2500 displayed selective and potent inhibition of platelet aggregation in the collagen and adrenaline-induced thromboembolism model and the laser-induced arterial vessel injury model (Hechler et al., 2006). It prevented thrombosis in electrolytic-damaged carotid arteries in cynomolgus monkeys. It was also shown to have increased antithrombotic efficacy when used in combination with clopidogrel compared to either drug used alone (Hechler et al., 2006; Wong et al., 2016).

Another candidate molecule, GLS-409, an adenosine tetraphosphate (A4P) analogue, was shown to inhibit both P2Y1 and P2Y12 receptors. It was shown

to effectively, almost immediately, prevent thrombosis in a canine model with an insignificant effect on bleeding time (Gremmel, T. et al., 2017). However, despite promising results of P2Y1 antagonism in both in vitro and in vivo models, neither of these candidates progressed to human trials thus far.

1.6.4 $\alpha_{IIb}\beta_3$ inhibitors

These ligand-mimetic molecules prevent activated platelet aggregation by preventing fibrinogen binding. There are currently three drugs approved for use in this class: eptifibatide, a cyclic heptapeptide which contains a lysine-glycine-aspartic acid motif which mimics the binding site of fibrinogen on $\alpha_{IIb}\beta_3$, Abciximab, a humanised monoclonal antibody, and tirofiban, a non-peptide based small molecule that mimics the binding site of fibrinogen similar to eptifibatide (Figure 1.6) (McFadyen et al., 2018). These classes of drugs have been available since the mid-1990s and are potent antithrombotic drugs; however, bleeding complications occur in ~50% of patients administered with these drugs and, as such, have limited their clinical use to very high-risk sub-groups (Serebruany et al., 2004).

Despite falling out of favour for use in all but a select few patients due to their consequent severe bleeding profile, there has been a renewed interest in the development of new drugs which target the platelet integrin $\alpha_{IIb}\beta_3$. The molecule RUC-4 (zalunfiban) is a second generation $\alpha_{IIb}\beta_3$ antagonist that differs from first generation Abiximab, tirofiban and eptifibatide in that it locks the $\alpha_{IIb}\beta_3$ integrin within its inactive state by displacing the mg^{2+} from the ion-dependant binding site of the β_3 integrin (Xia et al., 2004; Springer et al., 2008). The currently available first-generation $\alpha_{IIb}\beta_3$ antagonist requires an initial bolus and continuous infusion via a pump to maintain their effects, limiting their use in the immediate emergency setting. RUC-4 differs in that it is administered via subcutaneous injection, which provides a rapid and potent inhibition of platelet aggregation within two hours and is fully reversible (Zhu et al., 2012; Li et al., 2014).

Initial studies were performed in non-human primates and administered at doses 1 – 3.86mg/kg, which led to dose-dependent inhibition within 15 – 30 minutes of platelet aggregation and lasted approximately 2 hours before restoration of platelet function with no adverse effects on safety were reported (Li et al., 2014). This led to progression to human phase 1 trials in which patients with stable coronary artery disease on aspirin monotherapy and healthy volunteers were administered RUC-4 following treatment with ADP to induce platelet activation. Treatment with RUC-4 produced potent platelet inhibition within 15 minutes of sub-cutaneous injection with the return of normal platelet function within 2 hours post-dose (Kereiakes et al., 2020). In addition, patients undergoing ST-elevated myocardial infarctions (STEMI) were administered a single subcutaneous dose of RUC-4 at doses of (0.075, 0.090 and 0.110mg/kg) which showed potent dose-dependant inhibition of platelet activation within 15 minsutes post-dose (Bor et al., 2021).

RUC-4 recently completed phase 2b and is undergoing a phase 3 clinical trial CELEBRATE to assess RUC-4 treatment in patients undergoing STEMI vs. placebo administered in the ambulance setting. The trial consists of 1600 patients and is a double-blinded, randomised, controlled international study to assess the effect treatment will have on restoring coronary artery blood flow before PCI in a hospital setting (NCT04825743) (Rikken et al., 2023).

1.6.5 Phosphodiesterase/ adenosine reuptake inhibitors

Platelets contain three main phosphodiesterases (PDEs) – PDE2, PDE3 and PDE5- accounting for most PDE activity within human platelets (Hidaka and Asano, 1976). PDEs work by hydrolysing cAMP and cGMP, reducing cAMP and cAMP activity within platelets. Phosphodiesterase inhibitors work as antiplatelet agents by preventing the activity of PDEs, therefore increasing cAMP and cGMP levels, which help to dampen the activation of $\alpha_{IIb}\beta_3$ integrin, rearrangement of the actin cytoskeleton and secretion of soluble agonists by

essentially interfering with all platelet activation signalling pathways (Sun et al., 2007). The drug Cilostazol works as a phosphodiesterase inhibitor. It is a quinolinone derivative that strongly inhibits PGE3 with (IC50 = 0.2μM) in platelets and smooth muscle cells via the lowering of intracellular calcium, consequently leading to platelet inactivation and vascular relaxation (Sun et al., 2007). In addition, cilostazol also acts as an adenosine reuptake inhibitor, therefore enhancing levels of adenosine, which in turn stimulates adenylyl cyclase, generating increased levels of cAMP.

The use of Cilostazol as an antiplatelet agent has been researched extensively, particularly in the context of two large-scale clinical trials, CSPS.com and PICASSO. The CSPS.com trial aimed at evaluating the combination of cilostazol with aspirin or clopidogrel to reduce the annual incidence of cardioembolic stroke and showed that incidence was reduced by half when used in combination compared to the use of monotherapy, particularly in high-risk patients (Toyoda et al., 2019). The PICASSO trial showed that Cilostazol was not inferior to aspirin in the prevention of cardiovascular events in ischemic stroke patients at high risk of cerebral haemorrhage but it did not reduce the incidence of haemorrhagic stroke when compared to aspirin (Kim et al., 2020).

Another drug, Dipyridamole, synthesised initially as a vasodilator for coronary arteries over 60 years ago, has also been shown to provide a robust antithrombotic effect by inhibiting platelet aggregation (Gibbs and Lip, 1998). It exerts its action by preventing the reuptake of adenosine by red blood cells, thus resulting in higher circulating levels of adenosine, which in turn bind to and activate platelet A_{2A} and A_{2B} receptors, therefore stimulating adenyl cyclase and generation of cAMP. In addition, Dipyridamole also acts as a phosphodiesterase inhibitor in platelets by inhibiting PDE3 and PDE5, albeit with a higher IC50 than the adenosine reuptake action (Kim and Liao, 2008). Despite previous use as an antiplatelet in the secondary prevention of MI and post-coronary artery bypass surgery, it only holds approval for use as an

adjunct treatment in patients undergoing replacement of cardiac prosthetic valves. However, more recently, Dipyridamole can now be used in conjunction with aspirin in patients for the secondary prevention of atherothrombotic cerebrovascular events following the success of two large-scale clinical trials (Diener et al., 1996; Halkes et al., 2006).

1.6.6 PAR1 antagonists

Human platelets contain both PAR1 and PAR4, with the original theory being that PAR1 was the primary thrombin receptor, with PAR4 serving as a redundant backup (Coughlin, 2000; Han and Nieman, 2018b). As such, the focus is on targeting PARs as an antiplatelet strategy focused on PAR1. This led to the development of the small molecule inhibitor based on the natural product himbacine, Vorapaxar (Figure 1.6) (Chackalamannil et al., 2008). Vorapaxar is a potent, reversible and orally available inhibitor of PAR1, preventing thrombin-mediated platelet activation (McFadyen et al., 2018). Vorapaxar was approved for clinical use in 2014 based on the results of two large-scale phase 3 clinical trials. The Thrombin receptor antagonist in secondary prevention of Atherothrombotic ischemic events-thrombolysis in myocardial infarction 50 (TRA 2P-TIMI 50) trial found a significant reduction in mortality, non-fatal MI, non-fatal stroke and composite cardiovascular death; however, it showed an increased risk of intracranial haemorrhage in patients with a history of ischemic stroke and was therefore not recommended for use in this patient group (Scirica et al., 2012). The second large-scale trial, Thrombin Receptor Antagonist for Clinical Event Reduction in Acute Coronary Syndrome (TRACER), showed a reduced risk of death from cardiovascular causes when compared to placebo. The triple antiplatelet arm (vorapaxar, aspirin and clopidogrel) showed a significantly increased risk of bleeding compared to placebo with aspirin and clopidogrel. Of more concern, the risk of intracranial haemorrhage was found to be five-fold higher in vorapaxar-treated patients compared to placebo. This increased risk of intracranial haemorrhage resulted in the trial being stopped six months earlier than the planned end-

point (Tricoci et al., 2012). Schering-Plough originally developed Vorapaxar under the candidate name SCH-530348 before the company was acquired by Merck in 2011. More recently, however, the rights to sell Vorapaxar in the US and Canada were bought by Aralez Pharmaceuticals in 2016, and it retained its FDA approval as a secondary prevention drug for cardiovascular events in the US; Vorapaxar was never approved for use in the EU (Algahtani, 2017). More recently, Aralez Pharmaceuticals was bought over by Nuvo Pharma in 2019, resulting in Nuvo Pharma acquiring Vorapaxar. The bleeding profile associated with using Vorapaxar has limited its use in the clinic, and as such, attention has turned to PAR4 as a novel antiplatelet strategy.

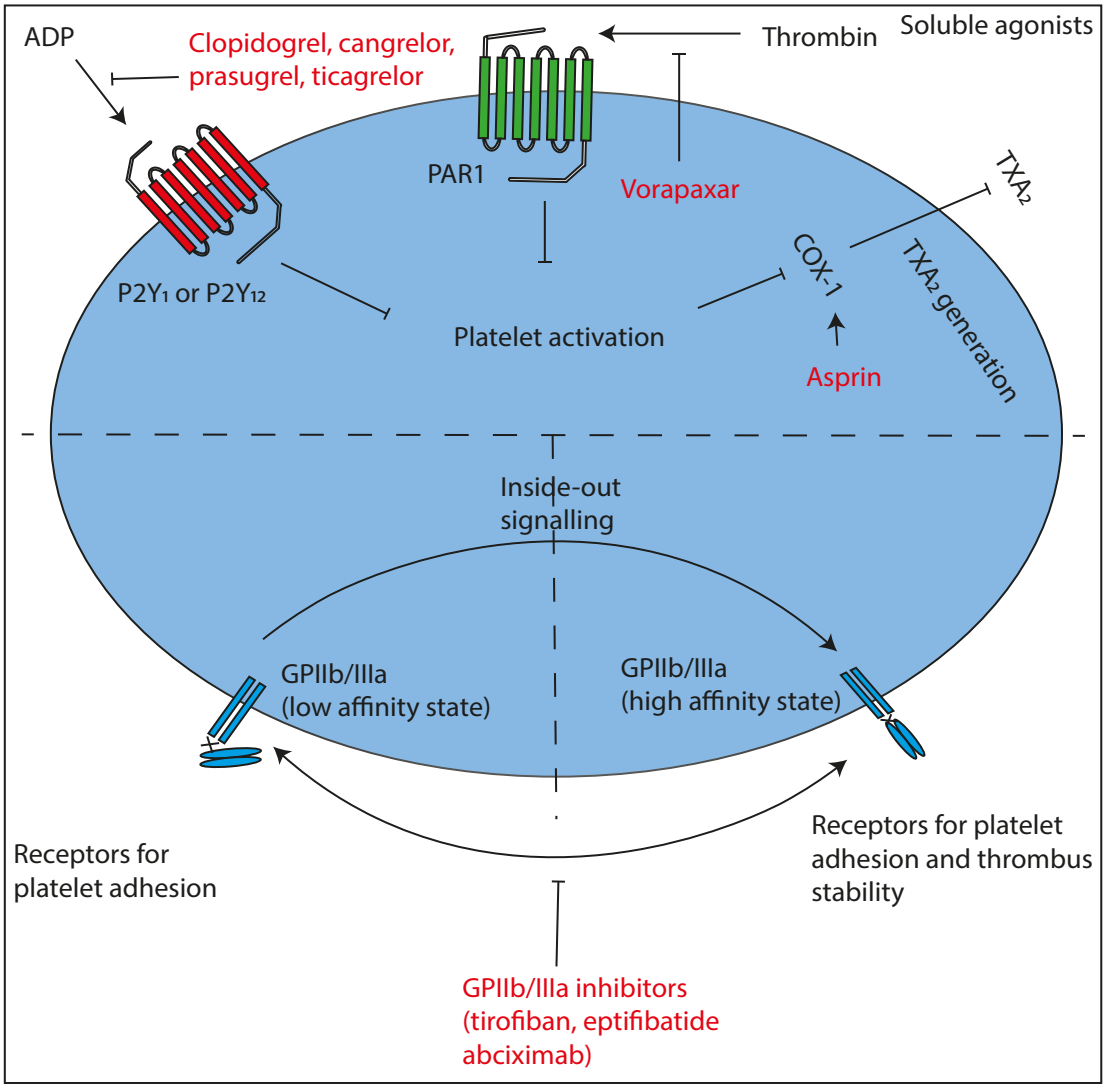

Figure 1.6 Currently available antiplatelet therapies and their targets. An overview of the current antiplatelet strategies available in the clinic and their major target and mechanism of action on platelets (red). Clockwise: $P2Y_{12}$ inhibitors (clopidogrel, cangrelor, prasugrel and ticagrelor) work by antagonizing the $P2Y_{12}$ receptor preventing the binding of ADP to the receptor reducing activation and aggregation. Vorapaxar is the first in class inhibitor of PAR1 which potently inhibits the activation of PAR1 by thrombin. Aspirin is an irreversible inhibitor of the enzyme COX-1 which is essential in the generation of TXA_2 therefore preventing the activation and aggregation of platelets by TXA_2. GPIIb/IIIa inhibitors work by preventing the binding of fibrinogen to GPIIb/IIIa therefore preventing aggregation of activated platelets.

1.7 Novel antiplatelet targets

1.7.1 CLEC-2

CLEC-2 is a type-II transmembrane that exists as a dimer and contains an extracellular lectin-like recognition domain and a short cytoplasmic tail with a single YxxL sequence. CLEC-2 is highly expressed in megakaryocytes and platelets and contains around 2000-4000 copies per platelet (Meng et al., 2021). It is required for GPIb$_{\alpha}$-vWF signalling via interaction GPIb$_{\alpha}$ in a sialylation-dependant manner and is required for the activation of $\alpha_{IIb}\beta_3$ integrin. Interest in targeting CLEC-2 as a novel antithrombotic target came from the deletion of CLEC-2 in mouse platelets in a mouse model of TTP, which led to a decrease in thrombus formation and thrombocytopenia (Shao et al., 2022). However, given CLEC-2 being essential in various biological processes, such as the development of lymph nodes, maintaining the integrity of endothelial venules, and development of lymphatic vasculature, the targeting of CLEC-2 may lead to undesirable side effects (Herzog et al., 2013; Benezech et al., 2014; Boulaftali et al., 2014).

However, despite this, interest in developing pharmacological inhibitors of CLEC-2 continues to be pursued, with the development of a small molecule derived from 4-O-benzoyl-3-methoxy-beta-nitrostyrene (2CP) being shown to act as an inhibitor of platelet aggregation (Chang et al., 2015). In addition development of a recombinant rhodocytin (obtained from the venom of the Malayan pit viper) was developed using deletion mutant and site mutagenesis approaches. It was shown to inhibit CLEC-2-podoplanin interaction dependant human platelet interaction (Sasaki et al., 2018) (Figure 1.7). Despite these developments, no evidence of moving into human trials of CLEC-2 antagonism for antiplatelet therapies has been explored.

1.7.2 GPVI/Collagen interaction

Being a member of the Ig superfamily, the GPVI receptor is associated with dimeric Fc receptor γ-chain (FcRγ) and is a covalently linked homodimer. Each GPVI monomer contains an immune receptor tyrosine-based activation motif (ITAM), essential for GPVI receptor signalling in platelets (Bergmeier and Lucia, 2013). GPVI is expressed exclusively on megakaryocytes and platelets (3000 – 4000 receptors per platelet) and is the primary receptor for collagen signalling (Mangin et al., 2012). Collagen binds GPVI via the D1 domain through a glycine-proline-hydroxyproline sequence, leading to phosphorylation of the Immunoreceptor tyrosine-based activation motif (ITAM) and cascade reaction involving Src kinase phosphorylation, binding of the syk SH_2 domains and activation of phospholipase-$C_{\gamma 2}$ ($PLC_{\gamma 2}$) (Bergmeier and Lucia, 2013).

Regarding targeting GPVI to prevent collagen-induced activation of platelets, two molecules have shown promise in studies. The first is Revacept, a fully human recombinant fusion protein consisting of the Fc part of human IgG1, a hinge region, and the extracellular domain of human GPVI, which displays a high affinity for collagen. In pre-clinical in vitro studies, Revacept, combined with aspirin and a P2Y12 antagonist, displayed synergistic effects in preventing platelet aggregations from atherosclerotic plague homogenates than either of the drugs alone (Munoz et al., 2017). In vivo studies using doses (1 -10mg/kg) showed that Revacept inhibited thrombus formation at the site of vascular injury, reduced infarct size and subsequent oedema following ischemic stroke, and improved vascular dysfunction and thrombus size (Massberg et al., 2004; Ungerer et al., 2013).

Successful preclinical testing of Revacept resulted in progression to phase I clinical studies to evaluate PK/PD in a dose escalation study (10 – 160mg/kg), which showed the drug was well tolerated with no apparent side effect or increased bleeding profile. It also showed that inhibition of platelet aggregation

occurred within 2 hours of dose administration and lasted up to 24 hours (Ungerer et al., 2011). In addition, two phase II clinical studies have been conducted. The first involving 334 patients with stable coronary artery disease who were undergoing elective PCI were administered 80mg/kg, 160mg/kg or placebo on top of standard therapy for PCI (clopidogrel, aspirin and heparin (or bivalirudin)). The endpoint was determined as either death or myocardial injury (raised troponin) following revascularization. Results concluded that administration of Revacept did not prevent myocardial injury compared to placebo and standard therapy. However, no increase in bleeding events was recorded in the Revacept arm compared to placebo (Mayer et al., 2021). The other phase II study looked at patients with symptomatic coronary artery stenosis who were at high risk of recurrent ischemic events. It was found that administration of 120mg/kg Revacept on top of standard antiplatelet therapy reduced the recurrence of an event when compared to placebo (Uphaus et al., 2022).

The second ACT017 (Glenzocimab) is an antibody fragment (Fab), a humanised monoclonal antigen-binding fragment directed against human platelet GPVI. It was shown to inhibit collagen-stimulated platelet aggregation and procoagulant activity, as well as thrombus formation and platelet adhesion under arterial flow conditions on collagen-coated surfaces. This was achieved without causing thrombocytopenia or down-regulation of GPVI (Lecut et al., 2003; Mangin et al., 2012; Lebozec et al., 2017). In addition, studies on non-human primates showed that treatment with Glenzocimab was well tolerated without increased bleeding time or events of spontaneous bleeding (Lebozec et al., 2017; Jadoui et al., 2021).

The success of pre-clinical testing resulted in Glenzocimab progressing into phase I clinical trials on healthy volunteers in a dose escalation study. Results showed a dose-dependent inhibition of collagen-induced platelet aggregation with no adverse events or prolongation of baseline bleeding time (Voors-Pette et al., 2019). Progression onto phase II studies, with two underway, the first in

patients with acute stroke, known as the ACTIMIS study (NCT03803007), has completed evaluation with results in preprint for publication (Mazighi et al., 2023). The other is looking at adding Glenzocimab on top of standard therapy rt-PA (Alteplase), given within the first 4.5 hours following acute ischemic stroke, which is in Phase II/III for the evaluation of safety and efficacy of this combination ACTISAVE (NCT05070260), the trial is still ongoing (Figure 1.7).

1.7.3 GPIb-vWF interaction

The vWF-binding GPIb-IX-V complex, of which GPIb is a central component, is critical in initiating thrombus formation under high-shear stress, such as in arterial blood flow. It is a leucine-rich repeat protein family member and is a type-1 transmembrane receptor of which vWF is the main ligand. Other ligands such as $\alpha_M\beta_2$ integrin, P-selectin, thrombospondin, thrombin, and Factors XI and XII also activate GPIb. The importance of GPIb-IX-V has been shown in the genetic disease Bernard-Soulier syndrome, in which deficiency of GPIb-IX-V causes macrothrombocytopaenia and prolonged bleeding times (Andrews and Berndt, 2013; Bury et al., 2021).

vWF acts as a molecular bridge between sub-endothelial collagen and platelets and as a chaperone for factor VIII, protecting it from proteolytic inactivation and during vascular damage and exposure of sub-endothelial collagen, vWF to bind, causing a conformational change which uncoils it, allowing for the exposure of the GPIb binding site that mediates platelet adhesion. The binding of GPbI to vWF depends on the interaction of the vWF A1 domain; the higher the shear stress, the more efficiently binding occurs due to the enhanced uncoiling of vWF (Paolo Gresele, Gustav V.R. Born, Carlo Patrono, 2012). At shear stresses above 1500 $s^{-1,}$ platelet adhesion to damaged vasculature is purely dependent on vWF/GPIb interaction for adhesion, making it particularly important in the case of atherothrombosis, where resultant shear stress can be especially high (Gragnano et al., 2017).

Various molecules have been developed that target the vWF/GPIb axis, most of which are still undergoing preclinical validation. However, one candidate Anfibatide, a snaclec (snake C-type lectin) purified from the venom of the Agkistrodon actus snake, has successfully progressed to human clinical trials. It was shown to inhibit both vWF and α-thrombin binding to GPIb (Lei, A., et al. 2014). Preclinical investigations confirmed its specificity to GPIb by inhibiting restocetin-induced platelet aggregation in human and murine ex-vivo platelets but not ADP, collagen and TRAP-induced platelet aggregation (Li et al., 2015). Its success in vivo animal models showed it inhibited thrombus formation in laser-induced and ferric chloride-induced platelet aggregation in mesenteric and cremaster arteries in mice (Lei, A., et al. 2014).

Phase I studies to assess the PK/PD in humans involved 94 healthy volunteers receiving a 24-hour infusion of Anfibatide. Results showed up to 90% inhibition of ristocetin-induced platelet aggregation with no significant increases in bleeding time or alteration to blood coagulation. The effects of the drug were shown to be completely reversed after 8 hours post-withdrawal. No observable thrombocytopenia or anti-anfibatide antibodies were observed during the trial (Li et al., 2021). There was a phase II study conducted in which patients with NSTEMI were randomised to receive an i.v bolus of Anfibatide (2, 3 or 5U/60kg) vs placebo on top of normal antiplatelet therapy (aspirin and clopidogrel). Results showed that administration of Anfibatide was safe in patients; however, the study wasn’t large enough to fully evaluate the antithrombotic efficacy of Anfibatide administration (Zheng et al., 2021) (Figure 1.7).

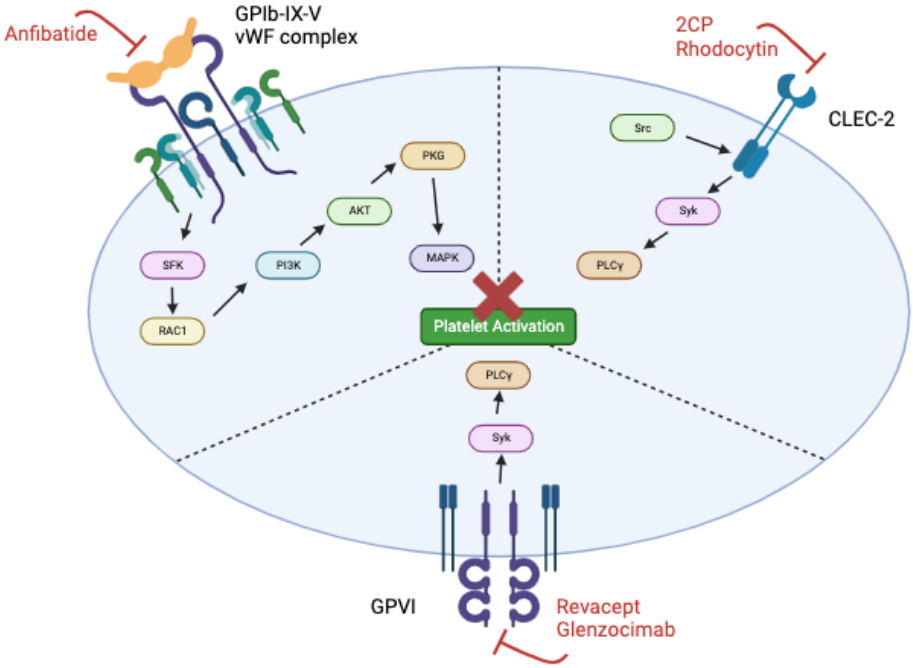

Figure 1.7. Novel Targets of Anti-platelet therapy currently undergoing clinical evaluation. Shows current novel antiplatelet treatments which have progressed into clinical evaluation and their targets and downstream signalling cascades that they inhibit.

1.8 Targeting PAR4

As previously discussed, PAR4 is now recognised as an essential receptor in platelet activation and thrombus formation in the presence of higher concentrations of thrombin, EC50 of 5nM, compared to PAR1, with EC50 of 0.2nM. In the pathological context, PAR1 is responsible for initiating thrombus formation, whereas PAR4 was shown to be more important for rapid thrombi growth, platelet accumulation and stability of the thrombus further away from the vessel wall. This was shown in a study of vessel injury in wt-PAR4 and PAR4$^{-/-}$ mice (Vandendries et al., 2007). PAR4 activation results in sustained calcium signalling primarily due to the continued presence of catalytically active thrombin and is, therefore, more effective in mounting calcium signalling responses in an autocrine fashion from secreted ADP. This sustained high intracellular calcium levels helps to enhance thrombi growth and stability throughout the late phase of platelet aggregation (Covic et al., 2000). As such, it has become an attractive target as a novel antiplatelet therapy for treating ACS, and various strategies have been employed to target it (Rudinga et al., 2018).

1.8.1 PAR4 antibodies

Various PAR4 function-blocking antibodies have been developed and work by blocking the cleavage site of PAR4 by thrombin or the thrombin binding site on PAR4. These include a rabbit polyclonal antibody which blocks the thrombin cleavage site on PAR4 and was shown to prevent human platelet aggregation at a dose of 1mg/kg, an antibody against the PAR4 sequence C54ANDSDTLELPD a site essential for thrombin interaction with PAR4 and was shown to inhibit activation in the presence of PAR activating peptide AYPGKF (Mumaw et al., 2014). In addition, various other antibodies have been developed, which are not mentioned here; however, there is no evidence of these function-blocking antibodies being tested in humans (Rudinga et al., 2018)

1.8.2 Peptidomimetics

Two compounds have been developed by adding a trans-cinnamoyl (tc) group to the peptide; these are tc-YPGKF-NH2 and tc-APGKF-NH2, with studies showing that they inhibited the aggregation of human platelets in vitro as well as demonstrating potent inhibition of mouse platelets. They work by binding to the amino terminal part of PAR4, thus preventing the cleavage and exposure of the tethered ligand. However, these classes of compounds have shown a limited capacity to be used as an effective inhibitor in humans; no evidence of progressing these to human studies is available (Rudinga et al., 2018).

1.8.3 YD-3

1-benzyl-3 ethoxy carbonyl phenyl-indazole (YD-3) was the first low molecular weight antagonist of PAR4 discovered (Le et al., 2001; Wu et al., 2002a). Studies showed that this compound selectively prevented platelet aggregation in rabbits with an IC_{50} of 28μM and PAR4 platelet activation with PAR4-AP but not to thrombin concentrations lower than 0.5nM in human platelets that express both PAR1 and PAR4. (Wu et al., 2002b, 2003) The ability to progress this compound to human studies has been stalled due to its high lipophilicity; however, it remains used as a research tool in PAR4 studies (Rudinga et al., 2018).

1.8.4 Pepducins

Lipidated peptides, pepducins easily pass through the cell membrane to exert their effects; the pepducin designed to target PAR4 combines the N-terminal end of the peptide with a palmitate (pal) and is known as P4pal-10. Specifically, P4pal-10 has sequence specificity to the intracellular loop 3 (ICL3) of the PAR4 receptor and works by preventing G-protein coupling, thus preventing downstream activation signalling. Studies showed this pepducin inhibited human platelet aggregation when exposed to PAR4-AP and increased tail

bleeding time in mice (Covic et al., 2002). However, even with their ability to effectively inhibit platelet aggregation, pepducins of PAR4 still lack the specificity to make them effective candidates, which has resulted in the stalling of their clinical development (Carr et al., 2016; Lind et al., 2019).

1.8.5 The promise of success (BMS-986120/986141) and beyond

In a screen of 1.1 million compounds by Bristol-Meyers Squibb (BMS), candidate BMS-986120 was shown to be an effective and selective antagonist of PAR4. BMS-986120 is a novel, first-in-class, reversible, highly selective, orally available PAR4 antagonist. In preclinical studies, it was shown to decrease thrombus weight by over 83% in monkeys and increase bleeding time by 2-fold compared to the current standard of care drug clopidogrel (Wong et al., 2017). Success in these preclinical studies has resulted in BMS-986120 reaching phase I clinical trial (NCT02439190). The parallel group prospective randomised open-blinded end-point (PROBE) trial showed a substantial reduction in thrombus formation in conditions of deep arterial injury in the stenosed coronary artery in an *ex vivo* human model (Wilson et al., 2018). However, despite showing success with efficacy and lack of adverse effects, no phase II studies of this compound were undertaken. Instead, a related compound, BMS-986141, also underwent a phase I study (NCT02341638) and progressed to a phase II clinical trial (NCT02671461) to prevent mini-strokes (French and Hamilton, 2017). In addition, recently published research has shown BMS986141 to be a safe and effective PAR4 inhibitor in a dose escalation study in healthy Japanese and non-Japanese participants (Merali et al., 2023). A further study has shown that PAR4 antagonism with BMS141986 had additive antithrombotic effects in patients with stable coronary artery disease who received ticagrelor, aspirin, or a combination (Nash et al., 2024)of both. Despite published research on the effectiveness of BMS141986 as a potent and selective PAR4 antagonist, evidence of the drug candidate identity has been removed from Bristol Myers Squibb pipeline,

indicating that despite its promise, it is unlikely BMS is pursuing it any further clinically.

In addition, a compound SCH-28, a synthetic non-anticoagulant heparin analogue, targets a novel site on PAR4 at exosite II and is found to specifically inhibit PAR4 activation without significant anticoagulant activity. It inhibited thrombus formation in vitro, representing a promising novel target (Lin et al., 2019).

1.9 Importance of actin/tubulin dynamics in megakaryopoesis and platelet production

Megakaryocytes undergo complex developmental stages to produce platelets and maintain a circulating volume of 150 – 400X10^9/l platelets in human blood (Leeksma and Cohen, 1955; Giles, 1981). These can be surmised into four main stages: maturation, extension of proplatelets, delivery of proplatelet cargo, and platelet release. In order to achieve this, megakaryocytes have to dynamically alter their actin and tubulin cytoskeletons at various stages. The molecular mechanisms and downstream regulators of this have been identified through various techniques to derive specific phenotypes (Poulter and Thomas, 2015).

In the context of normal cells during cellular division, they increase their nuclear content from 1N to 2N to produce identical daughter cells. The process of cellular fission is driven by RhoA, a small GTPase recruited to the cellular furrow and promotes division through F-actin and contraction via myosin-II (Pecci, V., et al. 2011). However, in the context of megakaryocytes, they must undergo multiple cycles of endomitosis to increase their ploidy from 2N up to 128N. Therefore, they need to prevent cell division from taking place. Two Rho-GEFS GEF-H1 and ECT2 are required to localise and activate RhoA at the cleavage furrow; in megakaryocytes, this is downregulated during their

maturation (Gao et al., 2012). The subsequent inactivation of RhoA is what drives the polyploidisation of megakaryocytes. This has been demonstrated in mice RhoA$^{-/-}$ megakaryocytes, which are larger and have an even higher level of ploidy than their wild-type counterparts (Suzuki et al., 2013).

Extending proplatelets from the vascular niche into the sinusoidal blood vessels requires the action of both actin and microtubular systems to work concordantly to produce platelets. Actin works by helping megakaryocytes adhere to and degrade the basement membrane using specialised structures called podosomes (Schachtner et al., 2013). In addition, actin does not prevent the production of proplatelets, as was demonstrated by the pharmacological inhibition of actin; however, it was shown that actin aids in the bifurcation of proplatelet tips, increasing the tip number (Italiano et al., 1999). Microtubules are, however, essential in producing proplatelets, though not by the classical polymerisation of tubulin but instead via the sliding of microtubules driven by the motor protein dynein, which drives the extension of proplatelets into the vascular blood vessels (Italiano et al., 1999; Patel et al., 2005; Bender et al., 2015). Studies of molecular regulators of cytoskeleton dynamics have displayed their importance in forming proplatelets. Studies in RhoA$^{-/-}$ mice show macrothrombocytopenia, suggesting it as a regulator of proplatelet formation with likely causes due to membrane stiffness and deformity (Pleines et al., 2012; Suzuki et al., 2013). In addition, the PKC isoform PKC$_\varepsilon$ is a known modulator of RhoA activity, and mice with knockdown of PKC$_\varepsilon$ again display aberrant proplatelet formation, confirming the role of RhoA-mediated cytoskeleton dynamics in proplatelet formation (Gobbi et al., 2013).

Megakaryocytes undergo numerous endomitotic cell cycles to increase their nuclear content, partly to produce the cargo necessary to be packaged into platelets before release into the bloodstream. However, no direct link of the actin cytoskeleton in cargo shuttling from the megakaryocyte into the proplatelet tip has been established. The role of microtubules in this process has been well-characterised. The motor protein kinesin is responsible for the

shuttling of cargo along microtubules into the proplatelet tip and the sliding of microtubules, aiding in this process (Patel et al., 2005; Richardson et al., 2005). Furthermore, the importance of cytoskeletal dynamics in granule production has been shown through specific knockouts of cytoskeletal regulators CDC42 and RAC1. CDC42 and RAC1 are small Rho GTPases, with CDC42 being a master regulator of actin and microtubule cytoskeleton dynamics (Pleines et al., 2010). Studies on mice with a double knockout of both CDC42/RAC1 display a severe macrothrombocytopaenia phenotype, with the study also showing its importance in proper formation of the demarcation membrane system, trafficking of granules and cargo, protein synthesis and megakaryocytes structural integrity during maturation (Pleines et al., 2013).

The final stage of platelet production occurs in the bloodstream and involves pre-platelets (2μM - 10μM), which are discoid and barbell-shaped platelets. It has been shown that the tubulin cytoskeleton is responsible for the interconversion of pre-platelets and barbell-shaped platelets due to microtubule twisting (Thon et al., 2010). In addition, the terminal stage of platelet formation is the fission of preplatelets into two terminal blood platelets. The microtubule coil is driven at each end of preplatelets and accelerated by the sheer force of blood.

1.10 Actin dynamics in platelet shape change and spreading

Within the circulation platelets maintain a discoid shape aided by maintaining a complex actin cytoskeleton (Smyth et al., 2015). However, in contrast to most mammalian cells, platelets must have the ability to rapidly react and dynamically change their shape to respond to and plug sites of vascular injury, prevent blood loss, and maintain haemostasis. The ability of platelets to achieve this is driven by an ability to rapidly rearrange their cytoskeleton in response to agonist stimulation of platelet GPCRs. In general, two main steps

in agonist-induced platelet shape change result in the formation of a stable platelet plug: actin severing, resulting in platelets forming spheres, and actin assembly, resulting in the formation of lamellipodia and filopodia (Figure 1.8) (Sandmann and Köster, 2016).

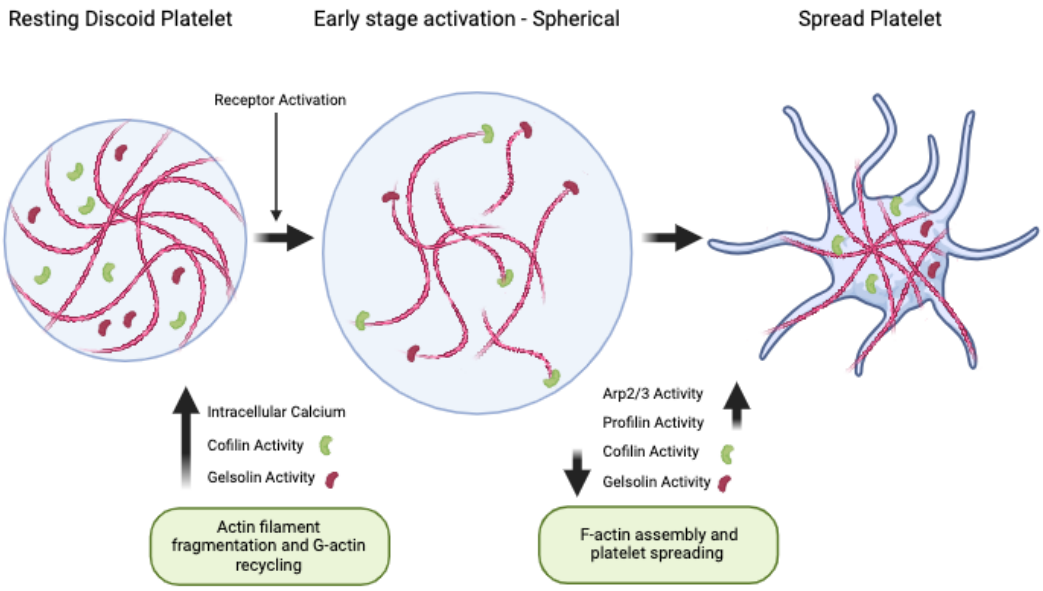

Figure 1.8. Alteration of the actin cytoskeleton in Platelets following activation. Following receptor activation (PAR1, PAR4, GPVI, P2Y12 etc.) via engagement of a platelet activating ligand (Thrombin, collagen, ADP etc.), resting platelets which are discoid in shape increase intracellular calcium, activate Cofilin and Gelsolin resulting in the severing of F-actin. Platelets then take on an enlarged spherical shape due to the loss of actin cytoskeletal structure. Platelets then down regulate Cofilin activity via phosphorylation and upregulate the activity of Arp2/3 and profilin resulting in the formation of new F-actin filaments and the projection of lamellipodia and filipodia resulting in platelet spreading and aggregation.

Each stage of platelet shape change involves the participation of a variety of actin-related proteins, which are activated downstream of GPCR receptor activation. The first stage consists of severing actin filaments, resulting in platelets becoming spherical. This is followed by dismantling spectrin networks composed of filamin A, spectrin and GPIb/IX. While at rest, actin filaments extend from the core to the plasma membrane and are tightly bound to the membrane skeleton by spectrin/filamin A complexes (Kovacsovics and Hartwig, 1996). Upon agonist receptor engagement, downstream activation of PLCγ induces the generation of inositol-1, 4, 5-triphosphate (IP3), which increases intracellular calcium (Berridge et al., 2000; Zheng et al., 2015). One protein responsible for severing actin filaments and capping the barbed ends is an actin-binding protein, Gelsolin. At normal physiological levels of intracellular calcium, gelsolin is inactive but switched to an active state upon increases in intracellular calcium. After fragmentation, gelsolin binds to the barbed ends, preventing actin assembly (Smyth et al., 2015). Another important protein at this platelet activation stage is an actin-binding and severing protein, Cofilin; in its phosphorylated state, Cofilin remains inactive, unable to bind actin. However, upon increases in intracellular calcium, an activator of Cofilin Slingshot homolog phosphatase-1 (SSH1) dephosphorylates Cofilin, allowing it to bind and sever actin filaments (Bravo-Cordero et al., 2013).

The second stage, which involves spherical platelets beginning to spread and form lamellipodia and filopodia, achieves this through various mechanisms. First, it must expose the barbed end of actin to allow actin nucleation and the formation of new actin filaments. Polyphosphoinositides (PPI) are upregulated and are known to deactivate gelsolin, dissociating from the cap of actin filaments and exposing the barbed end for nucleation and elongation (Smyth et al., 2015). The formation of lamellipodia is driven by the GTPase Rac1, which activates the WASP-family verprolin-homologous complex (WAVE), resulting in Arp2/3 activation (Miki et al., 1998). Filipodia works similarly and is driven by the GTPase CDC42, which activates Wiskott-Aldrich syndrome

proteins (WASP), which in turn activates the ARP2/3 complex, resulting in the activation of actin barbed ends, allowing for actin elongation (R Rohatgi et al., 1999). In addition to these two main pathways, a group of proteins known as formins have also been linked to actin elongation, in particular mDia and Daam, which are activated by Rho GTPases and work by exposing the central domain for actin polymerisation to become exposed, allowing for the formation of actin filaments and elongation to occur (Kühn and Geyer, 2014).

1.11 Aims and Hypothesis

Given that PAR4 is largely accepted to control platelet shape change, mapping of the PAR4-protein interaction network was focused on actin-related proteins, with the hypothesis that it may reveal new avenues that could be important for PAR4 platelet function. This research aimed to uncover new regulatory mechanisms of PAR4, providing a foundation for innovative therapeutic approaches to manage platelet-related disorders in ACS.

We aimed at identifying and investigating novel regulatory pathways and protein interactions involved in PAR4 activity. Proteomic datasets were employed using previously published PAR4 recombinant tools (Cunningham et al., 2012). Quantitative proteomics using Stable Isotope Labelling by Amino Acids in Cell Culture (SILAC) on recombinant PAR4-CFP HEK293 cells was used to identify novel actin-related regulatory proteins and pathways that modulate PAR4 activity. This hypothesis is grounded in the premise that understanding the protein interactions and pathways involved in PAR4 regulation will provide insights into how platelet function can be controlled, potentially leading to more effective treatments for thrombotic diseases.

Chapter Two:

Materials and Methods

2. Materials and Methods

2.1 Materials

Table 2.1 List of materials used

Company	*Material*
Fisher scientific (Geel, Belgium)	Tris base
	Sodium Dodecyl sulfate (SDS)
	Glycine
	Methanol
	Sodium Chloride
	N,N,N',N'-tetramethylethylene-1,2-diamine (Temed)
	Bovine serum albumin (BSA)
	Ammonium Persulfate (APS)
Sigma-Aldrich (now Merck, UK)	Dimethylsulfoxide (DMSO)
	Hydrogen peroxide (H_2O_2)
	β-Mercaptoethanol
	Tween-20
	Luminol
	p-coumeric acid
	Mowiol 4-88
	Triton-X100
	Formaldehyde (36% solution)
	Glutamine (200 mM)
Biosera FR (Rue de la Caille, France)	Foetal Calf serum (FCS)
	Pen/Strep
Oxoid (Hampshire, England)	Phosphate buffered saline (PBS) Tablets
Life technologies (Paisley, Scotland)	Dulbecco's Modified Eagle Medium (DMEM)
	Minimum Essential Medium (MEM)
	Rosewell Park Memorial Institute-1640 (RPMI-1640) medium

	Geneticin (50mg/mL) Accutase
Carl Roth (Karlsruhe, Germany)	Acrylamide (30% (w/w))
GE Healthcare Life sciences (Chicago, USA)	Nitrocellulose membranes 0.45μm pore size
Polysciences, Inc	Polyethylenimine (PEI)
Thermofisher Scientific (Paisley, Scotland)	Bovine Fibronectin 2mg

Table 2.2 List of Prepared solutions and recipes

Solution	*Recipe*
PBS	1X PBS tablet per 100mL dH_2O (pH 7.4)
Buffer 1 – resolving gel	1500 mM Tris base, 500 mM sodium dodecyl sulfate (SDS) in dH_2O (pH 8.8)
Buffer 2 – Stacking gel	500 mM Tris base, 14 mM SDS in dH_2O (pH 6.8)
Running buffer (1 litre)	25 mM Tris base, 3.5 mM SDS, 192 mM glycine in dH_2O
Transfer buffer (1 litre)	25 mM Tris base, 192 mM glycine, 20% (v/v) methanol in dH_2O
Tris-buffered Saline-Tween 20 (TBS-T) (0.5%) (1 litre)	20 mM Tris base, 150 mM Sodium Chloride (NaCl), 0.05% (w/v) Tween20 in dH_2O (pH 7.5)
ECL-1	88.5% (v/v) dH_2O, 10% (v/v) 1M Tris base (pH 8.5), 1% (w/v) 250 mM luminol and 0.5% (w/v) 250 mM p-coumeric acid.
ECL-2	89.9% (v/v) dH_2O, 10% (w/v) 1M Tris base (pH 8.5) and 0.1% (v/v) Hydrogen peroxide (H_2O_2)
Stripping Buffer (1 litre)	31 mM Tris base, 35 mM SDS in dH_2O (pH 6.7)
3.6% Formaldhyde solution	90% 1XPBS and 10% (v/v) Formaldhyde
3% BSA (TBS-T)	20 mM Tris base, 150 mM Sodium Chloride (NaCl), 0.05% (w/v) Tween20 in dH_2O (pH 7.5), 3% (w/v) BSA

1% BSA (PBS)	1X PBS tablet per 100mL dH_2O (pH 7.4), 1% (w/v) BSA
0.1% BSA (PBS)	1X PBS tablet per 100mL dH_2O (pH 7.4), 0.1% (w/v) BSA
PBS-T	1X PBS tablet per 100mL dH_2O (pH 7.4), 0.1% (w/v) Triton-X100

Table 2.3. List of primary antibodies

Name	*Company*	*Catalogue number*	*Concentration*	*Origin animal*	*Dilution used*
6G6 α-Red (anti-RFP)	Chromotek	AB_2631395	100 mg/mL	Mouse	1:3000
Anti-α-tubulin	Sigma-Aldrich	T5168	Not available	Mouse	1:60000
Anti-Cofilin	Cell Signalling technology	5175	53 μg/mL	Rabbit	1:100000
Anti-phosphoCofilin	Cell Signalling technology	3313	42 μg/mL	Rabbit	1:15000
Anti-Total ERK1	Santa Cruz Biotechnology	Sc-94 Lot L2115	100 μg/mL	Rabbit	1:15000
Anti-Phospho ERK	Santa Cruz Biotechnology	Sc-7383	200 μg/mL	Mouse	1:10000
Anti-GFP	Chromotek	3H9 Lot: 80626001AB	1 mg/mL	Rat	1:2500
Anti-LIMK2	Cell signalling technology	3845	Not available	Rabbit	1:5000
Anti-TESK1	Cell signalling technology	4655	50 μg/mL	Rabbit	1:5000

Anti-ROCK1	Cell signalling technology	4035	123 μg/mL	Rabbit	1:5000
Anti-Chronophin/PDXP	Cell signalling technology	4686	Not available	Rabbit	1:5000
Anti-SSH1	Cell signalling technology	13578	Not available	Rabbit	1:5000
Anti-pAKT	Cell signalling technology	9271	10 μg/mL	Rabbit	1:3000
Anti-tAKT	Cell signalling technology	9272	31 μg/mL	Rabbit	1:5000
Anti-Hsp70	Santa Cruz Biotechnology	Sc-32239	200 μg/mL	Mouse	1:5000

Table 2.4. List of Secondary antibodies

Name	*Company*	*Catalogue number*	*concentration*	*Origin animal*	*Dilution used*
Donkey anti-mouse IgG	Jackson Immunoresearch	715-035-150	0.8mg/mL	Donkey	1:7500
Goat Anti-Rat	R+D Systems	HAF005		Goat	1:2500
Goat Anti-Rabbit	Jackson ImmunoResearch	111-035-144	0.8mg/mL	Goat	1:7500
Alexafluor-488 Goat Anti-Rabbit	Thermofisher Scientific	PA5-17646	2mg/mL	Goat	1:200
Alexafluor-488 Goat Anti-Mouse	Thermofisher Scientific	PA5-53498	2mg/mL	Goat	1:200

Table 2.5 List of Immunofluorescence stains

Name	*Catalogue number*	*Concentration*	*Dilution used*
DAPI	D-9542	1 mM	1:2000 (PBS)
Phalloidin			1:100 (PBS)

2.2 Methods

Disclaimer: method (2.2.18) was carried out in the Bristol Proteomic Facility as part of a service provided by Dr Katie Keesom (University of Bristol). This work was funded by Tenovus Scotland.

2.2.1 Preparation of growth media for culturing

Human keratinocyte cell line (NCTC 2544) stably expressing wt-PAR4 (10h9 cells) were cultured in complete Dulbecco's Modified Eagle Medium (DMEM) supplemented with 10% (v/v) foetal calf serum (FCS) and 1% (v/v) penicillin/streptomycin (P/S). Human embryonal kidney 293 (HEK293) cells were cultured in Minimum Essential Media (MEM) supplemented with 10% (v/v) FCS and 1% (v/v) P/S. All media was cultured for a minimum of 3 days to ensure sterility of the media before usage with cell lines. MEG-01 cells were cultured in Roswell Park Memorial Institute (RPMI) 1640 media without glutamine (Corning) supplemented with 2 mM Glutamine, 10% (v/v) FCS and 1% (v/v) P/S.

2.2.2 Cryopreservation

To prepare cells for cryopreservation, leftover cells were centrifuged at 175 RCF for 5 minutes, and the supernatant was aspirated. Cells were then resuspended in 90% (v/v) FCS and 10% (v/v) Dimethylsulfoxide (DMSO). 1mL aliquots were added to cryovials, quickly transferred, and stored at -80°C for short-term storage. Cells required for longer-term storage were transferred to liquid nitrogen.

2.2.3 Bringing up cells from cryopreservation

1mL of cryopreserved cells were brought from storage at -80°C and allowed to defrost rapidly. The contents of the 1mL cryovial were transferred to a 15mL falcon tube, and 9mL of appropriate media was added. Cells were centrifuged at 175 RCF for 5 minutes, and the supernatant was aspirated off to remove the DMSO. The cell pellet was resuspended in 5mL of complete media, and the contents were transferred to a T25 flask. Cells were cultured for 24 hours in a 5% CO_2 humidified atmosphere at 37°C. Media was then removed, and fresh media was added. Cells were cultured until confluent (>80%) for the first split.

2.2.4 Culturing of 10h9 cells

The Human keratinocyte cell line stably expressing wt-PAR4 was cultured in DMEM supplemented with 10% (v/v) FCS and 1% (v/v) P/S. Stable expression of wt-PAR4 was maintained by supplementing media with a final concentration of 600μg/mL geneticin (50mg/mL stock) as a selection medium. Cells were maintained in a T75 flask in a 5% CO_2 humidified atmosphere at 37°C with media replaced every 2-3 days. Once cells had reached >80% confluency (approximately 7 days), they were passaged using versine (0.48 mM ethylenediaminetetraacetic acid (EDTA(Na4)) in PBS).

2.2.5 Culturing HEK293 cells

HEK293 cells were cultured in MEM supplemented with 10% (v/v) FCS and 1% (v/v) P/S and maintained in a T75 flask in a 5% CO_2 humidified atmosphere at 37°C cells and were passaged every 3 days once >80% confluency was reached. Cells were passaged using Accutase 1mL per 25cm^3 (total 3mL Accutase for T75 flask) and incubated at room temperature for 10 minutes for optimum detachment and separation.

2.2.6 Culturing TSA201 cells

TSA201 cells were cultured in DMEM supplemented with 10% (v/v) FCS and 1% (v/v) P/S and maintained in a T75 flask in a 5% CO_2 humidified atmosphere at 37°C cells and were passaged using versene (0.53 mM EDTA in PBS) every 3 days once >80% confluency was reached.

2.2.7 Culturing MEG-01 cells

MEG-01 cells were cultured in RPMI 1640 supplemented with 2 mM glutamine, 10% (v/v) FCS, and 1% (v/v) P/S and maintained in a T25 flask (Thermofisher) in a 5% CO_2 humidified atmosphere at 37°C. Once the suspension had reached a suitable density, cells were passaged every four days.

2.2.8 Fluo-4 direct calcium assay

100µl of cell suspension was seeded into each well of a 96-well black polystyrene plate (corning, Sigma-Aldrich) and incubated at 37°C in a 5% CO_2 incubator until confluent. Fluo-4 direct protocol was followed as per the manufacturer's instructions. In Brief, a 250 mM stock of probenecid was prepared by adding 1mL of fluo-4 direct calcium assay buffer to the 77mg vial of water-soluble probenecid and vortexed until dissolved. A 2X stock of fluo-4 calcium reagent was prepared by adding 10mL fluo-4 direct calcium assay buffer and 200µl probenecid to the reagent bottle and vortexed thoroughly to ensure it dissolved entirely.

50µl of media was removed from each of the wells, and 50µl of the 2X stock reagent was added. A 96-well plate was then covered to protect it from light and incubated at 37°C in a 5% CO_2 incubator for 1 hour. Assays were performed on a Flexstation 3 multi-mode microplate reader with calcium assay performed (Excitation λ = 488nm/ Emission λ = 530nm) and data acquired by

SoftMax Pro 5 (Molecular Devices). Calcium signalling was measured for thrombin (0-10IU/mL) and AYPGKF-NH_2 (0-500μM). Data was extracted to Microsoft Excel, and dose-response curves were generated using GraphPad Prism 8.1 non-linear regression curve fitting (variable slope).

2.2.9 Transfection of HEK293/TSA201 cells

Cells were seeded into 12-well plates with 1 mL of appropriate media and maintained in a 5% CO_2 humidified atmosphere at 37°C until cells were ~40% confluent.

To transfect, 150μl of media was added to 1.5mL Eppendorf (2x per well for transfection), 5.7μl of polyethyleneimine (PEI) was added to one Eppendorf, and 1μl of PAR4-mCherry plasmid DNA (1μg/μl) was added to the other Eppendorf. The mixture was incubated for 5 minutes, then added to the media/PEI mix and incubated for 30 minutes.

DNA:PEI media was added to the wells slowly drop-wise. The plate was then maintained in a 5% CO_2 humidified atmosphere at 37°C for 48 hours to allow uptake of DNA and translation and protein expression.

2.2.10 Immunofluorescence of transfected cells

Cells were grown on 13mm coverslips and transfected as described in 3.2.8. The coverslips were washed by adding 500μl of PBS and then fixed in ice-cold methanol for 10 minutes. The residual methanol was removed by washing twice with 750μl of PBS. 4',6-diamidino-2-phenylindole (DAPI) diluted 1:2000 in PBS was added to cells as a counter stain, incubated for 5 minutes, and then removed. To ensure the removal of residual DAPI coverslips, they were washed with PBS three times for 5 minutes each. Each coverslip was mounted on glass slides cell side down using 50μl mowiol mounting medium and dried overnight in the dark at room temperature. Slides were then stored at 4°C.

Cells were imaged using the Lecia Sp8 inverted confocal microscope using the preprogrammed screen for YFP, RFP, and DAPI across all slides imaged. Images were processed using FIJI ImageJ (v2.1.0/1.53c), and contrast matched across all images processed.

2.2.11 Colocalization analysis

Cells were transfected as described in 2.2.8; however, dual constructs were transfected (1μg wt-PAR4 YFP and 1μg mut-Y157C mCherry) or (1μg wt-PAR4 YFP and 1μg wt-PAR4 mCherry) and processed and imaged as described in 2.2.9. Once images were obtained, they were analysed using FIJI ImageJ (v2.1.0/1.53c), and images were contrast matched for YFP and RFP before colocalisation analysis. Images for (Wt/Wt) and (Wt/Mut) were analysed using the Just Another colocalisation plugin (JACoP), and thresholding was matched for both analyses. Scatterplots were obtained using the plugin ColocalisationFinder.

2.2.12 Immunofluorescence of suspension cells

The method is adapted from a Protocol taken from Thermofisher. In brief, cells were serum starved for 2 hours in 1.5ml Eppendorf's and stimulated with appropriate agonists. Cells were centrifuged at 217 RCF for 5 minutes, and the supernatant was discarded. Cells were then washed in 1mL PBS and vortexed before centrifuging at 217 RCF for 5 minutes and the supernatant discarded. Cells were then fixed by adding 700 µl per tube of 3.6% paraformaldehyde (1ml 36% Paraformaldehyde in 9mL PBS) and then incubated at 37°C for 10 minutes before centrifuging at 217 RCF for 5 minutes and the supernatant discarded. Cells were washed in 800 µl of PBS and centrifuged at 217 RCF for 5 minutes. Cells were then permeabilised by adding 700 µl of PBS-T (1X PBS and 0.1% Triton X-100) and incubating cells at room temperature for 15 minutes, followed by centrifugation at 217 RCF for 5

minutes and the supernatant discarded. Cells were washed by adding 800 µl of PBS vortexing and centrifuging at 217 RCF for 5 minutes.

Cells were then blocked in 1% BSA in PBS and incubated at room temperature for 1 hour before centrifuging at 217 RCF for 5 minutes and the supernatant discarded. Cells were then incubated with 100 µl of appropriate primary antibody (1:200 in 0.1% BSA in PBS) for 2 hours at room temperature or overnight at 4°C. The primary antibody was removed by centrifugation at 217 RCF for 5 minutes and then washed 3X in PBS (500 µl PBS, vortexed and centrifuged at 217 RCF for 5 minutes). Cells were then incubated with 100 µl of appropriate Alexafluor-488 secondary antibody (1:200 in 0.1% BSA in PBS) for 1 hour before centrifugation at 217 RCF for 5 minutes and the supernatant discarded. Cells were then washed 2X in PBS-T (500 µl PBS-T, vortexed and centrifuged at 217 RCF for 5 minsutes). Cells were then incubated with counterstains, firstly Rhodamine Phalloidin (1:40 in PBS) for 20 minutes before being washed with 500 µl PBS and centrifuged at 217 RCF for 5 minutes and the supernatant discarded. Cells were then counterstained with nuclear stain DAPI (1:2000 in PBS) for 10 minutes before washing with 500 µl PBS, centrifuging at 217 RCF for 5 minutes, and the supernatant discarded. Cells were then resuspended in 50 µl of PBS, added to glass slides along with 50 µl Mowiol mountant, and covered with rectangular coverslips to set ready for imaging.

2.2.13 Adhering Suspension cells using Fibronectin

Fibronectin bovine plasma (Sigma F1141-2mg) was diluted 1:100 in sterile 1X PBS and then added to wells with minimal volume to coat the required area. Plates were then incubated at 37°C for a minimum of 30 minutes in a 5% CO_2 incubator. The excess solution was removed, and the plates were air-dried in a culture hood for 30 minutes. Cells were added in the appropriate number and volume of media and then allowed to adhere for a minimum of 2 hours at 37°C in a 5% CO_2 incubator. Cells were tested for adherence for up to 72 hours with

no issues in lifting. However, experiments were carried out on the same day once cells had adhered (approx. 2 hours).

2.2.14 Immunofluorescence of Adherent cells

Cells were seeded to 100% confluence (0.5×10^6) in serum-free media onto fibronectin-coated coverslips in 12-well dishes and then incubated at 37°C for 2 hours minimum in a 5% CO_2 incubator to allow them to adhere. Once adhered, cells were stimulated with appropriate agonists for the required time before removing the media and washing the cells 3X with 500 µl PBS. Cells were then fixed using 400 µl of 3.6% paraformaldehyde (1ml 36% Paraformaldehyde in 9mL PBS) for 10 minutes at 37°C. Paraformaldehyde was then removed, and cells were washed 3X with 500 µl PBS. Cells were then permeabilised by adding 400 µl of PBS-T (1X PBS and 0.1% Triton X-100) and cells incubated at room temperature for 15 minutes before removing the PBS-T and washing the cells 3X with 500 µl PBS.

Cells were then blocked in 1% BSA in PBS and incubated at room temperature for 1 hour. The primary antibody was made up of 0.1% BSA in PBS and then 100 µl added to the coverslip in a humid chamber on parafilm to retain the antibody on the coverslip. Cells were then incubated for 2 hours at room temperature or overnight at 4°C. Primary antibody was removed, coverslips replaced in their wells, and washed 3X in 500 µl PBS. Cells were then incubated and protected from light with appropriate AlexaFluor-488 secondary antibody in the same manner described for the primary and then incubated for 1 hour at room temperature. The secondary antibody was then removed, and coverslips were replaced in their wells and washed 3X in 500 µl PBS-T. Cells were then incubated with counterstains and Rhodamine Phalloidin (1:40 in PBS) by adding 40 µl to parafilm and inverting coverslips cell side down for 20 minutes before coverslips were replaced in their wells and washed with 500 µl PBS. Cells were then counterstained with nuclear stain DAPI (1:2000 in PBS) by adding 400 µl per well for 10 minutes before washing with 500 µl PBS. Cells

were then mounted side down onto glass slides using Mowiol mountant and allowed to set overnight, protected from light before imaging.

2.2.15 Inducing differentiation of MEG01 cells using Phorbol 12-myristate 13-acetate

Stocks of 10μM Phorbol 12-myristate 13-acetate (PMA) were made in sterile DMSO as a solvent due to PMA's limited solubility in water.
Three times, stock solution of the required PMA concentration was prepared in 10mL RPMI-1640 media (e.g. 75 nM stock for a final concentration of 25 nM PMA). PMA media and PMA stock were protected from light for the duration of the method. MEG01 cells were passaged as described in 2.2.7 until cells were resuspended in 20mL RPMI-1640 media and added to a T75 flask with the 10mL PMA media. Cells were then incubated in a 5% CO_2 humidified atmosphere at 37°C for 72 hours minimum.

2.2.16 Agonist stimulation of MEG-01 cells

Cells were resuspended in serum-free RPMI and transferred to 1.5mL Eppendorf's at a cell number of 200,000 cells; the suspension was made up to 1mL with additional serum-free RPMI. Cells were then serum starved for 2 hours in a 5% CO_2 humidified atmosphere at 37°C. Cells were then stimulated over a time course of (1 – 120 minutes) with thrombin (1 U/mL), AYPGKF-NH_2 (300 μM) and TFLLR-NH_2 (100 μM). Samples were then centrifuged at 217 RCF for 5 minutes, and then media was removed, leaving the cell pellet intact. 150μl of 1X Laemmli sample buffer (4X Laemmli LDS sample buffer 1:3 ddH_2O) and then vortexed for 10 seconds to dislodge the pellet into the sample buffer. The sample was then syringed to shear cells and chromosomal DNA, boiled at 95°C for 5 minutes, and then stored at -18°C until ready for SDS-PAGE gel electrophoresis.

2.2.17 Preparation of cellular lysates

Cells were grown to confluency in appropriate experimental dishes, and experiments were performed. Media was aspirated off, and lysis buffer was added (50 mM Tris-HCl, 1% (v/v) Triton X-100, pH7.4), and one mini protease inhibitor cocktail tablet (Roche) was added to 10mL of lysis buffer. 150μl of lysis buffer was added to each well of a 12-well plate, and cells were crushed and mixed. Scrapped cell lysates were removed, added to 1.5mL Eppendorf tubes, and rotated at 4°C for 1 hour before being centrifuged at 9632 RCF for 5 minutes. Once spun. Supernatants were removed into new Eppendorf tubes, and the pellet was discarded. Lysates were then frozen until protein concentration was determined by BCA assay.

2.2.18 Protein determination of cell lysates using BCA assay

Protein concentration was determined using the Pierce™ BCA protein assay kit (ThermoFisher Scientific). In brief, BSA Albumin standards were made up using a 1mL vial of BSA stock standard (2mg/mL). The working reagent was prepared by mixing BCA reagent A with BCA reagent B in a ratio of (50:1).

In a 96-well plate, 10μl of BCA standards were added in duplicate wells and 5μl of sample lysates. 200μl of working reagent was added to each well with standard and sample (working range 125-2000μg protein). The plate was placed on an orbital shaker at high speed for 30 seconds, then covered with aluminium foil and incubated at 37°C for 30 minutes. The plate was then removed, allowed to cool at room temperature, and then read at 562nm using the Flexstation 3 multi-mode microplate reader and data acquired by SoftMax Pro 5 (Molecular Devices). Standard curves and protein concentrations were determined using Microsoft Excel (16.45).

2.2.19 SDS-PAGE and Western blotting

For SDS-PAGE, 10% resolving gels were prepared by adding 10% (v/v) acrylamide, 60 mM Tris base, 0.6 mM SDS with 0.13% (w/v) Ammonium persulfate (APS) and 0.13% (w/v) TEMED. 15% resolving gels were prepared by adding 15% (v/v) acrylamide, 60 mM Tris base, 0.6 mM SDS with 0.13% (w/v) APS and 0.13% (w/v) TEMED. This was layered with isopropanol on top of the gel to ensure the interface between the resolving and stacking phases was even during polymerisation. Once set, isopropanol was removed, and 4% stacking gel (4% (v/v) acrylamide, 20 mM Tris base, 0.6 mM SDS, 0.13% (w/v) APS and 0.13% (w/v) TEMED) was added to the top of the resolving gel and a Teflon comb inserted and left to polymerise and set ~15 minutes. 3μl of PageRuler Plus Prestained protein ladder (Thermofisher Scientific) was loaded into the first well of the gel along with 15-25μl of sample into the subsequent wells. Gel electrophoresis was performed in a Bio-Rad Mini-PROTEAN II™ tank topped with running buffer (25 mM Tris base, 3.5 mM SDS, 192 mM glycine) to the appropriate level. Gels were run at 120V for 120 minutes.

Protein gels were transferred to nitrocellulose membrane (GE Healthcare life sciences, Amersham® Protran® 0.45μm) by preparing a transfer cassette comprising two sponges, two 0.92 mM cellulose chromatography grade filter paper (Whatman), one nitrocellulose membrane. The transfer was completed in a Biorad Mini Trans-Blot™ tank topped up with transfer buffer (25 mM Tris base, 192 mM glycine, 20% (v/v) methanol) and an ice block and run at 280 - 300mA for 110 minutes. Once the transfer was complete, membranes were blocked in 3% BSA in TBS-T (20 mM Tris base, 150 mM Sodium Chloride (NaCl), 0.05% (w/v) Tween20) overnight to prevent non-specific binding. The primary antibody (table 3.3) was added to the membrane and incubated overnight, followed by 3X 5 minutes washes in TBS-T, then incubated with the secondary antibody (table 3.4) for 2 hours. Membranes were then washed in

TBS-T 3X for 5 minutes each. The HRP-conjugated secondary antibody was activated by incubating with ECL1 (88.5% (v/v) dH_2O, 10% (v/v) 1M Tris base (pH 8.5), 1% (w/v) 250 mM luminol and 0.5% (w/v) 250 mM p-coumeric acid) and ECL2 (89.9% (v/v) dH_2O, 10% (w/v) 1M Tris base (pH 8.5) and 0.1% (v/v) H_2O_2) in a ratio of 1:1. The membranes were then transferred to an exposure cassette and exposed to UltraCruz Autoradiography blue film (Santa Cruz Biotechnology) and developed using an automatic X-ray film processor (model JP-33).

2.2.20 Analysis of Western blot data

Western blot films were scanned using (HP Deskjet 2540) at a resolution of 600Dpi and saved in .tif format to maintain resolution. Images were then processed on FIJI ImageJ (v2.1.0/1.53c) and quantified using the plot lane function and densitometry to obtain band intensity values. Values were transferred to Microsoft Excel (v16.45), and protein normalisation was performed using the function (= housekeeping signal/highest observed housekeeping signal) to obtain the normalisation factor for each lane. The normalised signal was then determined using (=target band/normalisation factor). Normalised protein values were then graphically presented using GraphPad Prism (v8.1).

2.2.21 Stripping and reprobing Western blot membranes

Antibodies were removed from membranes by adding 15mL stripping buffer and 105µl of β-mercaptoethanol and incubating for 15 minutes at 60°C in a heating cabinet on an orbital shaker. Stripping buffer was removed by washing with TBS-T 3X for 5 minutes each, and membranes were blocked for 2 hours in 3% BSA in TBS-T. The membrane was then incubated with the appropriate primary antibody (i.e., α-tubulin) for 1-2 hours, with the remaining protocol following that of 3.2.10.

2.2.22 Proteomics Methods

All methods carried out in this section (2.2.18) were carried out in Bristol. HEK293 cells were purchased from ATCC (HEK293ATCC CRL-1573^{TM}). All Stable isotope labelling using amino acids in cell culture (SILAC) media was purchased from Dundee Cell Products. Samples were processed by Dr Kate Heesom (Bristol Proteomics Facility) using LC-MS/MS analysis on an Orbitrap Velos (Thermo) mass spectrometer. The methodology has previously been described in detail and published (Steinberg *et al.,* 2012). Cells were grown in cell culture media that contained L-arginine and L-lysine labelled with different stable isotopes of carbon and nitrogen. SILAC media was prepared by adding 0.5ml of L-arginine (84 mg/ml in PBS) and L-lysine (146 mg/ml in PBS) to Arg/Lys free DMEM. 50 ml of dialysed FBS and 5 ml of penicillin/streptomycin were added to the DMEM. The HEK293 cells remained in DMEM lacking in arginine and lysine and combined with light (R0K0), medium (R6K4) or heavy (R10K8) amino acids. Cells remained in media for at least five cell divisions to guarantee complete labelling. Twenty-four hours before the transfection, labelled cells were seeded at 3.5 x 10^6 cells per 10cm^2 dish.

Plasmids encoding the proteins of interest (WT PAR4-CFP or Y157C mutation) or the control CFP plasmid were transfected into the labelled cells. This process involved removing the media from cells and substituting it with 9ml of SILAC light, medium or heavy DMEM. Ten µg of plasmid of interest was prepared in 500µl of free SILAC DMEM, which was then mixed with 500µl of SILAC DMEM, which included 10µl of transfection reagent (polyethyleneamine, PEI, 1mg/mL). Transfected cells were incubated at 37^{o}C and 10% CO_2 for 48 hours before affinity purification (Figure 2.1).

SILAC-labelled HEK293 cells expressing the CFP (in R0K0 media), PAR4-CFP (in R6K4 media) or PAR4-Y157C-CFP (in R10K8) were scraped from the dish into ice-cold PBS. Cells were collected by centrifuging the suspension at 220 x g, 4^{o}C for 5 minutes. Cells were washed a further three times in 10ml of

ice-cold PBS. The cell pellet was resuspended in 200µl of cell lysis buffer (50 mM Tris-HCL (pH 7.4), 1% triton-X-100 and Roche mini protease inhibitor cocktail tablet). Samples were centrifuged again at 13,000 x g, 4ºC for ten minutes to recollect supernatant as a soluble cell lysate. A lysis buffer containing a protease inhibitor cocktail was added to make the final volume up to 500µl. The volume was then made up to 1ml by adding 500µl of dilution buffer. 50µl of the sample was retained, and the lysate was stored on ice while anti-GFP (Chromotek) beads were prepared. The beads were resuspended by vortexing the bead slurry. 75µl of beads from each sample was transferred to a fresh tube. For each bead sample, 20 volumes (1,500 µl per 75 µl slurry) of dilution buffer was added, and the tube was centrifuged at 2700 x g for five minutes. This process was repeated two times to wash the beads.100 µl of dilution buffer was added to each bead slurry. 85 µl from each of them were added to the SILAC labelled samples. Bead samples were incubated on a rotator for two hours at 4oC. For MS analysis, samples were centrifuged at 2,700 at 4ºC for 5 minutes. 50µl of the supernatant was retained as the unbound sample; the rest was removed. The beads were resuspended by adding 1 ml of dilution buffer to each tube. The sample was centrifuged once again at 2,700 x g for 5 minutes. The supernatant was discarded and this process was repeated a further two times. Protein was eluted from beads by adding 50 µl of SDS loading buffer and incubating for 10 minutes at 95ºC. Beads were centrifuged at 2,700 x g for 2 minutes at 4ºC, forming a pellet and supernatant. The supernatant was stored at -80ºC in Eppendorf tubes. The labelled samples were mixed 1:1:1 and submitted for mass spectrometry analysis (Bristol Proteomics Facility) (Figure 2.1).

Proteins were eluted in sample buffer, separated on Nupage 4-12% precast gels (Invitrogen) and subjected to LC-MS-MS analysis on an Orbitrap Velos (Thermo) mass spectrometer. A detailed description of the mass spectrometric detection and quantification has been recently published (Steinberg *et al.,* 2012). LC-MS-MS data was filtered to remove the low-confidence peptides (those identified at >5% FDR). Using Proteome Discoverer software from Thermo, a SEQUEST search was performed against the UniProt Human

database. The ratio presented for each protein represents the median of the ratios of peptides matched to that protein, with the maximum fold change set to 100.

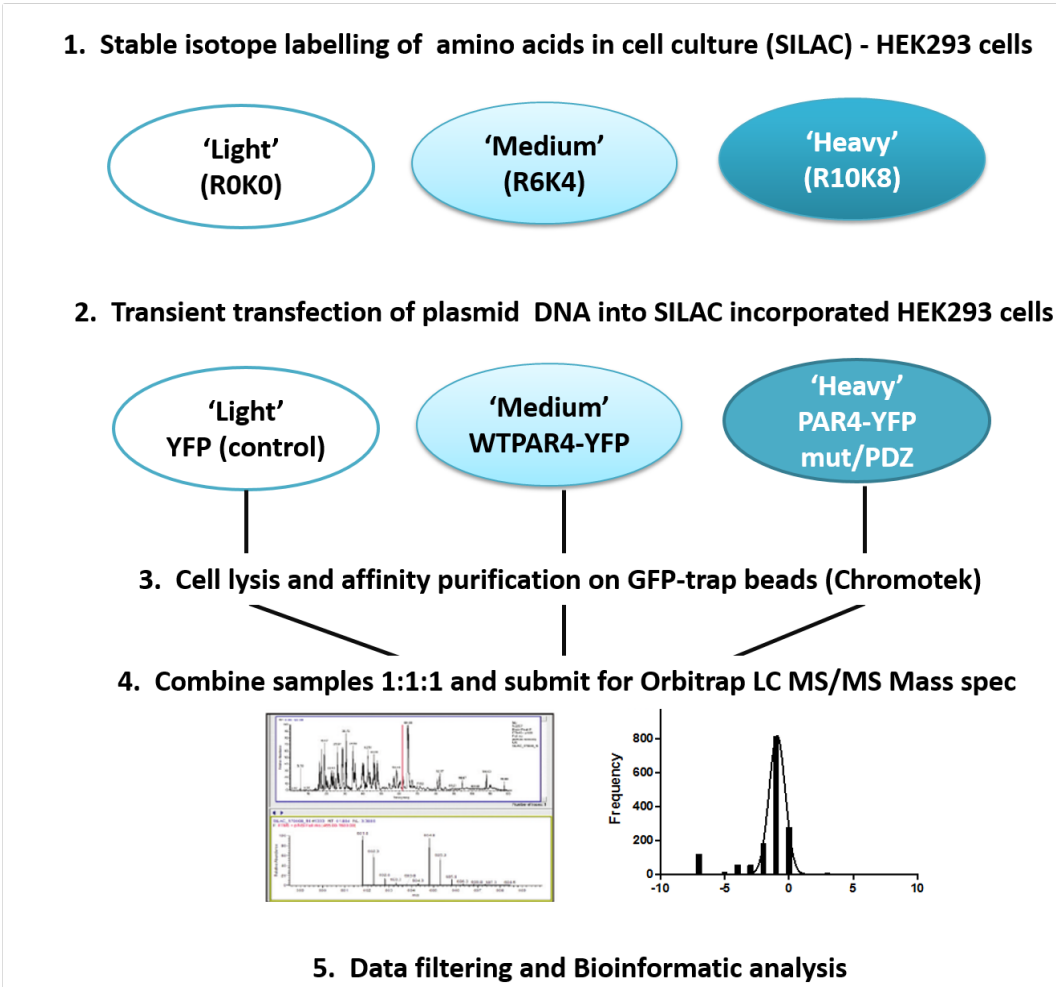

Figure 2.1 – Workflow diagram of the SILAC proteomic experimental design. Steps 1 – 4 were carried out at Bristol by Cunningham, M.R., step 5 was carried out as part of this research. N=3 datasets were filtered in order to determine high confidence interactors. High confidence interactors were subjected to bioinformatic analysis in order to identify a novel PAR4 protein interactor for validation.

2.2.23 Data filtering

The method used for data filtering and analysis is the same as previously published by Emmott and Goodfellow (Emmott, E., and Goodfellow, I. 2014). Raw data generated from the experiments were exported to Microsoft Excel (v16.45), and columns were removed except those containing the accession number, protein description, number of unique peptides, sample ratios and ratio variability. Initial low-confidence data was removed by removing proteins identified by one or fewer unique peptides and proteins lacking SILAC ratios. New columns were inserted next to SILAC ratios (Heavy/Light, Medium/Heavy and Medium/Light), and Log_2 values were calculated for each SILAC ratio using the formula *(=log(SILAC Ratio,2))*. As SILAC ratios are reported within a value of 0 to 1, conversion to Log_2 allows increased or decreased proteins to fit on a log scale, allowing for easier interpretation in abundance. The Log_2 data was then plotted to fit a Gaussian distribution using GraphPad Prism (v8.2.1). The results generated give the mean and standard deviation, which were used to calculate a threshold for each SILAC ratio column using the formula *(=Mean+(1.96*SD))*.

The experiments were performed in triplicate to generate high-confidence hits. These were then combined into a single Excel file using the formula *(=vlookup(Accession number, where to look, columns across, false)*. Once combined, interacting proteins were highlighted by selecting each ratio column, then using conditional formatting, highlighting cell rules, and more rules. Format was set to classic and highlight cells with a cell value ‘greater than or equal to’ the threshold generated for each SILAC ratio. This was repeated for all the SILAC ratios across the experiments; highlighted proteins across all three experiments were considered high-impact hits.

2.2.24 Correlation analysis

Raw data was extracted to a new Excel tab using the formula *(=vlookup(Accession number, where to look, columns across, false)* and contained the column's accession number and protein description. Data was segregated based on the experimental replicates to be compared (e.g., R1 Log_2 HL and R2 Log_2 HL), and data was extracted using the VLOOKUP formula as previously described. Identified proteins that lacked Log_2 values for both replicates were screened out, and only proteins that had log_2 values for both replicates were analysed for correlation. This process was carried out on each set of comparable replicates (Gonneaud, A., et al. 2016). Pearson correlation was carried out for identified proteins using GraphPad Prism (v8.2.1). Pearson correlation between wild-type (M/L) and mutant (H/L) was performed intra-experimentally over the three replicates.

2.2.25 Production of protein interaction networks using string and Cytoscape

According to the work published by Emmott and Goodfellow (Emmott, E., and Goodfellow, I. 2014). Proteins with SILAC ratios above the threshold in two or more replicates are defined as high-confidence hits. Therefore, protein accession numbers were extracted to STRINGdb to generate a protein interaction network. It also allowed for identifying protein accession numbers that were not identified to be searched and identified using UniProt. This method allowed all accession numbers to have their appropriate gene name identified and allowed a reanalysis on STRINGdb to be performed.

The data was then extracted from STRINGdb into Cytoscape (v3.9.1), and a protein interaction network was produced. Visualisation of the nodes was improved by converting the accession numbers to their gene names, and nodes were presented by size using degrees of centrality. In addition, nodes were coloured based on the number of connections they had to other nodes (light yellow and smaller) for fewer connections and (larger redder) for higher degree of connections.

2.2.26 Comparing gene ontology families in identified proteins for wt-PAR4 and mut-PAR4 Y157C using PANTHER

Proteins identified across two or more replicates for wt-PAR4 (M/L) and mut-PAR4 Y157C (H/L) were analysed using a bioinformatics tool Protein Analysis Through Evolutionary Relationships (PANTHER). Proteins were extracted from Excel and put into STRINGdb, and analysis was performed. This allowed any proteins whose accession numbers couldn't be identified to be extracted and processed through UniProt to identify them. Gene names for all identified proteins were then added to PANTHER to distribute gene families based on molecular function, biological process, cellular components, and protein class.

2.2.27 Enrichment testing of gene ontology using BiNGO

Proteins were extracted from the interaction networks generated in Cytoscape and processed through a plugin for gene enrichment BiNGO. Maps were generated for Molecular function, biological processes and Cellular components. Determination of enriched clusters was generated using a hypergeometric test for statistical significance using the Benjamini and Hochberg false discovery rate (FDR) correction and statistical significance level set at (0.05). Maps generated showed overrepresented clusters on a scale of statistical significance with the minimum (0.05 being yellow) and highly significant clusters (<5.00E-7 being orange).

2.2.28 Determining overrepresent Biomolecular cascades using Reactome

Proteins were extracted from the interaction networks generated in Cytoscape and processed through a plugin for biomolecular cascades Reactome. Maps were generated by setting the false discovery rate (FDR) to 0.05. Enriched pathway cascades could then be visualised by being highlighted as yellow.

2.2.29 Identification of High confidence hits based upon reproducibility across data sets

Following on from (data filtering), proteins with SILAC ratios above the thresholds were highlighted in green. Proteins containing a SILAC ratio below the threshold (the cell was white) were screened out. Only proteins with SILAC ratios above the threshold across all sample/mock columns for the three replicate experiments were selected as high-confidence hits based on reproducibility across data sets. Twenty-nine proteins were identified through this screening and brought forward for further verification.

2.2.30 STRING Analysis and generation of a functional protein association network

The accession numbers of the 29 proteins identified in (1.4) were exported to (STRING-db.org) by selecting search and submenu multiple proteins and pasting the accession numbers in List of Names. The Organism was selected as Homo Sapiens and searched. From this, 25 out of 29 proteins were identified.

The four proteins not found by string search were screened on (UniProt.org) using the given accession number and/or protein description. Accession numbers for these four proteins had been updated, and the above was performed again, ensuring all 29 proteins were identified. The click continues; this then generates the string protein interaction network. The nodes were then rearranged to define them into their respective clusters, then coloured accordingly by selecting the clusters tab, Kmeans clustering and the number of clusters set according to the interaction network generated, i.e., number of clusters: 4 and apply. The string protein interaction network was then exported.

2.2.30 Quantitative data analysis of Immunofluorescence images

Coverslips were imaged using a Leica SP8 Inverted scanning confocal microscope, which uses channels for DAPI (excitation 405nm), Green for protein of interest (excitation 488nm), and Rhodamine Phalloidin (excitation 540nm). Images were acquired for each biological replicate using equal laser power and gain to ensure the quantifiability of the images. Images were saved as .lif files for each biological replicate and then processed using FIJI ImageJ v2.1.0/1.53c.

In brief, Images were loaded into ImageJ, and channels split so the protein of interest (green) could be quantified. Contrast enhancement was used to allow better visualisation of the cell outlines; however, this was not set so as not to alter the intensity of the raw images. Images processed were from ROIs (region of interest) images and included, on average, 3-8 cells per image. Outlines were drawn around each cell, and MFI (mean fluorescent Intensity) was measured, along with the standard deviation (SD) and the min (minimum) and max (maximum). The MFI was then averaged for each image from the number of cells measured using Microsoft Excel 2019 (v16.54). Technical replicates were acquired for each biological replicate and averaged. Values were then graphed and analysed using GraphPad Prism v8.2.1.

2.2.31 Statistical analysis

All data was transferred and stored on Microsoft Excel (v16.45). BCA and proteomic datasets were analysed using Excel exclusively.

Stimulation data was subjected to normality testing using the Shapiro-Wilk test, assuming a normal (Gaussian) distribution. The significance level (Alpha) was set to 0.05. Stimulation data run for western blot gave a P-value >0.05, passing the test for normality. Therefore, a one-sample t-test was used to analyse significance.

For IF data, normality testing was applied using the Shapiro-Wilk test, which assumed a normal (Gaussian) distribution. The significance level (Alpha) was set to 0.05. Data gave a P-value <0.05 and did not pass the normality test; thus, normal distribution was not assumed. Additional normality testing for the IF data (Anderson-Darling test, D'Agostino & Pearson test, Kolmogorov-Smirnov test) all gave P-values <0.05, meaning normality testing did not pass, and normal distribution cannot be assumed. Therefore, IF data was analysed using the Mann-Whitney U-test.

All statistics were calculated using GraphPad Prism v8.1. P-values <0.05 were considered statistically significant.

Chapter Three

Identifying novel PAR4 interacting proteins

3. Results Chapter 1

3.1 Emerging importance of PAR4

From its initial characterisation in 1998, PAR4 has gone from being considered a redundant backup to the primary thrombin receptor PAR1, to being a critical receptor in sustained platelet activation and stable thrombus formation (Han and Nieman, 2018b). The attention to targeting PAR4 as a novel anti-platelet therapy came from the success but eventual failure of targeting PAR1. Although successful in inhibiting platelet activation, the PAR1 antagonist Vorapaxar encountered the same issue that hindered antiplatelet agents' success, increasing bleeding risk (Scirica et al., 2012; Tricoci et al., 2012). So much so that Vorapaxar never achieved drug approval within Europe or the UK, and its use in the states has been limited. However, the importance of PAR4 in platelet activation has come from the characterisation of SNP variants of the receptor.

The rationale for targeting PAR4 as a novel antiplatelet therapy emerged in part from studies which identified racial disparities in reactivity and expression levels of PAR4 (Edelstein et al., 2014). These differences result in resistance to current antiplatelet therapies, hyperreactive platelets and overall poorer cardiovascular outcomes (Whitley et al., 2018). These poorer outcomes are present more often in black patients, whose platelets showed hyperresponsiveness to PAR4-AP, whereas non-black patient platelets did not; this hyperresponsive phenotype persisted even in the presence of treatment with vorapaxar and aspirin (Tourdot et al., 2018; Whitley et al., 2018). Subsequent interrogation of the Ensemble genome browser, the F2RL3 gene, which encodes PAR4, was shown to have 1548 variant alleles at various positions (https://www.ensembl.org/). However, although still rare, four of these have occurred frequently enough to be characterised and studied and have been shown to affect receptor function enough to be classed as clinically significant (Han and Nieman, 2020) (Table 3.1). The most frequently occurring

variant is rs773902, Ala120Thr missense substitution, which leads to platelets having a hyperactive PAR4, increased ex vivo thrombus formation, resistance to desensitisation, resistance to inhibition with YD-3 and increased sensitivity to low dose thrombin (Edelstein et al., 2014; Tourdot et al., 2018; Whitley et al., 2018). The importance of PAR4 receptor was further shown that patients with this mutation were at increased risk of stroke in the SiGN study.

Three clinically significant variants are deleterious to receptor function and provide further evidence of PAR4s importance in platelet function. The first is rs2227346, located on transmembrane 6 (TM6) and is a Phe296Val substitution. This mutation showed decreased PAR4 receptor function, as shown by reduced platelet aggregation with PAR4-AP and IP3 generation (Edelstein et al., 2014). This substitution is located in the consensus scaffold for ligand binding present on all Class A GPCRs. It is also present on a conserved Na^+ pocket microswitch, the rotation of which is essential for proper receptor activation (Venkatakrishnan et al., 2013). The second rs2227376 is located on the receptor's extracellular loop 3 (ECL3), resulting in a Pro310Leu substitution. This mutation results in reduced receptor response to thrombin and PAR4-AP and a 15% reduced relative risk of venous thromboembolism (VTE) through the International Network against venous thromboembolism (INVENT) (Han et al., 2020). The final variant is the Tyr157Cys substation located within the transmembrane 3 (TM3). Platelets with this mutation showed reduced responsiveness to thrombin and PAR4-AP compared to normal platelets. Interestingly, the reduced responsiveness of platelets with this mutation results from reduced anterograde receptor trafficking to the surface and retention of the receptor within the ER due to incorrect protein folding (Norman et al., 2016).

It was hypothesised that reduced reactivity resulted from defective trafficking to the cell surface, which is caused by the loss of Y157-Y322 hydrogen bonding and resultant incorrect protein folding (Norman et al., 2016) (Figure 3.1).

Table 3.1 clinically significant PAR4 variants

Amino acid substitution	Structural domain location	RefSNP	Frequency of minor allele	Predicted consequence	Structural modelling prediction
Ala120Thr	TM2	rs773902	0.22	Neutral	Neutral
Phe296Leu	TM6	rs2227346	$<10^{-3}$	Deleterious	Uncertain
Pro310Leu	ECL3	rs2227376	$<10^{-2}$	Neutral	Neutral
Tyr157Cys	TM3	rs750054844	$<10^{-4}$	Deleterious	Deleterious

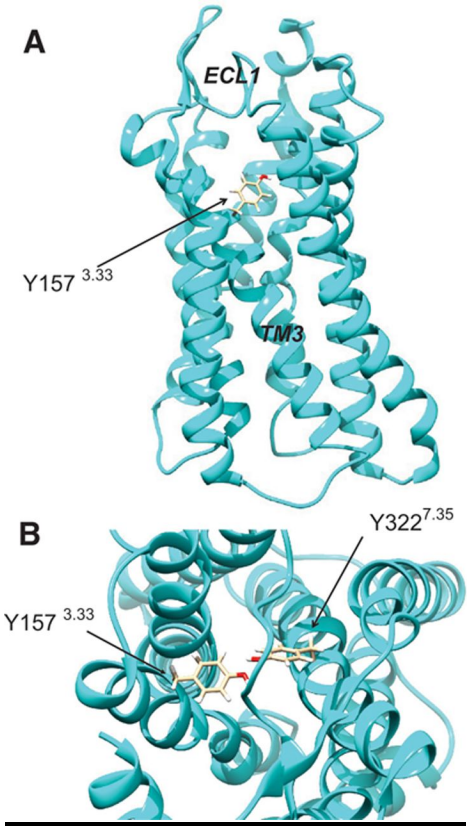

Figure 3.1. The structural interaction of PAR4 mutant Y157C. A) A homology model of PAR4 shows Y157 is contained in the TM3 domain of PAR4 and projects into the TM domain bundle. B) Shows that the close proximity of Y157 to Y322 in TM7 likely results in the formation of a hydrogen bond. Taken from (Norman et al., 2016).

The rationale of targeting the site based on the mutant Y157C in TM3 has recently been backed by new data demonstrating the importance of TM3 in PAR4 receptor signalling. In this particular study, residue Thr153 (four away from the proposed site) was shown to be critical in receptor activation (Han and Nieman, 2018b).

Using hydrogen/deuterium exchange mass spectrometry (H/D exchange) allowed for the first time to compare receptor dynamics between two states (resting and activated) and allowed for the identification of the tethered ligand dynamics and its binding site (Han et al., 2020). It was shown that Gly48 on the tethered ligand was predicted to interact with Thr153 within TM3. They proved the importance of this reside by generating two mutants of this site, Thr153Ala and Thr153Ser, both of which showed diminished calcium responses when stimulated with thrombin, with Thr153Ala showing a significant reduction and Thr153Ser showing an intermediate reduction (Han and Nieman, 2018b) (Figure 3.2).

In addition to the above, they also identified a significant difference in H/D uptake on ECL3 between resting and activated states. It was predicted based on computational modelling at its location to TM3 that ECL3 acts as a gatekeeper to the ligand binding site at TM3 and adopts an out position following thrombin activation to allow access by the tethered ligand. Within the ECL3, there are two proline residues, which, when located within loops, are there to maintain rigidity. As mentioned above, an already characterised polymorphism, Pro310Leu, has already been identified, which reduces PAR4 receptor activity (Lindström et al., 2019). To prove the importance of ECL3 in PAR4 activation, they generated mutants for the two prolines Pro310 and Pro312 (predicted to have an effect) and the residue in-between Ser311 (predicted to have no effect). It was shown that Pro310Leu completely abolished calcium response to AYP and significantly reduced response to thrombin; the mutant Pro312leu showed an intermediate reduction in calcium response. As predicted, the mutant Ser311Ala showed no reduction in calcium

response to AYP or thrombin, which proved the importance of the prolines in ECL3 rigidity maintenance and allowing the correct conformational change required upon receptor activation to allow the tethered ligand access to TM3 (Han et al., 2020).

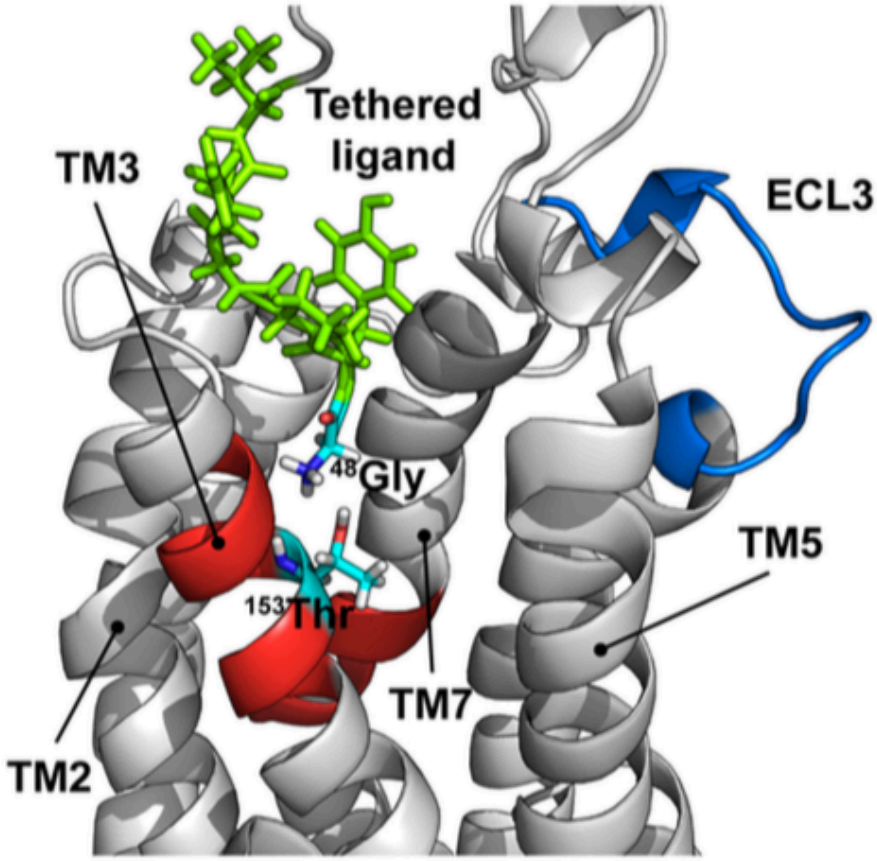

Figure 3.2. Model of PAR4 activation by the tethered ligand based on H/D exchange. A computational model of PAR4 activated by thrombin showing ECL3 in its active 'out' position (blue). Allowing access of the tethered ligand (green) to TM3 (red). Also shown in the predicted interaction of Gly48 of the tethered ligand with Thr153 within TM3. Taken from (Han, et al. 2020).

3.1.2 Rationale for the use of HEK293 cells

The original selection of HEK293 cells was based on the fact that they do not express PAR4 natively, and therefore, transfecting the protein allows interactions to be more reliably detected from SILAC LC-MS/MS. If the cell expressed the protein natively, there is the risk that native expression of the protein will interfere with the heavy-labelled forced expression and impact the mass spectrometry results.

Additionally, work was planned to continue on PAR4-transfected HEK293 cells. However, the unreliability of transfection efficiency and cell lifting could impact the reproducibility of results. In addition, overexpression systems can result in non-physiological signalling cascades due to the amount of protein that is expressed and therefore, due to trying to understand novel signalling mechanisms downstream of PAR4 following proteomic analysis, the justification was that validating this within a native PAR1 and PAR4 expressing cell line would provide more physiologically relevant and reliable results.

3.2 Aims

This chapter aimed to

1. Analyse proteomic datasets produced using HEK293 cells expressing wt-PAR4 and mutant Y157C to identify novel protein/protein interactions previously generated via SILAC LC-MS/MS.
2. Identify over-represented interacting families of proteins using bioinformatic analysis tools (PANTHER and BiNGO).
3. Identify protein familes near the F2RL3 gene, identify if any protein within that family emerges as a triple high-impact interactor, and determine the interaction of that protein family via AlphaFold.

3.3 Identifying novel PAR4 protein interactors in recombinant systems

The transfection of HEK293 cells and sample preparation were carried out by Cunningham, M.R. (University of Strathclyde). Samples were processed by Keesom, K (University of Bristol) at their proteomics facility using LC-MS/MS analysis on an Orbitrap Velos (Thermo) mass spectrometer. This work was funded by Tenovus Scotland.
The data generated was interrogated and analysed as part of this PhD project.

Determining how proteins interact is the central dogma of cell and molecular biology. It aids in understanding receptor trafficking and function and in the rational design of effective small molecule drugs to target these processes while mitigating unwanted 'off-target' effects. A key technique in identifying novel protein/protein interactions is using recombinant expression systems using stable isotope labelled amino acids (SILAC) and analysing these using mass spectrometry (Emmott and Goodfellow, 2014).

SILAC is a powerful quantitative proteomics technique for studying protein interactions and dynamics within cells. In SILAC, cells are cultured in media containing light or heavy isotopic forms of amino acids (typically arginine and lysine). These labelled amino acids are incorporated into newly synthesised proteins, allowing for precise quantification of protein expression and interaction dynamics using mass spectrometry (Chen et al., 2015). SILAC can identify proteins interacting with a target protein under specific conditions, providing insights into complex signalling pathways and protein networks. Since labelling occurs in living cells, the observed interactions and modifications are physiologically relevant and allow for global proteome analysis, enabling the identification of novel proteins and pathways (Mann, 2006; Chen et al., 2015).

Due to PAR1's focus in the context of PAR research, PAR4, although first characterised in 1998, was relatively neglected until its importance in platelet activation and thrombus formation emerged (Han and Nieman, 2018b). As a result, understanding many aspects of the molecular interaction network of PAR4 is relatively unknown. As such, this method could be invaluable in unravelling this area of research, which is still in its infancy.

3.3.1 Determination of threshold values from SILAC proteomic datasets

Methods for protein filtering were followed as detailed in the paper by Emmott and Goodfellow on identifying protein interaction partners using SILAC proteomics (Emmott, E., and Goodfellow, I. 2014). Experiments were performed in triplicate to allow for the identification of higher-confidence interactors. Replicate 1 gave an identification of (n=5626) proteins via LC-MS/MS, initial filtering of data removed proteins with one or fewer unique peptides (n=1092) and proteins which lacked SILAC ratios (n=1699). This left 2905 proteins, which were assessed for replicate 1. Log_2 of SILAC ratios were used to produce frequency distribution graphs plotted to Gaussian distribution (Figure 3.3A-C). These graphs' mean and standard deviations were used to calculate the threshold for each Sample/Mock ratio (Mean + 1.96SD) (Figure 3.3D).

Replicate 2 gave an identification of (n=6181) proteins via LC-MS/MS, initial filtering of data removed proteins with one or fewer unique peptides (n=2724) and proteins which lacked SILAC ratios (n=244). This left 3213 proteins, which were assessed for replicate 2. Log_2 of SILAC ratios were used to produce frequency distribution graphs plotted to Gaussian distribution (Figure 3.4A-C). These graphs' mean and standard deviations were used to calculate the threshold for each Sample/Mock ratio (Mean + 1.96SD) (Figure 3.4D).

Replicate 3 gave an identification of (n=3860) proteins via LC-MS/MS, initial filtering of data removed proteins with one or fewer unique peptides (n=1942) and proteins which lacked SILAC ratios (n=150). This left 1768 proteins, which were assessed for replicate 3. Log_2 of SILAC ratios were used to produce frequency distribution graphs plotted to Gaussian distribution (Figure 3.5A-C). These graphs' mean and standard deviations were used to calculate the threshold for each Sample/Mock ratio (Mean + 1.96SD) (Figure 3.5D).

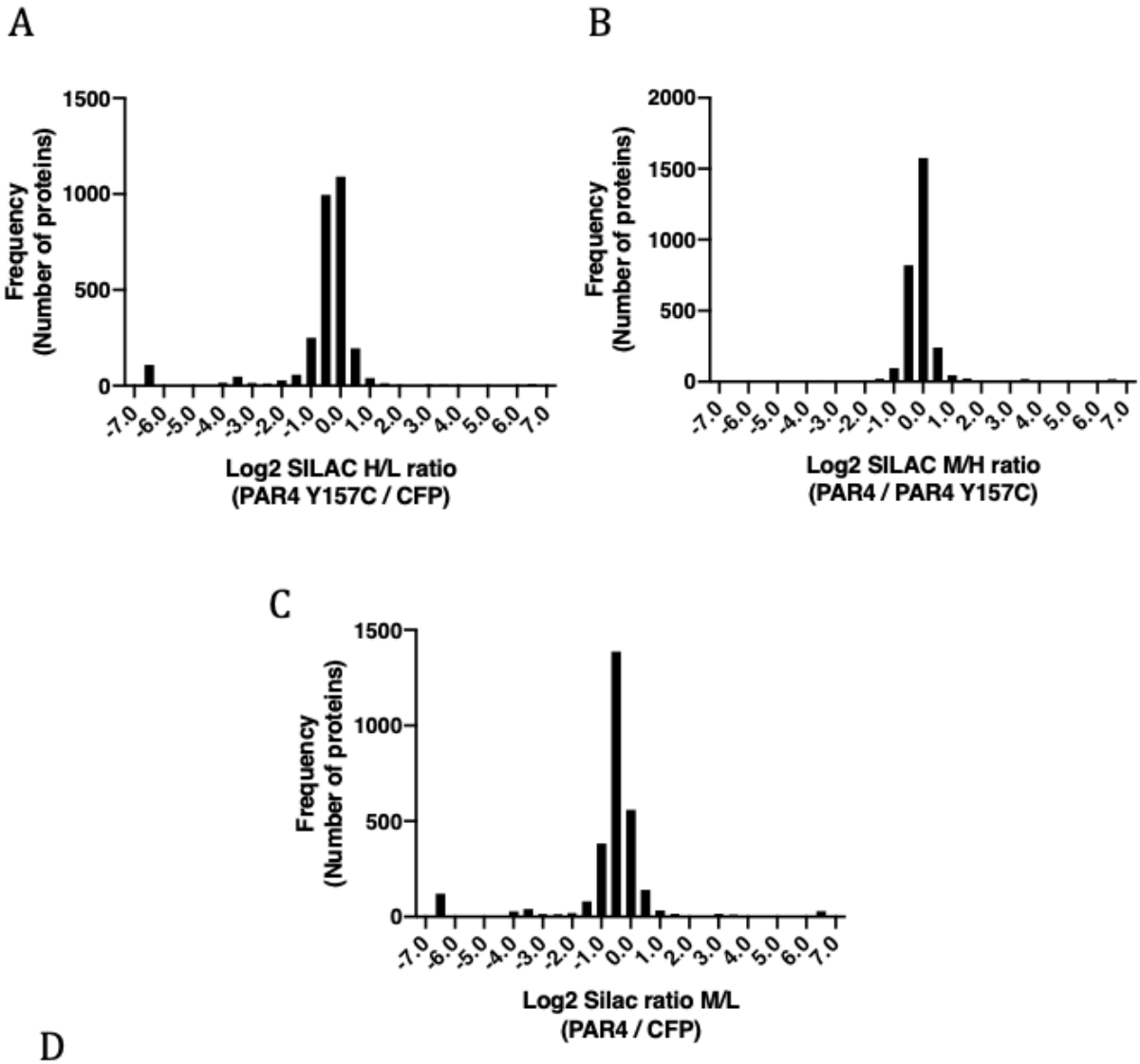

D

Replicate 1	Heavy/Light	Medium/Heavy	Medium/Light
Mean	-0.2371	-0.1206	-0.456
SD	0.4039	0.3179	0.3442
Threshold	0.554544	0.502484	0.218632

Figure 3.3 Threshold determination for SILAC ratios in replicate 1. A) Histogram showing the distribution of protein ratios for Heavy/Light, n=2905 proteins fitted to gaussian distribution. B) Histogram showing the distribution of protein ratios for Medium/Heavy, n=2905 proteins fitted to gaussian distribution. C) Histogram showing the distribution of protein ratios for Medium/Light, n=2905 proteins fitted to gaussian distribution. Table showing the mean and standard deviation generated from the gaussian distribution. Thresholds were determined by adding the mean to 1.96SD.

A

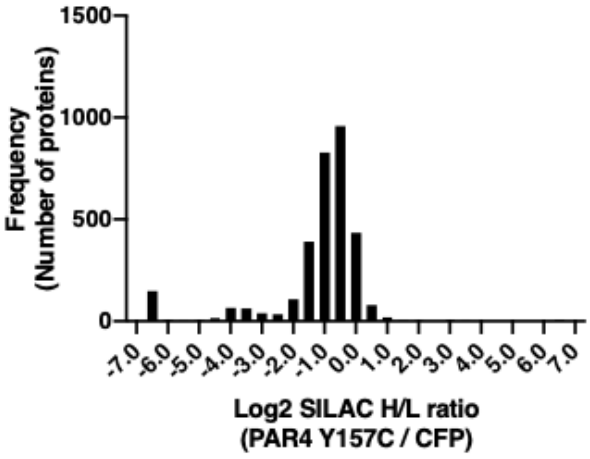

B

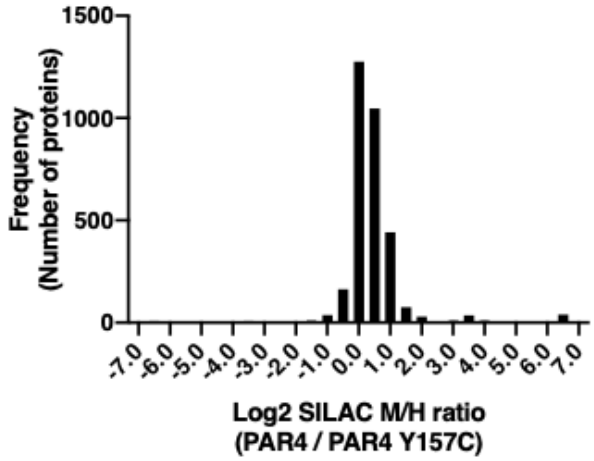

C

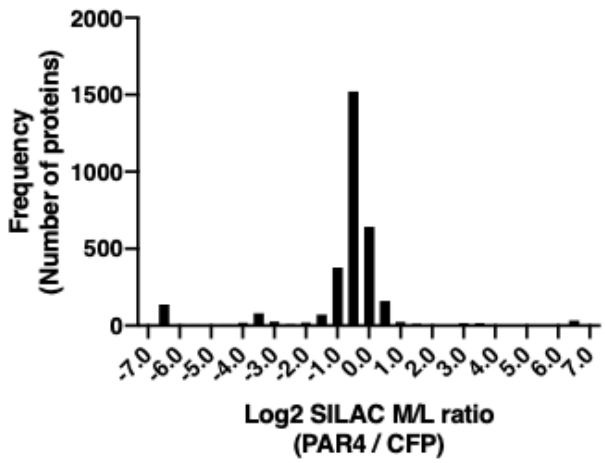

D

Replicate 2	Heavy/Light	Medium/Heavy	Medium/Light
Mean	-0.7097	0.2497	-0.44
SD	0.568	0.4351	0.3397
Threshold	0.40358	1.102496	0.225812

Figure 3.4 Threshold determination for SILAC ratios in replicate 2. A) Histogram showing the distribution of protein ratios for Heavy/Light, n=3213 proteins fitted to gaussian distribution. B) Histogram showing the distribution of protein ratios for Medium/Heavy, n=3213 proteins fitted to gaussian distribution. C) Histogram showing the distribution of protein ratios for Medium/Light, n=3213 proteins fitted to gaussian distribution. Table showing the mean and standard deviation generated from the gaussian distribution. Thresholds were determined by adding the mean to 1.96SD.

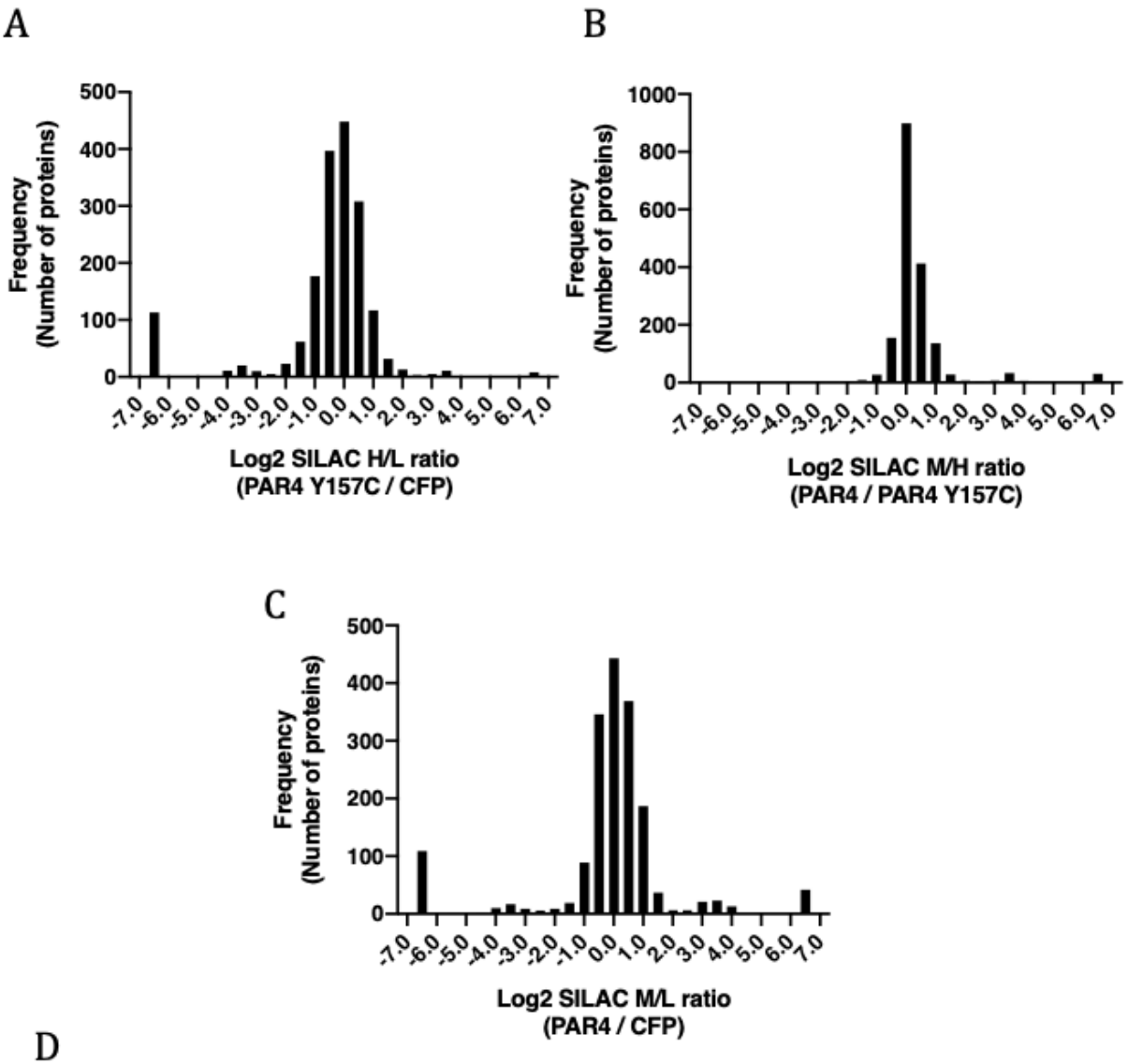

D

Replicate 3	Heavy/Light	Medium/Heavy	Medium/Light
Mean	-0.07869	0.1358	0.1435
SD	0.746	0.4863	0.7233
Threshold	1.38347	1.088948	1.561168

Figure 3.5 Threshold determination for SILAC ratios in replicate 3. A) Histogram showing the distribution of protein ratios for Heavy/Light, n=1768 proteins fitted to gaussian distribution. B) Histogram showing the distribution of protein ratios for Medium/Heavy, n=1768 proteins fitted to gaussian distribution. C) Histogram showing the distribution of protein ratios for Medium/Light, n=1768 proteins fitted to gaussian distribution. Table showing the mean and standard deviation generated from the gaussian distribution. Thresholds were determined by adding the mean to 1.96SD.

3.3.2 Evaluation of reproducibility between experimental replicates

To determine the reproducibility between experimental replicates, replicate Log_2 SILAC ratios were compared across all datasets. The total number of proteins pulled from all three experimental replicates was (n=4544). Using correlation analysis, only proteins that contained Log_2 SILAC ratios for both replicates were compared.

For Heavy/Light replicate one vs replicate two, a total of (n=2086) proteins had corresponding Log_2 SILAC ratios and gave a Pearson correlation of (R=0.4673). Replicate one vs replicate three had a total of (n=1122) proteins and gave a Pearson correlation of (R=0.4303), and replicate two vs replicate three had a total of (n=1127) proteins and gave a Pearson correlation of (R=0.4270) (Figure 3.6A). For Medium/Light replicate one vs replicate two, a total of (n=2085) proteins had corresponding Log_2 SILAC ratios and gave a Pearson correlation of (R=0.4302). Replicate one vs replicate three had a total of (n=1123) proteins and gave a Pearson correlation of (R=0.3623), and replicate two vs replicate three had a total of (n=1127) proteins and gave a Pearson correlation of (R=0.3624) (Figure 3.6B). For Medium/Heavy replicate one vs replicate two, a total of (n=2086) proteins had corresponding Log_2 SILAC ratios and gave a Pearson correlation of (R=0.05883). Replicate one vs replicate three had a total of (n=1123) proteins and gave a Pearson correlation of (R=0.07563), and replicate two vs replicate three had a total of (n=1127) proteins and gave a Pearson correlation of (R=0.07112) (Figure 3.6C).

The analysis showed that none of the experimental replicates showed an R>0.5, and therefore, there was no strong correlation between any for reproducibility. However, comparing Heavy/Light and Medium/Light gave a Pearson correlation between 0.3 – 0.5, showing that there was a medium association between replicate datasets for these SILAC ratios.

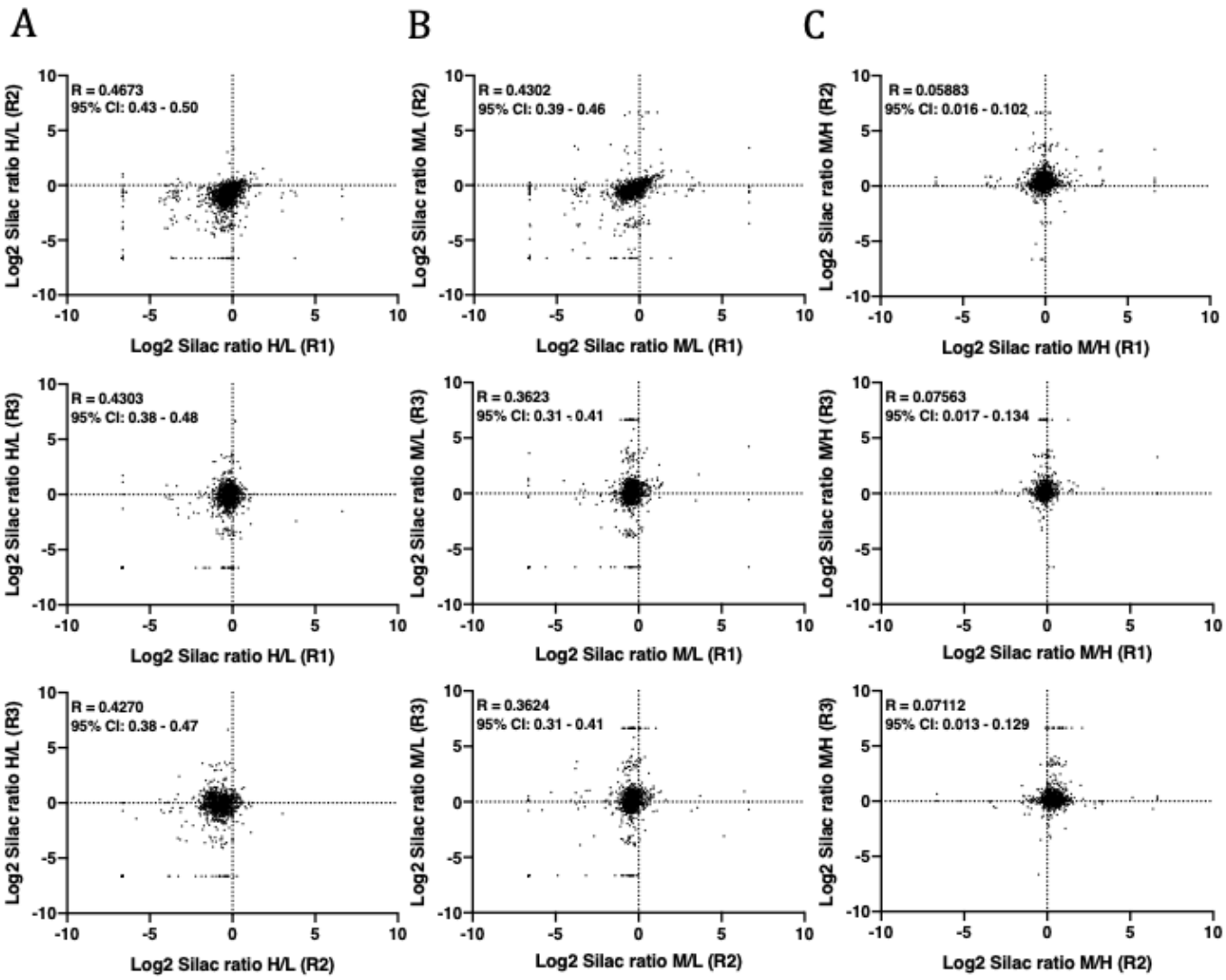

Figure 3.6 Evaluation of reproducibility between the ratios of experimental replicates for identified proteins. A) Heavy/Light ratios Replicate 1 (R1) (x axis) vs Replicate 2 (R2) (y axis). A correlation between R1 vs R2 was observed with a Pearson correlation (R = 0.4673). H/L ratios R1 vs R3, a correlation was observed with a Pearson correlation (R = 0.4303). H/L ratios R2 vs R3, a correlation was observed with a Pearson correlation (R = 0.4270). B) Medium/Light Replicate 1 (R1) (x axis) vs Replicate 2 (R2) (y axis). A correlation between R1 vs R2 was observed with a Pearson correlation (R = 0.4302). M/L ratios R1 vs R3, a correlation was observed with a Pearson correlation (R = 0.3623). M/L ratios R2 vs R3, a correlation was observed with a Pearson correlation (R = 0.3624). C) Medium/Heavy Replicate 1 (R1) (x axis) vs Replicate 2 (R2) (y axis). A correlation between R1 vs R2 was observed with a Pearson correlation (R = 0.05883). M/H ratios R1 vs R3, a correlation was observed with a Pearson correlation (R = 0.07563). M/H ratios R2 vs R3, a correlation was observed with a Pearson correlation (R = 0.07112).

3.3.3 Evaluating correlation between wild-type and mutant PAR4 in SILAC proteomic datasets

Following on from the previous determination that there was no correlation between replicate datasets, we next assessed if there was a correlation between the wild-type (Medium/Light) and mutant Y157C (Heavy/Light) within experimental replicates.

The total number of proteins identified in replicate 1 (n=2905), Pearson correlation between wild-type and mutant was determined as (R=0.8005) (Figure 3.7A). For replicate 2, the total number of proteins identified was (n=3213), and a Pearson correlation between wild-type and mutant was determined as (R=0.7577) (Figure 3.7B). For replicate 3, the total number of proteins identified was (n=1768), and a Pearson correlation between wild-type and mutant was determined as (R=0.8105) (Figure 3.7C).

These data show that there is a strong correlation in protein expression/interaction in both wild-type and mutant Y157C PAR4, as the Pearson coefficient was >0.5 for all replicate datasets.

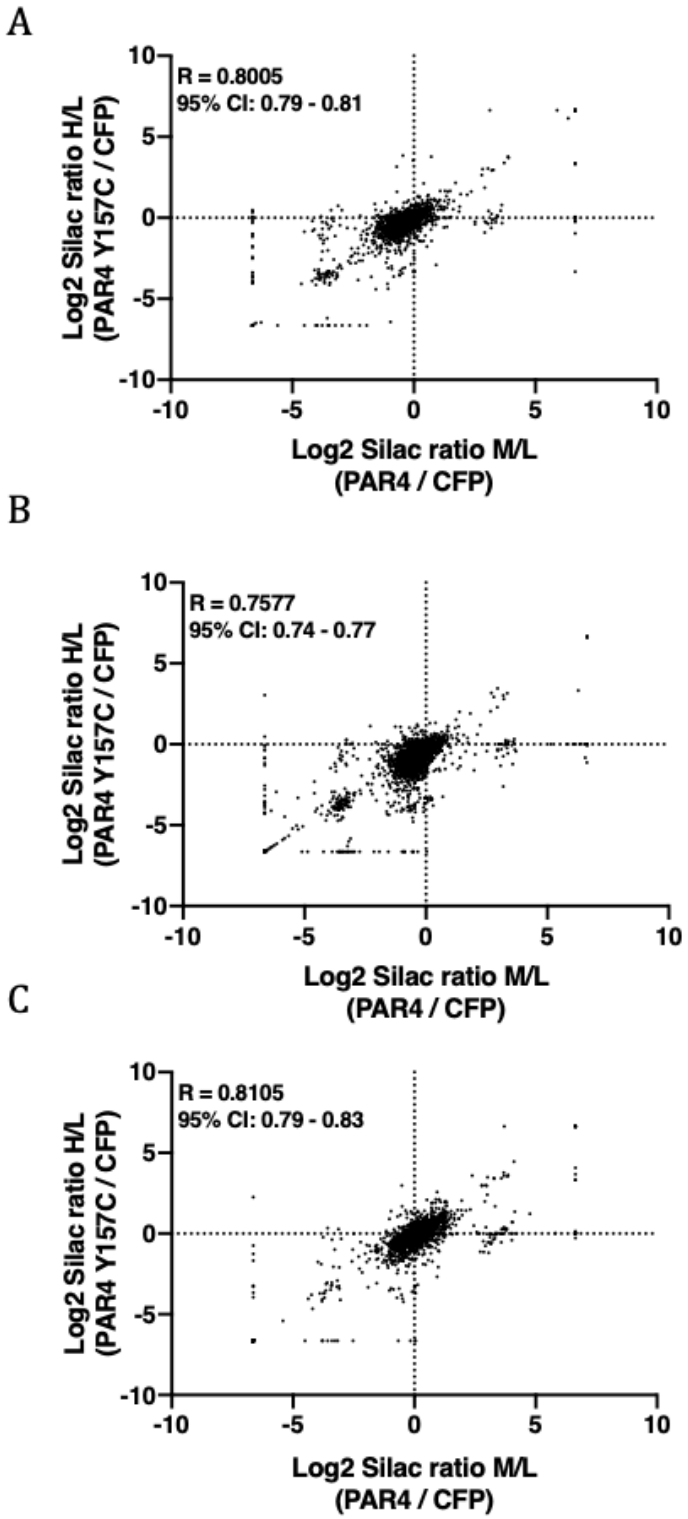

Figure 3.7 Evaluation of protein ratios between PAR4 wild type (M/L) and PAR4 mutant Y157C (H/L) within experimental replicates. A) wt-PAR4 (M/L ratios) vs mut-PAR4 (H/L ratios) in replicate 1, n=2905 proteins, a correlation between SILAC ratios M/L vs H/L was observed with a Pearson correlation (R = 0.8005). B) wt-PAR4 (M/L ratios) vs mut-PAR4 (H/L ratios) in replicate 2, n=3213 proteins, a correlation between SILAC ratios M/L vs H/L was observed with a Pearson correlation (R = 0.7577). C) wt-PAR4 (M/L ratios) vs mut-PAR4 (H/L ratios) in replicate 3, n=1768 proteins, a correlation between SILAC ratios M/L vs H/L was observed with a Pearson correlation (R = 0.8105).

3.3.4 Whole proteome – 2 or more hits

Following the method by (Emmott and Goodfellow, 2014) hits which are above the threshold across two or more replicates are considered as high confidence proteins. A protein interaction network was produced using STRING.db with the accession numbers in the proteomic datasets. This led to 230 proteins not being identified, and therefore, accession numbers were converted to their UniProt gene names. Analysis of two or more high-confidence hits identified (n=996) proteins, of which a total of (n=994) proteins were successfully identified using stringdb.org and UniProt searches.

The data was extracted into Cytoscape (v3.9.1), and a protein interaction network was produced (Figure 3.8). To improve visualisation, nodes were converted to their gene names. In addition, unconnected nodes were removed (n=4), and nodes were coloured and sized based on their degrees of centrality and the number of connections to other nodes (light yellow and smaller nodes) meant fewer connections and (orange/red and larger nodes) meant more connections and more central in the cluster.

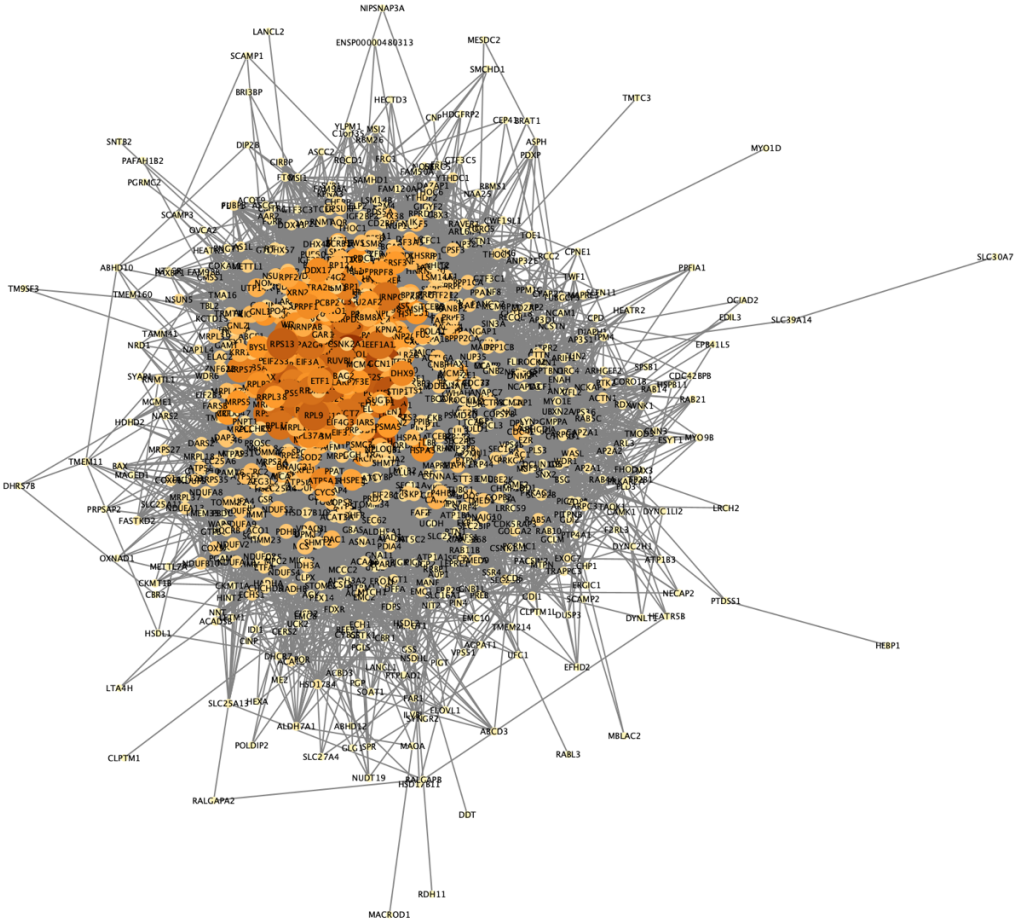

Figure 3.8. Interacting proteins with thresholds above the cut off across two or more replicates. Shows a protein interaction network (n=990) with thresholds above the cutoff (M/L, H/L and M/H) across two or more replicates. Total proteins (n=996), unidentified proteins (n=2) and unconnected proteins (n=4) are not present. The size and colour (yellow to red) depict the number of connections to neighbouring nodes in the network. Interaction network was produced using Cytoscape (v3.9.1).

3.3.5 Gene Ontology analysis of enriched clusters using BiNGO and Reactome

For easier visualisation of genes present over two or more datasets, we compared the genes present with the whole human genome. This was performed using the Cytoscape plugin BiNGO to determine the gene ontology clusters overrepresented in the PAR4 proteome. The gene ontology map was generated using a hypergeometric test for statistical significance using the Benjamini and Hochberg false discovery rate (FDR) correction and statistical significance level set at (0.05). This generated three network maps for Molecular function, biological process and cellular components shown in (Figures 3.9 – 3.11).

The first map generated was for molecular function. As can be seen, it formed three distinct clusters, two of which had a majority upregulated (yellow to Orange) and one which had a majority downregulated (white). The first major cluster was binding activity, with the top three overrepresented groups being RNA binding (185 genes, corrected p= $1.290X10^{-68}$), protein binding (654 genes, corrected p=$2.5807X10^{-37}$) and nucleotide binding (250 genes, corrected p=$7.9674X10^{-25}$). The second overrepresented cluster was catalytic activity, extending into four branches. The three most overrepresented groups in this cluster are pyrophosphatase activity (84 genes, corrected p=$2.4695X10^{-8}$), hydrolase activity (84 genes, corrected p=$2.8608X10^{-8}$) and helicase activity (24 genes, corrected p=$8.7511X10^{-8}$). The final cluster was for transporter activity and contained the most underrepresented groups. However, the three most overrepresented in the cluster are protein transporter activity (18 genes, corrected p=$2.8307X10^{-5}$), porin activity (5genes, corrected p=$2.3291X10^{-4}$) and protein transmembrane transporter (6 genes, corrected p=$2.5458X10^{-3}$) (Figure 3.9).

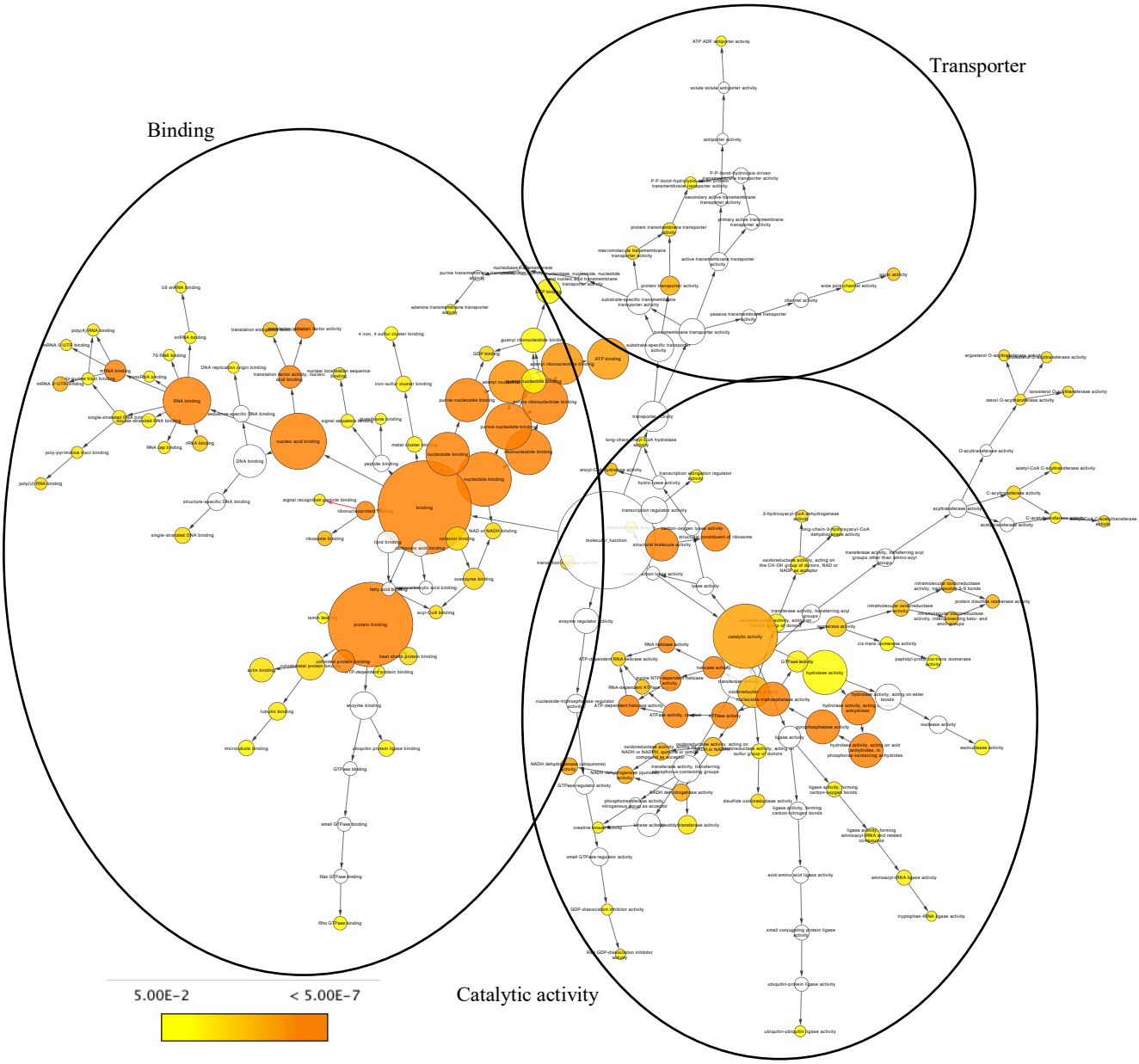

Figure 3.9 Clustering map of molecular function for the full PAR4/Y157C proteome. Shows a gene ontology map produced using BiNGO plugin on Cytoscape. Map shows five distinct clusters outlined on the map with the key function of the cluster labelled. Nodes are coloured shown overrepresentation as a function of the p-value (yellow 5.00E-2 to orange <5.00E-7). Three most overrepresented nodes are RNA binding (p 1,1290E-68, protein binding (p 2.5807E-37) and structural constituent of ribosome (p 3.2648E-28). Link to full network:

The second map generated concerned biological processes, which contained the most groups and, therefore, the most clusters of the maps generated, with a total of eight clusters. The most overrepresented group was gene expression, which is unsurprising due to the number of ribosomal proteins identified in the datasets. A corrected $p=7.161X10^{-70}$ gives an indication of just how overrepresented these proteins are in this proteome.

Although eight clusters are identifiable, three larger clusters are prominent in the ontology map, two containing the most overrepresented proteins and one which is underrepresented. The first major cluster was metabolism, with the top three overrepresented groups being cellular metabolic process (539 genes, corrected $p= 3.1715X10^{-68}$), cellular macromolecule metabolic process (423 genes, corrected $p=7.8272X10^{-60}$) and metabolic process (577 genes, corrected $p=2.7514X10^{-57}$). The second overrepresented cluster was protein processing, transport and localisation. The three most overrepresented groups in this cluster are cellular process (727 genes, corrected $p=5.143X10^{-44}$), cellular localisation (106 genes, corrected $p=2.1040X10^{-8}$) and protein transport (84 genes, corrected $p=4.4507X10^{-7}$). The final main cluster was for the biosynthetic process and contained the most underrepresented groups. However, the three most overrepresented in the cluster are regulation of translational initiation (16 genes, corrected $p=1.3741X10^{-7}$), regulation of cellular protein metabolic process (69 genes, corrected $p=1.7389X10^{-7}$) and negative regulation of translation (14 genes, corrected $p=4.6603X10^{-7}$).

In addition, five smaller clusters are also present, including the nucleotide and nucleic acid metabolic process, mRNA and tRNA metabolism, DNA, tRNA replication, and translation. The two other smaller clusters are the esterification of sterols, steroids, and lipids and the regulation of ligase activity (Figure 3.10).

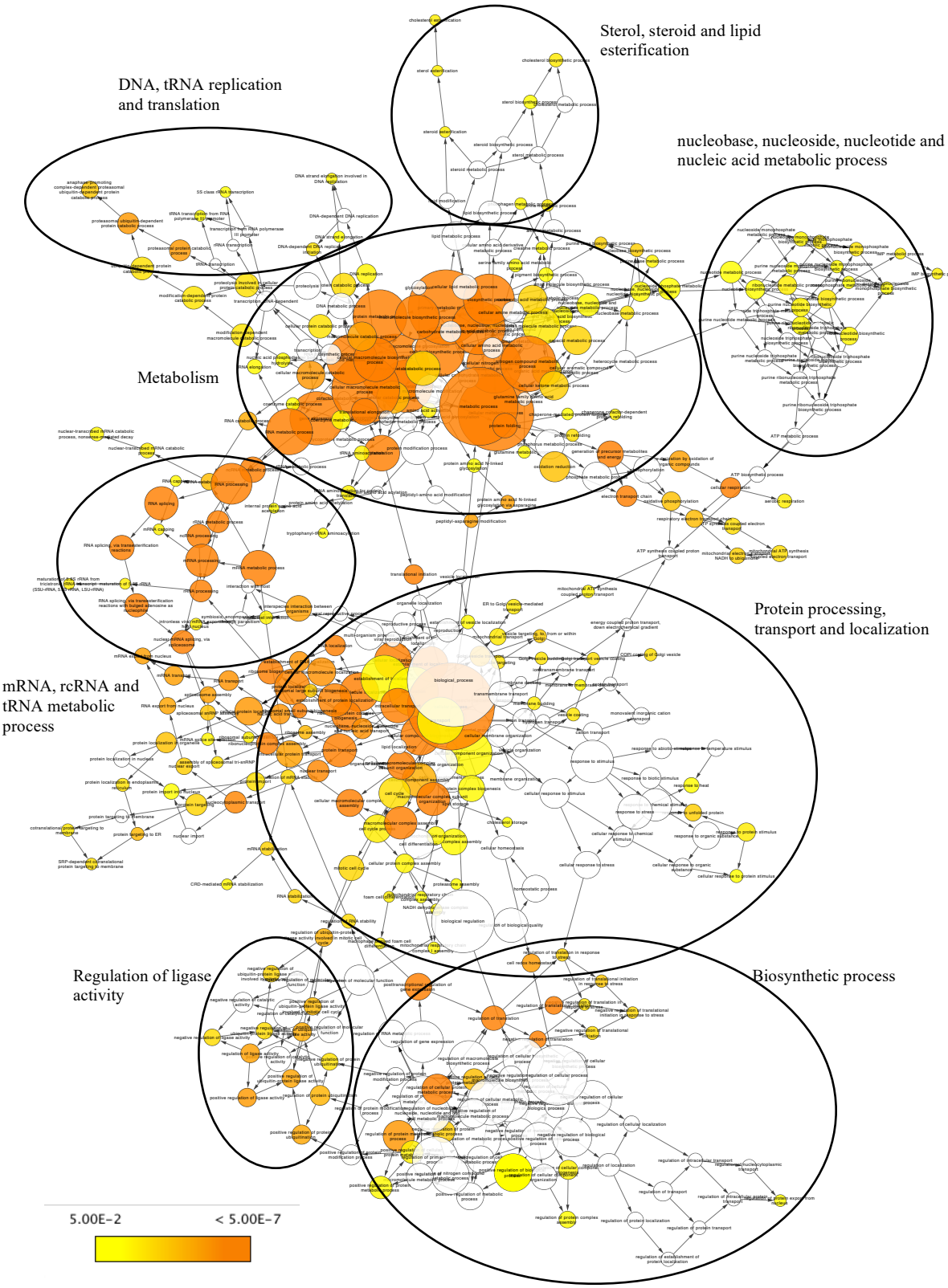

Figure 3.10. Clustering map of biological processes for the full PAR4/Y157C proteome. Shows a gene ontology map produced using BiNGO plugin on Cytoscape. Map shows eight distinct clusters outlined on the map with the key function of the cluster labelled. Nodes are coloured shown overrepresentation as a function of the p-value (yellow 5.00E-2 to orange <5.00E-7). Three most overrepresented nodes are gene expression (p 7.1610E-70, cellular metabolic process (p 3.1715E-68) and cellular macromolecule metabolic process (p 7.8272E-60). Link to full network:

The final enrichment ontology analysis performed using BiNGO for the whole PAR4 proteome was to look at the cellular components of the identified proteins. This network was the hardest to define specific clusters because it is quite compacted; this layout could be accounted for because many proteins are present within multiple cellular compartments, so the distinction is more challenging to delineate. However, three cellular components for highly overrepresented clusters were identifiable. The first major cluster was cytosolic, with the top three overrepresented groups being the intracellular part (850 genes, corrected p= $1.5325X10^{-96}$), intracellular (853 genes, corrected p=$5.1291X10^{-89}$) and cytoplasm (692 genes, corrected p=$6.2487X10^{-81}$). The second overrepresented cluster was ribosomal, with the three most overrepresented groups in this cluster being ribonucleoprotein complex (176 genes, corrected p=$3.5130X10^{-95}$), ribosome (73 genes, corrected p=$1.9062X10^{-41}$) and ribosomal complex (48 genes, corrected p=$9.7290X10^{-29}$). The final main cluster was for mitochondrial proteins, with the three most overrepresented in the cluster being mitochondrion (177 genes, corrected p=$3.3717X10^{-31}$), mitochondrial part (108 genes, corrected p=$6.9352X10^{-27}$) and mitochondrial lumen (51 genes, corrected p=$1.3104X10^{-17}$).

In addition, three smaller clusters appear within the network map. These include cytoplasmic vesicle transporters (55 genes), Cytoskeletal proteins (99 genes), and membrane and motility proteins (27 genes) (Figure 3.11).

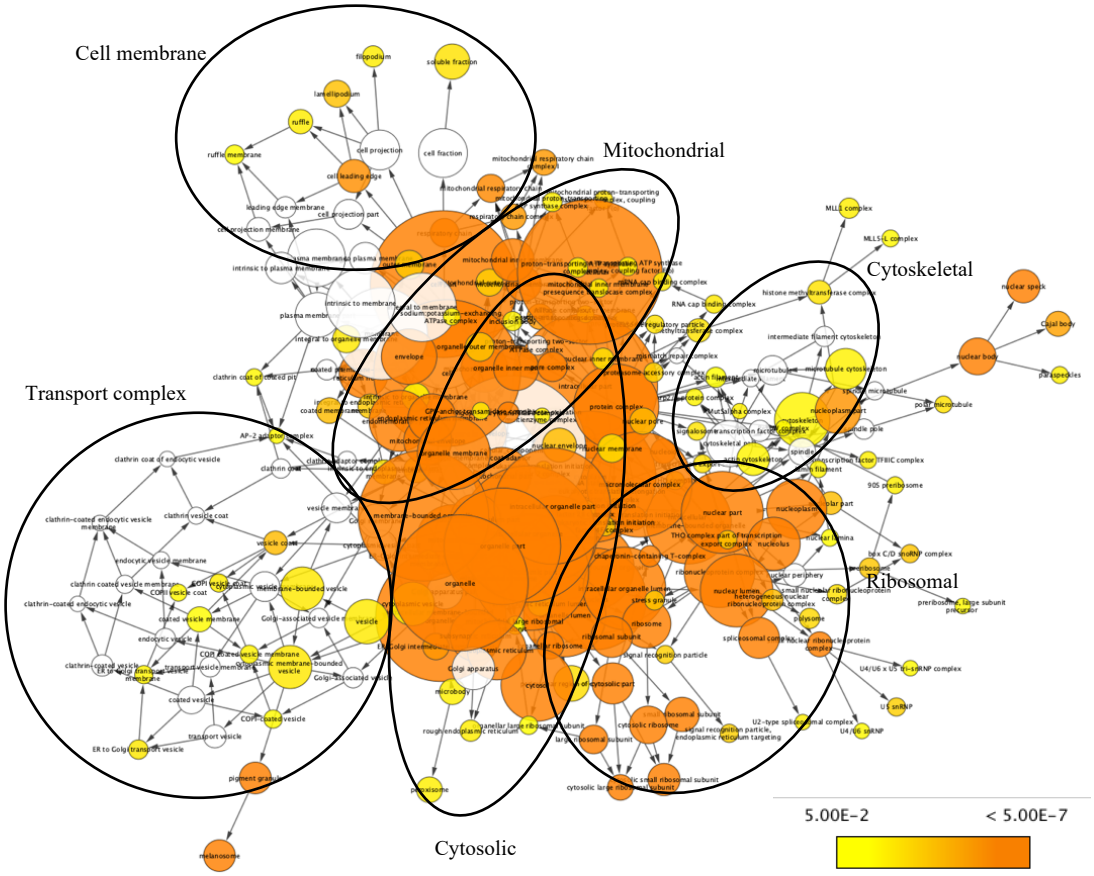

Figure 3.11 Clustering map of cellular component for the full PAR4/Y157C proteome. Shows a gene ontology map produced using BiNGO plugin on Cytoscape. Map shows six distinct clusters outlined on the map with the key function of the cluster labelled. Nodes are coloured shown overrepresentation as a function of the p-value (yellow 5.00E-2 to orange <5.00E-7). Three most overrepresented nodes are intracellular part (p 1.5325E-96, ribonucleoprotein complex (p 3.5130E-95) and intracellular (p 5.1291E-89).

3.3.6 Visualisation of biomolecular cascades using Reactome

The final analysis of the whole PAR4 proteome was carried out using the Cytoscape plugin Reactome. Reactome allows for the visualisation of biomolecular cascades present in a set of proteins. The map was generated using an FDR filter of 0.05, and the tool was used to confirm that the most enriched pathways were translation (114 genes, FDR $4.5519X10^{-15}$), metabolism (85 genes, FDR= $4.5519X10^{-15}$), and cell response to stimuli (47 genes, FDR= $1.1102X10^{-15}$) (Figure 3.12).

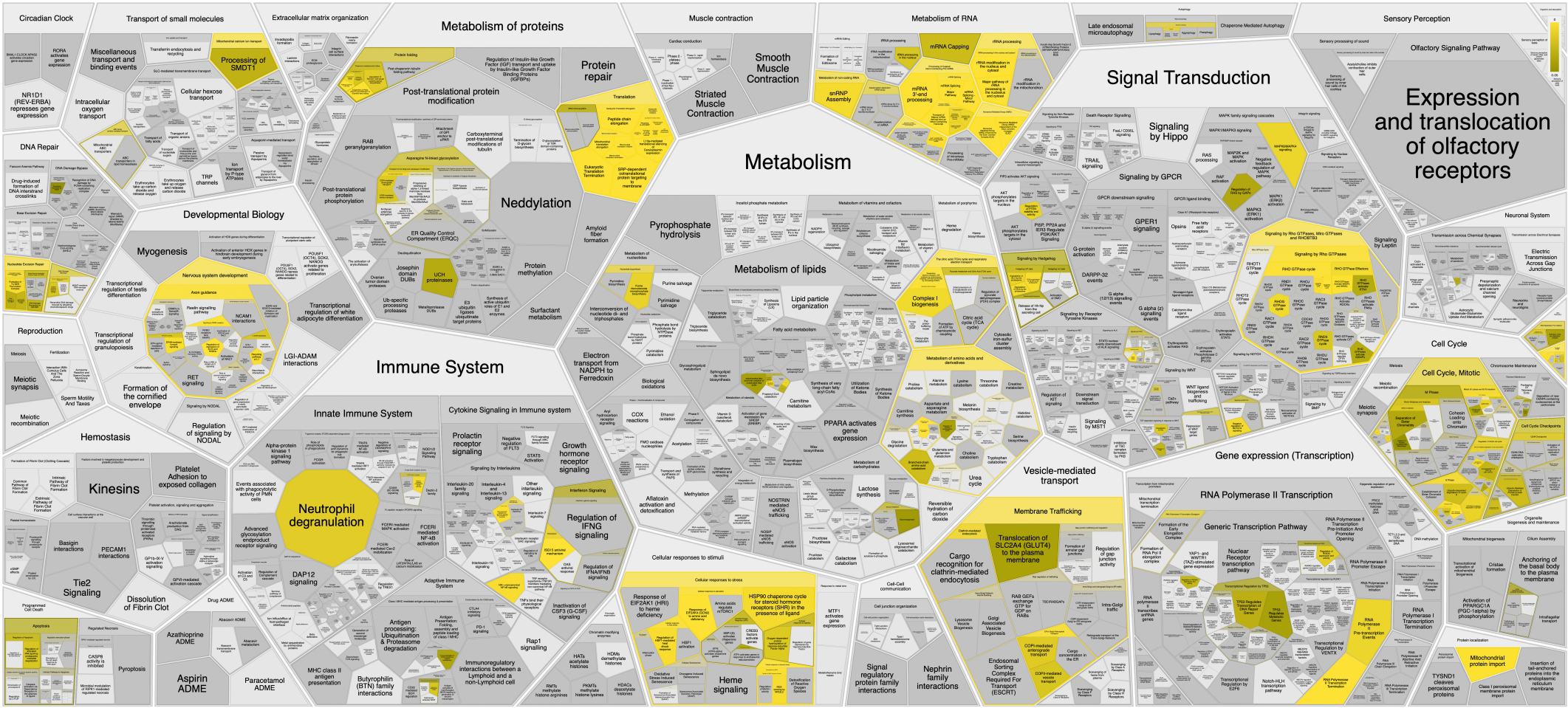

Figure 3.12. Reactome analysis of the whole PAR4 proteome. The most enriched pathways are around metabolism of proteins and RNA and translation. Enriched pathways are also present in vesicle-mediate transport particularly in membrane trafficking and in the cell cycle. The colour gradient is indicative of the false discovery rate (FDR) on a scale of 0 (yellow) to 0.05 (brown). Full image link:

3.3.7 Comparing identified proteins between wt-PAR4 and mut-PAR4 Y157C

Next, we compare proteins above the threshold across all three replicates for wt-PAR4 (M/L) and mut-PAR4 Y157C (H/L). For wt-PAR4, 224 proteins were identified above the threshold across all three replicates, and 150 proteins were identified for mut-PAR4 Y157C.

The data was extracted into Cytoscape (v3.9.1), and a protein interaction network was produced for wt-PAR4 (Figure 3.13) and mut-PAR4 Y157C (Figure 3.14). Unconnected nodes were removed (n=11 for wt-PAR4) and (n=13 for mut-PAR4 Y157C). To improve visualisation, nodes were converted to their gene names, and nodes were coloured and sized based on their degrees of centrality. The number of connections to other nodes (light yellow and smaller nodes) meant fewer connections, and (orange/red and larger nodes) meant more connections and more central in the cluster.

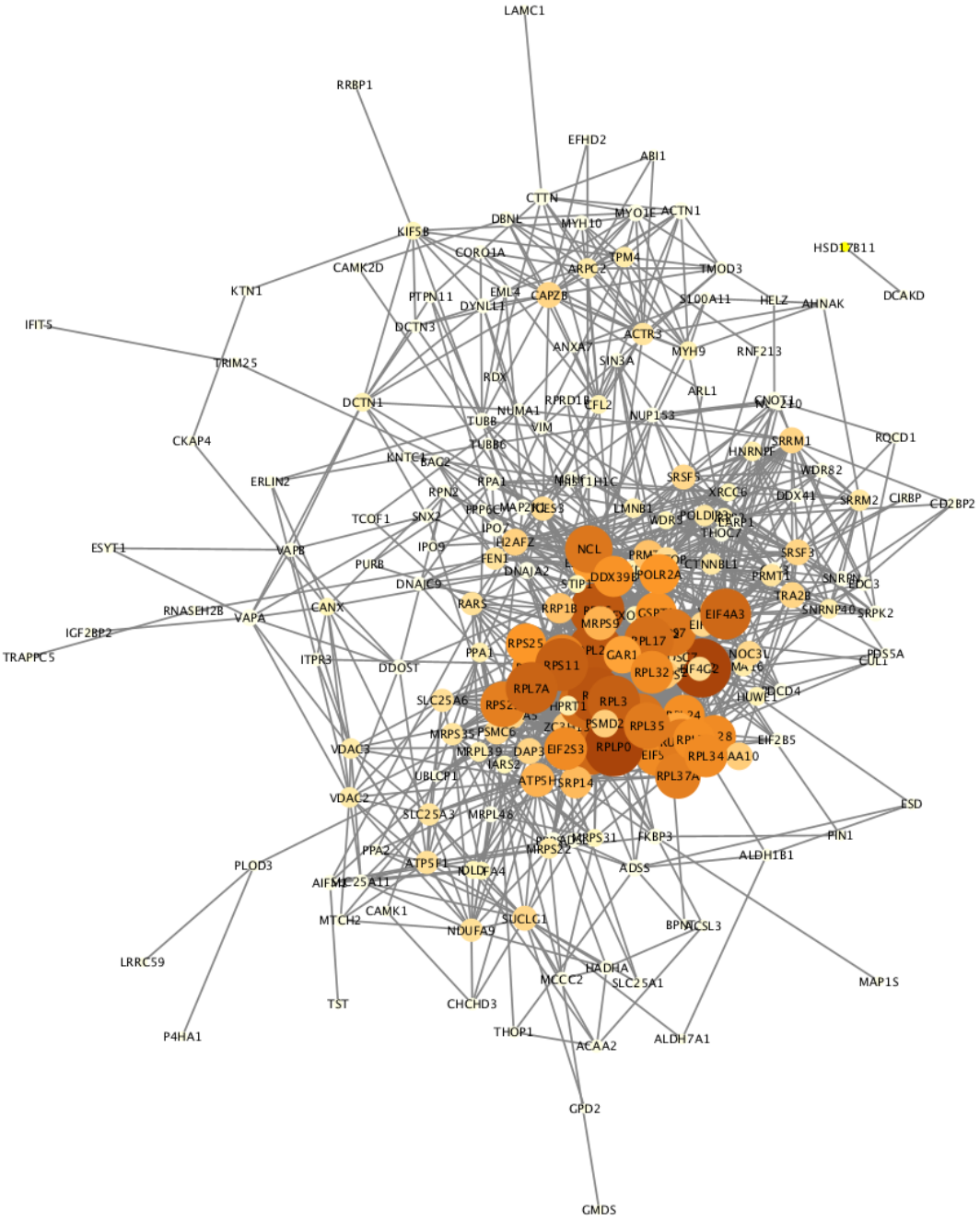

Figure 3.13. Interacting proteins with thresholds above the cut off across all replicates for wt-PAR4. Shows a protein interaction network (n=213) with thresholds above the cutoff (M/L) across all replicates. Total proteins (n=224), and unconnected proteins (n=11) are not present. The size and colour (yellow to red) depict the number of connections to neighbouring nodes in the network. Interaction network was produced using Cytoscape (v3.9.1).

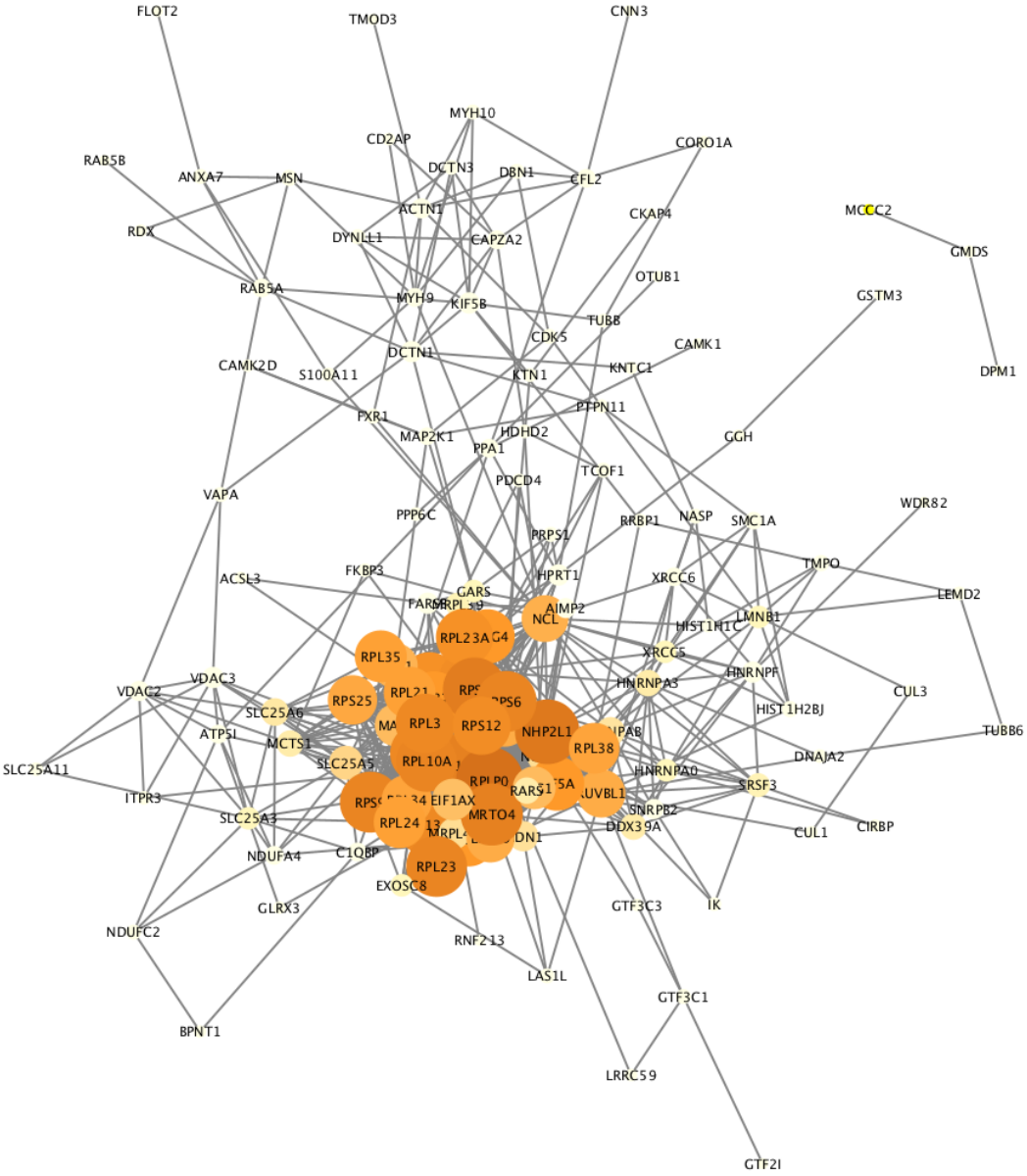

Figure 3.14. Interacting proteins with thresholds above the cut off across all replicates for mut-PAR4 Y157C. Shows a protein interaction network (n=137) with thresholds above the cutoff (H/L) across all replicates. Total proteins (n=150), and unconnected proteins (n=13) are not present. The size and colour (yellow to red) depict the number of connections to neighbouring nodes in the network. Interaction network was produced using Cytoscape (v3.9.1).

3.3.8 Panther analysis to compare the gene ontology

Protein analysis through evolutionary relationships (PANTHER) is a bioinformatics tool that allows for the classification of proteins from proteomic data based on families of evolutionary-related proteins. It allows proteins to be grouped into molecular function, protein class, biological process and cellular component. The four groups were run separately to compare the results in the datasets for wt-PAR4 (n=224) and mut-PAR Y157C (n=150).

For molecular function, the main function shared between wt-PAR4 and mut-PAR4 Y157C were very similar, with the first being binding (wt-PAR4= 42.2% and mut-PAR4 Y157C= 37.6%), the second was catalytic activity (wt-PAR4= 22.4% and mut-PAR4 Y157C= 21.3%), and the third was structural molecule activity (wt-PAR4= 11.2% and mut-PAR4 Y157C= 12.8%). Although wt-PAR4 contained two molecular function groups not present in the mut-PAR4 Y157C dataset (molecular transducer activity 0.9% and molecular adaptor activity 0.9%) (Figure 3.15A).

For biological process, the three most prominent processes were similar between wt-PAR4 and mut-PAR4 Y157C and were cellular process (wt-PAR4= 61.9% and mut-PAR4 Y157C= 61.0%), metabolic process (wt-PAR4= 42.2% and mut-PAR4 Y157C= 39.7%), and biological regulation (wt-PAR4= 16.6% and mut-PAR4 Y157C= 15.6%). Again, with molecular function, wt-PAR4 contained proteins involved in biological processes not present in mut-PAR4 Y157C, which included reproductive process (0.4%), the biological process involved in interspecies interaction (0.4%), reproduction (0.4%) and biological adhesion (0.4%) (Figure 3.15B).

The cellular component was the most similar between wt-PAR4 and mut-PAR4 Y157C, containing only two components across both, which were cellular anatomical entity (wt-PAR4= 75.8% and mut-PAR4 Y157C= 64.5%) and protein-containing complex (wt-PAR4= 40.8% and mut-PAR4 Y157C= 34.8%) (Figure 3.15C).

The final ontology group assessed using PANTHER was protein class, again the three most prominent classes were similar between wt-PAR4 and mut-PAR4 Y157C and were translational protein (wt-PAR4= 19.7% and mut-PAR4 Y157C= 24.8%), metabolite interconversion enzyme (wt-PAR4= 13.0% and mut-PAR4 Y157C= 11.3%), and RNA metabolism protein (wt-PAR4= 12.1% and mut-PAR4 Y157C= 9.9%). Again, wt-PAR4 contained protein classes that were not present in the mut-PAR4 Y157C dataset; these were extracellular matrix proteins (0.4%), gene-specific transcriptional regulator (0.9%) and transmembrane signal receptor (0.9%) (Figure 3.15D)

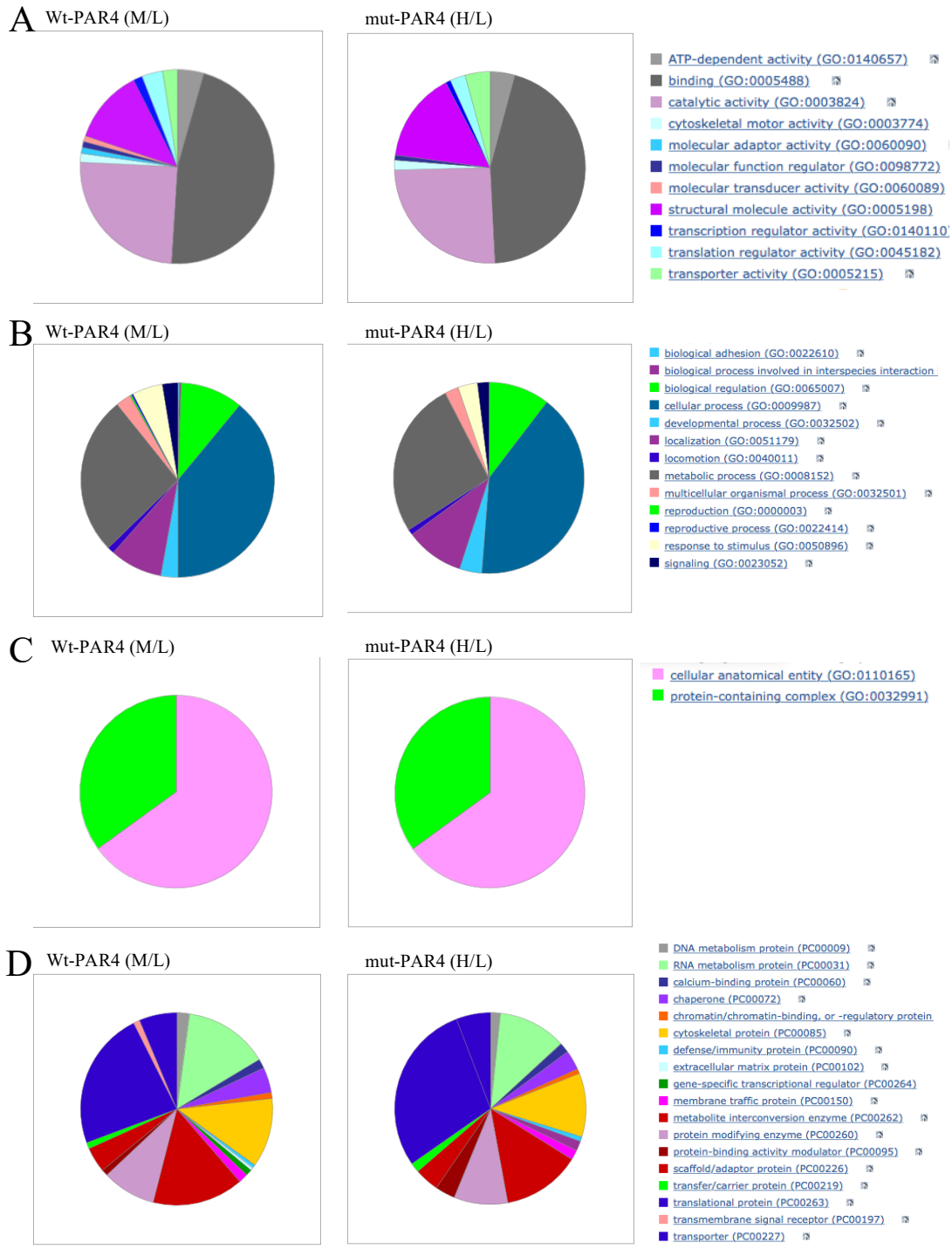

Figure 3.15. PANTHER gene ontology pie charts for wt-PAR4 and mut-PAR4 Y157C. A) shows molecular function comparison between wild-type and mutant, the three common functions were binding, catalytical activity and structural binding activity. B) shows biological process comparison between wild-type and mutant, the three common processes were cellular, metabolic and biological regulation processes. C) shows cellular component comparison between wild-type and mutant, the two common processes were cellular anatomical entity and protein-containing complex. D) shows protein class comparison between wild-type and mutant, the three common classes were translational, metabolite interconversion enzyme and RNA metabolism proteins.

3.3.9 Gene Ontology analysis of enriched clusters in wt-PAR4 using BiNGO and Reactome

For easier visualisation of genes present over the threshold for all replicates for wt-PAR4 (M/L), we compared the genes present with the whole human genome. This was performed using the Cytoscape plugin BiNGO to determine the gene ontology clusters overrepresented in the wt-PAR4 proteome. The gene ontology map was generated using a hypergeometric test for statistical significance using the Benjamini and Hochberg false discovery rate (FDR) correction and statistical significance level set at (0.05). This generated three network maps for Molecular function, biological process and cellular components, shown in (Figures 3.16– 3.18).

The first map generated was for molecular function. As can be seen, it formed three distinct clusters and one smaller cluster, two of which had a majority upregulated (yellow to Orange) and one which had a majority downregulated (white). The first major cluster was binding activity, with the top three overrepresented groups being RNA binding (44 genes, corrected p= $4.177X10^{-15}$), protein binding (163 genes, corrected p=$4.379X10^{-13}$) and nucleotide binding (54 genes, corrected p=$7.4459X10^{-4}$). The second overrepresented cluster was catalytic activity, extending into two branches. The three most overrepresented groups in this cluster are pyrophosphatase activity (23 genes, corrected p=$4.2517X10^{-3}$), hydrolase activity, acting on acid anhydrides in phosphorous-containing anhydrides (23 genes, corrected p=$4.2517X10^{-3}$) and actin dependant ATPase activity (3 genes, corrected p=$4.2517X10^{-3}$). The final cluster was for transporter activity and contained the most underrepresented groups. However, the three most overrepresented in the cluster are C-acyltransferase activity (3 genes, corrected p=$1.7805X10^{-2}$), acetyl-CoA C-acyltransferase activity (2 genes, corrected p=$2.1996X10^{-2}$) and porin activity (2 genes, corrected p=$4.7539X10^{-2}$). The fourth smaller cluster contained only two but highly overrepresented groups involved in the structure and was a structural constituents of ribosome (29 genes, corrected

p=1.6807X10^{-22}) and structural molecule activity (40 genes, corrected p=4.177X10^{-15}) (Figure 3.16).

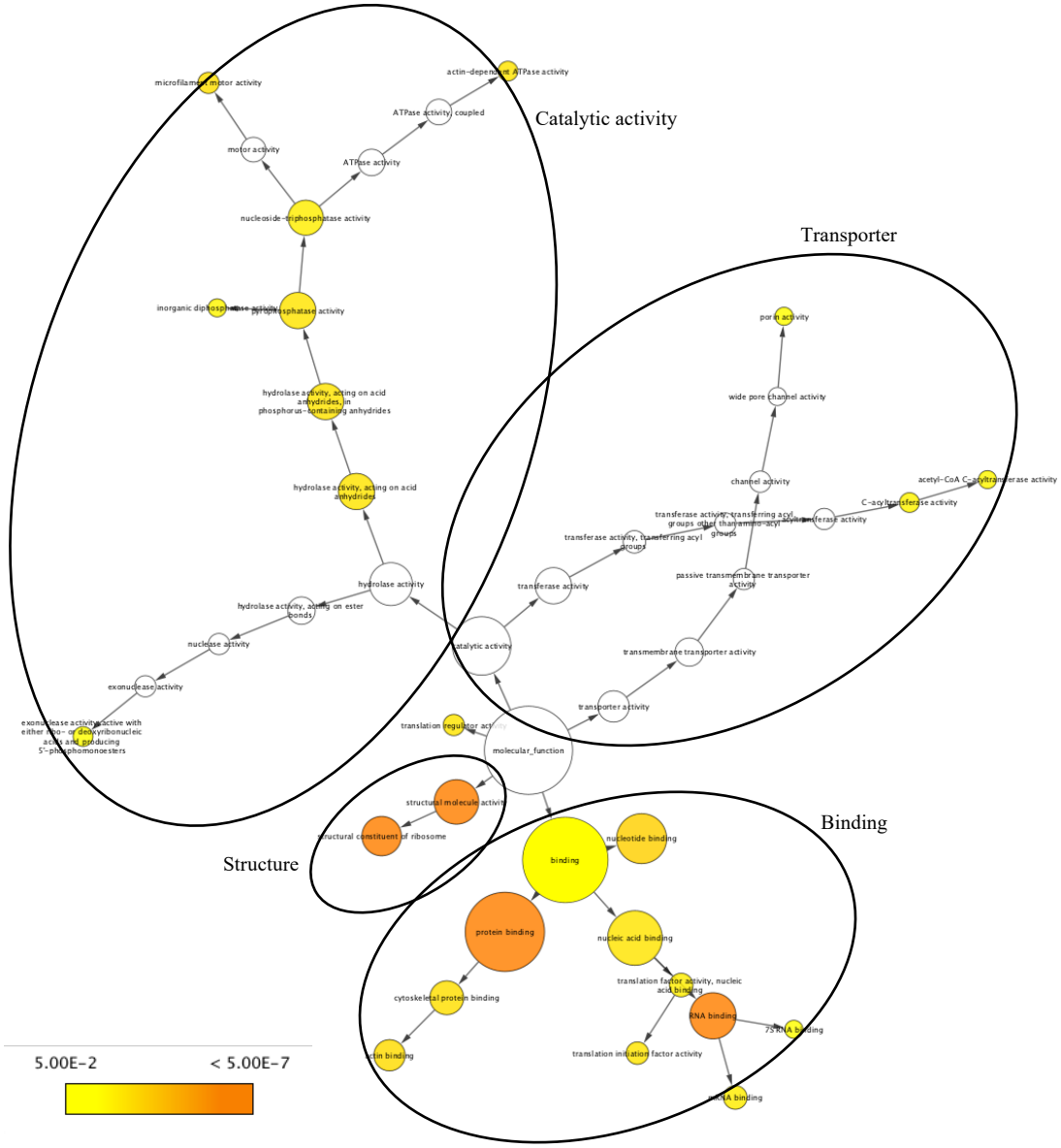

Figure 3.16. Clustering map of molecular function for wt-PAR4 triple hit proteome. Shows a gene ontology map produced using BiNGO plugin on Cytoscape. Map shows three distinct clusters and one smaller cluster outlined on the map with the key function of the cluster labelled. Nodes are coloured shown overrepresentation as a function of the p-value (yellow 5.00E-2 to orange <5.00E-7). Three most overrepresented nodes structural constituent of the ribosome (corrected $p=1.6807X10^{-22}$), RNA binding (corrected $p=4.177X10^{-15}$) and structural molecule activity (corrected $p=4.177X10^{-15}$).

The second map generated concerned biological processes, which contained the most groups and, therefore, the most clusters of the maps generated, with a total of five clusters, two of which were overrepresented and three of which contained mostly underrepresented groups, in comparison to the full proteome, which contained eight.

The first major cluster was metabolism, with the top three overrepresented groups being cellular metabolic process (125 genes, corrected p= $6.5428X10^{-15}$), cellular macromolecule metabolic process (98 genes, corrected p=$5.7317X10^{-13}$) and cellular protein metabolic process (70 genes, corrected p=$4.5908X10^{-11}$). The second overrepresented cluster was cellular and organelle organisation. The three underrepresented clusters were biological regulation, with the most overrepresented groups in this cluster being positive regulation of ligase activity (6 genes, corrected p=$1.221X10^{-2}$), regulation of ubiquitin-protein ligase activity (6 genes, corrected p=$1.92X10^{-2}$) and regulation of actin filament polymerisation (5 genes, corrected p=$2.0055X10^{-2}$). The next cluster was for biological response to stimuli; the three most overrepresented in the cluster are somatic diversification of immunoglobulins (3 genes, corrected p=$3.5913X10^{-2}$), DNA damage response, detection of DNA damage (2 genes, corrected p=$4.5066X10^{-2}$) and virus-host interaction (3 genes, corrected p=$4.5066X10^{-2}$). The final underrepresented cluster is for transport and localisation, with the three most over-represented groups being cytoskeleton-dependent intracellular transport (6 genes, corrected p=$1.4695X10^{-3}$), intracellular transport (19 genes, corrected p=$3.3125X10^{-2}$) and ribosomal import into the nucleus (2 genes, corrected p=$2.3389X10^{-2}$) (Figure 3.17).

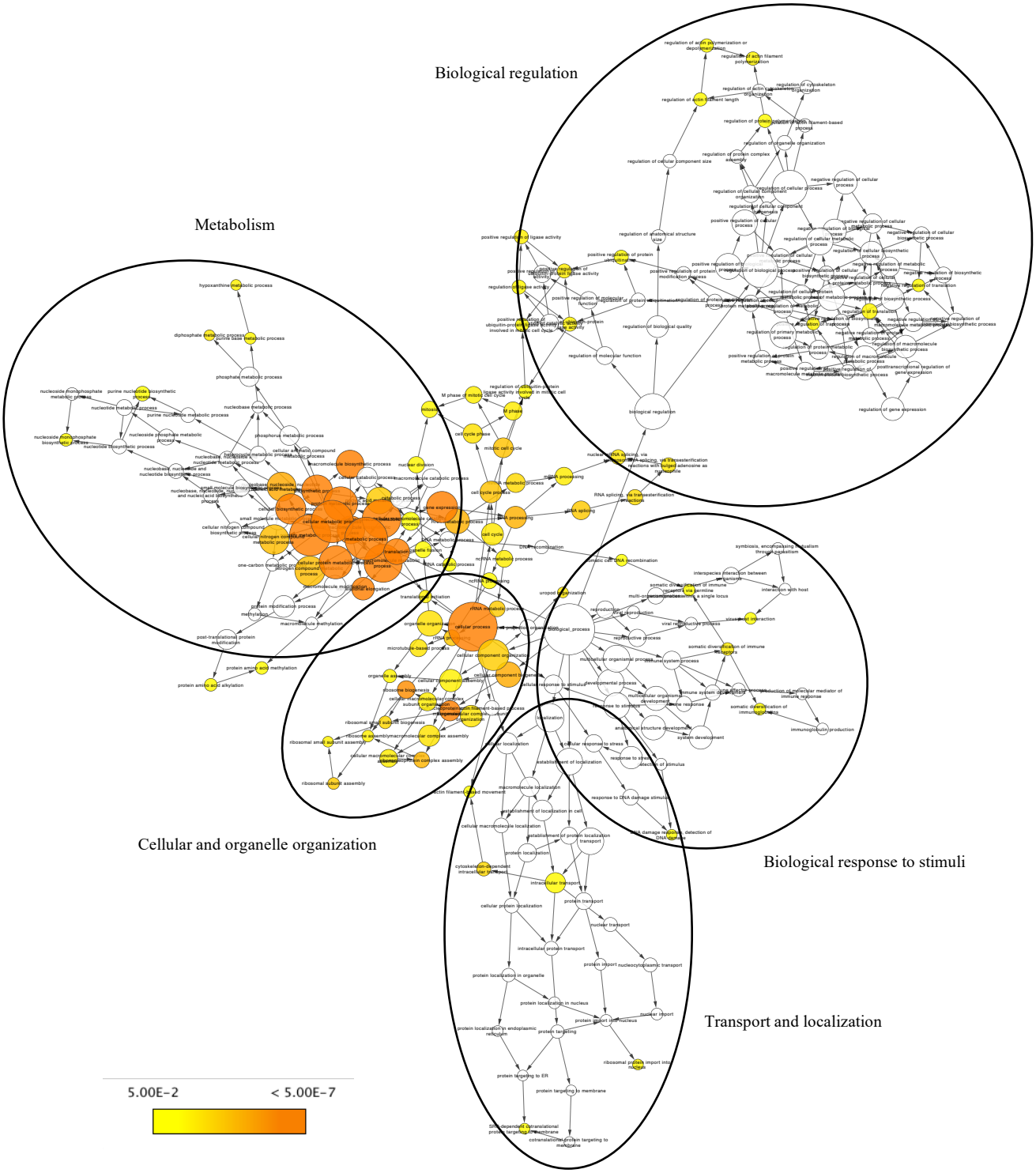

Figure 3.17. Clustering map of biological process for wt-PAR4 triple hit proteome. Shows a gene ontology map produced using BiNGO plugin on Cytoscape. Map shows five distinct clusters the map with the key function of the cluster labelled. Nodes are coloured shown overrepresentation as a function of the p-value (yellow 5.00E-2 to orange <5.00E-7). Three most overrepresented nodes are translational elongation (corrected $p=8.1499X10^{-24}$), translation (corrected $p=5.6873X10^{-23}$) and gene expression (corrected $p=3.6909X10^{-16}$). Link to full network:

The final enrichment ontology analysis performed using BiNGO for the triple wt-PAR4 proteome was to look at the cellular components of the identified proteins. This network was the hardest to define specific clusters because it was compacted. However, five major clusters could be identified. The first major cluster was cytosolic, with the top three overrepresented groups being macromolecular complex (118 genes, corrected p= $2.3678X10^{-31}$), ribonucleoprotein complex (52 genes, corrected p=$6.6535X10^{-31}$) and ribosome (35 genes, corrected p=$1.1336X10^{-28}$). The second overrepresented cluster was nuclear proteins, with the three most overrepresented groups in this cluster being the nuclear part (56 genes, corrected p=$2.8313X10^{-10}$), nuclear lumen (45 genes, corrected p=$5.8947X10^{-9}$) and nucleolus (23 genes, corrected p=$2.0201X10^{-7}$). The third cluster was for mitochondrial proteins, with the three most overrepresented in the cluster being mitochondrial matrix (20 genes, corrected p=$8.9450X10^{-11}$), mitochondrial lumen (20 genes, corrected p=$8.9450X10^{-11}$) and mitochondrial part (31 genes, corrected p=$4.0871X10^{-10}$). The fourth cluster was for cytoskeletal proteins, with the three most overrepresented groups being actin cytoskeleton (13 genes, corrected p=$3.7857X10^{-4}$), cytoskeleton (35 genes, corrected p=$5.3249X10^{-4}$) and cytoskeletal part (27 genes, corrected p=$6.0499X10^{-4}$). The final cluster was for cell membrane proteins, with the three most overrepresented being mitochondrial inner membrane (15 genes, corrected p=$4.9631X10^{-5}$), cell leading edge (11 genes, corrected p=$6.1867X10^{-5}$) and lamellipodium (6 genes, corrected p=$3.7546X10^{-3}$) (Figure 3.18).

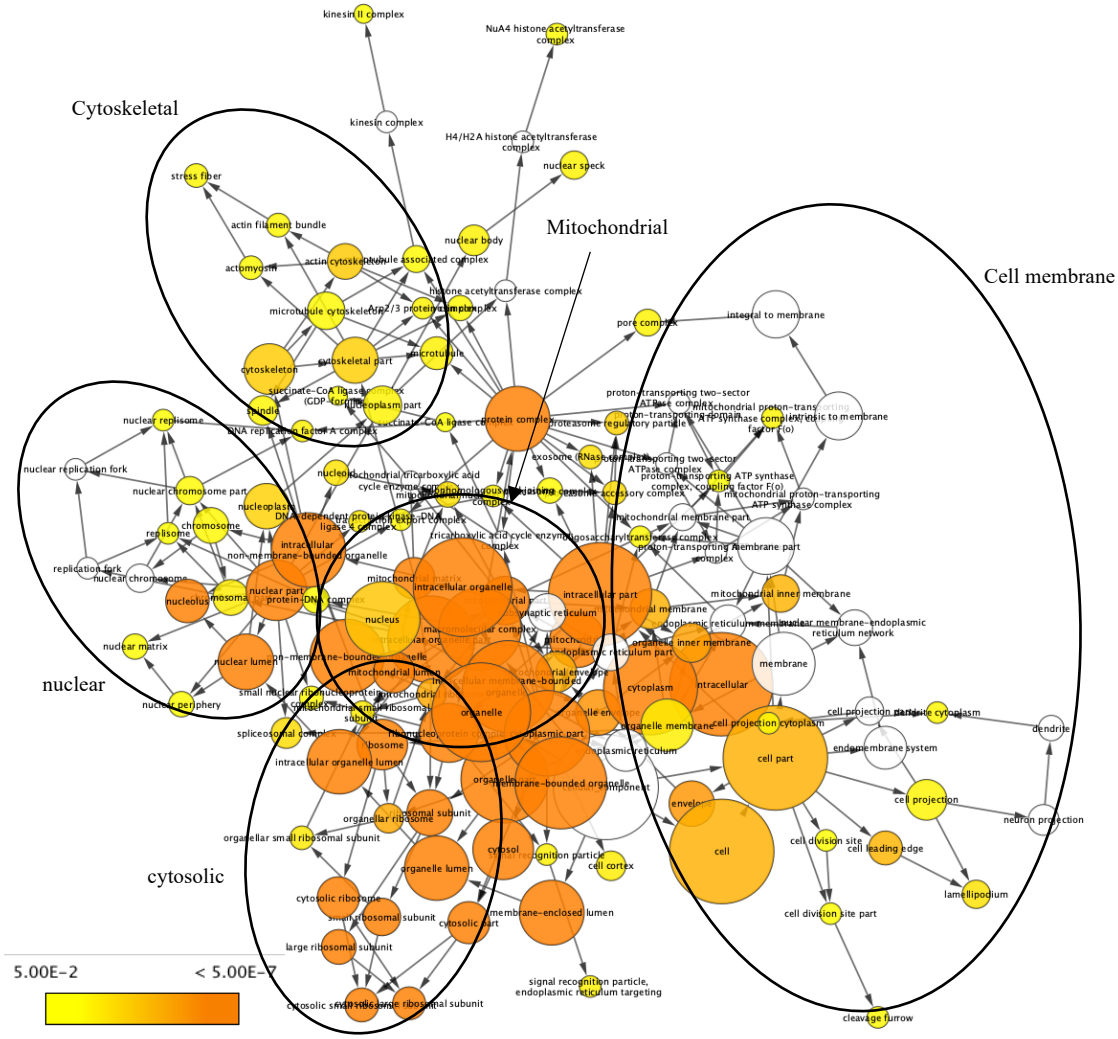

Figure 3.18. Clustering map of cellular component for wt-PAR4 triple hit proteome. Shows a gene ontology map produced using BiNGO plugin on Cytoscape. Map shows five distinct clusters the map with the key function of the cluster labelled. Nodes are coloured shown overrepresentation as a function of the p-value (yellow 5.00E-2 to orange <5.00E-7). The three most overrepresented groups are macromolecular complex (corrected p= $2.3678X10^{-31}$), ribonucleoprotein complex (corrected p=$6.6535X10^{-31}$) and ribosome (corrected p=$1.1336X10^{-28}$).

3.3.10 Gene Ontology analysis of enriched clusters in mut-PAR4 Y157C using BiNGO and Reactome

For easier visualisation of genes present over the threshold for all replicates for mut-PAR4 Y157C (H/L), we compared the genes present with the whole human genome. This was performed using the Cytoscape plugin BiNGO to determine the gene ontology clusters overrepresented in the mut-PAR4 Y157C proteome. The gene ontology map was generated using a hypergeometric test for statistical significance using the Benjamini and Hochberg false discovery rate (FDR) correction and statistical significance level set at (0.05). This generated three network maps for Molecular function, biological process and cellular components, shown in (Figures 3.19 – 3.21).

The first map generated was for molecular function. As can be seen, it formed three distinct clusters and one smaller cluster, two of which had a majority upregulated (yellow to Orange) and one which had a majority downregulated (white). The first major cluster was binding activity, with the top three overrepresented groups being RNA binding (33 genes, corrected p= $3.5767X10^{-13}$), protein binding (103 genes, corrected p=$2.1317X10^{-7}$) and nucleotide binding (38 genes, corrected p=$1.5876X10^{-3}$). The second overrepresented cluster was catalytic activity, which extends to only one branch. The three most overrepresented groups in this cluster are pyrophosphatase activity (17 genes, corrected p=$7.0466X10^{-3}$), hydrolase activity, acting on acid anhydrides in phosphorous-containing anhydrides (17 genes, corrected p=$7.0466X10^{-3}$) and hydrolase activity, acting on acid anhydrides (17 genes, corrected p=$7.0466X10^{-3}$). The final cluster was for transporter activity and contained the most underrepresented groups. However, this included one overrepresented group: porin activity (2 genes, corrected p=$2.9249X10^{-2}$) (Figure 3.19).

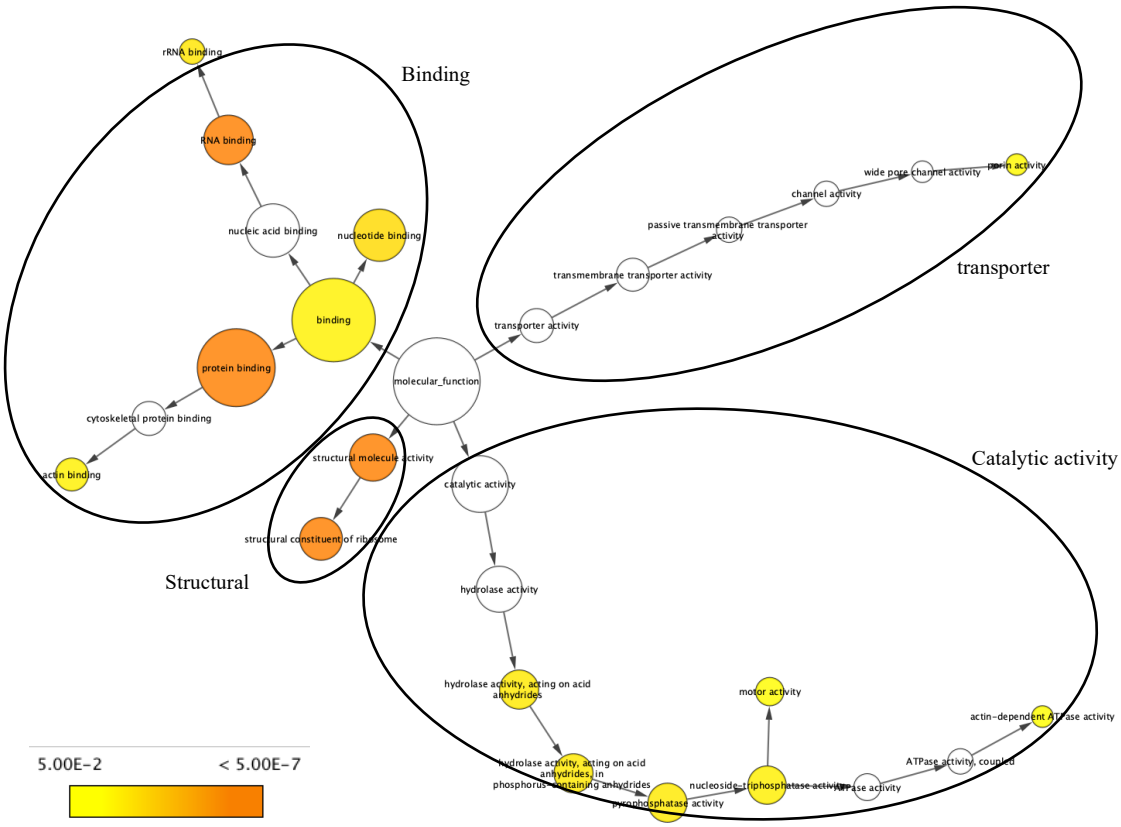

Figure 3.19. Clustering map of molecular function for mut-PAR4 Y157C triple hit proteome. Shows a gene ontology map produced using BiNGO plugin on Cytoscape. Map shows three distinct clusters and one smaller cluster outlined on the map with the key function of the cluster labelled. Nodes are coloured shown overrepresentation as a function of the p-value (yellow 5.00E-2 to orange <5.00E-7). Three most overrepresented nodes structural constituent of the ribosome (corrected $p=3.2535X10^{-18}$), RNA binding (corrected $p=3.5767X10^{-13}$) and structural molecule activity (corrected $p=3.2911X10^{-12}$).

The second map generated concerned biological processes, which contained the most groups and could be divided into five distinct clusters. The three larger clusters are prominent in the ontology map, comprising the most overrepresented proteins and two underrepresented ones. The first major cluster was metabolism, with the top three overrepresented groups being translation (30 genes, corrected p= $5.3652X10^{-21}$), translation elongation (21 genes, corrected p=$5.3652X10^{-21}$) and gene expression (44 genes, corrected p=$1.7183X10^{-13}$). The second overrepresented cluster was cellular and organelle organisation, with the three most overrepresented groups in this cluster being cellular process (119 genes, corrected p=$1.0637X10^{-11}$), cellular component biogenesis (30 genes, corrected p=$5.8884X10^{-7}$) and ribonucleoprotein complex biogenesis (13 genes, corrected p=$1.6684X10^{-6}$). The third overrepresented cluster was for cell cycle, with the three most overrepresented in the cluster being nuclear division (10 genes, corrected p=$1.9476X10^{-3}$), mitosis (10 genes, corrected p=$1.9476X10^{-3}$) and M phase of the mitotic cell cycle (10 genes, corrected p=$2.1722X10^{-3}$). In addition, two clusters contained mainly underrepresented groups. These were for Transport and localisation, which contained just two overrepresented groups: uropod organisation (2 genes, corrected p=$3.0023X10^{-3}$) and regulated secretory pathway (3 genes, corrected p=$1.4908X10^{-2}$). The final cluster for biological regulation contained only three overrepresented groups, which were regulation of cell cycle (11 genes, corrected p=$4.6994X10^{-2}$), provirus integration (2 genes, corrected p=$4.6994X10^{-2}$) and lysogeny (2 genes, corrected p=$4.6994X10^{-2}$) (Figure 3.20).

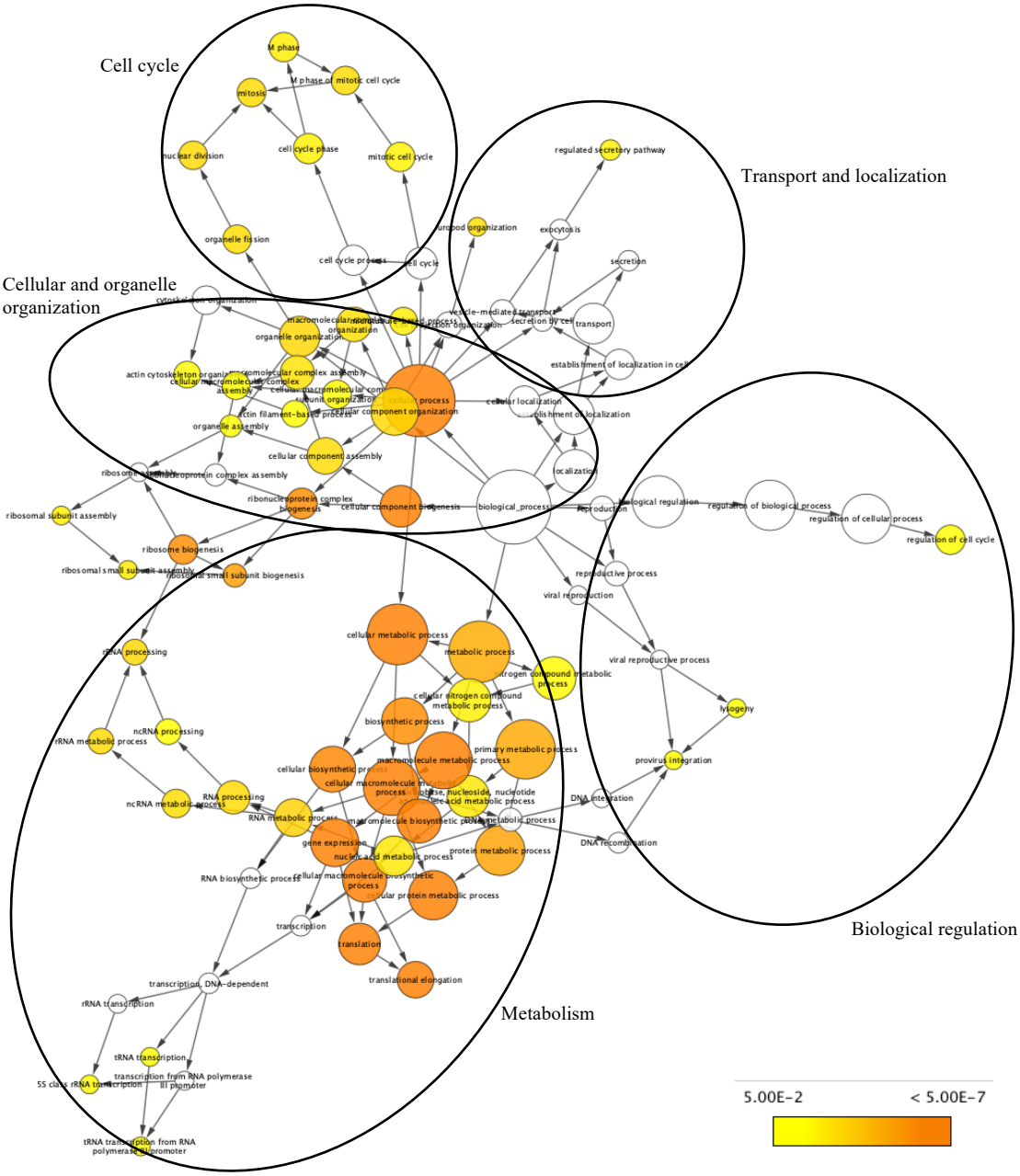

Figure 3.20. Clustering map of Biological process for mut-PAR4 Y157C triple hit proteome. Shows a gene ontology map produced using BiNGO plugin on Cytoscape. Map shows five distinct clusters outlined on the map with the key function of the cluster labelled. Nodes are coloured shown overrepresentation as a function of the p-value (yellow 5.00E-2 to orange <5.00E-7). Three most overrepresented nodes are translation (corrected p= $5.3652X10^{-21}$), translation elongation (corrected p=$5.3652X10^{-21}$) and gene expression (corrected p=$1.7183X10^{-13}$).

The final enrichment ontology analysis performed using BiNGO for the triple mut-PAR4 Y157C proteome was to look at the cellular components of the identified proteins. This network was the hardest to define specific clusters because it was compacted. However, five major clusters could be identified. The first major cluster was cytosolic, with the top three overrepresented groups being ribonucleoprotein complex (36 genes, corrected p= $1.0888X10^{-21}$), organelle part (96 genes, corrected p=$1.4987X10^{-21}$) and non-membrane bound organelle (69 genes, corrected p=$1.4987X10^{-21}$). The second overrepresented cluster was nuclear proteins, with the three most overrepresented groups in this cluster being nucleolus (20 genes, corrected p=$1.3532X10^{-8}$), nuclear part (39 genes, corrected p=$3.6474X10^{-8}$) and nuclear lumen (31 genes, corrected p=$6.4999X10^{-7}$). The third cluster was for mitochondrial proteins, with the three most overrepresented in the cluster are mitochondrial part (19 genes, corrected p=$6.0649X10^{-6}$), mitochondrial matrix (10 genes, corrected p=$1.4506X10^{-4}$) and mitochondrial lumen (10 genes, corrected p=$1.4506X10^{-4}$). The fourth cluster was for cytoskeletal proteins, with the three most overrepresented groups being actin cytoskeleton (9 genes, corrected p=$3.1208X10^{-3}$), microtubule (8 genes, corrected p=$1.0079X10^{-2}$) and cytoskeleton (22 genes, corrected p=$1.1178X10^{-2}$). The final cluster was for cell membrane proteins, with the three most overrepresented being membrane enclosed lumen (41 genes, corrected p=$1.7866X10^{-9}$), envelope (17 genes, corrected p=$3.1865X10^{-4}$) and cell leading edge (8 genes, corrected p=$5.4509X10^{-4}$) (Figure 3.21).

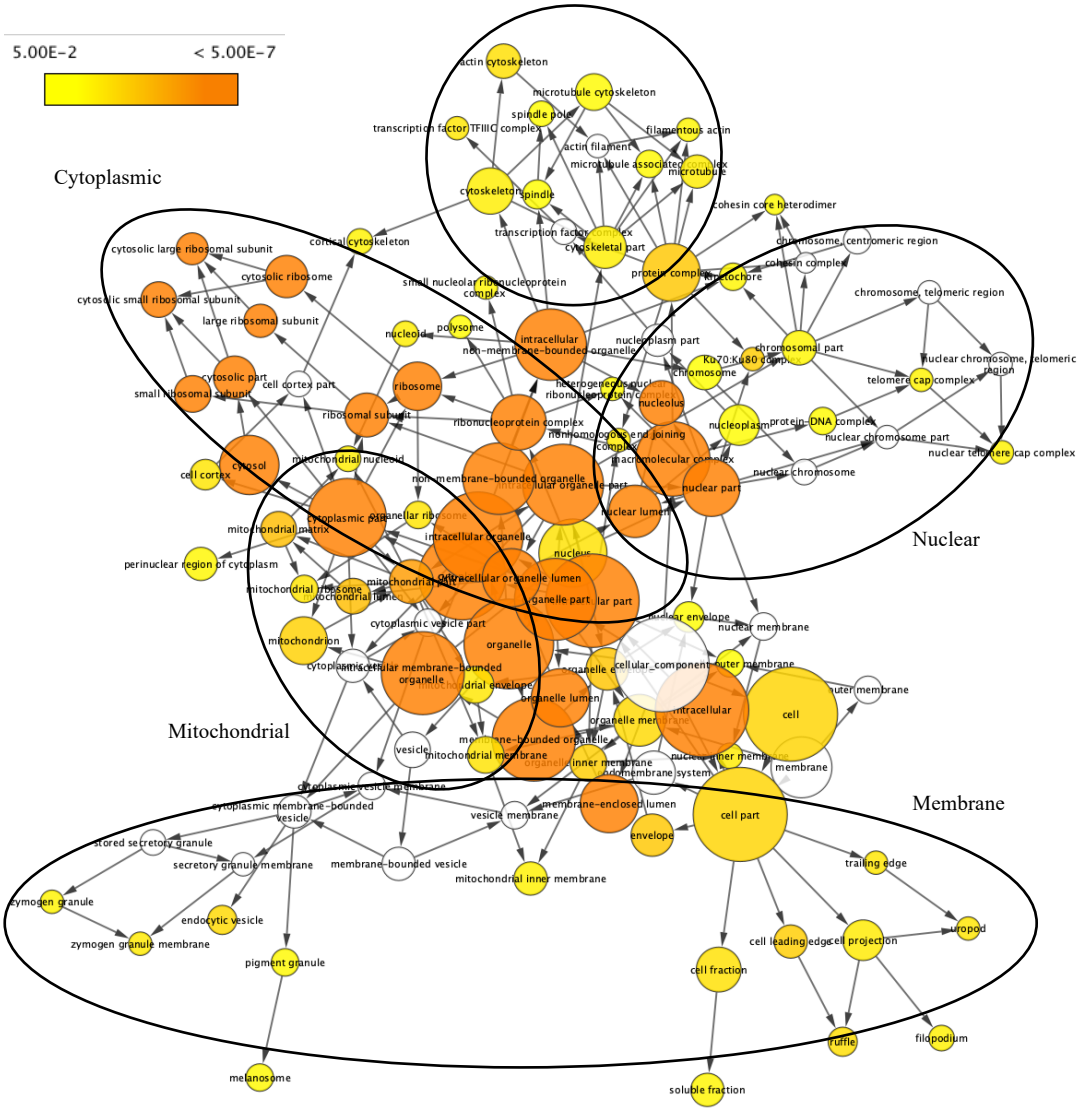

Figure 3.21. Clustering map of cellular component for mut-PAR4 Y157C triple hit proteome. Shows a gene ontology map produced using BiNGO plugin on Cytoscape. Map shows five distinct clusters outlined on the map with the key function of the cluster labelled. Nodes are coloured shown overrepresentation as a function of the p-value (yellow 5.00E-2 to orange <5.00E-7). Three most overrepresented nodes are ribonucleoprotein complex (corrected p= $1.0888X10^{-21}$), organelle part (corrected p=$1.4987X10^{-21}$) and non-membrane bound organelle (corrected p=$1.4987X10^{-21}$).

3.3.11 Visualisation of biomolecular cascades in wt-PAR4 and mut-PAR4 Y157C using Reactome

The final analysis was carried out to compare the triple hit wt-PAR4 and mut-PAR Y157C proteomes using the Cytoscape plugin Reactome. Reactome allows the visualisation of biomolecular cascades present in a set of proteins. The map was generated using an FDR filter of 0.05, and the tool was used to confirm the most enriched pathways for wt-PAR4 were translation (29 genes, FDR $3.4417X10^{-15}$), cellular response to stimuli (27 genes, FDR= $3.4417X10^{-15}$) and metabolism (26 genes, FDR= $3.4417X10^{-15}$). The most enriched pathways for mut-PAR Y157C were translation (21 genes, FDR= $2.9976X10^{-15}$), metabolism (21 genes, FDR= $2.9976X10^{-15}$) and cellular response to stimuli (20 genes, FDR= $2.9976X10^{-15}$) (Figure 3.22).

When comparing the Reactome enrichment maps of both wt-PAR4 and mut-PAR4, some key pathways are enriched in one but not the other. This is particularly noticeable within the wt-PAR4 map, which shows enrichment in mRNA processing, splicing and transport, which is not in mut-PAR4. As well as enrichment within cell cycle and pyrophosphate hydrolysis, what is most interesting is that the main enrichment family present in wt-PAR4 and not mut-PAR4 is key pathways downstream of GPCR activation, namely signalling by RhoGTPase, miroGTPases and RHOBTB3, RhoGTPase cycle and RhoGTPase effectors. This fits the picture of functionality in that wt-PAR4 would be expressed and signal as expected, whereas mut-PAR4 is intracellularly retained and, therefore, is non-functional, resulting in loss of enrichment of RhoGTPase signalling and effector function.

A Wt-PAR4 (M/L)

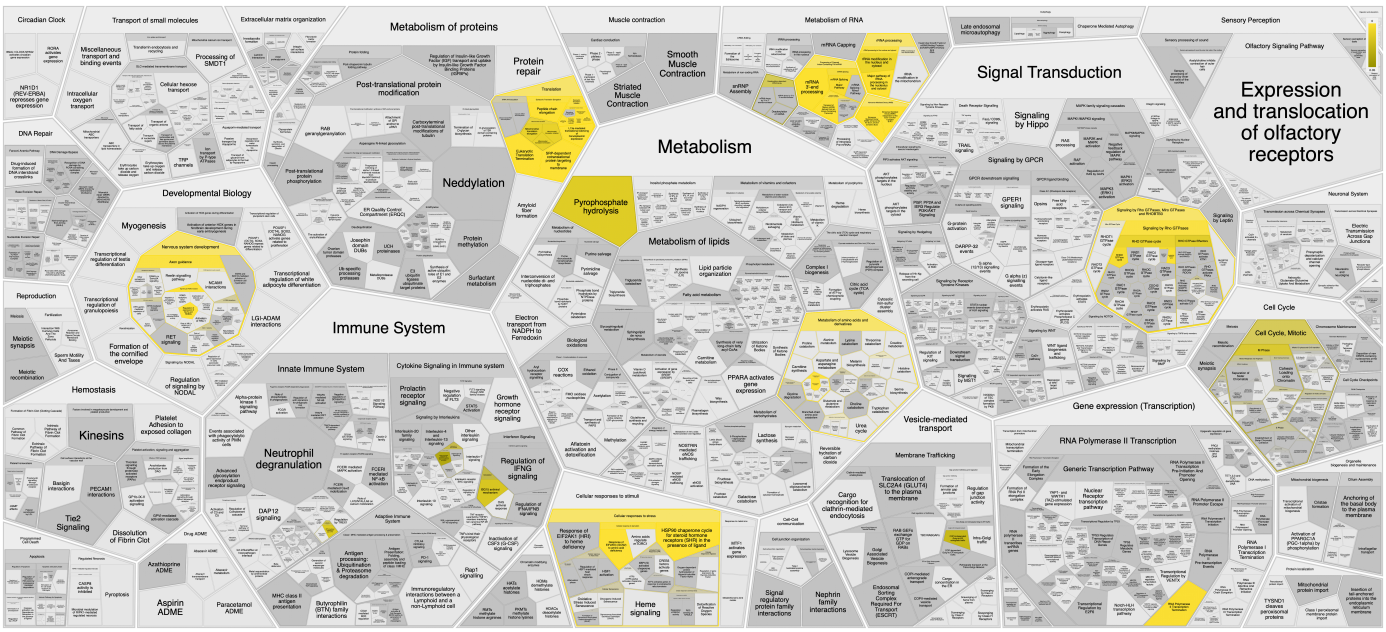

B mut-PAR4 (H/L)

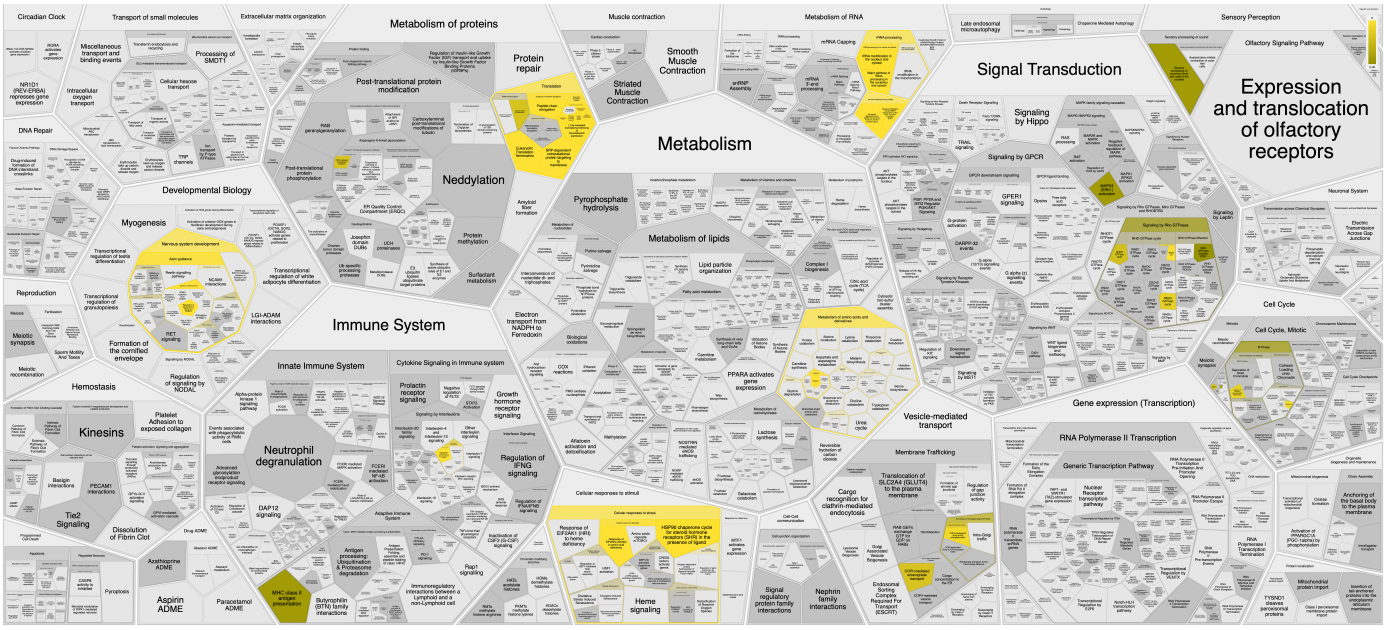

Figure 3.22. Reactome analysis for wt-PAR (M/L) and mut-PAR4 Y157C (H/L). The most enriched pathways are around metabolism of proteins and RNA and translation. Enriched proteins are similar between wt-PAR4 and mut-PAR4 Y157C although as expected wt-PAR4 has more enriched pathways due to having higher number of identified proteins (n=224) compared to mut-PAR4 Y157C (n=150). The colour gradient is indicative of the false discovery rate (FDR) on a scale of 0 (yellow) to 0.05 (brown). Full image link for wt-PAR4: and full image link for mut-Y157C PAR4:

3.3.12 Homing in on novel PAR4 interacting proteins for validation

To identify novel PAR4 interactors, we returned to the protein network generated with hits across all three groups above the threshold across two or more replicates (n=996) proteins. This was then analysed using STRINGdb.org, which again created a very complex network that made it hard to extrapolate meaningful clustering. The minimum interaction score was changed from medium confidence (0.400) to high confidence (0.700), and disconnected nodes were removed from the network. A kmeans clustering analysis was performed to better define clusters, with clustering set at nine to define networks in detail from the vast protein numbers identified. This produced the string network shown in (Figure 3.23)

The cluster containing the PAR4 gene (F2RL3) was extracted from stringdb.org to further define novel proteins within proximity (n=134 genes) that were present in the cluster (Figure 3.24).

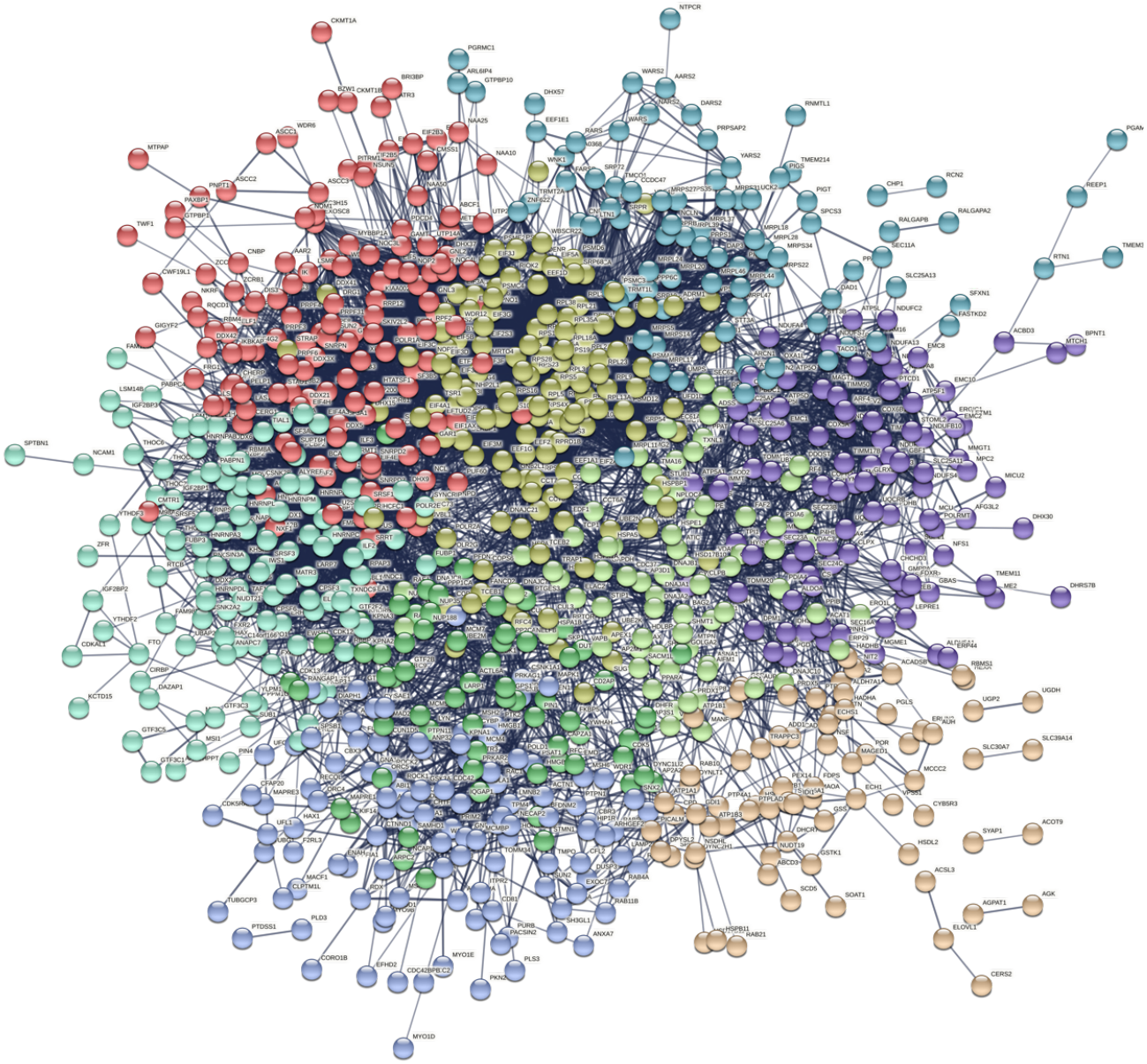

Figure 3.23. Sting interaction network of proteins across two or more replicates. A) Shows a protein interaction network (n=996) with thresholds above the cut-off (M/L, H/L and M/H) across two or more replicates. String thresholding was changed from medium confidence (0.400) to high confidence (0.700) and kmeans clustering applied (n=9) to differentiate distinct clusters of proteins. Full network image:

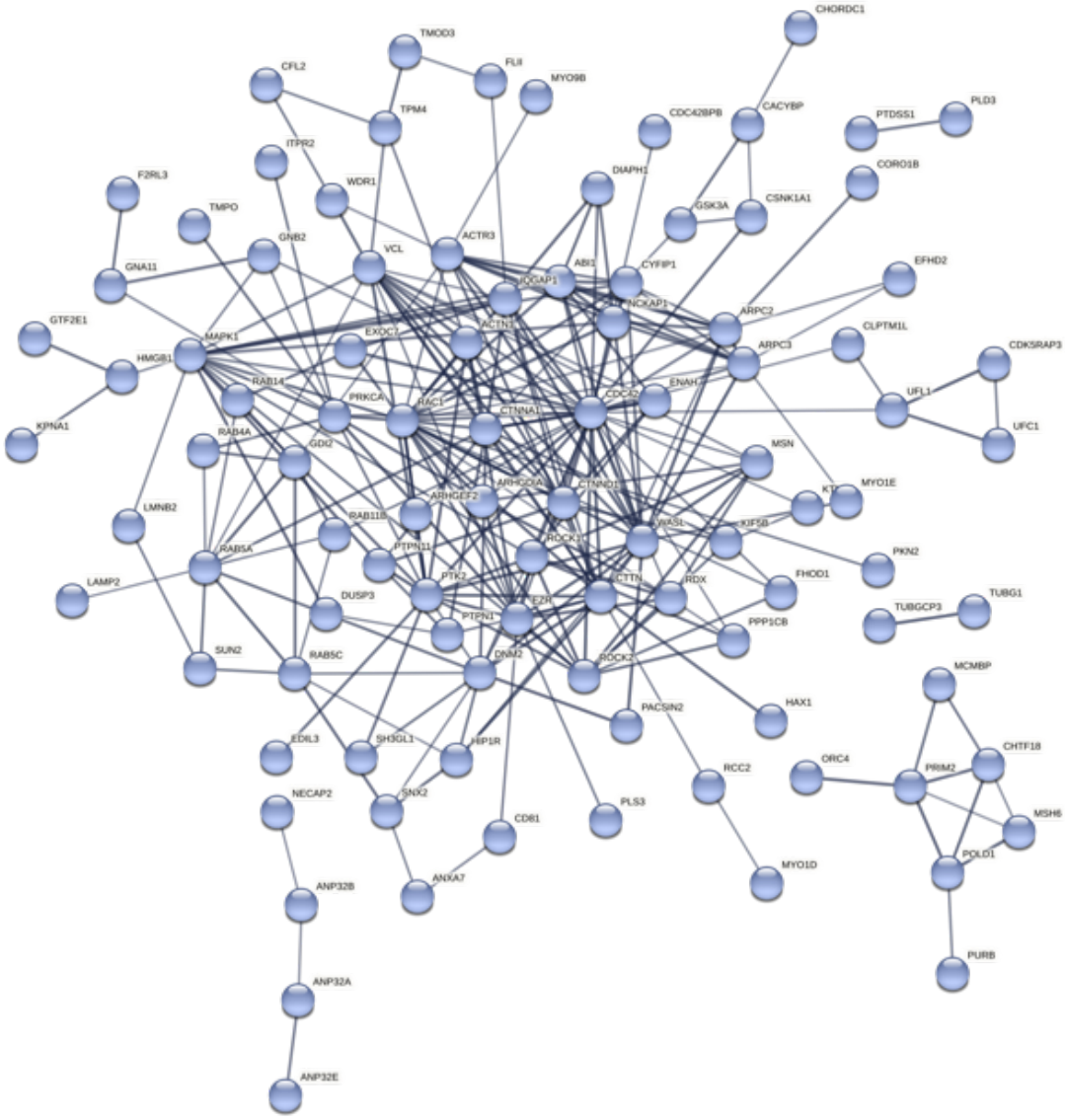

Figure 3.24. Extracted string cluster containing F2RL3 (PAR4) gene. Shows a protein interaction network extracted via kmeans clustering from Figure 3.26 that contains the PAR4 gene. String thresholding was changed from medium confidence (0.400) to high confidence (0.700) and kmean clustering applied (n=9) to differentiate distinct clusters of proteins (n=134 genes).

3.3.13 Gene Ontology analysis of enriched clusters in PAR4 containing cluster using BiNGO

For easier visualisation of genes with PAR4 gene-containing clusters, we compared the genes with the whole human genome. This was performed using the Cytoscape plugin BiNGO to determine the gene ontology clusters overrepresented in this cluster. The gene ontology map was generated using a hypergeometric test for statistical significance using the Benjamini and Hochberg false discovery rate (FDR) correction and statistical significance level set at (0.05). This generated three network maps for Molecular function, biological process and cellular components, shown in (Figures 3.25 – 3.27).

The first map generated was for molecular function. As can be seen, it formed three distinct clusters, two of which had a majority upregulated (yellow to Orange) and one which had a majority downregulated (white). The first major cluster was binding activity, with the top three overrepresented groups being cytoskeletal protein binding (33 genes, corrected p= $1.3781X10^{-19}$), actin binding (24 genes, corrected p=$3.2928X10^{-15}$) and Rho GTPase binding (6 genes, corrected p=$5.6327X10^{-6}$). The second overrepresented cluster was catalytic activity, which extends to only one branch. The three most overrepresented groups in this cluster are nucleoside-triphosphatase activity (18 genes, corrected p=$2.5283X10^{-4}$), pyrophosphatase activity (18 genes, corrected p=$2.8540X10^{-4}$) and hydrolase activity, acting on acid anhydrides, in phosphorous-containing anhydrides (18 genes, corrected p=$2.8540X10^{-4}$). The final cluster was for kinase activity and contained the most underrepresented groups. However, the most overrepresented groups were protein kinase activity (2 genes, corrected p=$4.3887X10^{-2}$), MAP kinase two activity (2 genes, corrected p=$4.8874X10^{-2}$) and calcium-dependant protein kinase C activity (1 gene, corrected p=$4.3887X10^{-2}$) (Figure 3.25A). Protein networks for the three most overrepresented groups were generated using STRINGdb.org (Figure 3.25B).

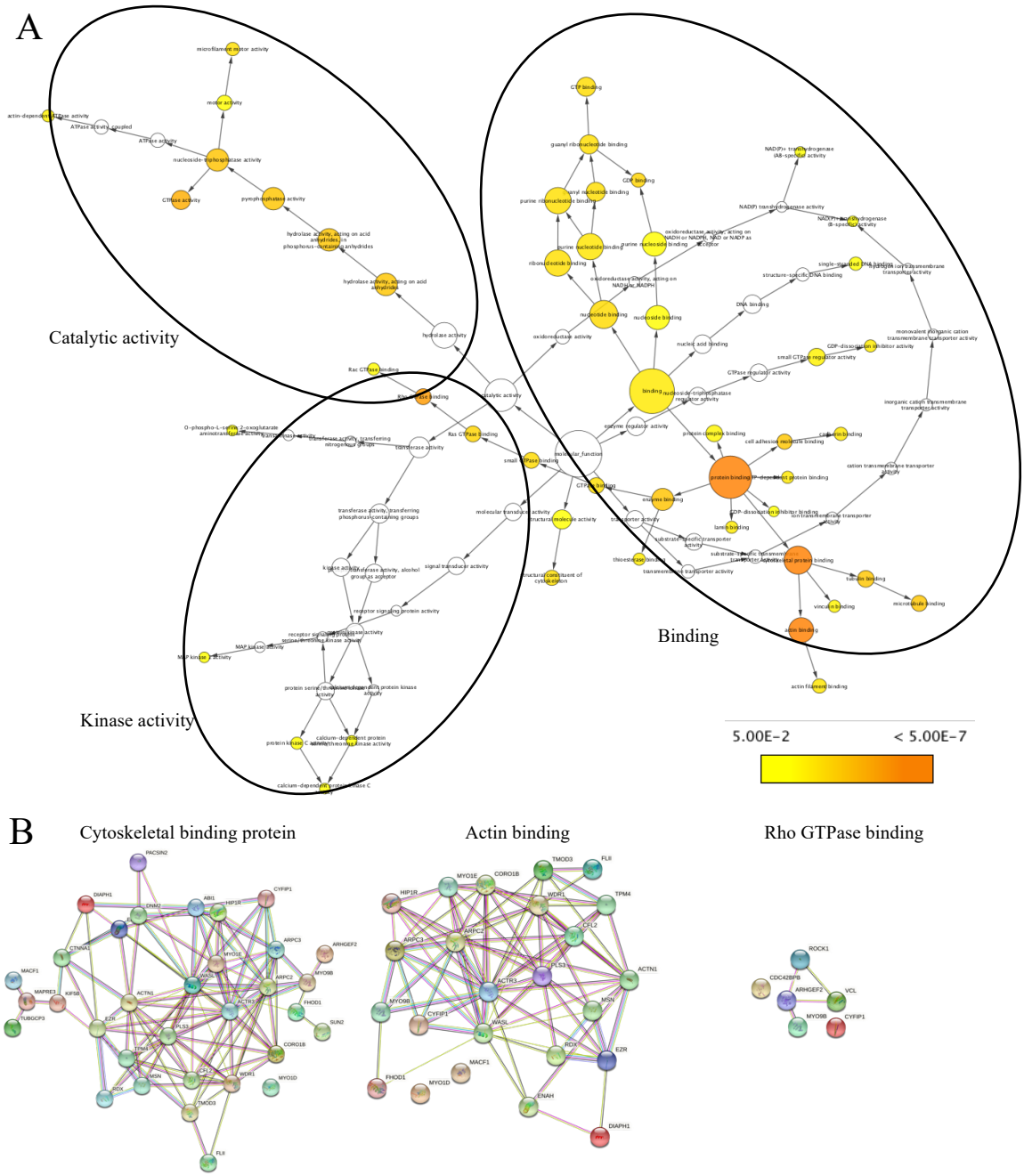

Figure 3.25. Clustering map of molecular function for PAR4 cluster extracted from stringdb.org. A) Shows a gene ontology map produced using BiNGO plugin on Cytoscape. Map shows three distinct clusters outlined on the map with the key function of the cluster labelled. Nodes are coloured shown overrepresentation as a function of the p-value (yellow 5.00E-2 to orange <5.00E-7). B) Shows string networks for the top three overrepresented groups being cytoskeletal protein binding (33 genes, corrected p= $1.3781X10^{-19}$), actin binding (24 genes, corrected p=$3.2928X10^{-15}$) and Rho GTPase binding (6 genes, corrected p=$5.6327X10^{-6}$).

The second map generated the biological process, containing three distinct clusters comprising the most overrepresented proteins in the ontology map. The first major cluster was a cellular component organisation, with the top three overrepresented groups being actin filament-based process (14 genes, corrected p= $7.4983X10^{-6}$), actin cytoskeleton organisation (13 genes, corrected p=$1.5672X10^{-5}$) and cytoskeleton organisation (17 genes, corrected p=$1.8075X10^{-5}$). The second overrepresented cluster was localisation, with the three most overrepresented groups in this cluster being protein localisation (20 genes, corrected p=$1.6499X10^{-3}$), cellular localisation (20 genes, corrected p=$3.1662X10^{-3}$) and macromolecule localisation (21 genes, corrected p=$5.2302X10^{-3}$). The third overrepresented cluster was for biological regulation, with the three most overrepresented in the cluster are regulation of cellular component organisation (18 genes, corrected p=$3.5133X10^{-5}$), regulation of cellular component biogenesis (9 genes, corrected p=$4.8020X10^{-4}$) and regulation of protein complex assembly (6 genes, corrected p=$5.2302X10^{-3}$) (Figure 3.26A). Protein networks for the three most overrepresented groups were generated using STRINGdb.org (Figure 3.26B).

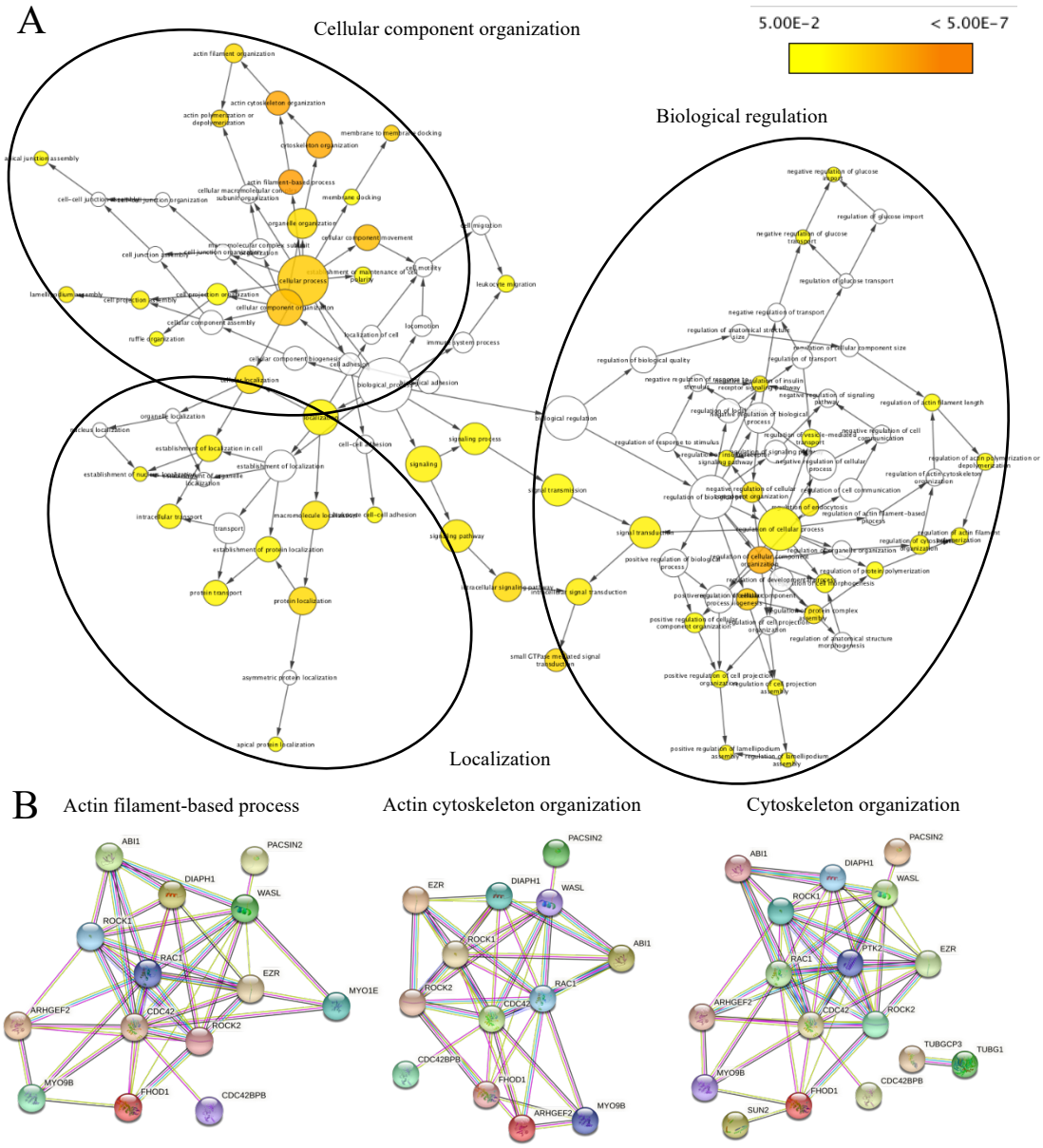

Figure 3.26. Clustering map of biological process for PAR4 cluster extracted from stringdb.org. A) Shows a gene ontology map produced using BiNGO plugin on Cytoscape. Map shows three distinct clusters outlined on the map with the key function of the cluster labelled. Nodes are coloured shown overrepresentation as a function of the p-value (yellow 5.00E-2 to orange <5.00E-7). B) Shows string networks for the top actin filament-based process (corrected p= $7.4983X10^{-6}$), actin cytoskeleton organization (corrected p=$1.5672X10^{-5}$) and cytoskeleton organization (p=$1.8075X10^{-5}$).

The final map generated concerned cellular components, which contained four distinct clusters in the ontology map, containing the most overrepresented proteins. The first major cluster was membrane, with the top three overrepresented groups being cell leading edge (21 genes, corrected p= $1.0298X10^{-17}$), lamellipodium (12 genes, corrected p=$5.6369X10^{-11}$) and cell projection (26 genes, corrected p=$2.5428X10^{-9}$). The second overrepresented cluster was cytoplasmic, with the three most overrepresented groups in this cluster being cytoplasm (96 genes, corrected p=$1.1220X10^{-10}$), cytoplasmic part (74 genes, corrected p=$2.5428X10^{-9}$) and cytosol (33 genes, corrected p=$1.4481X10^{-10}$). The third overrepresented cluster was for nuclear proteins, with the three most overrepresented in the cluster being centrosome (6 genes, corrected p=$7.8025X10^{-3}$), nuclear chromosome (6 genes, corrected p=$9.4648X10^{-3}$) and centriole (3 genes, corrected p=$1.2447X10^{-2}$). The final overrepresented cluster was for cytoskeletal proteins, with the three most overrepresented in the cluster being cytoskeleton (46 genes, corrected p=$1.9291X10^{-16}$), actin cytoskeleton (17 genes, corrected p=$1.2122X10^{-9}$) and cytoskeletal part (25 genes, corrected p=$1.2472X10^{-6}$) (Figure 3.27A) Protein networks for the three most overrepresent groups were generated using STRINGdb.org (Figure 3.27B).

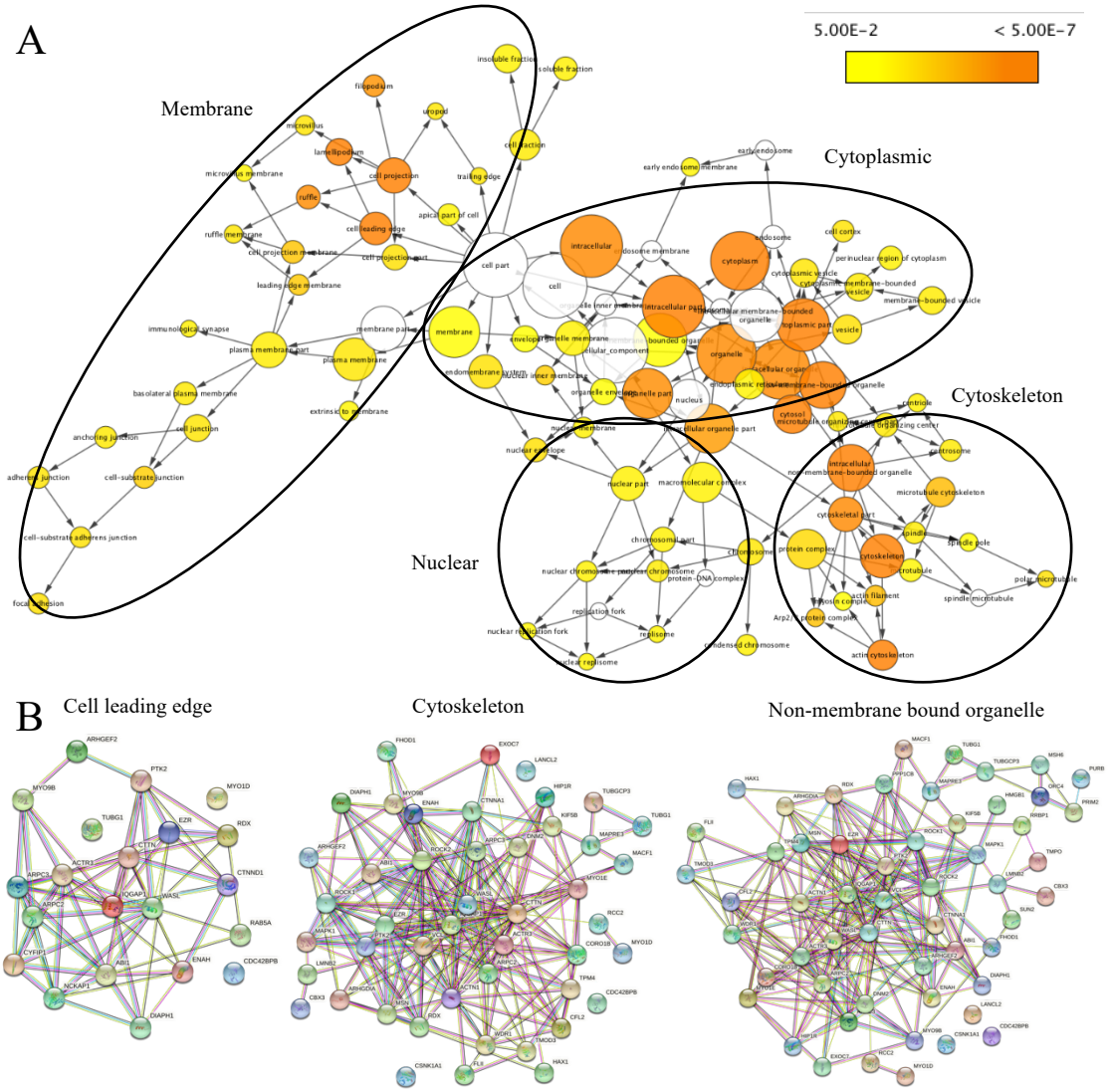

Figure 3.27. Clustering map of cellular component for PAR4 cluster extracted from stringdb.org. A) Shows a gene ontology map produced using BiNGO plugin on Cytoscape. Map shows three distinct clusters outlined on the map with the key function of the cluster labelled. Nodes are coloured shown overrepresentation as a function of the p-value (yellow 5.00E-2 to orange <5.00E-7). B) Shows string networks for the top overrepresented groups which are cell leading edge (corrected p= $1.0298X10^{-17}$), cytoskeleton (corrected p=$1.9291X10^{-16}$) and non-membrane bound organelle (p=$20329X10^{-13}$).

3.3.14 Analysis of SILAC proteomics data

To assess the interacting proteins within each of the experimental replicates, SILAC ratios which fell below the threshold for each Heavy/Light (PAR4 Y157C / CFP), Medium/Light (PAR4 / CFP) and Medium/Heavy (PAR4 / PAR4 Y157C) were screened out. Venn diagrams were produced for each experimental replicate using the Venn diagram tool on Bioinformatics and Evolutionary Genomics (http://bioinformatics.psb.ugent.be/cgi-bin/liste/Venn/calculate_venn.htpl). Common proteins among all three were identified in the centre, proteins identified between two of the three were displayed in the middle shell, and proteins identified as unique to a specific set were displayed in the outer circle.

For replicate one total proteins identified (n=2905) after screening to remove proteins below the threshold for Heavy/Light (n=2446), Medium/Light (n=2681) and Medium/Heavy (n=2821). For replicate two total proteins identified (n=3213) after screening to remove proteins below the threshold for Heavy/Light (n=2384), Medium/Light (n=2914) and Medium/Heavy (n=2014). For replicate one total proteins identified (n=1768) after screening to remove proteins below the threshold for Heavy/Light (n=354), Medium/Light (n=416) and Medium/Heavy (n=905) (Figure 3.28A).

From screening of the triplicate datasets, 29 proteins were identified as having SILAC ratios above the threshold for (Heavy/Light, Medium/Light and Medium/Heavy) across all replicates. The accession numbers of the identified proteins were constructed into a protein network using (https://string-db.org); of these 29 proteins, five were identified, and accession numbers were inputted into (https://www.UniProt.org) to retrieve the correct accession numbers. STRING-db proteins were identified as grouped into four distinct clusters (Figure 3.28B), and the table of proteins identified is shown in Table 3.2 below.

From extracting the cluster that contained the F2RL3 (PAR4) (Figure 3.24) and performing bioinformatic analysis using BiNGO (Figure 3.25 – 3.27), the

prominent overarching enriched functions primarily involved the actin cytoskeleton. Molecular function (Figure 3.25) showed cytoskeleton binding proteins, actin binding and RhoGTPase binding. Biological function (Figure 3.26) showed an actin filament-based process and actin cytoskeleton organisation and cytoskeleton organisation. The cellular component (Figure 3.27) showed the cell leading edge, cytoskeleton and non-membrane bound organelle. When further analysed, proteins that showed high confidence hits across all three replicates (29 proteins) were identified. Cofilin was identified (Figure 3.28, Table 3.2). Cofilin is an actin-severing protein that aids in actin depolymerisation and polymerisation, as well as the formation of cell protrusions and locomotor activity (Bravo-Cordero et al., 2013). In addition, Cofilin was also present within the F2RL3 (PAR4) cluster (Figure 3.24) and, therefore, seems like an interesting target to explore further with PAR4.

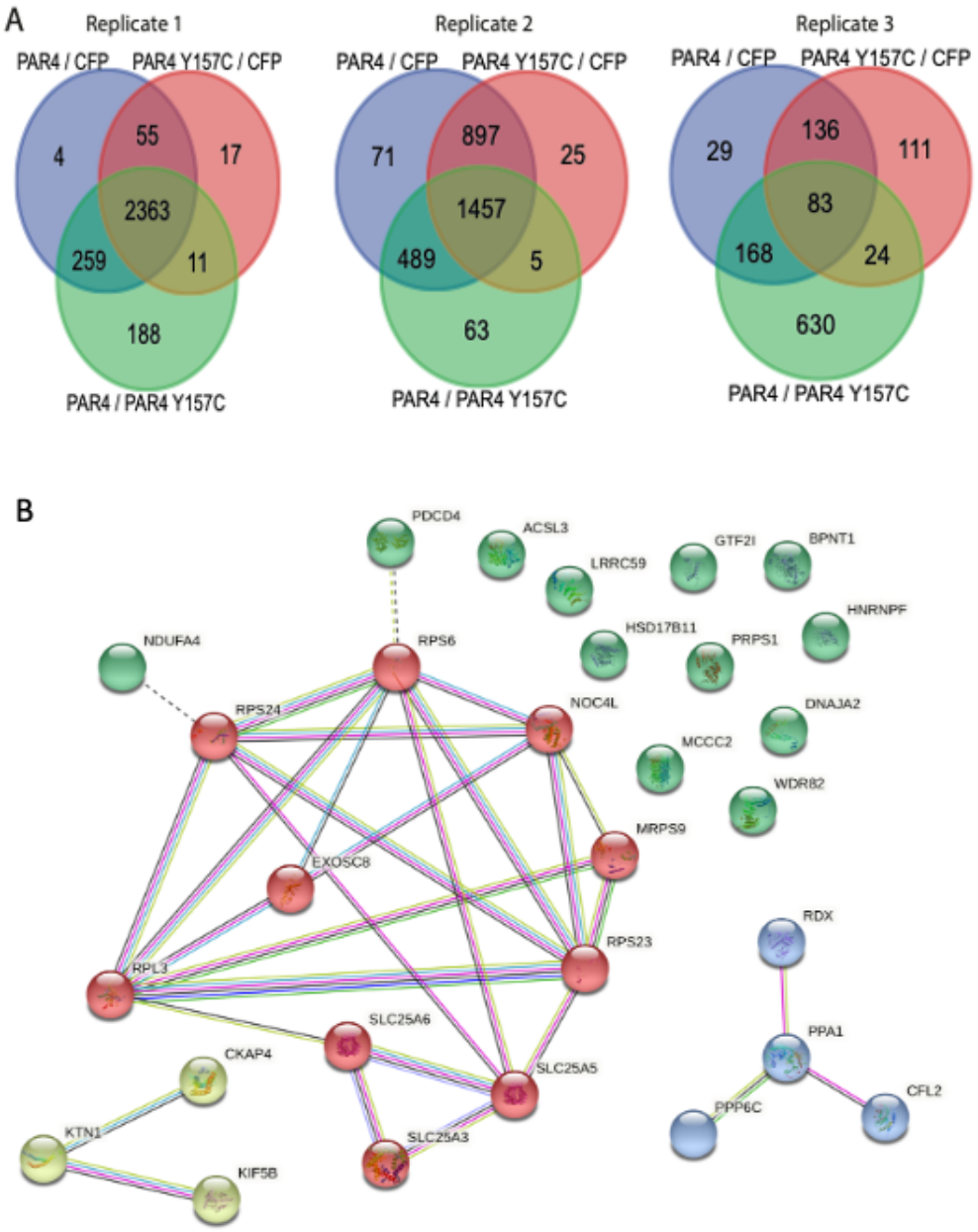

Figure 3.28 Result of SILAC proteomic analysis for PAR4 and Y157C interactome. A) Venn diagrams for each of the individual replicates. Common proteins are shown in the centre. Proteins which are above the threshold in two out of the three are shown in the middle shells and proteins unique to each individual group are shown in the outer shell. B) String protein network generated for the 29 protein hits across all three replicates. Clustering shows four distinct clusters which are labelled with different colours. Solid lines represent known high confidence interactions, broken lines represent probable interactions.

TABLE 3.2. PROTEINS IDENTIFIED AS HIGH CONFIDENCE HITS FROM SILAC PROTEOMICS

CELLULAR LOCALISATION	Accession number	Full name	Abbreviated name	Function
NUCLEAR	B4DKX4	Programmed cell death protein 4	PDCD4	Inhibits eIF4A1 activity Tumour suppressor
	Q96B26	Exosome complex component RRP43	EXOSC8	RNA maturation Elimination and degradation of mRNA
	P52597	Heterogeneous nuclear ribonucleoprotein F	HNRNPF	Processing of pre-mRNA
	A8K905	Nucleolar complex protein 4 homolog	NOC4L	RNA binding and rRNA processing
	Q6UXN9	WD repeat-containing protein 82	WDR82	Role in chromatin structure and histone H3 methylation
	Q96AG4	Leucine-rich repeat-containing protein 59	LRRC59	Nuclear import of FGF-1
	X5D2J9	General transcription factor IIi isoform D	GTF2I	Roles in transcription and signal transduction.
CYTOPLASMIC	P60891	Ribose-phosphate pyrophosphokinase 1	PRPS1	Synthesis of purine and pyrimidine nucleotides

	Q15181	Inorganic pyrophosphatase	PPA1	Catalyses the conversion of pyrophosphate into two phosphate ions
	O95861	3’(2’),5’-bisphosphate nucleotidase 1	BPNT1	Catalyses the production of AMP from adenosine 3’,5’-bisphosphate
CYTOPLASMIC AND ENDOPLASMIC RETICULUM	P62753	40S ribosomal protein S6	RPS6	Part of the 40S small ribosomal subunit. Translation of particular classes of mRNA into immature proteins.
	E7ETK0	40S ribosomal protein S24	RPS24	Component of the 40S ribosomal subunit
	P62266	40S ribosomal protein S23	RPS23	Component of the 40S ribosomal subunit
	P39023	60S ribosomal protein L3	RPL3	A component of the large subunit of ribosomes
	O60884	DnaJ homolog subfamily A member 2	DNAJA2	Co-chaperone to Hsp70. Facilitates correct protein folding of native and non-native proteins
MITOCHONDRIAL	Q9HCC0	Methylcrotonoyl-CoA carboxylase beta chain, mitochondrial	MCCC2	A critical enzyme in the catabolism of leucine and isovaleric acid
	Q86WV4	28S ribosomal protein S9	MRPS9	Component of the 28S mitochondrial ribosome subunit
	B3KN05	Long-chain-fatty-acid—CoA ligase 1	ACSL1	Catalyses the conversion of long-chain fatty acids to acyl-CoA

	O00743	Serine/threonine-protein phosphatase 6 catalytic subunit	PPP6C	COPII vesicle coating, protein dephosphorylation. Catalytic subunit of PP6
	P12236	ADP/ATP translocase 3	SLC25A6	Catalyses the exchange of cytosolic ADP with mitochondrial ATP across the mitochondria inner membrane
	P05141	ADP/ATP translocase 2	SLC25A5	Catalyses the exchange of cytosolic ADP with mitochondrial ATP across the mitochondria inner membrane
	A0A024RBE8	Mitochondrial phosphate carrier protein	SLC25A3	The transport of phosphate groups from the cytosol into the mitochondria
	O00483	Cytochrome c oxidase subunit NDUFA4	NDUFA4	A component of cytochrome c oxidase, important in the mitochondrial electron transport chain
ENDOPLASMIC RETICULUM	D6RCD0	Estradiol 17-beta-dehyrogenase 11	HSD17B11	Oxidoreductase catalyses production of NADH and NADPH. Androgen and Estrogen metabolism
	Q86UP2	Kinectin	KTN1	Receptor for Kinesin. Involved in cadherin and kinesin binding, post-translational protein modification and protein transport.
CYTOSKELETAL	Q9Y281	Cofilin-2	CFL2	Controls the polymerization and depolymerization of actin in a reversible manner
	P33176	Kinesin-1 heavy chain	KIF5B	Microtubule dependant motor powered by the hydrolysis of ATP.

				Regulation of protein localization to the plasma membrane.
	Q07065	Cytoskeleton-associated protein 4	CKAP4	Anchors the ER to microtubules and responsible for structure of the ER
PLASMA MEMBRANE	P35241	Radixin	RDX	Binding of the barded end of actin filaments to the plasma membrane

3.3.15 Cofilin family proteins as potential regulators of PAR4

Cofilin family proteins are actin-binding proteins that play a crucial role in regulating the dynamics of the actin cytoskeleton (Bravo-Cordero et al., 2013). The primary members of this family include Cofilin-1, Cofilin-2, and actin-depolymerizing factor (ADF). These proteins are essential for various cellular processes, including cell movement, shape change, and division. Although Cofilin 2 has been identified in Table 3.1, the potential for other Cofilin family members, such as Cofilin 1, to be involved in PAR4 function may be possible. AlphaFold was used to predict potential complex formation between PAR4 and Cofilin 1 (CFL1), shown in Figure 3.29.

Based on predictive modelling, there is a suggestion that the primary interface is ICL3, with some additional contacts at H8. (and one interaction with TM4). – all hydrogen bonding. (Mean pLDDT = 81.14, Predicted Template Modelling score (pTM-score) = 0.630 Interface Predicted Template Modelling score (ipTM-score) = 0.220).

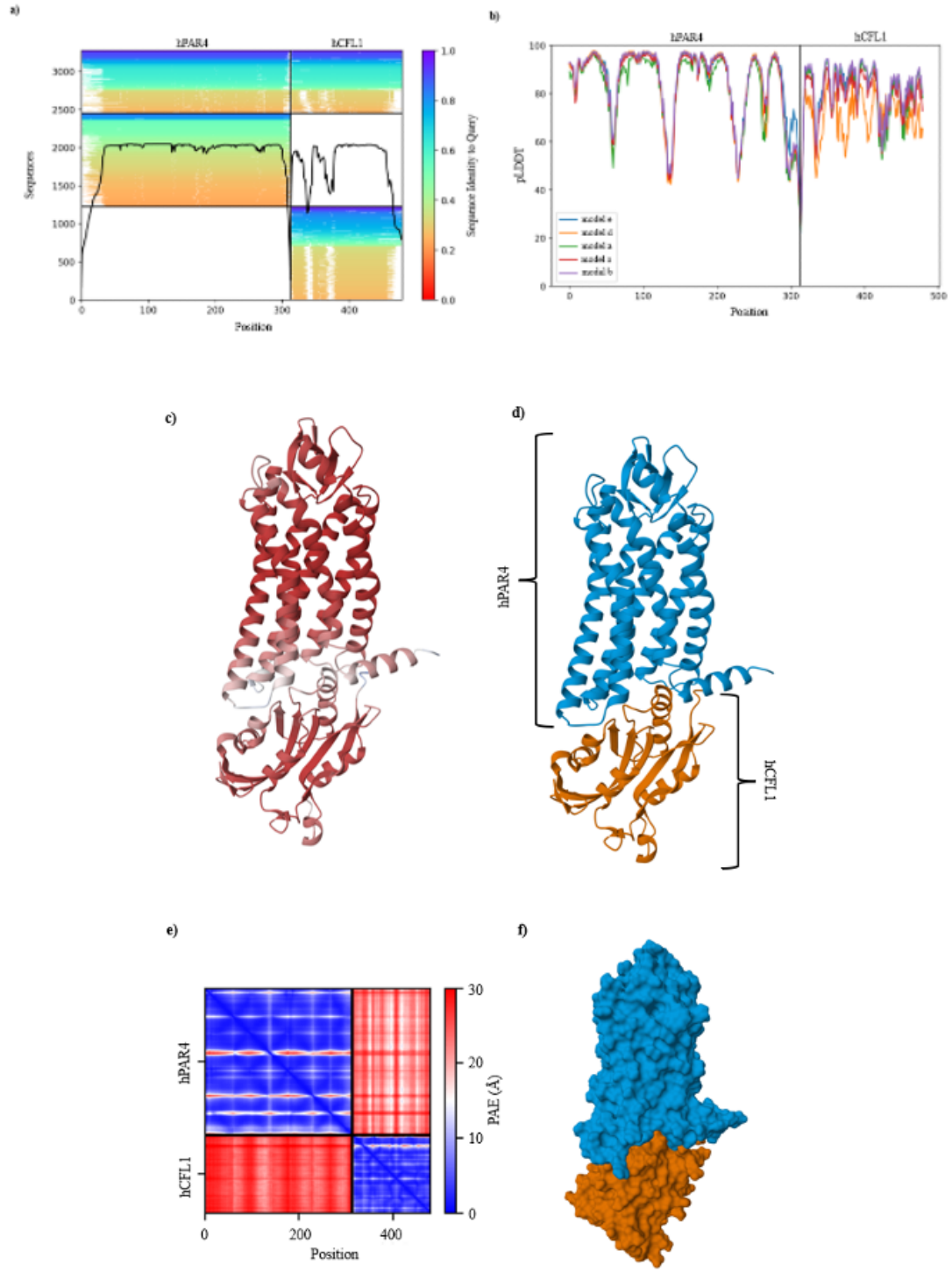

Figure 3.29 AF2M predicts a hPAR4–CFL1 complex with a low intra-chain confidence. a) is a heat-map of the MMSeqs2 MSA, carried out against the ColabFoldDB. It shows hits across both proteins, where the length of the line indicates the length of the sequence match, and the colour represents the similarity of that sequence to the query sequence. The total matches are shown on a per residue basis by the black trace. **b)** represents the per residue pLDDT of five models (a-e) generated by AF2M, where model e was the top-ranked model. **c)** ribbon diagram, showing the per-residue pLDDT of the top-ranked model (e). **d)** ribbon diagram, depicting the overall complex assembly between WT hPAR4 (blue) and WT hCFL1 (orange). **e)** PAE plot. A high PAE at position (*x,y*) in the matrix indicates a high expected error at the residue *x*, where the predicted and true structures are aligned on *y*. **f)** molecular surface rendering, showing the topological structure of the complex between WT hPAR4 (blue) and WT hCFL1 (orange).

3.4 Discussion

3.4.1 Overview and discussion

Proteomic mass spectrometry generates a vast amount of data, and the ability to filter it appropriately allows for useful inferences to be extracted and further explored. SILAC proteomic data generated for wt-PAR4 and mut-Y157C was filtered using the method described by Emmott and Goodfellow to produce ratios that excluded proteins or highlighted proteins above the threshold used for comparison with other replicates in the set. In total, we used three replicates in this study, which is the minimum required to derive significance from identified protein interactors. First, proteins were plotted to fit Gaussian distribution against their $\log_2$ SILAC ratios (Figures 3.3 – 3.5).

Replicate 1 identified n=5626 proteins (n=2905 after filtering), replicate 2 identified n=6181 proteins (n=3213 after filtering) and replicate 3 identified n=3860 proteins (n=1768 after filtering). When reviewing the data, it can be seen that replicate 1 and replicate 2 have similarities in the number of proteins identified. What's interesting is that replicate 3 identified significantly fewer proteins than the other two replicates. This can also be seen in the Gaussian distribution graphs that were generated in replicate 1 (Figure 3.3) and replicate 2 (Figure 3.4), which have similar distributions across all three graphs SILAC H/L ratio (PAR4 Y157C / GFP), SILAC M/H ratio (PAR4 / PAR4 Y157C) and SILAC M/L ratio (PAR4 / GFP). However, the distribution of proteins in replicate 3 SILAC M/L ratio (PAR4 / GFP) is quite different in the spread compared to replicate 1 and replicate 2.

Given the apparent variability in data, we aimed to assess the reproducibility of the data sets between experimental replicates. Interestingly, the data from this showed that none of the replicates showed a true correlation in reproducibility, which was displayed by the fact that all gave Pearson correlations of less than 0.5 (Figure 3.6). However, it did show that SILAC H/L ratio (PAR4 Y157C / GFP) had the highest degree of reproducibility with

R>0.4, which means some degree of correlation, the same being true for SILAC ratio M/L (PAR4 / GFP) with R in the range of 0.35 – 0.45. However, the SILAC ratio M/H (PAR4 / PAR4 Y157C) showed no correlation across the experimental replicates. This could be explained by the fact this was a dual transfected cell line model; therefore, the degree to which protein is expressed in the sample might not necessarily be equal across samples analysed as opposed to singly transfected cell lines.

Proteins which gave SILAC ratios above the threshold across two or more replicates gave a PAR4 proteome of (n=996) proteins. To visualise this with a protein interaction network generated using Cytoscape (Figure 3.8), in total, 990 proteins made up the full network (n=2) excluded due to identification and (n=4) excluded as no connecting nodes with the rest of the network. The degrees of centrality (colour) and number of connecting nodes (size) were used to enhance the visualisation of the network. Unfortunately, due to the vast number of identified and plotted proteins, it wasn't possible to derive valuable information from the network. The degree of centrality and number of connecting nodes did help in identifying key interactors. However, most of these were ribosomal proteins, which makes sense in protein interaction due to their role in protein translation.

Therefore, to derive more valuable information about the protein families that were most overrepresented in the PAR4 proteome, they were assessed using the gene ontology software plugin BiNGO to determine overrepresented clusters in the PAR4 proteome. Statistical significance was generated using the hypergeometric test for statistical significance using the Benjamnini and Hochberg FDR correction; statistical significance was set at 0.05; overrepresented clusters were coloured from yellow 0.05 to orange 0.0000005 on a sliding scale. Clustering on BiNGO is split into three main functional families in which proteins can be grouped into molecular function, biological process and cellular component.

3.4.2 Whole PAR4 proteome shows vast complexity of PAR4 interactome

The first cluster map assessed for the whole PAR4/Y157C proteome was for molecular function. In this map, it was possible to delineate three distinct clusters whose major families were Binding activity, transporter activity and catalytic activity (Figure 3.9). Within the cluster map, two of the three showed that most functions were overrepresented. It was shown the most overrepresented clusters within this network were RNA binding (185 genes, corrected p= 1.290×10^{-68}), protein binding (654 genes, corrected p= 2.5807×10^{-37}) and nucleotide binding (250 genes, corrected p=7.9674×10^{-25}). These three majorly overrepresented nodes are expected, given that it is hard to ascertain any valuable data from the Cytoscape protein network from the whole proteome. The most prominent visible nodes were ribosomal constituent proteins (Figure 3.9). This ties into the fact that all proteins require transcription and translation, a primarily expected outcome within this protein network.

The second cluster map, assessed for the complete PAR4/Y157C proteome, was for the biological process. In this map, it was possible to delineate eight distinct clusters whose major families were DNA, tRNA replication and translation, sterol, steroid and lipid esterification, nucleobase, nucleoside, nucleotide and nucleic acid metabolic process, metabolism, mRNA, rcRNA and tRNA metabolic process, Protein processing, transport and localisation, regulation of ligase activity and Biosynthetic process (Figure 3.15). Within the cluster map, two of the eight clusters contained most protein family clusters and showed that most biological processes were overrepresented. In the first, which was metabolism, the most overrepresented clusters within this network were cellular metabolic process (539 genes, corrected p= 3.1715×10^{-68}), cellular macromolecule metabolic process (423 genes, corrected p= 7.8272×10^{-60}) and metabolic process (577 genes, corrected p=2.7514×10^{-57}). The second was protein processing, transport and localisation. The most overrepresented clusters within this network were cellular process (727 genes, corrected p= 5.143×10^{-44}), cellular localisation (106 genes, corrected p=

2.1040x10^{-8}) and protein transport (84 genes, corrected p=4.4507x10^{-7}). The most overrepresented groups of clusters within this ontology map for biological processes would again be expected as PAR4 is a surface-expressed GPCR which exerts downstream signalling upon receptor cleavage and activation (Dorsam et al., 2002; Offermanns, 2006). Proteins that are overrepresented within protein transport and localisation and cellular metabolic processes are within the expected results shown in (Figure 3.10).

The final cluster map, assessed for the whole PAR4/Y157C proteome, was for the cellular component. In this map, it was possible to delineate six distinct clusters whose major families were cell membrane, mitochondrial, ribosomal, cytosolic, cytoskeletal and transport complex (Figure 3.11). Within the cluster map, three of the six showed the majority of functions overrepresented, whereas one cluster contained moderately overrepresented nodes. It was revealed the most overrepresented cluster within this network was for cytosolic proteins, with the three most overrepresented nodes being for the intracellular part (850 genes, corrected p= 1.5325x10^{-96}), intracellular (853 genes, corrected p= 5.1291x10^{-89}) and cytoplasm (692 genes, corrected p=6.2487x10^{-81}). The second most overrepresented cluster within this network was for ribosomal proteins, with the three most overrepresented nodes being for ribonucleoprotein complex (176 genes, corrected p= 3.5130x10^{-95}), ribosome (73 genes, corrected p= 1.9062x10^{-41}) and ribosomal complex (48 genes, corrected p=9.7290x10^{-29}). The final most overrepresented cluster within this network was for mitochondrial proteins, with the three most overrepresented nodes being mitochondrion (177 genes, corrected p= 3.3717x10^{-31}), mitochondrial part (108 genes, corrected p= 6.9352x10^{-27}) and mitochondrial lumen (51 genes, corrected p=1.3104x10^{-17}). In addition, the cluster which contained moderately overrepresented nodes was for cytoskeletal proteins, with the three most overrepresented nodes being for cytoskeleton (100 genes, corrected p= 1.5450x10^{-2}), microtubule cytoskeleton (48 genes, corrected p= 1.2113x10^{-2}) and actin cytoskeleton (26 genes, corrected p=1.8691x10^{-2}).

Given that this is assessing the whole wt-PAR4 and mut-Y157C proteome combined, it isn't surprising that the two most overrepresented groups within the cellular component ontology map are cytosolic proteins and ribosomal proteins. However, what is surprising is that the third most overrepresented group was mitochondrial proteins. There has been a shift in the paradigm of GPCR biology in that they are plasma membrane-expressed receptors which exert downstream signalling via exogenous ligand binding. It has now been shown that the mitochondria also harbour GPCRs on the mitochondrial membrane, and this list is ever-increasing, mainly from the ability to isolate mitochondria from cells and study them as functional and separate units. Receptors identified within the mitochondria include AT_1R, AT_2R, cannabinoid receptors, and $P2Y_1$ and $P2Y_2$ (Fasciani et al., 2022).
Interestingly, $P2Y_1$ is an integral GPCR in platelet activation cascades, and its presence in the mitochondria opens new insights into signalling bias in cellular localisation (Belous et al., 2004). Thus far, PARs haven't been identified as localising anywhere besides the plasma membrane. However, this proteomic data has shown a high association with mitochondrial proteins and, therefore, opens up a new avenue for exploration in future work.

Although BiNGO was more helpful in analysing overrepresented groups in the wt-PAR4/mut-Y157C whole proteome, given the vastness of identified proteins, the networks generated were still difficult to fully visualise. Therefore, the final analysis of the whole proteome was carried out through a Cytoscape plugin called Reactome. The map was generated using a false discovery rate filter of (0.05), with the most enriched pathways being highlighted in yellow (0) to brown (0.05). The most enriched families within the network were cellular response to stimuli, vesicle-mediated transport, cell cycle, RNA metabolism and signalling of Rho GTPases. In addition, the most enriched single pathways were translation (114 genes, FDR $4.5519X10^{15}$), metabolism (85 genes, FDR $4.5519X10^{-15}$) and cell response to stimuli (47 genes, FDR $1.1102X10^{-15}$) (Figure 3.12). Again, this map corroborated what was seen in previous analyses performed in that translation (with an abundance of RNA proteins

identified), metabolism (again with it being a membrane-expressed receptor with downstream intracellular responses) and cell response to stimuli. Although the intrinsic value of this analysis provided a somewhat clearer visualisation of enriched pathways over bingo, the resultant information derived is the same and, therefore, assures the results obtained.

Next, we aimed to compare the protein ratios between wt-PAR4 (M/L ratios) and Mut-Y157C PAR4 (H/L ratios) in experimental replicates. Replicate 1 (n = 2905 proteins) gave a Pearson correlation of (R = 0.8005) (Figure 3.7A). Replicate 2 (n = 3213 proteins) gave a Pearson correlation of (R = 0.7577) (Figure 3.7B). For replicate 3 (n = 1768 proteins), it gave a Pearson correlation of (R = 0.8105) (Figure 3.7C). All replicates gave a Pearson correlation greater than 0.5, indicating a strong positive correlation in interacting proteins between wt-PAR and mut-Y157C PAR4 within experimental replicates. This result would be expected despite mut-Y157C PAR4 being intracellularly retained due to incorrect folding protein interaction up to that point, which should be measurably the same (Norman et al., 2016). This is shown by the strong correlation coefficient across the three replicates. If compared, it could be inferred that wt-PAR4 vs Wt-PAR4 would give a similar or slightly stronger Pearson correlation. Still, a perfect correlation wouldn't be achieved due to intra-experimental variability, and therefore, Pearson correlations >0.75 across as three experimental replicates show interacting proteins between wt-PAR4 and mut-Y157C are similar.

3.4.3 Comparison of wt-PAR4 and mut-PAR4 proteome

Following this, we next compared the proteins identified as high confidence hits across the three replicates—comparing proteins identified in wt-PAR4 (M/L) (n = 224 proteins) (Figure 3.13) vs Mut-Y157C PAR4 (H/L) (n = 150 proteins) (Figure 3.14). Wt-PAR4 clearly showed more identified interacting proteins when compared with mut-Y157C PAR4 (224 vs. 150). This could partly be explained by the paradigm of mut-Y157C PAR4s eventual retention within the endoplasmic reticulum and, therefore, significantly reduced expression on the surface of the plasma membrane. Thus, mut-Y157C PAR4 will likely interact with fewer proteins than wt-PAR4, which completes the whole cycle of membrane expression.

3.4.4 Bioinformatic analysis of wt-PAR4 and mut-PAR4 proteomes using PANTHER

The proteins identified as high-impact interactors with PAR4 and mut-Y157C PAR4 were then assessed and compared using gene ontology classes using the bioinformatics programme PANTHER (Mi and Thomas, 2019). The distribution in molecular function showed a very similar distribution of proteins between wild-type and mutant PAR4; however, it showed proteins with molecular adaptor function and molecular transducer function that were present in wt-PAR4 but not in mut-Y157C PAR4 (Figure 3.15A). The distribution in the biological process was almost visually similar between wt-PAR and mut-Y157C. However, small groups of proteins for biological adhesion, biological processes involved in interspecies interaction, reproductive processes, and reproduction were present in the wt-PAR4 gene ontology map but not in mut-Y157C PAR4 (Figure 3.15B). Cellular components showed identical distributions of proteins in wt-PAR4 and mut-Y157C (Figure 3.15C). The distribution in protein class was more varied visually comparing wt-PAR4 and mut-Y157C with additional protein classes for extracellular matrix, gene-specific transcriptional regulator, transmembrane

signal receptor and transporter protein classes being present in wt-PAR4 and not in mut-Y157C PAR4 gene ontology maps.

Interestingly, proteins that perform transporter functions in wt-PAR4 but not in mut-Y157C PAR4 are present. This would be exactly what would be expected as a major omission in mut-Y157C PAR4 due to its retention within the endoplasmic reticulum. In addition, Proteins present in the class of transmembrane signal receptors and extracellular matrix proteins would all be proteins expected to interact with surface-expressed and functional receptors. This could tie in with the results discussed in the previous section in which wt-PAR4 showed (n = 223 proteins) and mut-Y157C PAR4 showed (n = 150 proteins). At least in part, the increased number of proteins seen in wt-PAR4 can be accounted for by these additional protein classes, which intracellularly retained mut-Y157C PAR4 do not interact with.

3.4.5 Bioinformatic analysis of wt-PAR4 and mut-PAR4 proteomes using BiNGO

As performed with the whole wt-PAR4/mut-Y157C proteome, BiNGO analysis was performed on the individual wt-PAR4/mut-Y157C proteomes. The first cluster map assessed for the individual wt-PAR4 and mut-Y157C proteomes was for molecular function. For wt-PAR4, it was possible to determine four distinct clusters, with major families being Binding activity, transporter activity, catalytic activity and structural activity (Figure 3.16). Within the cluster map, two of the four showed the majority of enriched functions; these were for binding and structural activity. It was shown the most overrepresented clusters within this network were RNA binding (44 genes, corrected p= 4.177×10^{-15}), protein binding (163 genes, corrected p= 4.379×10^{-13}) and nucleotide binding (54 genes, corrected p=7.4459×10^{-4}). The other cluster, which contained only two overly enriched clusters, was structural activity, which was for a structural constituent of the ribosome (29 genes, corrected p=1.6807×10^{-22}) and structural molecule activity (40 genes, corrected p=4.177×10^{-15}).

In comparison, for mut-Y157C PAR4, it was again possible to determine four distinct clusters, the major families being Binding activity, transporter activity, catalytic activity and structural activity (Figure 3.19). Within the cluster map, three of the four showed the majority of enriched functions; these were for binding activity, structural activity, and catalytic activity. It was shown that for the first cluster binding activity, the most overrepresented clusters within this network were RNA binding (33 genes, corrected p= $3.5767x10^{-13}$), protein binding (103 genes, corrected p= $2.1317x10^{-7}$) and nucleotide binding (38 genes, corrected p=$1.5876x10^{-3}$). The other cluster, which contained only two overly enriched clusters, was structural activity for a structural constituent of the ribosome (corrected p=$3.2535X10^{-18}$) and structural molecule activity (corrected p=$3.2911X10^{-12}$). The final group, which was for catalytic activity, contained majority of enriched clusters which is in contrast to wt-PAR4, the most overrepresented clusters within this network were pyrophosphatase activity (17 genes, corrected p= $7.0466x10^{-3}$), hydrolase activity, acting on acid anhydrides, in phosphorous-containing anhydrides (17 genes, corrected p= $7.0466x10^{-3}$) and hydrolase activity, acting on acid anhydrides (17 genes, corrected p=$7.0466x10^{-3}$).

The second cluster map, assessed for the individual wt-PAR4 and mut-Y157C proteomes, was for the biological process. For wt-PAR4, it was possible to determine five distinct clusters: metabolism, biological regulation, biological response to stimuli, transport and localisation, and cellular and organelle organisation (Figure 3.17). Within the cluster map, two of the five showed the majority of enriched functions for metabolism and cellular and organelle organisation. For metabolism, it was shown that the top three overrepresented groups were the cellular metabolic process (125 genes, corrected p= $6.5428X10^{-15}$), cellular macromolecule metabolic process (98 genes, corrected p=$5.7317X10^{-13}$) and cellular protein metabolic process (70 genes, corrected p=$4.5908X10^{-11}$). The other enriched cluster, which was for cellular and organelle organisation, showed the three most overrepresented clusters were cellular process (176 genes, corrected p= $1.5278X10^{-14}$), ribonucleoprotein

complex biogenesis (19 genes, corrected p=1.7680X10^{-9}) and ribosome biogenesis (13 genes, corrected p=1.9157X10^{-6}). In comparison, for mut-Y157C PAR4, it was again possible to determine five distinct clusters with major families being metabolism, biological regulation, transport and localisation, and cellular and organelle organisation; however, this time, cell cycle made up the fifth distinct group, which is in contrast to the wt-PAR4 map in which biological response to stimuli made up the fifth (Figure 3.20). Within the cluster map, three of the five showed the majority of enriched functions: metabolism, cell cycle and cellular and organelle organisation. For metabolism, it was shown that the top three overrepresented groups were translation (30 genes, corrected p= 5.3652X10^{-21}), translation elongation (21 genes, corrected p=5.3652X10^{-21}) and gene expression (44 genes, corrected p=1.7183X10^{-13}). The second enriched cluster, which was for the cell cycle, showed the three most overrepresented clusters were nuclear division (10 genes, corrected p= 1.9476X10^{-3}), mitosis (10 genes, corrected p=1.9476X10^{-3}) and M phase of the mitotic cell cycle (10 genes, corrected p=2.1722X10^{-3}). The final enriched cluster, which was for cellular and organelle organisation, showed the three most overrepresented clusters were cellular process (119 genes, corrected p= 1.0637X10^{-11}), cellular component biogenesis (30 genes, corrected p=5.8884X10^{-7}) and ribonucleoprotein complex biogenesis (13 genes, corrected p=1.6684X10^{-6}).

The final cluster map, assessed for the individual wt-PAR4 and mut-Y157C proteomes, was for cellular components. For wt-PAR4, it was possible to determine five distinct clusters, the major families being cell membrane, cytosolic, nuclear, mitochondrial and cytoskeletal (Figure 3.18). Within the cluster map, all of them showed that the majority of functions were enriched. The first major cluster was cytosolic, with the top three overrepresented groups being macromolecular complex (118 genes, corrected p= 2.3678X10^{-31}), ribonucleoprotein complex (52 genes, corrected p=6.6535X10^{-31}) and ribosome (35 genes, corrected p=1.1336X10^{-28}). The second overrepresented cluster was nuclear proteins, with the three most overrepresented groups in

this cluster being the nuclear part (56 genes, corrected p=2.8313X10^{-10}), nuclear lumen (45 genes, corrected p=5.8947X10^{-9}) and nucleolus (23 genes, corrected p=2.0201X10^{-7}). The third cluster was for mitochondrial proteins, with the three most overrepresented in the cluster being mitochondrial matrix (20 genes, corrected p=8.9450X10^{-11}), mitochondrial lumen (20 genes, corrected p=8.9450X10^{-11}) and mitochondrial part (31 genes, corrected p=4.0871X10^{-10}). The fourth cluster was for cytoskeletal proteins, with the three most overrepresented groups being actin cytoskeleton (13 genes, corrected p=3.7857X10^{-4}), cytoskeleton (35 genes, corrected p=5.3249X10^{-4}) and cytoskeletal part (27 genes, corrected p=6.0499X10^{-4}). The final cluster was for cell membrane proteins, with the three most overrepresented being mitochondrial inner membrane (15 genes, corrected p=4.9631X10^{-5}), cell leading edge (11 genes, corrected p=6.1867X10^{-5}) and lamellipodium (6 genes, corrected p=3.7546X10^{-3}). In comparison, for mut-Y157C PAR4, it was again possible to determine five distinct clusters, with the major families being cell membrane, mitochondrial cytoplasmic, cytoskeletal and nuclear (Figure 3.21).

The first major cluster was cytosolic, with the top three overrepresented groups being ribonucleoprotein complex (36 genes, corrected p= 1.0888X10^{-21}), organelle part (96 genes, corrected p=1.4987X10^{-21}) and non-membrane bound organelle (69 genes, corrected p=1.4987X10^{-21}). The second overrepresented cluster was nuclear proteins, with the three most overrepresented groups in this cluster being nucleolus (20 genes, corrected p=1.3532X10^{-8}), nuclear part (39 genes, corrected p=3.6474X10^{-8}) and nuclear lumen (31 genes, corrected p=6.4999X10^{-7}). The third cluster was for mitochondrial proteins, with the three most overrepresented in the cluster are mitochondrial part (19 genes, corrected p=6.0649X10^{-6}), mitochondrial matrix (10 genes, corrected p=1.4506X10^{-4}) and mitochondrial lumen (10 genes, corrected p=1.4506X10^{-4}). The fourth cluster was for cytoskeletal proteins, with the three most overrepresented groups being actin cytoskeleton (9 genes, corrected p=3.1208X10^{-3}), microtubule (8 genes, corrected p=1.0079X10^{-2})

and cytoskeleton (22 genes, corrected p=1.1178X10^{-2}). The final cluster was for cell membrane proteins, with the three most overrepresented being membrane enclose lumen (41 genes, corrected p=1.7866X10^{-9}), envelope (17 genes, corrected p=3.1865X10^{-4}) and cell leading edge (8 genes, corrected p=5.4509X10^{-4}).

3.4.6 Wt-PAR4 and mut-PAR4 proteomes share many similarities but reveal distinct differences

The comparability between wt-PAR4 and mut-Y157C gene enrichment maps was generally similar. However, there were some differences between the gene enrichment maps generated to compare the wt-PAR4 and mut-Y157C proteomes. For molecular function, the four general groups remained the same for both. However, the wt-PAR4 gene enrichment map for molecular function was more complex than the mut-Y157C one. In particular, for binding activity, cytoskeletal protein binding was overrepresented in wt-PAR4 but underrepresented in mut-Y157C, with actin-binding having a higher degree of overrepresentation in wt-PAR4 compared to mut-Y157C.

Additionally, extra branches in RNA binding were present in wt-PAR4 that were not in mut-Y157C. Wt-PAR4 contained two distinct branches for transporter activity: a transferase branch and a transporter activity branch. The mut-Y157C arm completely lacked the transferase branch. Finally, for catalytic activity, wt-PAR4 contained two distinct branches, which branched off from hydrolase activity. The mut-Y157C enrichment map contained only a single branch for catalytic activity; this again shows that wt-PAR4 interacts with more proteins along the biosynthetic pathway as mut-Y157C is retained within the endoplasmic reticulum (Norman et al., 2016). In addition, wt-PAR4 could have a more complex and enriched molecular function map than mut-Y157C because wt-PAR4 is a fully functional protein. In contrast, the Y157C mutation is known to be deleterious to PAR4 functionality, and, therefore, its molecular function is impaired (Cunningham et al., 2012; Norman et al., 2016).

For biological processes, the differences in visual complexity are much more apparent when comparing the enrichment maps of wt-PAR4 and mut-Y157C. This time, although five clusters were identified in both, one group, which was present in wt-PAR4, biological response to stimuli, was not present in mut-Y157C, which contained cell cycle instead. This difference is particularly interesting but also gives validity to the results that would be expected when comparing the two enrichment maps.

Fully functional wt-PAR4s' primary role is to initiate downstream signalling upon receptor cleavage and tethered ligand binding, and therefore, being a primary biological process is expected; it is noted, however, that the majority of processes within this group are underrepresented. Although protein association determined in the proteomic analysis is in unstimulated PAR4, it, therefore, is reasonable to hypothesise that if a comparison were made between this unstimulated PAR4 proteomic dataset and a dataset with thrombin-stimulated wt-PAR4, a comparable difference in enrichment would be observed. The lack of a biological response to the stimuli group in the mut-Y157C shows that it doesn't associate with proteins that typically work downstream of receptor activation. This confirms the previous work that Y157C is intracellularly retained and the mutation deleterious to receptor function. Another cluster that showed distinct differences in the number of pathways was biological regulation. For wt-PAR4, this cluster group was fairly dense when compared to that of mut-Y157C, given the downstream effects of receptor activation of PAR4, such as in platelets where PAR4 activation leads to increases in intracellular calcium, platelets shape changes, release of alpha and dense granules (Coughlin, 2000; Dorsam et al., 2002).

The receptor is expected to interact with many different proteins responsible for regulating biological processes. This group in wt-PAR4 is again majority underrepresented. Still, as mentioned previously, we would expect a shift to overrepresented with the biological response to stimuli when comparing unstimulated wt-PAR4 with thrombin-stimulated PAR4 groups. Again, this

contrasts with the picture seen in mut-Y157C, which lacks a dense network in biological regulations that were seen in the wt-PAR4 group, as mut-Y157C is a deleterious mutation that results in reduced to almost absent receptor function its lack of association with proteins responsible for biological regulation would be expected. Similar to the previous two, another group that showed a distinctly different expression pattern was transport and localisation. Unsurprisingly, in wt-PAR4, the network was again more visually dense when compared to mut-Y157C. In the context of mut-Y157C, some clusters are present within transport and localisation, which would be expected, from transport to the endoplasmic reticulum, addition of groups to establish where in the cell it localises, etc. However, the mutation which results in its retention within the ER means transport to the Golgi and then through the cytoplasm to the plasma membrane doesn't occur. Wt-PAR4 completes the full cycle of receptor transport and receptor internalisation post-stimulation and transport through degradation pathways, resulting in a more established association network with proteins involved in transport and receptor localisation. Again, in wt-PAR, a lot of the nodes are underrepresented; as this is looking at protein association in an unstimulated state, there would be the expectation that certain nodes would become overrepresented in the context of receptor stimulation, particularly ones involved in receptor internalisation and transport along receptor degradation pathways.

For cellular components visually, both wt-PAR4 and mut-Y157C were similar in complexity in the produced enrichment maps. The only discernible visual difference that could be inferred was that the size of the nodes in wt-PAR4 was larger or more deeply coloured for statistical significance when compared to mut-Y157C. The main enrichment groups for both proteins remained the same, including cytoplasmic, mitochondrial, cell membrane, nuclear and cytoskeletal. However, despite visual similarity, there were some distinct differences. In particular, the cell membrane in wt-PAR4 contained more nodes than mut-Y157C and larger, more overrepresented nodes. The presence of a more complex network for the cell membrane in wt-PAR4 isn't surprising, given

that mut-Y157C doesn't reach the surface plasma membrane. Therefore, association with proteins in this context would be reduced compared to wt-PAR4. In addition, other differences, such as the number of proteins overrepresented in a node and the degree of significance, tended to be higher in wt-PAR4 than in mut-Y157C. This could be explained by the fact that for wt-PAR4 (n=224) and mut-Y157C (n=150), the network complexity and groups were comparably similar and not as distinctly different as thus observed in molecular function and biological process.

3.4.7 Reactome enrichment mapping visually confirms difference in wt-PAR4 signalling over mutant

Although BiNGO was more helpful in analysing overrepresented groups comparing the wt-PAR4 vs. mut-Y157C proteome, given the vastness of identified proteins, the networks generated were still difficult to fully visualise. Therefore, the final analysis was conducted to compare wt-PAR4 vs mut-Y157C proteome through a Cytoscape plugin called Reactome. The map was generated using a false discovery rate filter of (0.05), with the most enriched pathways being highlighted in yellow (0) to brown (0.05). The most enriched families within both networks were the same: cellular response to stimuli, vesicle-mediated transport, cell cycle, metabolism of RNA, signalling of Rho GTPases, and protein repair. In addition, the most enriched single pathways for wt-PAR4 were translation (29 genes, FDR $3.4417X10^{-15}$), cellular response to stimuli (27 genes, FDR $3.4417X10^{-15}$) and metabolism (26 genes, FDR $3.4417X10^{-15}$) (Figure 3.22A). The most enriched single pathways for mut-Y157C were translation (21 genes, FDR $2.9976X10^{-15}$), metabolism (21 genes, FDR $2.9976X10^{-15}$) and cellular response to stimuli (20 genes, FDR $2.9976X10^{-15}$) (Figure 3.22B). Again, this map corroborated what was seen in previous analyses performed in that translation (with an abundance of RNA proteins identified), metabolism (again with it being a membrane-expressed receptor with downstream intracellular responses) and cell response to stimuli. Although the intrinsic value of this analysis provided a somewhat clearer

visualisation of enriched pathways over bingo, the resultant information derived in the BiNGO analysis was more complex. It allowed for more information regarding differences in expressed protein groups to be derived.

3.4.8 Bioinformatic comparison confirms loss of protein function in mut-PAR4 compared to wt-PAR4

Comparison between the proteins identified in just the wt-PAR4 group and the mut-Y157C group allowed for the differences in intracellular retention of the mutant protein on the number of interacting proteins that PAR4 has. In total, wt-PAR4 had more high-impact hits (n=224) when compared to that of mut-Y157C (n=150), as would be expected. In addition, testing for correlation showed that proteins identified in wt-PAR4 and mut-Y157C showed a strong correlation (R>0.8), as would also be expected. Again, due to intracellular retention, the perfect correlation wouldn't be expected due to the inherent variation from mass spectrometry proteomic data. However, the correlation identified showed that, at least for the most part, wt-PAR4 and mut-Y157C interact with similar proteins along the biosynthetic pathways and alludes to the fact that analysis was performed correctly as it falls within the expected result. Further analysis using PANTHER and BiNGO is where distinct differences in proteins between wt-PAR4 and mut-Y157C became apparent, particularly in molecular function and biological process, which contained more complex gene maps and enriched nodes in the wt-PAR4 compared to the mut-Y157C maps. Thus far, It could be concluded that wt-PAR4 includes a more complex interaction network than mut-Y157C, which ties to the fact that mut-Y157C is intracellularly retained and has deleterious functionality compared to wt-PAR4. This, in part, could explain the results discussed above.

The final analysis in the chapter tries to identify a novel protein and molecular pathway to explore and validate in further studies in the following chapter. To do this, proteins that gave SILAC ratios above the threshold across two or more replicates were used. Any with less than this were screened out. This

gave a total number of proteins (n=996) assessed for a protein and molecular pathway for further validation. The network was produced using STRINGdb, and any misidentified protein was extracted. The protein identity was determined using UniProt before being readded to the STRINGdb network. To choose a protein of interest, the minimum interaction score was changed from medium confidence (0.400) to high confidence (0.700), and disconnected nodes were removed. Kmeans clustering was applied to the interaction network with an (n=9) to select a defined cluster for further assessment. The protein map generated showed the interaction network with separation into nine distinct clusters determined by the colour of the nodes (Figure 3.23).

3.4.9 Bioinformatic analysis of F2RL3 cluster reveals novel pathways and protein for validation

To determine proteins of interest close to PAR4, the cluster containing the F2RL3 gene (PAR4 gene) was extracted, and the network was further explored. The cluster which contained the F2RL3 gene contained a total of (n=134) proteins shown in (Figure 3.24). Therefore, to derive more valuable information about the protein families most overrepresented in the PAR4 gene-containing cluster, we were assessed using the gene ontology software plugin BiNGO to determine clusters overrepresented in this cluster. Statistical significance was generated using the hypergeometric test for statistical significance using the Benjamnini and Hochberg FDR correction; statistical significance was set at 0.05; overrepresented clusters were coloured from yellow 0.05 to orange 0.0000005 on a sliding scale. Clustering on BiNGO is split into three main functional families in which proteins can be grouped into molecular function, biological process and cellular component.

The first cluster map, which was assessed for the F2RL3 gene-containing cluster, was for molecular function. For this enrichment map, it was possible to determine three distinct clusters, the major families being Binding activity,

catalytic activity and kinase activity (Figure 3.25). Within the cluster map, two of the three showed the majority of overrepresented functions; these were for binding and catalytic activity. It was shown the most overrepresented clusters within binding activity were cytoskeletal protein binding (33 genes, corrected p= $1.3781x10^{-19}$), actin binding (24 genes, corrected p= $3.2928x10^{-15}$) and Rho GTPase binding (6 genes, corrected p=$5.6327x10^{-6}$). String networks for the three most overrepresented groups were produced (Figure 3.25B). The other overrepresented cluster was for catalytic activity, showed that the three most overrepresented clusters were for nucleoside-triphosphatase activity (18 genes, corrected p=$2.5283X10^{-4}$), pyrophosphatase activity (18 genes, corrected p=$2.8540X10^{-4}$) and hydrolase activity, acting on acid anhydrides, in phosphorous-containing anhydrides (18 genes, corrected p=$2.8540X10^{-4}$). The final cluster, which showed the majority of nodes underrepresented, was for kinase activity; however, the three most overrepresented groups in the cluster were protein kinase activity (2 genes, corrected p= $4.3887x10^{-2}$), MAP kinase 2 activity (2 genes, corrected p= $4.8874x10^{-2}$) and calcium dependant protein kinase C activity (1 gene, corrected p=$4.3887x10^{-2}$).

The second cluster map, assessed for the F2RL3 gene-containing cluster, was for the biological process. In this map, it was possible to delineate three distinct clusters whose major families were cellular component organisation, biological regulation and localisation (Figure 3.26A). Within the cluster map, the majority of protein family clusters were overrepresented. In the first, which was cellular component organisation, the most overrepresented clusters within this network were actin filament-based process (14 genes, corrected p= $7.4983x10^{-6}$), actin cytoskeleton organisation (13 genes, corrected p= $1.5672x10^{-5}$) and cytoskeleton organisation (17 genes, corrected p=$1.8075x10^{-5}$). String networks for the three most overrepresented groups were produced (Figure 3.26B). In the second, which was localisation, the most overrepresented clusters within this network were protein localisation (20 genes, corrected p= $1.6499x10^{-3}$), cellular localisation (20 genes, corrected p= $3.1662x10^{-3}$) and macromolecule localisation (21 genes, corrected p=$5.2302x10^{-3}$). In the third,

which was for biological regulation, the most overrepresented clusters within this network were regulation of cellular component organisation (18 genes, corrected p= $3.5133x10^{-5}$), regulation of cellular component biogenesis (9 genes, corrected p= $4.8020x10^{-4}$) and regulation of protein complex assembly (6 genes, corrected p=$5.2302x10^{-3}$).

The final cluster map assessed for the F2RL3 gene-containing cluster was for the cellular component. For this enrichment map, it was possible to determine four distinct clusters with major families: cytoplasmic, cytoskeleton, nuclear and membrane (Figure 3.27A). Within the cluster map, the majority of functions were overrepresented. It was shown the most overrepresented clusters within the membrane were cell leading edge (33 genes, corrected p= $1.3781x10^{-19}$), lamellipodium (24 genes, corrected p= $3.2928x10^{-15}$) and cell projection (6 genes, corrected p=$5.6327x10^{-6}$). The second overrepresented cluster, which was for cytoplasmic components, showed that the three most overrepresented clusters were for cytoplasm (96 genes, corrected p=$1.1220X10^{-10}$), cytoplasmic part (74 genes, corrected p=$2.5428X10^{-9}$) and cytosol (33 genes, corrected p=$1.4481X10^{-10}$). The third overrepresented cluster was for nuclear protein components; the three most overrepresented nodes within this cluster were centrosome (6 genes, corrected p=$7.8025X10^{-3}$), nuclear chromosome (6 genes, corrected p=$9.4648X10^{-3}$) and centriole (3 genes, corrected p=$1.2447X10^{-2}$). The last cluster was for cytoskeletal proteins, with the three most overrepresented nodes being cytoskeleton (46 genes, corrected p=$1.9291X10^{-16}$), actin cytoskeleton (17 genes, corrected p=$1.2122X10^{-9}$) and cytoskeleton part (25 genes, corrected p=$1.2472X10^{-6}$). This time, the three most overrepresented nodes were contained within three different cellular components; string networks were produced for these: the cell leading edge, cytoskeleton and non-membrane bound organelle (Figure 3.27B).

Extraction of this cluster allowed us to hone in on proteins of interest, which were proximity interactors downstream of PAR4. Despite the large network (n=134) (Figure 3.26), further analysis using BiNGO to determine

overrepresented clusters provided an interesting avenue of protein pathways for further exploration. Across all three BiNGO maps, a specific set of pathway proteins was apparent. These are proteins that are involved in the regulation of the cytoskeleton and actin dynamics. For molecular function, cytoskeletal binding, actin binding and Rho GTPase binding were the three most overrepresented groups (Figure 3.25). For the Biological process, actin filament-based process, actin cytoskeleton organisation, and cytoskeleton organisation were the three most overrepresented groups (Figure 3.26). For cellular components, cell leading edge, cytoskeleton, and non-membrane bound organelle were the three most over-represented groups (Figure 3.27).

The apparent importance of PAR4 in regulating actin dynamics has been shown through the association of F2RL3 with actin and cytoskeleton-associated proteins in the following analysis. Although, surprisingly, every BiNGO analysis for clustering showed this, it cannot be ignored that an abundance of literature highlights the importance of PAR4 in mediating platelet shape change upon activation (French and Hamilton, 2016; Rigg et al., 2020). Despite this, there doesn't appear to be much in the way of identifying the specific pathways downstream of PAR4 that mediate this change. However, the importance of untangling the roles of actin-associated proteins downstream of PAR4 activation has recently been highlighted in a study which showed that PAR4-medicated RhoA/ROCK signalling pathways are essential for morphological changes in MEG01 cells when treated with thrombin. The RhoA/ROCK pathway is a key in modulating actin dynamics and, therefore, provides evidence to explore additional proteins involved in actin dynamics, which may be modulated by PAR4 activity.

3.4.10 Triple hit mapping reveals actin severing protein Cofilin as a protein of interest

A final analysis was conducted on proteins that provided SILAC ratios above the threshold across all three replicates. All proteins identified on (n=29) had SILAC ratios above the thresholds for all replicates. STRING.db produced a protein interaction network for these (n=29) proteins (Figure 3.28). From the data, most of these proteins were ribosome-associated proteins, which is hardly surprising given their role in translating every single transcript into functional proteins. However, given the previous analysis performed in (Figures 3.25 – 3.28) which showed a high association of PAR4 with actin and cytoskeleton proteins, it can be shown that one protein in particular, CFL2, was identified as a hit across all three replicates. Cofilin (CFL) is an actin-severing protein essential in actin dynamics and filament turnover and, therefore, seems like a likely candidate to explore in experimental studies. Studies have shown the importance of Cofilin phosphorylation in response to thrombin in the past. However, no delineation of the role of PAR1 or PAR4 was determined. In addition, the previous study that shows the essential roles of the RhoA/ROCK pathway in PAR4-mediated morphological changes in MEG01 cells provides additional support for exploring Cofilin further, (Heo et al., 2022)as ROCK is known to be a regulator of LIMK, which is responsible for the phosphorylation of Cofilin which is essential in modulating its activity (Lawler, 1999).

3.4.11 Limitations and Future directions

Despite providing a vast amount of raw data for analysis, there are still some areas in which improvements could have been made to provide additional robustness to the data presented. As was stated in the paper by Emmett and Goodfellow, the minimum replicate dataset for SILAC proteomic data is (n=3). Although the data quantified above was an (n=3), it could be seen that replicate 1 and replicate 2 were very similar in terms of the proteins identified and data

distribution. However, there is quite a noticeable difference in replicate 3. Whether this was due to some experimental error in set-up or analysis, etc., remains to be determined; a way of improving this would have been to obtain more replicates than the minimum of (n=3) with something like (n=5). Therefore, if any obvious variation out with the expected spread could have been disregarded or the addition of replicates could have provided more additional robustness to the proteins identified.

In addition, the SILAC proteomic data for wt-PAR4 and mut-Y157C PAR4 was assessed in unstimulated transfected HEK293 cells. This obviously provided a good foundation for identifying novel interacting proteins and pathways downstream of PAR4. However, having datasets from cells stimulated with either thrombin or AYPGKF would have allowed for the determination of proteins that interacted with PAR4 downstream of receptor activation. In addition, it would have allowed for comparing protein expression to unstimulated cells, such as could have been displayed by volcano plots, which would have allowed for the determination of proteins whose expression increased upon receptor activation and those whose expression was downregulated. This would have added a layer of data that would have been useful in selecting a pathway/protein to evaluate further downstream of PAR4. It would have also allowed for the comparison of receptor function between wt-PAR4 and mut-Y157C; given that mut-Y157C is intracellularly retained, it would have been interesting to evaluate protein interaction and expression between unstimulated and stimulated cells to assess and validate this previously shown finding. A final point which would have been an interesting area of further investigation would have been the high abundance of mitochondrial proteins identified as potential interactors with PAR4. Given the emergence of literature showing the presence of GPCRs within mitochondria, exploring whether PAR4 was also present would have been interesting. However, it was beyond the scope of this study and thesis.

3.4.12 Conclusions

To summarise, the data analysis showed that SILAC proteomic data displayed the data within a standard Gaussian distribution; two replicates showed similarities in the number of proteins identified and the data spread. However, one showed a significant reduction in the number of proteins identified, bringing into question whether an error occurred during the preparation or analysis to obtain the data. The data showed that there was no correlation between experimental replicates, meaning reproducibility in SILAC proteomics is a slight issue; however, there was a correlation between wt-PAR4 and mut-Y157C between experimental replicates, at least providing validity to the data that similarities in identified proteins were apparent between them.

When comparing the proteins expressed between wt-PAR4 and mut-Y157C, it was shown that wt-PAR4 had more proteins identified as interacting compared to mut-Y157C, which was expected. As well, there were more complex interacting cascades, as was shown through PANTHER and bingo analysis.

Finally, looking home into pathways/proteins downstream of PAR4, a cluster was extracted, which was differentiated via Kmeans clustering, from the entire PAR4 proteome. The cluster which contained the F2RL3 gene was extracted and further analysed; this showed that pathways involved in cytoskeleton dynamics were consistently overrepresented across all BiNGO groups. These results tie in with previous works stating the importance of PAR4 in Platelet shape change and aggregation. The ability of PAR4 to modulate the actin and tubulin cytoskeletons upon receptor activation would be essential. Therefore, PAR4 would need to excrete the effects on the proteins responsible for this. The identification of Cofilin-2, which had SILAC ratios above the threshold across all three replicates and is a protein responsible for the severing of actin filaments, appeared to be a good protein to further validate, including proteins which are involved in Cofilin regulation.

Although there are areas where improvement could have been made or where additional areas could have been explored further, the data allowed for the identification of a vast network of proteins, which, following additional levels of analysis led to groups of proteins responsible for actin dynamics and, specifically, the actin-severing protein Cofilin to be further explored in the context of PAR4 activation.

Chapter Four:

Optimisation and Validation of the MEG-01 cell line as a Suitable Platelet Cell Model System

4. Results Chapter 2

4.1 Introduction

4.1.1 ADF/Cofilins in actin dynamics

The actin cytoskeleton is an essential structural protein network consisting of two parallel ADP-actin strands with the same polarity, coming together to form a helical structure known as filamentous actin (F-Actin). The actin cytoskeleton is dynamic, undergoing repeated cycles of depolymerisation and polymerisation in a spatially and temporally coordinated fashion. Studies of actin polymerisation in vitro show that the assembly of F-actin will occur spontaneously when the pool of actin monomers (G-actin) is at a sufficiently high threshold. Although useful in determining how actin monomers assemble to form F-actin filaments, this doesn't necessarily translate to actin dynamic regulation within an in vivo system. Instead, proteins which sequester G-actin monomers prevent spontaneous actin assembly within the cell. Therefore, actin assembly occurs at sites of actin severing or positions on the actin filament associated with nucleation factors.

The ADF/Cofilin family of proteins are essential regulators of actin dynamics. They are expressed in all eukaryotes within the animal kingdom, and their importance in various physiological and disease processes is studied in mice, rats, yeast, fruit flies, etc. ADF/Cofilin family proteins are small proteins of approximately (~18KDa). They were first discovered in the 1980s for their ability to bind actin and regulate its dynamics via their ability to sever actin and enhance the depolymerisation of F-actin (Bamburg et al., 1980). Humans express three forms of ADF/Cofilin: Actin-depolymerizing factor (ADF), Cofilin-1 (non-muscle Cofilin) and Cofilin-2 (muscle Cofilin) (Maciver and Hussey, 2002).

Despite having similar functionality in their ability to sever actin and promote depolymerisation, ADF, Cofilin-1 (CFL1) and Cofilin-2 (CFL2) are all encoded on different genes and are not the product of alternative splicing from the same gene. However, despite this, CFL1 and CFL2 share 80% sequence identity at the amino acid level, and ADF shares 70% sequence identity with Cofilins (Figure 4.1) (Kanellos and Frame, 2016).

Figure 4.1 Comparison of human ADF/Cofilin family amino acid sequence homology. A) Amino acid sequence alignment for CFL1, CFL2 and ADF using CLUSTAL multiple sequence alignment MUSCLE v3.8. * Denotes identical amino acid homology between the three proteins, nothing, . or : denotes differences in amino acid sequence between at least one of the proteins in comparison to the other two. B) Shows a comparison of human Cofilin-1 and Cofilin-2 generated using VectorBuilder v2.1.774, proteins highlighted in orange denotes differences in amino acid sequence. Calculation performed shows an amino acid identity of 134/168 which gives an identity scored between CFL1 and CFL2 of 80.24%. C) Shows a comparison of human Cofilin-1 and ADF generated using VectorBuilder v2.1.774, proteins highlighted in orange denotes differences in amino acid sequence. Calculation performed shows an amino acid identity of 120/168 which gives an identity scored between CFL1 and ADF of 71.43%.

Cofilins are essential proteins in eukaryotic organisms required for normal development, and loss of regulation or functions has dire consequences on tissue homeostasis and the organism's overall health. Studies have been performed to provide insight into the essential roles Cofilins play in the maintenance of the actin cytoskeleton and actin dynamics. This has also provided insight into the non-redundant roles each of the three Cofilin proteins play within their physiological niches.

4.1.2 Inhibitory phospho-regulation of Cofilin activity

Regulation of Cofilin activity via phospho-regulation was first documented through studies of ADF using chicken myocyte cultures, which showed the presence of two forms of ADF in immunoblots. One form was shown to have a slightly higher mass and be more acidic than the other, which disappeared upon treatment with phosphatase (Morgan et al., 1993). They also showed that only the species insensitive to phosphatase treatment could bind to and sever actin, showing that the phosphorylation of ADF/Cofilins acts as a negative regulator of its actin binding and severing activity (Morgan et al., 1993). The location of this single phosphorylation site was identified as being on Serine3 (Ser3) within the encoded proteins of both ADF and Cofilin-1 and Cofilin-2 (Agnew et al., 1995; Moriyama et al., 1996).

Determination of the upstream regulators of Cofilin phosphorylation led to the identification of the first family of kinases which phosphorylate Cofilin at (Ser3), which were the LIM Kinases (LIMK) for which two isoforms have been identified so far: LIMK1 and LIMK2 (Mizuno et al., 1994; Nunoue et al., 1995; Okano et al., 1995). Although both function to phosphorylate and inactive ADF/Cofilin proteins, structural differences provide both location and phosphorylation sites, which are unique from the other. LIMK1 is palmitoylated on a di-cysteine motif (C7 and C8), which allows for LIMK1 to effectively membrane anchor, allowing for the efficient phosphorylation and activation of its T508 by members of the p21-activated kinase (PAK) family (George et al.,

2015). LIMK2 lacks this di-cysteine motif for membrane anchoring and, therefore, exists primarily as a non-membrane bound form and is activated via phosphorylation on T505, which is equivalent to the T508 activation site of LIMK1 (Maekawa et al., 1999; Ohashi et al., 2000; Sumi et al., 2001). In addition, a second family of kinases which phosphorylated ADF/Cofilin at Ser3 were identified in the testes and are known as Testis Associated Actin Remodelling Kinases (TESK1 and 2) and have structurally related kinase motifs similar to LIMKs (Toshima et al., 1995, 2001). A final member identified which phosphorylates ADF/Cofilin at Ser3 are members of the germinal centre kinase family and is known as Nik-related protein kinase (NRK/NESK), which is active during embryogenesis and has been shown to enhance the phosphorylation of Cofilin at Ser3 (Figure 4.2) (Nakano et al., 2003).

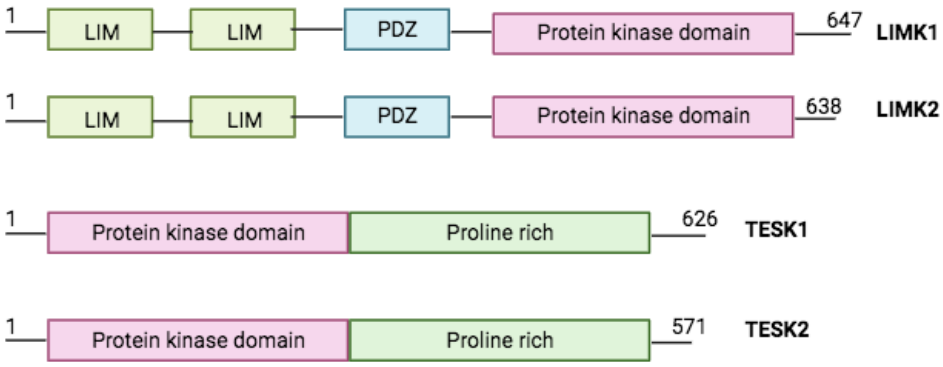

Figure 4.2. Structural differences and similarities between the main negative phosphoregulators of Cofilin activity. Figure shows the main regulators of Cofilin phosphorylation, LIMK1 and LIMK2 structurally similar containing conserved functional domains, which include two LIM domains, a PDZ domain, and the catalytically active protein kinase domain. LIMK1 is slightly larger containing 647 amino acids compared to the shorter LIMK2, which are 638 amino acids. The other group of Phospho-regulators of Cofilin is TESK1 and TESK2; these contain the same catalytically active protein kinase domain as LIMK1/2 however lack the LIM and PDZ domains of LIMKs. Instead, both TESK1 and TESK2 contain a proline rich domain conserved between the two. The only differences are that TESK1 is slightly longer at 626 amino acids compared to the shorter TESK2 at 571 amino acids.

To phosphorylate and inactivate Cofilin, LIMK first needs to be phosphorylated. Upstream regulation of LIMK activity is primarily regulated by the Rho-associated protein kinase (ROCK), for which there are two known isoforms, ROCK1 and ROCK2. ROCK's activity is determined by its effectors, the Rho family GTPases. Activation of Rho GTPases results in the downstream activation of ROCK, which phosphorylates and activates LIMKs, which phosphorylate and deactivate ADF/Cofilins, resulting in a dynamic and complex negative regulation pathway for Cofilin activity (Maekawa et al., 1999; Ohashi et al., 2000).

Despite Ser3 being the main phosphorylation site for the regulation of Cofilin activity, over time, additional sites have been identified which provide additional levels of complexity to the regulation of Cofilin activity within actin remodelling. An additional phosphorylation site was identified within leukemic cells and is catalysed by the protein kinase-C α (PKCα) and results in the phosphorylation of serine at positions Ser23 and/or Ser24 within Cofilin (Sakuma et al., 2012). It was found that phosphorylation at these sites caused the cessation of histamine release in basophilic leukemic cells stimulated to degranulate, increasing the available F-actin. This was determined in studies using mutagenesis of the Ser23/Ser24 sites using a non-phosphorylatable Ala23/Ala24 substitution. This mutant was found to show increased binding, severing and depolymerisation of F-actin, resulting in increased basophilic degranulation. In contrast, the opposite was observed when substituted with a glutamine Glu23/Glu24, which acts as a phosphomimetic (Sakuma et al., 2012).

Determination of additional phosphorylation sites of Cofilin was achieved through a global screening in myeloid cells. The screen identified various phosphorylation sites, including the Ser3 and Ser23/Ser24. The additional sites identified were Ser41, Ser108, Ser156, and tyrosine sites Y68, Y82, and Y140 (Prudent et al., 2018). The phosphorylation of the tyrosine site Y68 has been shown to target Cofilin for ubiquitylation and degradation (Yoo et al.,

2010). Despite their identification, the roles that the phosphorylation of Ser41, Ser108, Ser156, Y82, and Y140 have on the regulation of Cofilin function, activity or localisation has not been determined.

4.1.3 Activation of phospho-Cofilin via phosphatases

In contrast to this activation of Cofilin, it results from the dephosphorylation of Ser3 via the action of phosphatases. Phosphorylated Cofilin is usually complexed with the ζ-isoform of 14-3-3, which restricts the accessibility of these phosphatases to Cofilin, regulating their activation (Gohla and Bokoch, 2002). However, in general, the localised dephosphorylation of Cofilin and its subsequent activation is regulated by two families of unrelated phosphatases: the Slingshot Homolog (SSH) phosphatases and the pyridoxal-5-phosphate phosphatases (PDXP) or also known as chronophin (CIN) (Niwa et al., 2002; Gohla et al., 2005).

SSH was initially identified through the study of drosophila while screening for mutations that affect the morphology of the wing hairs and bristles. The wing hairs and bristles are cellular protrusions caused by the packing of actin filament bundles, and therefore, mutations in proteins that regulate actin dynamics and assembly lead to malformations in the wing hairs and bristles (Niwa et al., 2002). Drosophila with defects in the SSH gene caused disorganisation of epidermal cell morphogenesis and terminally bifurcated wing hairs and bristles, and therefore, Slingshot received its name (Niwa et al., 2002). Other studies involving the overexpression of Cofilin phosphorylates LIMKs and TESKs resulted in a similar phenotype to those expressed in SSH gene mutant drosophila.

In mammals, three genes encode for Slingshot proteins, termed (SSH1, SSH2 and SSH3), which, in addition to these various isoforms, can be expressed via alternative splicing of the SSH gene products. These include long isoforms of SSH proteins (SSHL1, SSHL2 and SSHL3) (Ohta et al., 2003). Studies

conducted within cultured cells showed that all isoforms of SSH dephosphorylate Cofilin counteract F-actin assembly induced by LIMKs or TESKs. However, SSH1 and SSH2 are much more efficient than SSH3 at dephosphorylating Cofilin; this was also confirmed in studies in cell-free assays (Niwa et al., 2002; Ohta et al., 2003). The observations on studies of SSH lead to the conclusion that they are primarily Cofilin phosphatases responsible for the dephosphorylation of p-Cofilin and reactivation of Cofilin, within cellular systems. Although all three SSH proteins have this Cofilin phosphatase activity, their distribution, localisation and expression differ within cell types and tissues, eluding to the fact that although they perform similar functions, they may also have distinct biological functions within the cellular and developmental context that has yet to be alluded too (Niwa et al., 2002; Ohta et al., 2003) (Figure 4.3).

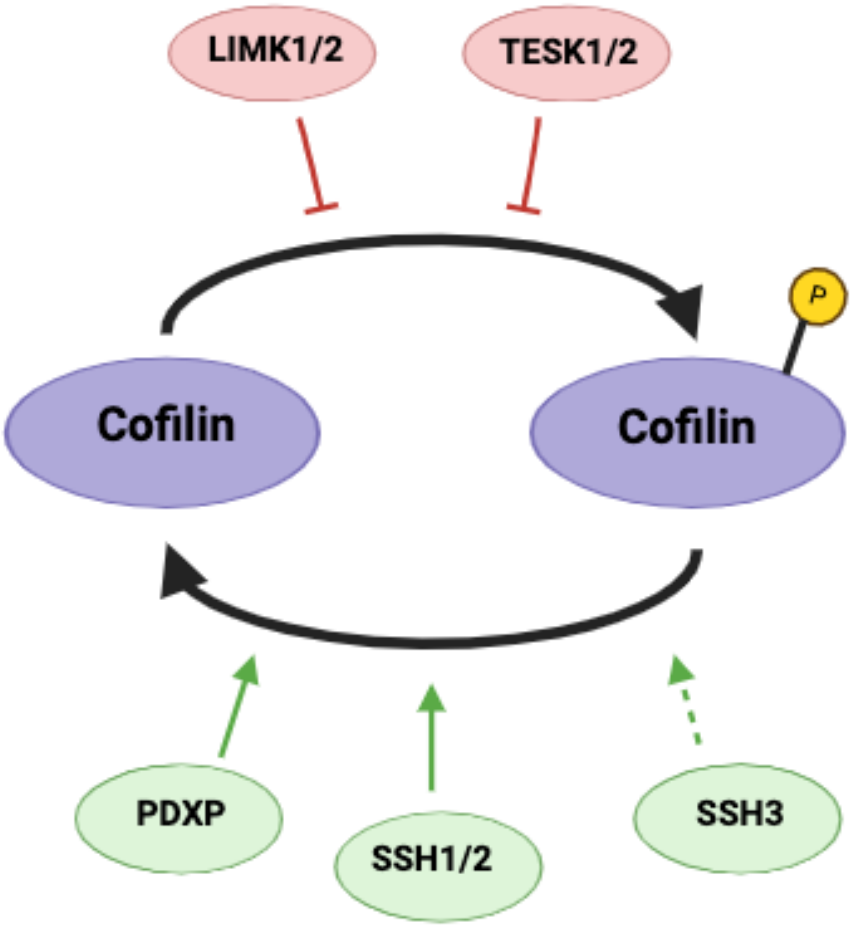

Figure 4.3 Phospho-regulation of Cofilin activity. Figure shows the main mechanisms of Cofilin activation and inhibition via phosphorylation (inhibition) and dephosphorylation (activation). LIMK1 and LIMK2 are the main proteins, which phosphorylate Cofilin into p-Cofilin resulting in the inhibition of Cofilins actin severing activity. Two additional proteins, which phosphorylate Cofilin at Ser3, are TESK1 and TESK2. In addition, phosphatases dephosphorylate p-Cofilin into active Cofilin, the main phosphatases responsible for this are SSH1 and SSH2. In addition, PDXP is known as an additional phosphatase that activates Cofilin via phosphatase activity. Also shown is SSH3 which is known to activate Cofilin but with a lot lesser affinity the SSH1/2 and PDXP and is shown as a dashed line.

The structure of the three SSH proteins has been characterised, and they have been shown to contain a phosphatase domain (P) with the active site sequence motif (HCxxGxxR) similar to those found in dual specificity phosphatases (DSP) (Niwa et al., 2002; Patterson et al., 2009). This was shown through the crystal structure of SSH2, which showed that the P domain adopts a folded structure similar to that of the vaccinia virus VH1-related phosphatase (VHR), a known DSP phosphatase (Jung et al., 2007). In addition, SSH proteins also contain two conserved N-terminal non-catalytic domains termed (A and B). Studies of SSH one showed that the B and P domains are essential for SSH Cofilin phosphatase activity (Kurita et al., 2008). Despite high conservation of the N-terminal (A and B) domains and P-domains, the C-terminal regions of the three SSH proteins are not similar at all, except for a short serine-rich domain (S), which is conserved between SSH1 and SSH2 but absent in SSH3 (Figure 4.4A) (Ohta et al., 2003).

SSHs Cofilin phosphatase activity is regulated by its association with other proteins and phosphorylation. One of the main regulators of SSH phosphatase activity is F-actin itself; SSH binding to F-actin results in massive activation of SSH Cofilin phosphatase activity. SSH1, bound to and colocalised with F-actin, shows a massive increase in Cofilin phosphatase activity (1200-fold increase) compared with unbound SSH1 (Nagata-Ohashi et al., 2004; Kurita et al., 2008). It has been shown that the amino acid residue Trp-458 is essential for F-actin-induced activation of SSH1 and the A domain in the N-terminal region of the protein (Nishita et al., 2005). Once bound to F-actin, SSH undergoes a conformational change, allowing for the exposure of SSH (B and P domains mentioned above), enhancing its phosphatase activity by exposing its catalytic site. F-actin, one of the main regulators of SSH activity, could partly explain how cells maintain appropriate pools of F- and G-actin within cells when F-actin accumulates allowing for the colocalisation and binding of SSH to F-actin thus leading to its activation and mass dephosphorylation of Cofilin leading to actin depolymerisation and increases in G-actin monomers maintaining actin

cytoskeleton homeostasis and cell integrity (Figure 4.4B) (Nagata-Ohashi et al., 2004).

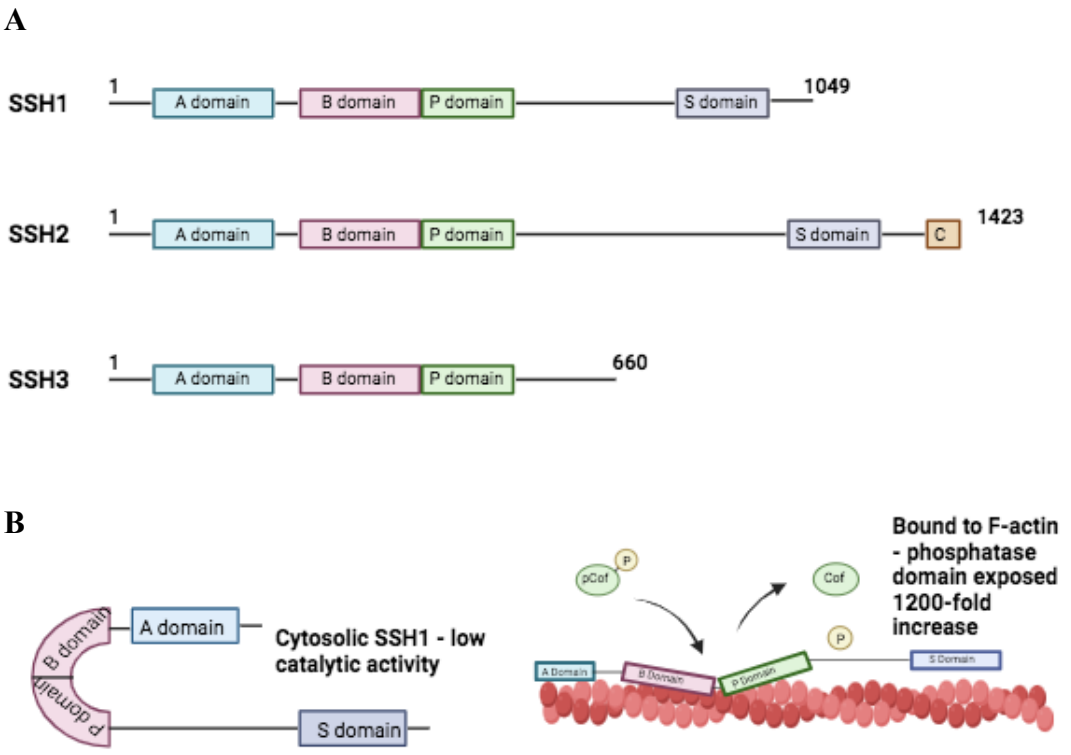

Figure 4.4 Structural differences between SSH family member proteins and phosphatase activity towards Cofilin. A) Shows the differences between the SSH family members (SSH1, SSH2 and SSH3). All three members contain three conserved domains and include and A domain, B domain and phosphatase (P) domain. SSH2 is the longest member at 1432aa, and contains a C domain absent from the rest. SSH1 also contains the S domain present in SSh2 however SSH1 is shorter than SSH2 at 1049aa. SSH3 is structurally different from that of SSH1 and SSH2. It lacks the S domain and is considerably shorter at 660aa. SSH3 has much lower affinity for Cofilin compared to SSH1 and SSH2. B) Left shows the basic structure of cytosolic SSH1, its conformation results in obstruction of the P domain resulting in a significantly reduced phosphatase activity towards Cofilin. Right shows SSH1 when bound to F-actin, this results in a conformational change resulting in the exposure of the P domain and a >1200-fold increase in phosphatase activity towards Cofilin.

In addition to regulating the activity of Cofilin via binding and restricting access, the 14-3-3- proteins have also been identified as binding to SSH proteins through biochemical and yeast hybridisation experiments, for 14-3-3 to bind to SSH1, phosphorylation of Ser937 and Ser978 is required within the S-domain of the C-terminal tail (Nagata-Ohashi et al., 2004). As the F-actin binding site is located within the C-terminal tail of SSH1 located at residues 973-975 (Leu-Lys-Arg motif) close to Ser978, it is believed that phosphorylation and subsequent binding of 14-3-3 to SSH1 sterically inhibits binding of SSH1 to F-actin therefore preventing the activation of SSH and subsequent dephosphorylation of p-Cofilin (Nagata-Ohashi et al., 2004; Yamamoto et al., 2006). Studies conducted in breast cancer cells which were stimulated with neuregulin (a protein which induces dephosphorylation of Ser978 on SSH1) resulted in the translocation of SSH1, which was sequestered in the cytoplasm to lamellipodium and dephosphorylation of Cofilin, this was in contrast to forced overexpression of 14-3-3, which inhibited SSH1 dephosphorylation preventing its translocation to lamellipodia and Cofilin dephosphorylation. The regulation of SSH1 activity via binding of 14-3-3 and sequestering within the cytoplasm depends on the phosphorylation of SSH1 at ser937 and ser978 proteins, which phosphorylate SSH1 at these residues (Nagata-Ohashi et al., 2004).

The protein kinase D (PKD) proteins have been identified as the kinases responsible for the phosphorylation of SSH at ser978 (Eiseler et al., 2009; Peterburs et al., 2009). Three isoforms of PKD (PKD1, PKD2 and PKD3) both directly interact with F-actin and have been shown to inhibit cell migration. They are activated downstream of RhoA activation and phosphorylate SSH at ser978, resulting in its dissociation from F-actin, binding to 14-3-3 and sequestration within the cytoplasm, preventing its phosphatase activity to Cofilin (Peterburs et al., 2009; Spratley et al., 2011). Studies confirming the role of PKD in phosphorylating SSH1 were conducted in breast cancer cells in which depletion of PKD2 resulted in increased invasive cell migration via increasing the activity of SSH1 and subsequent Cofilin dephosphorylation

(Peterburs et al., 2009). Furthermore, PKDs' role in regulating Cofilin activity has been shown via their ability to phosphorylate p21-activated kinase-4 (PAK4), which leads to PAK4 phosphorylating LIMKs (Spratley et al., 2011). Therefore, PKDs play a dual role in regulating Cofilin activity via inhibiting Cofilin activators SSHs and activating Cofilin inhibitors LIMKs. However, SSH has a limited number of substrates, with Ser3 of Cofilin being its main target, but it has also been shown to have phosphatase activity toward pT508 of LIMK1, deactivating it (Soosairajah et al., 2005). This, in turn, means that SSH can not only activate Cofilin but also deactivate the negative regulator of Cofilin activity LIMK1, showing a more complex interplay in the regulation of Cofilin activity and actin dynamics (Figure 4.5).

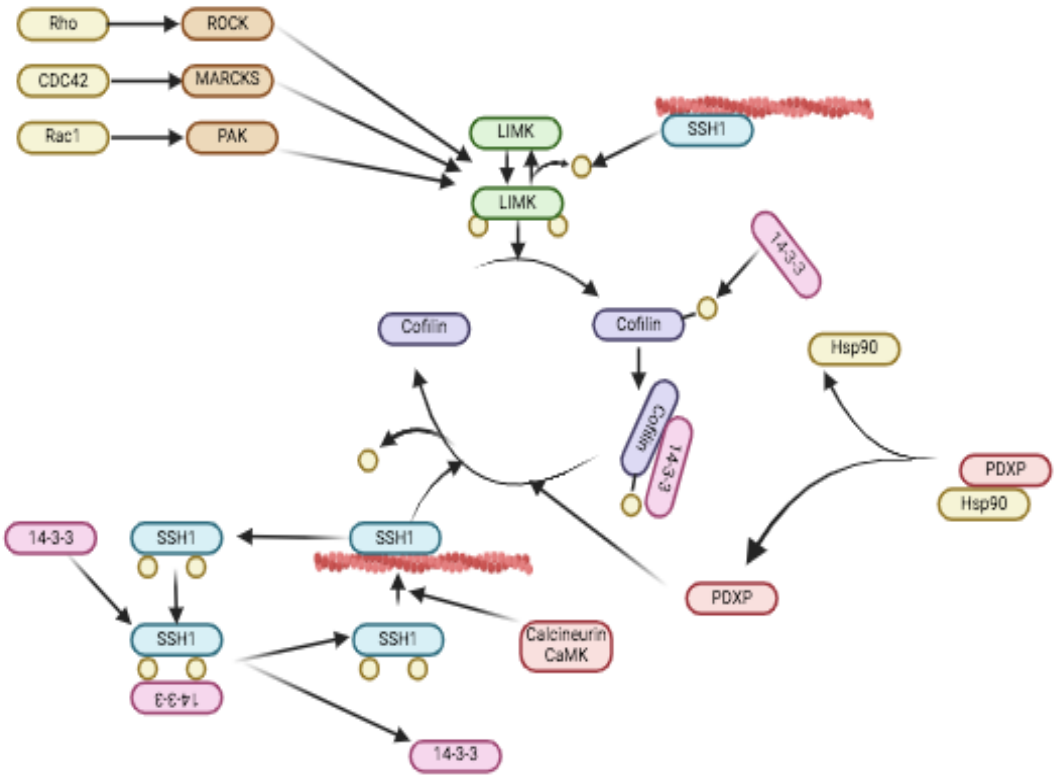

Figure 4.5 The major protein pathways in the phospho-regulation of Cofilin activity. The upstream activation of (ROCK, MARCKS and PAKs) via Rho, CDC42 and Rac1 leads to the cessation of autoinhibition of PAKs and the subsequent self-phosphorylation and subsequent phosphorylation of LIMK1/2 (at T508 and T505). PKD phosphorylates SSHL1 at two positions on its C-terminal tail including the site S978 which enhances the binding of 14-3-3 which enhances the inhibition of dephosphorylation and prevents its binding to F-actin. The removal of 14-3-3 from SSHL1 is achieved via the actions of (peroxide or ROS) via oxidation. SSHL1 is dephosphorylated by calcineurin/CaMK, which allows for its binding to F-actin and subsequent dephosphorylation and activation of Cofilin. In addition, SSHL1 also serves to dephosphorylate LIMK1 at T508 providing another level of Cofilin activation. In addition, PDXP is mainly held in an inactive state via its binding with Hsp90, detachment of PDXP from Hsp90 results in its activation allowing it to perform its Cofilin phosphatase activity.

4.1.4 The importance of Cofilins in normal development and maintaining cell and tissue integrity

The importance of ADF/Cofilin proteins has been confirmed through studies of animal models; in addition, the non-redundant roles they play have also been confirmed due to the other's inability to salvage the role of the other during loss of function or deletion. The deletion of CFL1 in mice is shown to be embryonic lethal due, in particular, to defects in neural crest cells, with proliferation, migration and polarization (Gurniak et al., 2005; Bellenchi et al., 2007). CFL1 and ADF are more widely expressed in many tissue types, and the expression of ADF could not compensate for the loss of CFL1, resulting in lethality in utero.

Studies were performed on ADF's function, in which mutations led to non-functional proteins or the protein being fully deleted. In mice, ADF is the prominent Cofilin family member expressed in the cornea of mice, which led to the development of corneal disease in mice. The resultant phenotype was aberrant actin cytoskeleton rearrangements, cellular hyperproliferation and eventual blindness in the mice (Ikeda et al., 2003; Bellenchi et al., 2007; Verdoni et al., 2008).

Due to the lethal phenotype present when CFL1 is knocked out in mice, studies were performed in adult mice in which CFL1 was knocked out in the epithelial cells of the skin. The studies involved either a single deletion of ADF or CFL1 or a double deletion of both. Deletion of either or both leads to disrupted actin structure, cell shape, perturbed morphogenic branching and cell motility. However, it was observed that in double deletion, a more severe phenotype was observed with hyperproliferation, marked accumulation of F-actin, loss of cell-to-cell contacts, extensive epidermal thickening and loss of tissue homeostasis. This also led to the observation of a degree of functional redundancy in the ADF/Cofilin family due to the more severe phenotype observed during double deletion of ADF and CFL1 as opposed to single knockouts (Kanellos et al., 2015).

4.1.5 Cofilin-2

While CFL1 and ADF are widely distributed throughout many tissues and cell types, the other member of the Cofilin family, Cofilin-2 (CFL2), is more generally accepted to be most prominent within muscle tissue cells. Studies conducted in mice in which CFL2 was knocked out caused lethality in mice pups eight days after birth, primarily due to aberrant actin accumulation within myofibrils and severe deficiencies in muscle development and function (Agrawal et al., 2012). In addition, mutations in CFL2 have been identified in humans, resulting in developmental myopathies. In particular, a condition known as Nemaline myopathy (NM) is a congenital condition characterised by the presence of nemaline bodies in affected myofibers. In particular, the CFL2 mutation was identified in siblings diagnosed with non-specific NM, i.e. in that specific classic mutations of the disease hadn't been identified (Agrawal et al., 2007; Ockeloen et al., 2012). However, through screening, both siblings were found to have a homozygous missense mutation within the CFL2 gene. Both of the patients presented with delayed developmental motor milestones, hypotonia and, in later development, frequent falling and an inability to run. Both siblings showed classical NM on muscle biopsy; however, the distribution of muscle weakness was distinct from that of classical NM; the identification of missense CFL2 mutations marked the first time that Cofilin-2 was a cause of NM (Agrawal et al., 2007).

As previously mentioned, Cofilin-2 is one of three members of the ADF/Cofilin family and is a small ~18KDa protein encoded by the CFL2 gene located on chromosome 14q12 in humans (Bamburg, 1999). Originally, its expression was believed to be restricted to skeletal and cardiac muscle, which helped coin the terms muscle-cofilin (CFL2) and non-muscle-cofilin (CFL1). However, expression of Cofilin-2 has now been detected in a wide variety of tissues, including the liver, lung, brain, kidney, testis and pancreas, which brings into question what role Cofilin-2 plays in tissues of non-muscle origin (Thirion et al., 2001). The structure of Cofilin-2 consists of five α-helices, five β-sheets and a short C-terminal tail; the gene contains four exons with four alternative

transcripts, which is the result of the alternative use of 5’ and 3’ untranslated regions (UTRs) (Figure 4.6) (Sun et al., 2019).

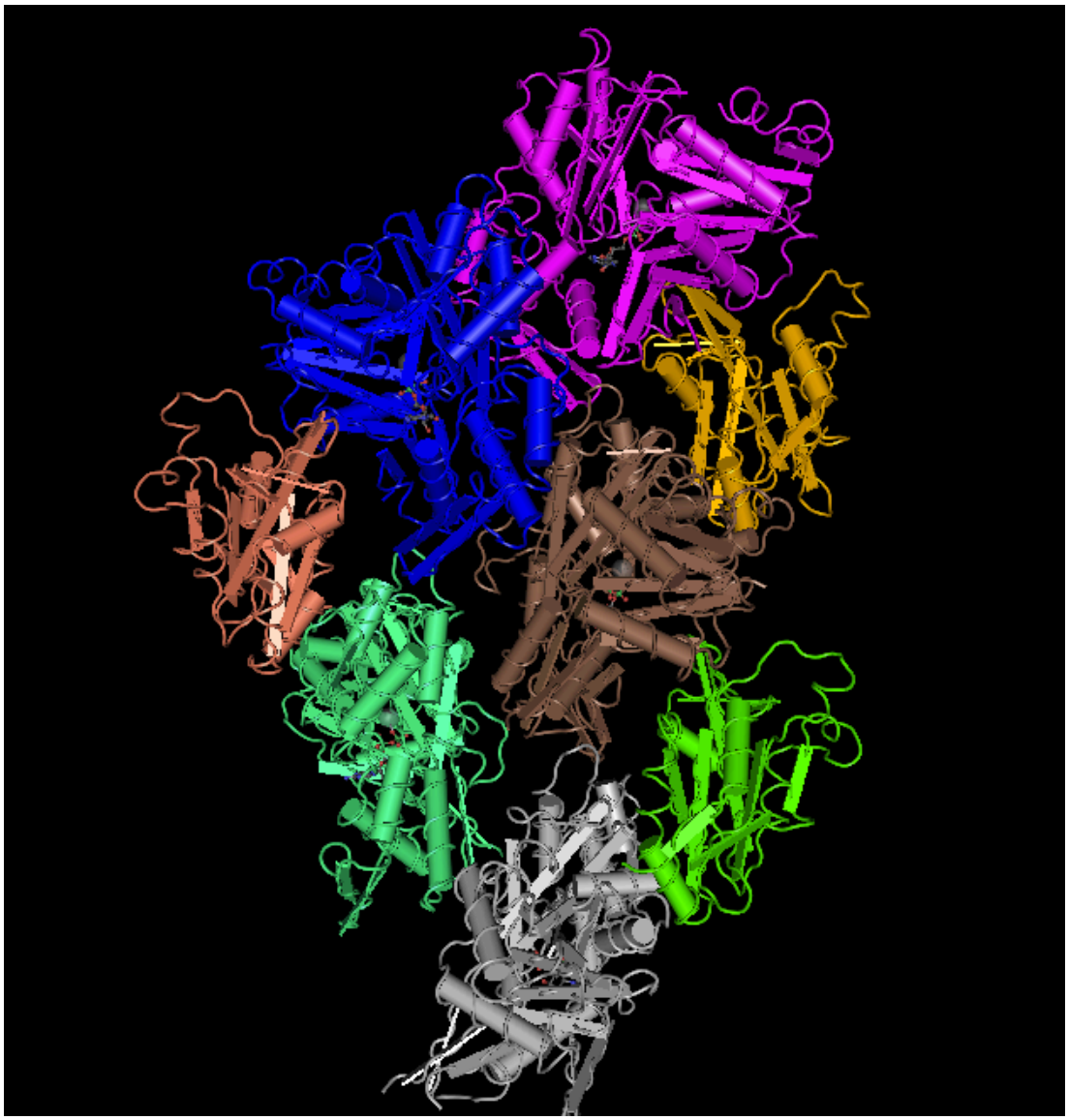

Figure 4.6 Structure of Cofilin-2. Figure was generated using the program Cn3D shows the protein structure of human Cofilin-2 (orange/brown, bright green and gold) bound to F-actin. G-actin monomers (n=5) bound together to form F-actin. Cofilin-2 is made up of five α-helices, five β-sheets and a short C-terminal tail.

In comparison, mouse CFL2 has four exons but only two transcripts, a short 1.8kb and a long 3kb transcript. The presence of the 1.8kb transcript appears in the skeletal muscles, reaching a peak at birth and gradually reduces after that with still some detectable levels at day 13; however, as the 1.8kb transcript reduces, the 3kb transcript increases in the skeletal and cardiac muscles reaching a peak and being the prominent transcript isoform in mice into adulthood (Mohri et al., 2000). In contrast, humans display both CFL1 and CFL2 in skeletal and cardiac muscle during embryonic development; when the muscles develop, CFL1 expression decreases while CFL2 expression increases, becoming the predominant isoform expressed within cardiac and skeletal muscles.

To add further complexity to Cofilin-2 compared to Cofilin-1, two splice variants of Cofilin-2 have been identified in humans; these arise from splicing using either exons 1a or 1b on the gene product (Gillett et al., 1996; Zhu et al., 2018). This leads to the expression of two Cofilin-2 isoforms, Cofilin-2a and Cofilin-2b, expression of these two isoforms differs; cofilin-2a is expressed and found in various cell types and tissues, whereas Cofilin-2b is the predominant isoform expressed mainly in mature skeletal muscle (Thirion et al., 2001). This, in turn, explains the paradigm that Cofilin-2 is a muscle-specific protein. However, more and more literature is emerging describing its presence in various cell and tissue types, making the distinction originally assumed no longer valid as our understanding increases (Xue and Robinson, 2013; Shishkin et al., 2017).

4.2 Hypothesis and Aims

Given that there is a variety of cell model systems to study downstream signalling of PAR4, including overexpression systems, stable expression systems and physiological expression systems. It was hypothesised that the physiological PAR4 expressing MEG-01 cell line would be the most appropriate cell model to study downstream effects of PAR4 activation.

This chapter aims to:

- Characterise the HEK293 transient transfected PAR4 overexpression cell model
- Characterise the human keratinocyte cell model 10h9 stably expressing untagged wild-type PAR4
- Characterise and validate the physiological PAR4 expressing cell model MEG-01

4.3 MEG-01 cells as a potential cell line for in vitro PAR4 investigations

Given that PAR4 is an important receptor abundantly expressed on platelets, a rational assumption is that the cells that produce them megakaryocytes express physiologically relevant levels of PAR4 as expressed on platelets. One such cell line which is well established is MEG-01 cells, originally generated from a patient with CML who has reached blast crisis. These cells display many properties of normal megakaryocytes (vWF, PPO and GPIIb-IIIa) as well as being able to differentiate into more mature megakaryocytes with the treatment of PMA enhancing expression of megakaryocyte markers (fibrinogen, beta-thromboglobulin and fibrinogen) (Ogura M et al., 1985). In addition, what makes these cells a particularly interesting model for the study of PAR4 is that they spontaneously produce platelet-like particles, indicating a functionally intact biosynthetic pathway and, therefore, the expression of physiologically relevant PAR4 expression.

4.3.1 Treating MEG-01cells with Phorbol-13-myrisate acetate (PMA) to induce differentiation

Although a useful model for studying physiological downstream signalling of PAR4 in MEG-01 cells, they are blast-stage cells. They could, in theory, lack the protein manufacturing and functionality required to produce functional platelets. Therefore, we aimed at inducing the differentiation of MEG-01 cells by treating them with PMA.

MEG-01 cells were treated with two different concentrations of PMA to induce differentiation (10 nM and 25 nM), with DMSO as a control. MEG-01 cells were imaged using brightfield microscopy to image for signs of differentiation. Images were taken 48 hours and 72 hours post-treatment (Figure 4.7A). The top images show MEG-01 cells treated with DMSO control (48hrs, left) and (72hrs, right). The DMSO-treated cells showed no signs of differentiation and some signs of cellular stress, with signs of cellular content extruded but no major signs of toxicity. The (top, middle) images show MEG-01 cells treated with 10 nM PMA (48hrs, left) and (72hrs, right). Treating MEG-01 cells with 10 nM PMA shows signs of cellular differentiation, as MEG-01 cells show signs of ploidy (blue arrow on the right image). The (bottom, middle) images show MEG-01 cells treated with 25 nM PMA (48hrs, left) and (72hrs, right). Treating MEG-01 cells with 25 nM PMA shows signs of cellular differentiation, as MEG-01 cells show signs of ploidy, dense granule formation and the production of proplatelet extensions. The images (bottom) show MEG-01 cells treated with 25 nM PMA shown at x40 magnification. The left image shows a mature MEG (oval shaped) with a proplatelet extension (black arrow), and the right image shows a MEG-01 cell beginning to show the formation of dense granules (dark/black circles within the cell) shown by the (yellow arrow). The images shown are representative of three independent replicates (n=3).

The experiment shows that treatment of MEG-01 cells does induce visual signs of differentiation at both treatment concentrations (10 nM and 25 nM). However, treatment with 25 nM showed more obvious signs of differentiation

and was, therefore, the more appropriate treatment concentration for any further experiments.

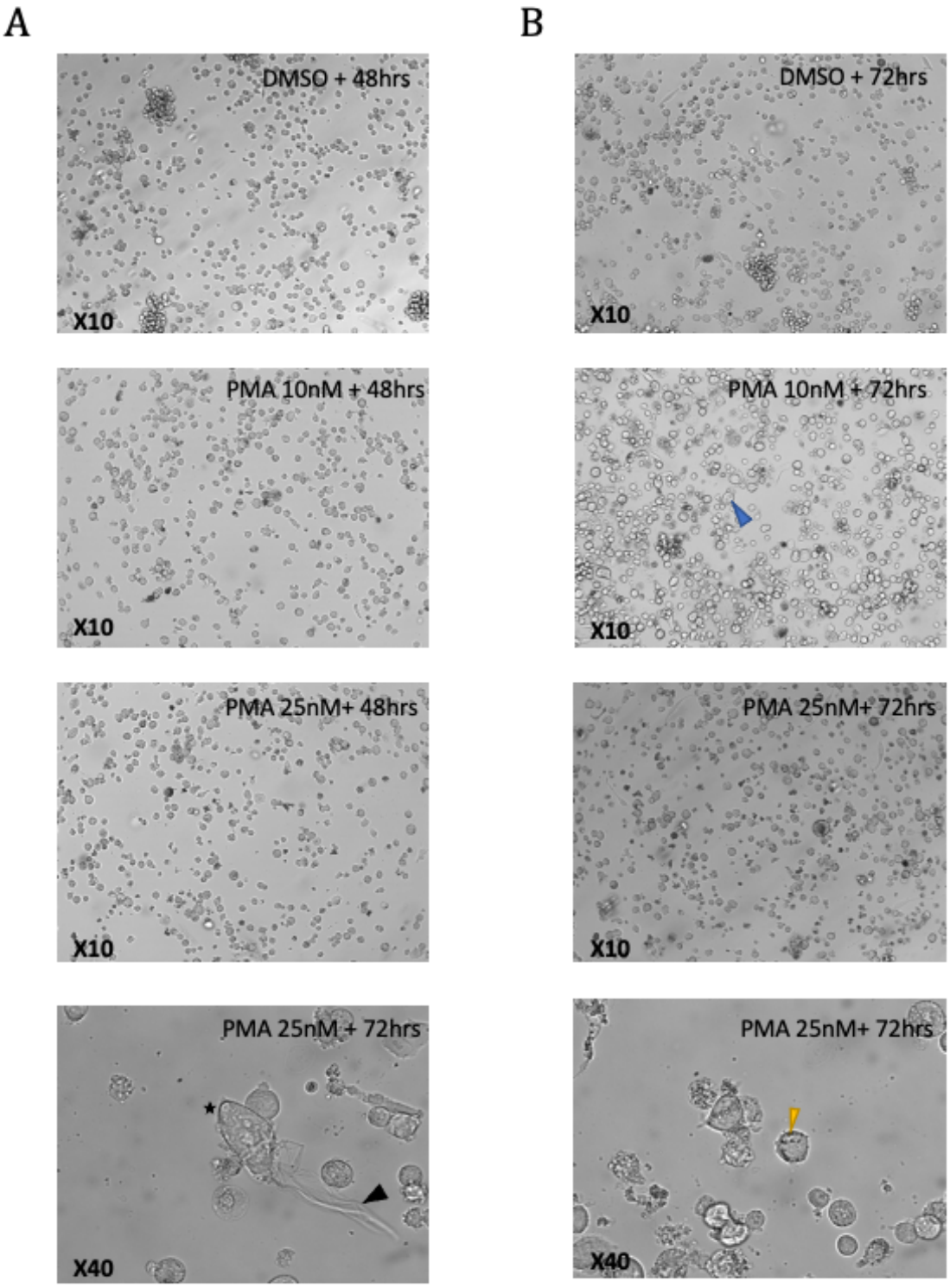

Figure 4.7 Differentiating MEG-01 cells into mature megakaryocytes using phorbol 12-myristate 13-acetate (PMA). A) shows brightfield images of MEG01 cells plated in DMSO control (top) at 48 hours (left) and 72 hours (right), 10 nM PMA (middle, top) or 25 nM (middle, bottom). Blue arrow indicates MEG cell undergoing ploidy. Images are shown at X10 magnification and are representative of (n=5) independent replicates. B) shows images at X40 magnification black star indicates a mature megakaryocyte with a much larger oval appearance. Black arrow indicates proplatelet extensions protruding from the megakaryocyte body (left image). Image on the right shows the presence of dense granule formation (yellow arrow).

4.3.2 Treatment of MEG-01 cells with Phorbol-13-myrisate acetate (PMA) induces cellular differentiation and the production of functional platelet like particles (PLPs)

Since MEG-01 cells are still at a stage of immaturity they do not produce platelet-like particles (PLPs) that mature megakaryocytes would. Therefore inducing the differentiation of MEG-01 cells with PMA to determine if they would produce functional PLPs would determine if MEG-01 cells retain the capacity to achieve full functionality of mature megakaryocytes.

MEG-01 cells were treated with 30 nM PMA for 72 hours to allow appropriate differentiation time. They were then prepared for IF imaging to visualise if treatment had led to the differentiation into more mature megakaryocytes.

Representative images of MEG-01 cells treated with PMA are shown in (Figure 4.8A). From the left, the image shows a maturing MEG, which has moved from a small spherical shape to a more oval/amoeboid shape and increased in diameter (>30 μm). The middle shows an MEG undergoing ploidy with multiple nuclei within a single cell. Left shows an image of a fully matured megakaryocyte, shown by the mass of nuclear content within the cell and its diameter (>70 μm)—scale bars 30 μm.

In addition, the maturing MEGs produce functional PLPs when treated with PMA; representative images of PLPs are shown in (Figure 4.8B) From left shows PLPs adhered to glass slides, indications of functionality are shown due to their adherence as well as the extension of lamellipodia and filopodia that allow them to spread on the glass. Scale bar (5 μm) The right image shows a PLP that has adhered to glass slides, showing the extensions of lamellipodia/filopodia, which has allowed it to adhere and spread. In addition, confirmation of PLP is due to the lack of nuclear content and small diameter—scale bar (2uM).

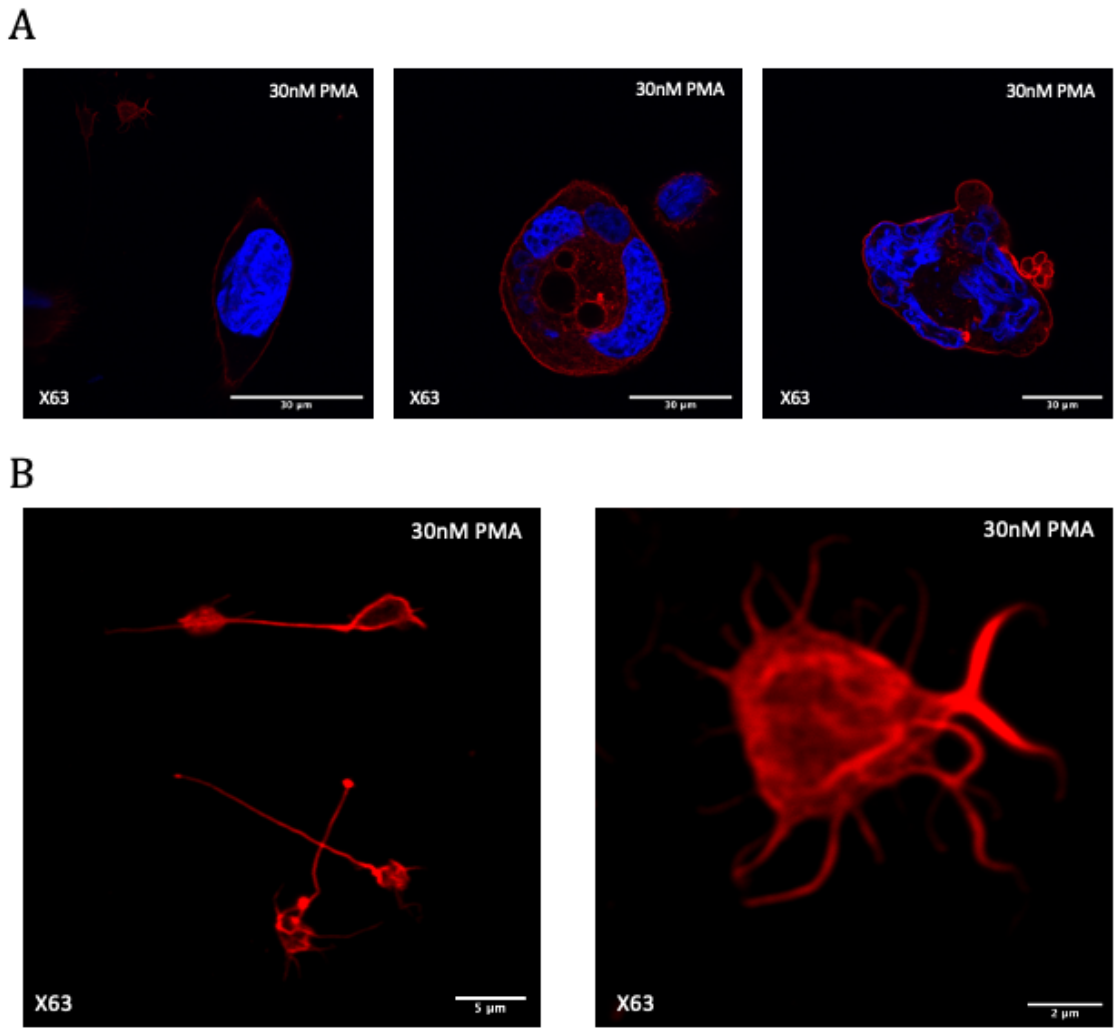

Figure 4.8 Treatment of MEG-01 cells with PMA induces differentiation and production of functional platelet like particles. A) shows representative images of mature megakaryocytes following treatment with 30 nM PMA for 72 hour. Differentiation is showing by the presence of polyploidization and increases in cell size. Top right image show a fully matured megakaryocyte, shown by the presence of extensive polyploidization with mass nuclear content shown as well as increase in cell size (>70µm). DAPI was used as a nuclear stain (Blue) and Rhodamine Phalloidin (red) was used to stain F-actin. B) shows representative images of platelet like particles produced by PMA treated MEG-01 cells. Size of (<5µm) and lack of nuclear content confirmed platelet like particles. PLP is shown by their adherence to slide and the presence of protrusions as shown (bottom right image). Images were taken at X63 magnification, oil immersion. A) scale bars are 30µm and B) scale bars (bottom left 5µm) and (bottom right 2µm). DAPI was used as a nuclear stain (Blue) and Rhodamine Phalloidin (red) was used to stain F-actin.

4.3.3 Quantifying differentiation in MEG-01 cells following treatment with PMA

The previous experiment showed that treatment of MEG-01 cells with 30 nM of PMA induced signs of differentiation, as shown by the ploidy of nuclear content and the production of functional platelet-like particles. Next, we aim to quantify differentiation to determine if PMA significantly affects differentiation. Therefore MEG-01 cells were treated with 30 nM PMA for 72 hour before being prepared for IF imaging with DAPI used as a nuclear stain (blue) and rhodamine red (actin).

Cells were assessed for signs of nuclear ploidy comparing No treatment (NT) vs 30 nM PMA treated. Representative images are shown in (Figure 4.9A); NT (top, left) shows that most cells contain a single large nucleus with scant cytoplasmic content, which indicates blast-stage MEG cells. The (top, left) image shows a MEG-01 cell treated with 30 nM PMA and shows a ploidy of nuclear content to 4N. The (bottom, left) image shows a MEG-01 cell treated with 30 nM PMA and ploidy of nuclear content of MEGs, one with 2N and one with 4N. The final images (bottom, right) show a MEG-01 cell treated with 30 nM PMA and shows ploidy of nuclear content of 8N. Scale bars show 30 μm.

Assessment of ploidy was carried out by counting the nuclei within MEG-01 cells vs the two treatment groups (NT vs 30 nM PMA); the NT groups were the results of (307cells, 387cells and 369 cells) averaged across three independent replicates (n=3). For the 30 nM PMA treated group ploidy, the average of (188cells, 311cells and 314cells) averaged across three independent replicates (n=3). Data was plotted as shown in (Figure 4.9B), and statistical analysis was carried out using multiple t-tests.
For 1N (NT 91.5% vs PMA 59.93%, $p<0.001$ ***, s), for 2N (NT 6.733% vs PMA 28.77%, $p<0.01$ **, s), for 4N (NT 1.567% vs PMA 8.533%, $p<0.001$ ***, s), for 6N (NT 0.2% vs PMA 1.6%, $p<0.01$ **, s) and for 8N (NT 0% vs PMA 1.167%, $p<0.001$ ***, s). Images were taken at X63 magnification under oil immersion, and data is the result of three independent replicates (n=3).

The data show that PMA was successful in inducing differentiation of MEG-01 cells. Quantification showed that the change in ploidy was significantly different from that of the NT group, confirming that PMA was successful in inducing significant differentiation.

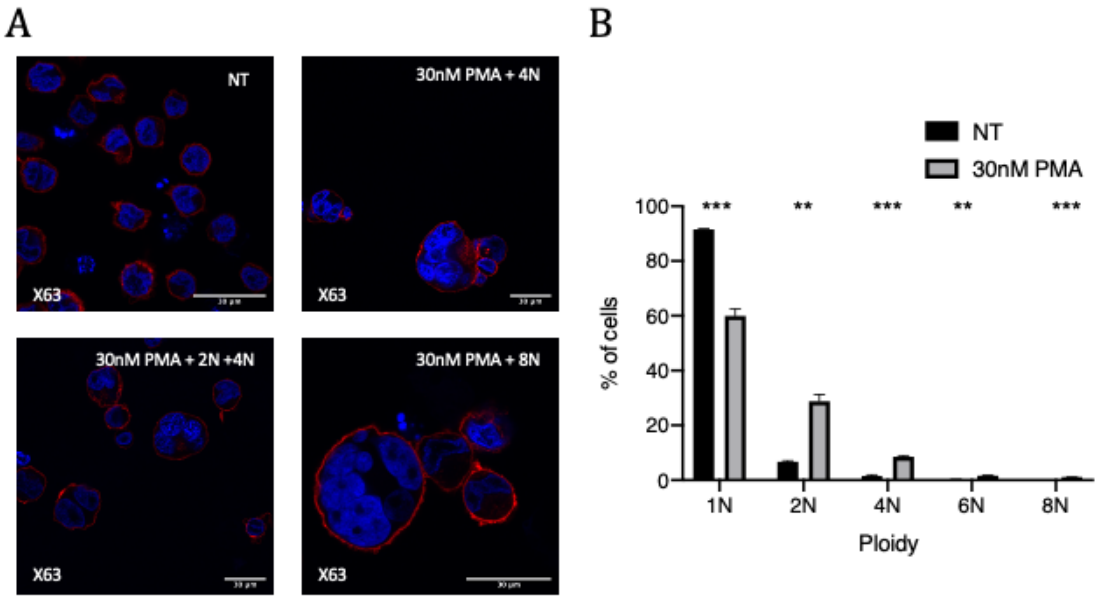

Figure 4.9 Quantifying MEG-01 differentiation using nuclear ploidy following treatment with PMA. A) Shows representative images for the treatment groups. (Top left) shows no treatment (NT) with the majority of cells showing a single nucleus. (Top right) shows an image of MEG01 cells treated with 30 nM PMA with a MEG-01 cells showing ploidy of 4N. (Bottom left) shows an image of MEG01 cells treated with 30 nM PMA with a MEG-01 cells showing ploidy of 2N and 4N. (Bottom right) shows a MEG-01 cell undergoing progressive differentiation when treated with 30 nM PMA showing ploidy of 8N. B) Cells from no treatment (NT) were compared with 30 nM PMA treated MEG-01 cells 72 hour after treatment. The percentage of cells showing ploidy were compared to that of NT using multiple t-test. Images were taken at X63 magnification. Data are mean ±SEM for the average ploidy from three independent replicates (n=3). The level of significance is shown compared with the NT control (* $p<0.05$, ** $p<0.01$, *** $p<0.001$ and ns (not significant).

4.3.4 Bringing Suspension MEG-01 cells down to an adherent phenotype using coating methods

MEG-01 cells exist primarily as a suspension cell line, although they show a propensity to spontaneously adhere to flask or plate bottoms and detach at random. This could be due to the heterogeneous cell population and its ability to begin the stages of differentiation. However, in general, MEG-01 cells exist primarily as a suspension cell line, with >95% existing in this form from observation.

To advance this cell line as a potential screening cell line for small molecule inhibitors of PAR4, adhering the cells to plates would make for a more reproducible method if cells weren't being extruded due to the pipetting action of automated plate readers.

In previous experiments, poly-D-lysine (PDL) was used to increase the adherence of HEK293 cells, which are semi-adherent and have a propensity to easily detach during preparation. PDL was used with relatively good success. In addition, Fibronectin is commonly used as a coating matrix to ensure firm adherence to plastic-coated flasks in cell line work.

The adherence of MEG-01 cells was tested using the two above methods: coating 12-well plates with either PDL or Fibronectin. Figure 4A showed brightfield images at 10X magnification taken at 2 hours and 72 hours when the experiment was terminated. Fibronectin showed almost complete adherence to the bottom by MEG-01 cells at 2 hours Figure 4.10A (top left), and complete adherence was still achieved at 72 hours Figure 4.10A (top right). The use of Fibronectin appears to have halted or slowed the proliferation of MEG-01 cells due to observable cell density appearing roughly the same as when the experiment began.

In contrast, PDL did not result in the adherence of MEG-01 cells to the bottom of the plates at either 2 hours Figure 4.10A (bottom left) or up to 72 hours

(bottom right). In addition, PDL appears to be toxic to MEG-01 cells. This is due to an observable reduction in cell density between the 2-hour and 72-hour images. In addition, at 72 hours, cells appear to look visibly stressed with extrusion of granular content and apoptotic cell debris present within the wells. Images in Figure 4.10A are representative of four independent replicates (n=4).

MEG-01 cells were then compared to their suspension counterparts to see if structural adherence was achieved. Figure 4.10B (left) shows a MEG-01 cell imaged via confocal stained with Rhodamine (Actin) and Dapi (Nucleus), which is in suspension; prominent actin structures aren't present, and only red actin outer layer is present; these cells are primarily spherical with the nucleus being the most notable structure. In contrast, Figure 4.10B (right) shows a confocal image of a MEG-01 cell adhered to fibronectin, with the cells stained with Rhodamine (actin) and DAPI (nucleus). In this image, noticeable structural differences are observed, with a more prominent and obvious actin network, much larger size and flattened appearance compared to the suspension cells (left). F-actin structures are prominent, and observable protrusions confirm firm adherence to cover slips. This shows that fibronectin was a suitable substrate for transforming MEG-01 cells into an adherent cell line.

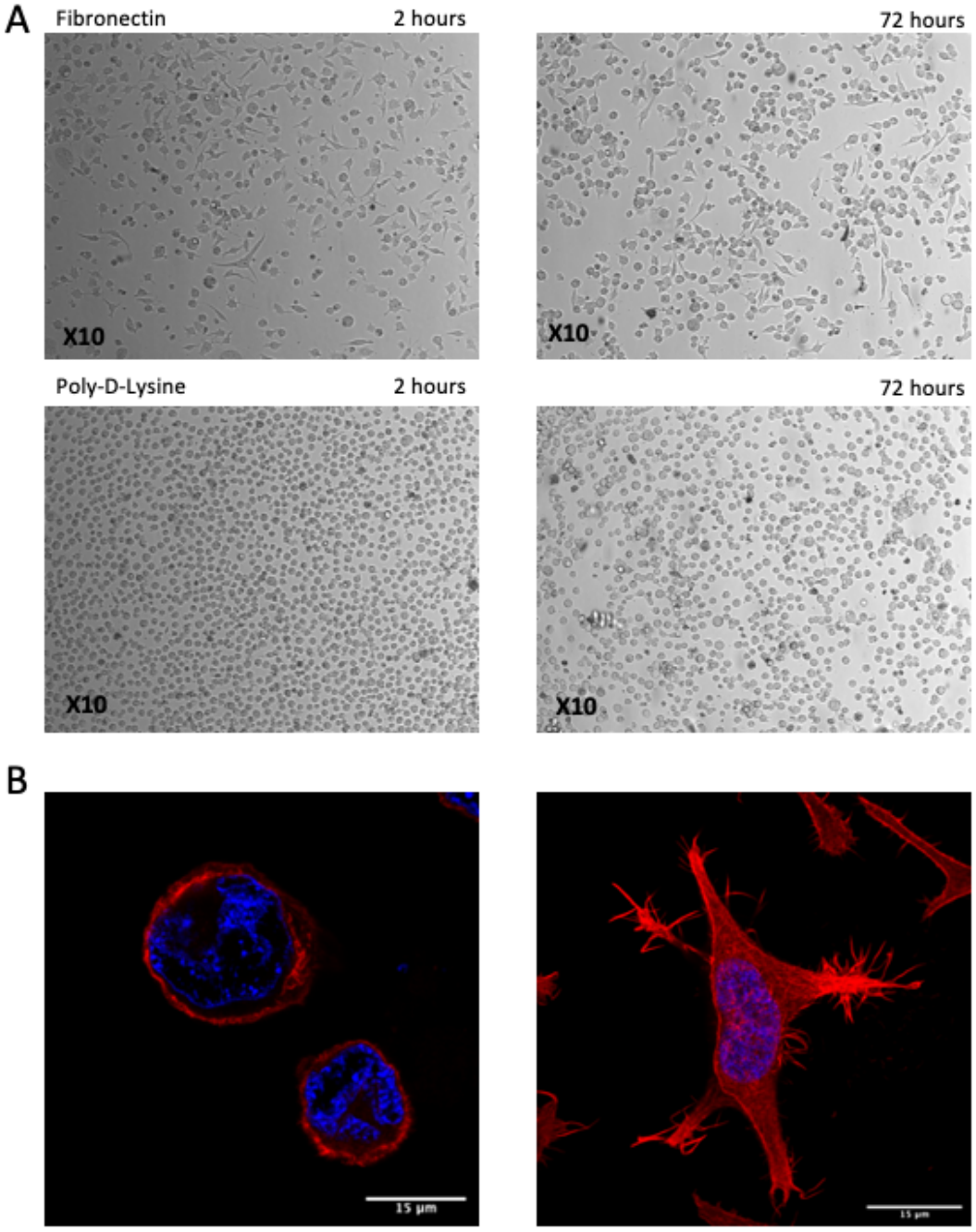

Figure 4.10 Testing coating conditions to bring Meg-01 cells from suspension cells to adherent. cells. A) shows brightfield images of MEG01 cells plated in Fibronectin (top) or Poly-D-lysine (PDL) (bottom) coated wells. Images are shown at X10 magnification and are representative of (n=4) independent replicates. MEG-01 cells show almost complete adherence on fibronectin. B) shows a comparison of MEG-01 cells in suspension (left) compared to adherence on fibronectin (right) imaged using confocal microscopy (x63 oil immersion). The actin cytoskeleton is stained up using rhodamine phalloidin (red) and DAPI for the nucleus (blue).

4.3.5 Validating Cofilin-2 antibody and testing for the presence of Cofilin-2 in MEG-01 cells

Since Cofilin-2 is predominantly cited as specific to muscle tissue, the assumption is that it would not be present in MEG-01 cells because they are not of muscle origin. However, some literature cites that Cofilin-2 exists as two isoforms, depending on the use of either exon (a or b), producing Cofilin-2a and Cofilin-2b. One is restricted to muscle tissue, while the other has been shown to be present in a variety of cell types.

The Cofilin antibody was initially tested in the AC16 cell type, a cell line derived from human cardiomyocytes and, therefore, should contain Cofilin-2. AC-16 cells were imaged using IF at X63 magnification under oil immersion. Representative images are shown in Figure 4.11A. From left to right, there are dye-only images, secondary antibody-only images, and two images of AC16 cells with Cofilin-2. The images show that AC-16 cells contain Cofilin-2 and, therefore, the antibody did indeed detect the target of interest.

MEG-01 cells were also shown to contain Cofilin-2 when prepared and imaged via IF (Figure 4.11B, left), with the (right) showing a region of interest (ROI) showing the presence of Cofilin-2 within MEG-01 cells. It can be seen from the images in (A and B) that MEG-01 cells show less Cofilin-2 than those present in the AC-16 cells.

A final method of validating the Coflin-2 antibody was to perform western blot analysis of differing cell densities of MEG-01 cells (200k, 500k, 1M and 2M) using whole rat heart cell lysate as a positive control. The Figure shows a strong band was in the positive control lane (rat heart), with increasing signal in the MEG-01 cell densities (Figure 4.11C). The 200K cell density showed virtually no signal or was so weak that use in additional experiments would be unquantifiable. The band seen in 500K was present but still weak, with the 1M cell density given the best band signal suitable for quantification. In the 2M cell density lane, a double band pattern formed due to poor running in the gel

caused by such a high protein concentration and was therefore not suitable. These experiments showed the antibody was specific for its target but also showed that MEG-01 cells do express Cofilin-2 at the protein level.

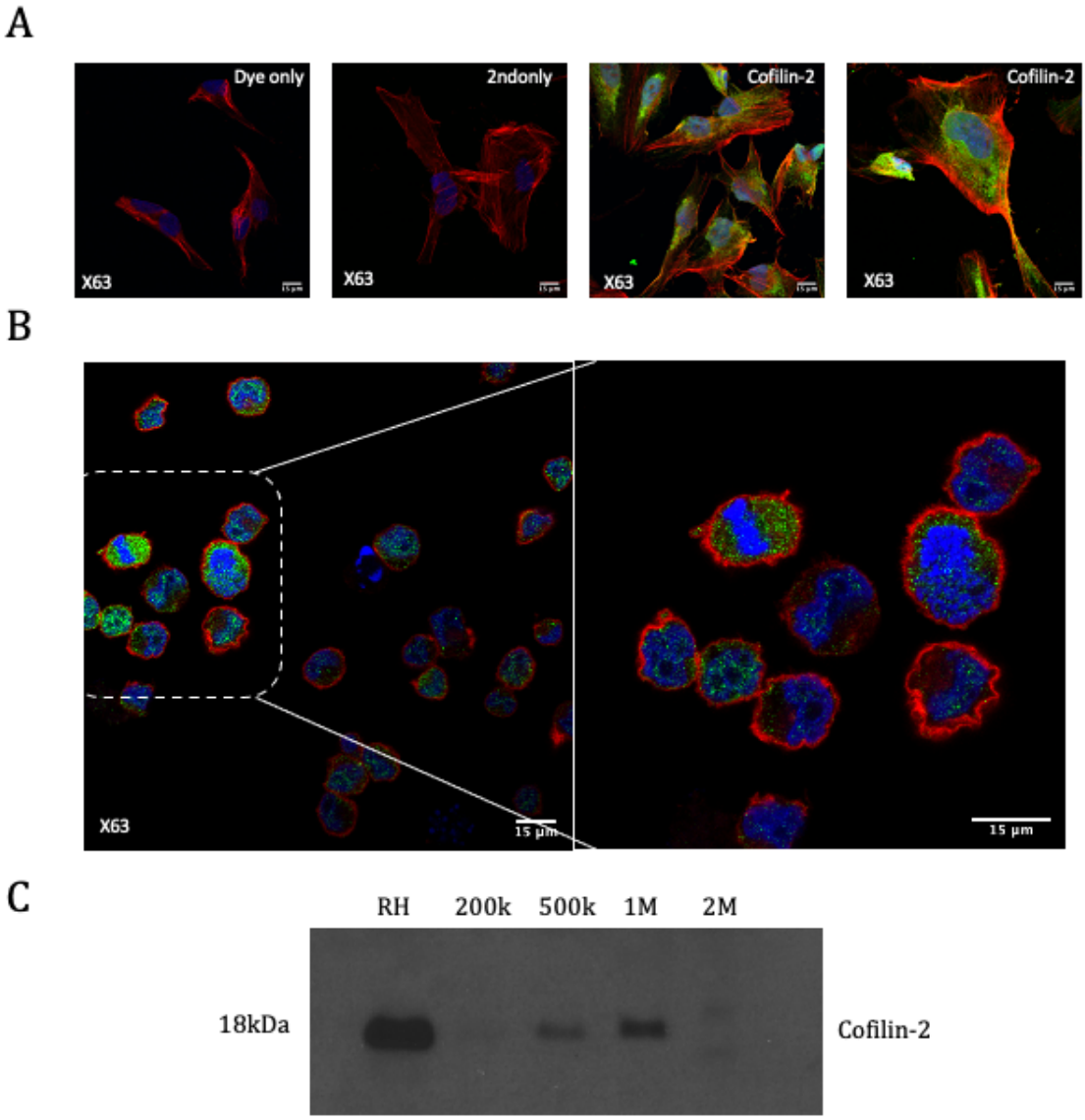

Figure 4.11 Validating Cofilin-2 (CFL2) antibody for use in MEG01 cells. A) shows confocal microscopy imaging of AC16 cardiac cells using (X63 magnification), from left dye only, antibody control, CFL2 labelled AC16 cells. Antibody control shows no non-specific staining indicating green signal is positive CFL2 signal. B) shows MEG-01 cells with positive staining for CFL2 (green) (left) and zoomed in region of interest (ROI) (right) imaged using confocal microscopy (x63 oil immersion). The actin cytoskeleton is stained up using rhodamine phalloidin (red) and DAPI for the nucleus (blue). Scale bars 15 µm. C) Shows western blot for the presence of CFL2 in MEG-01 cells left lane is whole rat heart lysate as a positive control, 200k cells, 500k cells, 1M cells and 2M cells.

4.3.6 Immunofluorescent analysis of pCofilin-2 changes following stimulation of MEG-01 cells with thrombin

Given that MEG-01 cells were shown to express Cofilin-2 at the protein level, we next aimed at quantifying changes in pCofilin-2 expression following stimulation with 1 U/mL and 3 U/mL thrombin using immunofluorescence analysis. Experimental work on Cofilin-1 later in the Chapter showed that pCof-1 levels showed the most significant change in expression levels when stimulated with thrombin at 15 minutes (Figure 4.18). Therefore, the 15-minute timepoint was used when assessing pCofilin-2 levels using immunofluorescence analysis.

MEG-01 cells were stimulated with either 1 U/mL or 3 U/mL of thrombin for 15 minutes before slides were prepared for IF imaging. Representative images are shown in (Figure 4.12A). The top four images (left to right) show MEG-01 cells in which a secondary labelled antibody was added to ensure that the signal detected wasn't due to non-specific binding of the secondary. As can be seen no green signal can be seen, meaning the secondary antibody is specific to its target, and the background signal is, therefore, minimal. The next shows MEG-01 cells treated with both primary and secondary antibodies, which are unstimulated (baseline); the green signal shows the presence of total Cofilin-2. The next image shows an expression of total Cofilin-2 in MEG-01 cells stimulated with 1 U/mL of thrombin, and the final image shows an expression of total Cofilin-2 in MEG-01 cells stimulated with 3 U/mL of thrombin. Generally, the expression of total Cofilin-2 seems relatively unchanged between baseline (BL) and stimulated MEG-01 cells, with perhaps slightly more variation in expression than what was seen in Cofilin-1.

The bottom four images (left to right) show MEG-01 cells in which a secondary labelled antibody was added to ensure the signal detected wasn't due to non-specific binding of the secondary. As can be seen no green signal can be seen, meaning the secondary antibody is specific to its target, and the background signal is, therefore, minimal. The next shows MEG-01 cells treated with both

primary and secondary antibodies, which are unstimulated (baseline); the green signal shows the presence of pCofilin-2. The next image shows an expression of pCofilin-2 in MEG-01 cells stimulated with 1 U/mL of thrombin, and the final image shows an expression of pCofilin-2 in MEG-01 cells stimulated with 3 U/mL of thrombin. The images show that pCofilin-2 expression increases with thrombin stimulation; however, it looks visually similar between the 1 U/mL and 3 U/mL treatment groups. It should be noted that changes in pCofilin-2 don't appear universal in MEG-01 cells, with some showing obvious increases in pCofilin-2 while others express relatively low levels.

Quantification was performed in ImageJ, taking individual cells' mean fluorescence intensity (MFI) across three independent replicates. The number of cells was analysed using grouped analysis. For total Cofilin-2, the number of values (n=160) for secondary only gave an (MFI of 4.288±0.08); for BL total Cofilin-2 the number of values (n=150) which gave an (MFI of 16.24±0.5180), for 1 U/mL of thrombin total Cofilin-2 the number of values (n=140) which gave an (MFI of 13.37±0.2205) and for 3 U/mL of thrombin the number of values (n=198) which gave an (MFI of 19.64±0.5108). Groups were compared using the Mann-Whitney U-test, with the hypothetical mean being the unstimulated (BL) total Cofilin-2 (MFI of 16.24±0.5180). For 1 U/mL (16.24 vs 13.37, $p<0.0001$ ****, s) and 3 U/mL thrombin (16.24 vs 19.64, $p<0.0001$ ****, s) (Figure 4.12B). These results show that thrombin stimulation does appear to alter the expression of total Cofilin-2 in MEG-01 cells, with analysis showing a significant effect.

For phospho-Cofilin, the number of values (n=105) for secondary only gave an (MFI of 3.102±0.02); for BL pCofilin-2 the number of values (n=120), which gave an (MFI of 4.737±0.059), for 1 U/mL of thrombin pCofilin-2 the number of values (n=144) which gave an (MFI of 6.610±0.094) and for 3 U/mL of thrombin the number of values (n=145) which gave an (MFI of 6.566±0.0788). Groups were compared using the Mann-Whitney U-test, with the hypothetical mean

being the unstimulated (BL) pCofilin-2 (MFI of 4.737±0.059). For 1 U/mL (4.737 vs 6.610, p<0.0001 ****, s) and 3 U/mL thrombin (4.737 vs 6.566, p<0.0001 ****, s) (Figure 4.12C). These results show that thrombin stimulation has a significant effect on increasing the phosphorylation of Cofilin-2 and that the concentration of thrombin used does not have an effect on levels of pCofilin-2. It should also be noted from the spread of the data that pCofilin-2 expression is not universal within MEG-01 cells, with some showing increased expression of pCofilin-2 following stimulation. In contrast, others expressed levels similar to baseline.

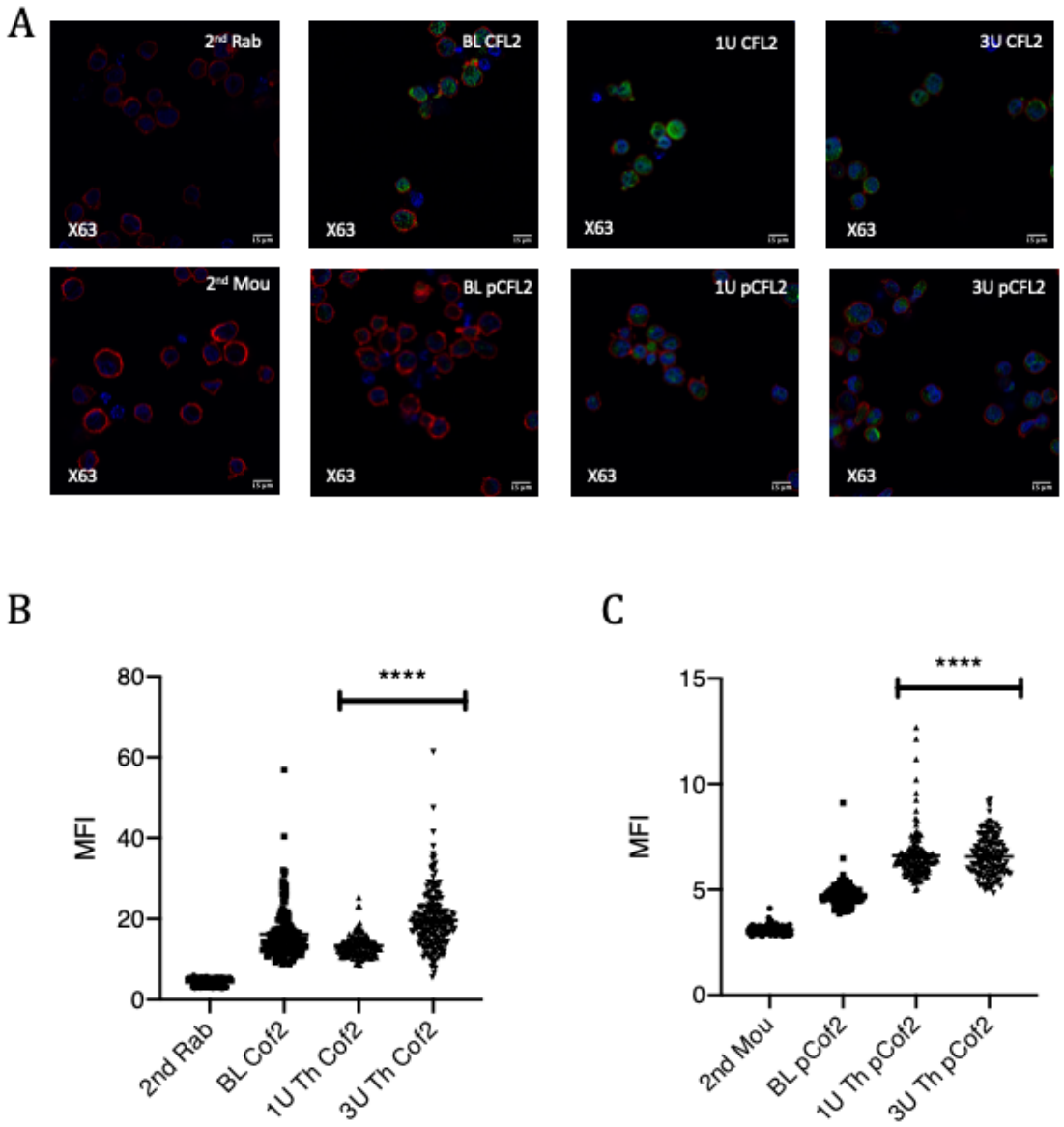

Figure 4.12 Immunofluorescent analysis of Cofilin-2 phosphorylation following stimulation of MEG-01 cells with Thrombin. A) shows confocal microscopy imaging of MEG-01 cells using (X63 magnification), top four images are total cofilin-2 and bottom four images are pcofilin-2. Antibody control shows no non-specific staining indicating green signal is positive for cofilin-2 signal. B) shows total cofilin-2 expression changes upon stimulation with 1 U/mL and 3 U/mL at 15 mins post stimulation. Mean fluorescent intensity was compared to the MFI of BL CFL2 using Mann-Whitney U-test. The assumed theoretical mean used was that of BL CFL2 (16.24). C) shows pcofilin-2 expression changes upon stimulation with 1 U/mL and 3 U/mL at 15 mins post stimulation. Mean fluorescent intensity was compared to the MFI of BL pCof-2 using Mann-Whitney U-test. The assumed theoretical mean used was that of BL pCof-2 (4.737). Data are mean ±SEM for the MFI of three independent replicate (n=3). The statistical significance is shown compared with the BL (unstimulated) signal (**** $p<0.0001$). DAPI was used as a nuclear stain (blue), Rhodamine Phalloidin was used to stain F-actin (red). Green signal shows proteins of interest labelled with AlexaFluor-488, total cofilin-2 (top) and pcofilin-2 (bottom)

4.3.7 Optimizing Phospho-Cofilin and total-Cofilin antibodies in MEG-01 whole cell lysates

Prior to beginning any major experiments with the total-Cofilin and p-Cofilin antibodies, the first aim was to optimise the cell density of MEG01 whole-cell preparations and the antibody concentrations to use in future experiments. Cell densities of MEG-01 cells tested were (10, 50, 100, 200, 300 and 500K) cells. With the antibody concentrations of p-Cofilin (1:5000, 1:10,000 and 1:15,000) and total-Cofilin concentrations of (1:20,000, 1:30,000, 1:40,000, 1:50,000 and 1:100,000).

Figure 4.13A shows MEG-01 cells tested for p-Cof; representative images of western blots are shown (left) with the concentrations (1:5000) at the top, (1:10,000) in the middle, and (1:15,000) at the bottom. Graphs were plotted as a proportion of cell density with raw signal intensity (Top, left). Signal intensity grew until a cell density of 200K cells; signal intensity started to plateau, indicating signal saturation.

Figure 4.13B shows MEG-01 cells tested for total-Cof; representative images of western blots are shown (left) with the concentrations (1:20,000) top, (1:30,000) second top, (1:40,000) middle, (1;50,000) second bottom, and (1:100,000) bottom. Graphs were plotted as a proportion of cell density with raw signal intensity (bottom, left). Signal intensity was shown to grow until a cell density of 200K cells; after that, signal intensity started to plateau, indicating saturation of signal, except for in the case of antibody concentration (1:100,000).

Therefore, from the results obtained, a MEG-01 cell density of 200,000 cells, total-Cofilin concentration of (1:100,000) and p-Cof concentration of (1:10,000) was used for all subsequent Western blot experiments.
To note, the purchase of an additional antibody for p-Cof a concentration of (1:15,000) was used due to what appears to be an increase in antibody strength.

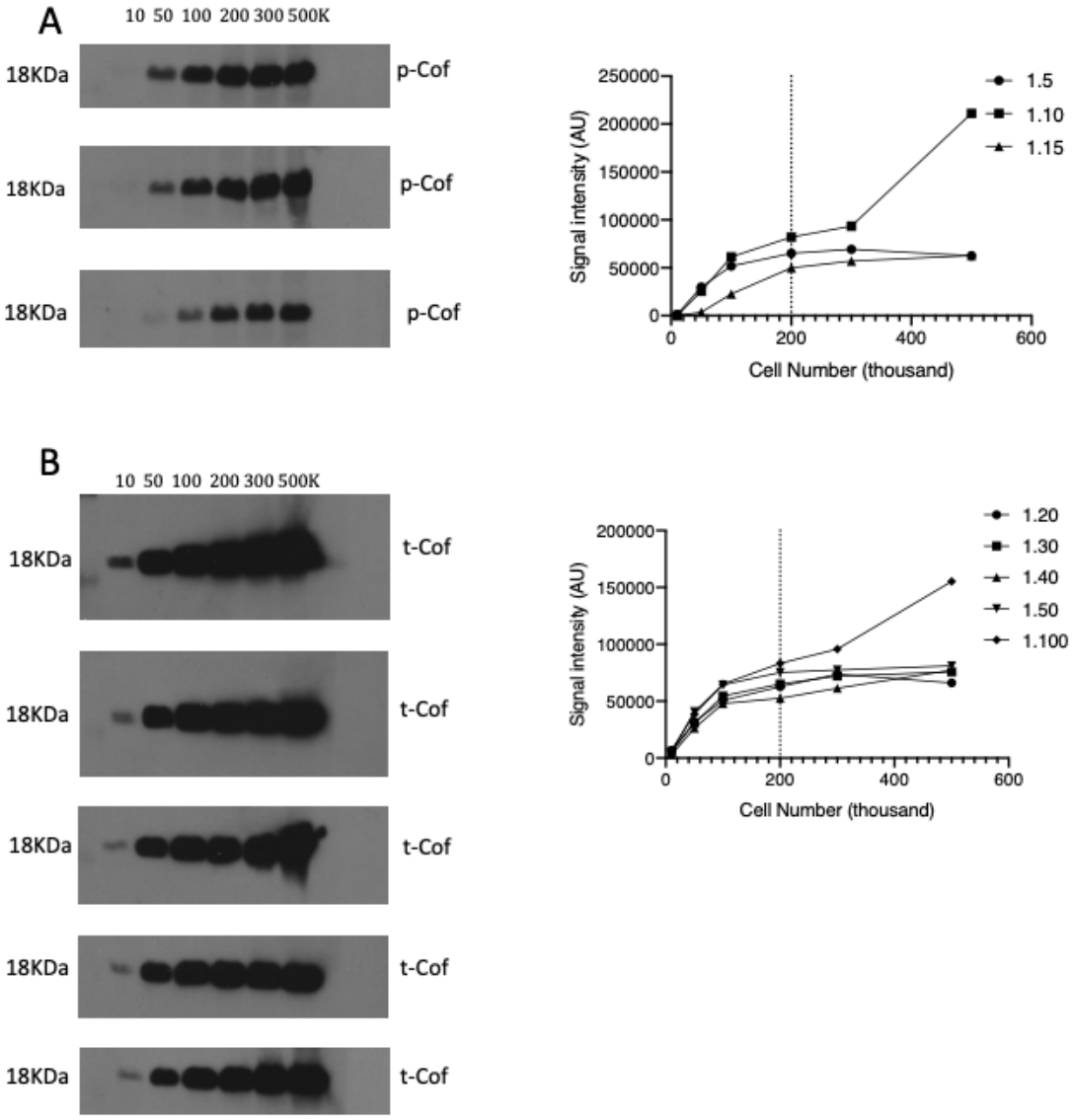

Figure 4.13. Optimisation of total-Cofilin and p-Cofilin antibodies in MEG-01 cells. A) shows western blot results for p-Cofilin in MEG-01 cells at different cell densities (10,000 – 500,000) at various antibody titrations (1:5000 – 1:15000). Signal intensity was plotted and shows plateau after 200,000 cells due to lane saturation. B) shows western blot results for total-Cofilin in MEG-01 cells at different cell densities (10,000 – 500,000) at various antibody titrations (1:20000 – 1:100000. Signal intensity was plotted and shows plateau after 200,000 cells due to lane saturation.

4.3.8 The effect of serum starvation on MEG-01 cells

Traditionally, before stimulation experiments are carried out, Cells are incubated in serum-free media to starve them. This allows for the baseline signal of many proteins to reduce to baseline while also allowing cells to sync up to the same stages of the cell cycle. The theory behind this is that it reduces a variable of reproducibility in experimental results while also allowing for antibody signal to remain at a low enough level to not become easily saturated when, in some instances, the signal increases upon adding a ligand.

As MEG-01 cells were a newly purchased cell line, the effects of serum starvation needed to be established before running any time-course simulation experiments. Therefore, MEG-01 cells were plated in 6-well dishes in either RPMI supplemented with 10%FCS or RPMI with no FCS (serum-free) and imaged over 4 hours. Images were taken at (0, 1, 2 and 4 hours) with a bright field microscope (Figure 4.14A). Serum images are shown along the top, while serum-free images are on the bottom. The images shown are representative of five independent replicates (n=5). The images showed no observable differences between the serum and serum-free groups regarding cell size, granular secretion or signs of visible stress.

In addition, western blots were performed on various markers within the Cofilin pathway (p-Cofilin, total-Cofilin, LIMK2) over the time course under serum-free conditions. The zero (baseline) would give a representative expression of protein levels that would be seen under serum conditions. Figure 4.14B shows representative western blot images of p-Cofilin (top) and total-Cofilin (bottom). Results were plotted as a fold change to baseline (0 hours), and p-Cofilin was normalised against total-Cofilin. For 1 hour (1.035±0.18 fold over control, p=0.6251, ns), 2 hours (1.003±0.32 fold over control, p=0.9815, ns) and 4 hours (1.037±0.28 fold over control, p=0.7448, ns). The experiment was the result of seven independent replicates (n=7).

Figure 4.14C shows the representative western blot images of LIMK2 (top) and alpha-tubulin (bottom). Results were plotted as a fold change to baseline (0 hours), and LIMK2 was normalised against alpha-tubulin. For 1 hour (0.9229±0.16 fold over control, p=0.2476, ns), 2 hours (0.9494±0.15 fold over control, p=0.4020, ns) and 4 hours (1.024±0.17 fold over control, p=0.7404, ns). The experiment resulted from seven independent replicates (n=7) except for 4 hours, which was (n=6) due to damage to the blot film, which obscured the end band, meaning analysis wasn't possible.

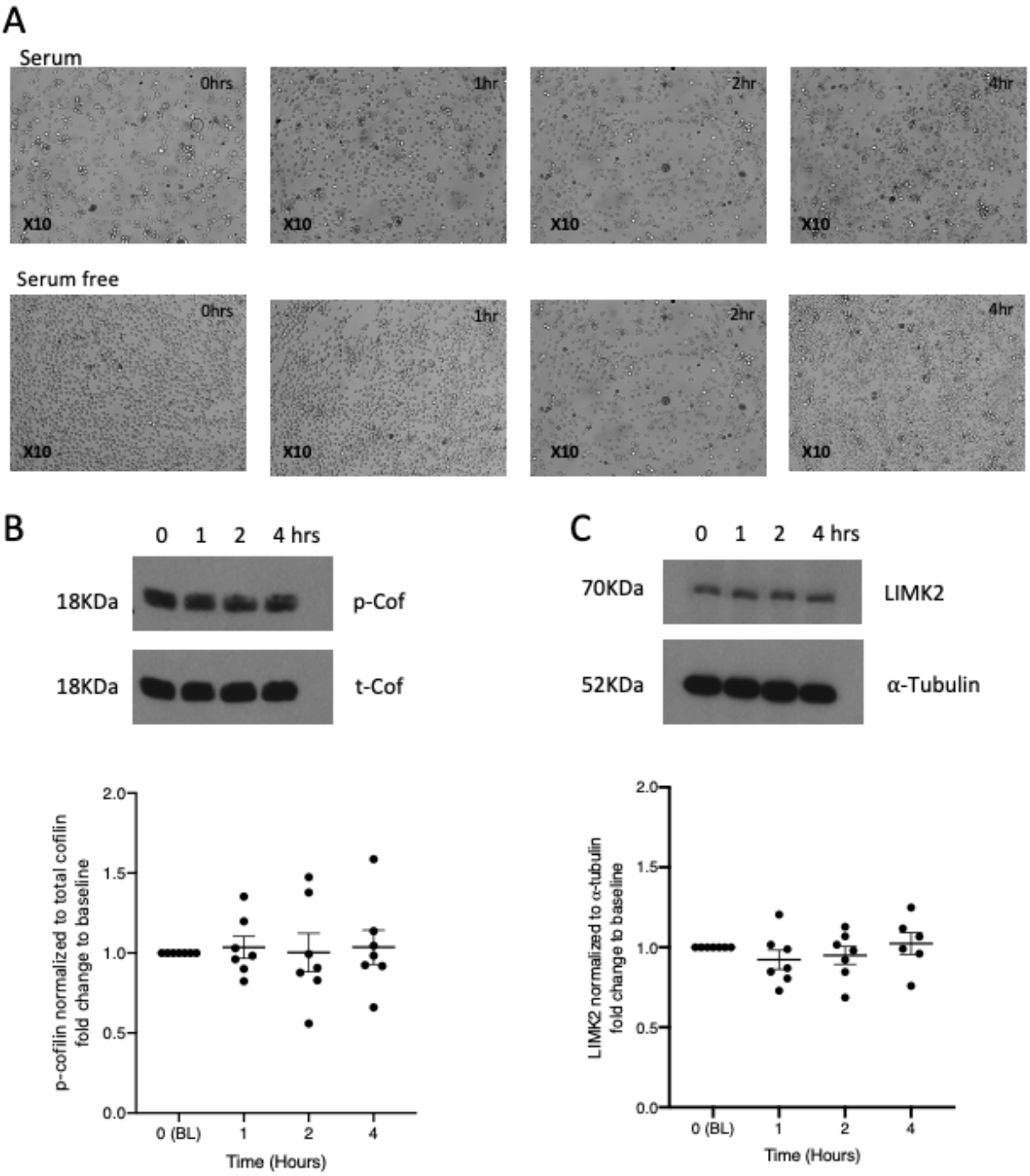

Figure 4.14 The effects of serum starvation of expression of p-Cofilin and LIMK2 in MEG01 cells. A) shows brightfield images of MEG01 cells in full serum (10%) (top) and in serum free conditions (bottom) over the time course (0-4 hours). Images are shown at X10 magnification representative of (n=5) independent replicates. B) shows p-Cofilin expression over the time course (0-4 hours) representative western blot (top) and graph plotted as fold change over 0 hours (below). C) shows LIMK2 expression over the time course (0-4 hours) representative western blot (top) and graph plotted as fold change over 0 hours (below). Data are the mean ±SEM for normalized signal from seven independent replicates (n=7), six independent replicates LIMK2 (4 hours) (n=6). The statistical significance is shown compared with 0(BL) (ns, not significant).

4.4 Discussion

4.4.1 Validating cell models to study PAR4

This chapter initially aimed at validating cell models for studying PAR4 and downstream signalling following its activation. The first cell model tested was HEK293 cells; these cells are known not to contain PAR4 endogenously but do express PAR1. HEKs are classic cell lines used to express non-endogenous proteins due to their high degree of transfectability, ease, and speed of growth. Transfection was initially trialled using Wt-mCherry PAR4 plasmids, with the success of the transfection confirmed with western blot (Figure S1). The double band pattern and absence of detectable signals in the control wells confirmed the detection of the wild-type PAR4. This experiment was originally set as a stable transfection cell line with maintenance of the plasmid DNA maintained via geneticin. However, subsequent experiments showed a loss of protein expression despite being maintained in geneticin, which should kill any cells not containing the plasmid DNA. As a result, a small experiment was carried out to determine the cause of the loss of PAR4 expression and the continued survival of the cells.

Fresh HEKs from a different batch were used in parallel with the transfected HEKs, and a kill curve with geneticin used (0 – 1000ug); standard death should occur at 400ug (data not presented). What was discovered, though, was the new batch of HEKs showed 100% death at 400ug+ geneticin, whereas the batch of HEKs used for the transfections showed survival at all concentrations used. It was revealed that the HEK cells used to produce stably transfected cells were, in fact, TSA201 cells. TSA201 cells are HEK293 cells, SV40 T-antigen transformed, resulting in resistance to hygromycin and G418 (geneticin) (Venkatachalan et al., 2007). As a result, the cells took up the DNA and expressed it but then lost expression due to resistance conferred by the SV40 T-antigen. Given that incorrectly labelled cells had resulted in weeks of wasted work and time, transient transfections had shown success. Therefore,

we aimed to optimise those conditions before generating further stable cell lines.

Continuing transient transfection studies on HEK293 cells aimed at comparing transfection of wt-mCherry PAR4 and Y157C-mCherry PAR4 to confirm previous work (Cunningham et al., 2012). Transfection of both these proteins was successful (Figure S2). The wt-PAR4 was mainly surface expressed, forming the classic honeycomb pattern of overexpressed surface proteins (Figure S2A), whereas the Y157C-mCherry PAR4 transfected cells showed expression restricted to inside the cells (Figure S2B). This confirmed the observations of previous work showing that Y157C is a deleterious PAR4 mutation resulting in ER retention of the protein due to incorrect folding (Norman et al., 2016). In addition, western blot analysis showed a double band pattern for wt-mCherry PAR4 (immature protein and glycosylated surface-expressed protein). In contrast, the Y157C-mCherry PAR4 showed a single band pattern (ER retained and hasn't undergone modification for surface expression). These results further confirmed the previous works while favouring using HEK293 as a model to study PAR4 signalling (Figure S3).

Further aims at confirming the differences in expression patterns of wt-PAR4 and Y157C was to induce the co-expression of both within the same cell; however, using mCherry tagged for both wouldn't allow for any differences in expression to be detected; therefore, a YFP-tagged wt-PAR4 construct was used. We first induced a single expression of the wt-YFP PAR4 construct, which interestingly worked a lot better than the mCherry construct, whether due to optimisation of the method or the construct was better accepted by the cells (Figure S4A). We also used varying concentrations of DNA, which showed that protein expression correlated with DNA concentration (Figure S4B). Given the previous observations, we assessed the transfection efficiency of wt-YFP PAR4 and Y157C-mCherry PAR4, which showed that the wt-YFP had a much greater transfection efficiency when compared to mutant (29.77% vs 11.51%) (Figure S4C). Despite this, we were able to achieve dual

transfection of wt-YFP PAR4 and Y157C-mCherry PAR4 in HEK293 cells as well as achieving dual transfection of wt-mCherry PAR4 and wt-YFP PAR4 in HEK 293 cells. This showed that when wt/wt was co-transfected, it achieved a Pearson correlation of 0.957 (Figure S5A + B), and when wt/mut were co-transfected, it achieved a Pearson's correlation of 0.64 (Figure S5C + D). The Pearson's correlation of wt/wt showed that there was a high degree of association between the location of the two proteins, while the lower Pearson's correlation in wt/mut of 0.64 shows that the proteins associate in location to some degree but that there is a loss of association at some point, in this case, the wt. is expressed mainly on the surface of the cell, whereas mutant is intracellularly retained.

However, despite showing promise in these early validation experiments, HEK293 cells were dropped for further experiments due to various factors. The first was due to HEK293 cells semi-adherent nature and, therefore, having a propensity to lift with very little mechanical stress. This resulted in problems obtaining IF and western blot data.

Additionally, as previously shown, the transfection efficacy in HEKs between wt and mutant differed considerably. In the context of preparing stimulation experiments, successful transfection isn't guaranteed, and therefore, setting up experiments which could ultimately fail to achieve the required transfection efficiency to elicit a response meant reproducibility of replicates would be more challenging to accomplish. Furthermore, HEK293 cells were also assessed for calcium assays. They obtained variable results (as mentioned with transfection efficiency), and the dispensing action of the flexstation dislodged cells in the centre of the well, causing drops in signal or, in some cases, complete loss of response. Despite turning the station to the lowest dispensing action and coating the wells with PDL (which helped IF), this automated assay did not achieve the desired effect. Despite these issues, the plan was to continue to run them in conjunction with other cell lines and to generate stable tagged and untagged PAR4 cell lines. Unfortunately, a mass infection of the floor with mycoplasma identified in multiple groups of HEK293 lines meant destroying all

stocks, losing the stable lines again and having to order fresh lines from a supplier. As a result, the assessment of other potential cell lines was explored, including a cell line forced to express the wt-PAR4 receptor stably.

4.4.2 Wt-PAR4 stably expressing keratinocyte cell line 10h9

Previous work conducted in another lab aimed at generating and characterising the keratinocyte cell line NCTC-2544 (clone 10h9) that was induced to express the wt-PAR4 receptor stably (Nilsson, 2010). These cell lines express no endogenous PARs, and therefore, activation with either thrombin or AYPGKF should be solely the response of PAR4 activation and not PAR1 (unlike HEK293 cells, which express PAR1). We aimed to assess the calcium response of 10h9 cells in response to thrombin and AYPGKF. Despite initially showing a dose-dependent calcium influx response to thrombin (Figure S7), with each replicate, the degree of response declined, illustrated by the large error bars observed. The same occurred in the AYPGKF-treated group (Figure S6); further replicates (data not shown) resulted in a complete loss of calcium response to thrombin and AYPGKF despite maintenance with geneticin selection.

The diminishing calcium response led to the assumption that there may have been issues with the geneticin that resulted in the loss of PAR4 plasmid DNA from the 10h9 cells. A new stock of G418 and fresh cells from the same stock the originals were taken from resulted in poor responses to thrombin and AYPGKF. In addition, testing was carried out involving western blotting for pERK in 10h9 cells following stimulation with thrombin and AYPGKF, but again, no response was shown. No increases in pERK over 120 minutes were observed, which confirmed the loss of PAR4 receptor expression in this cell line—given pERK as a canonical signalling molecule downstream of receptor activation, including PAR1 and PAR4. Stimulation of wt-PAR4 expressing 10h9 cells should have shown a robust response in ERK phosphorylation over

a stimulation time course. The complete lack of any change in the phosphorylation state confirmed that the 10h9 cells had lost the plasmid or, more likely, they had stopped expressing the protein on their surface. Due to the above observations, 10h9 cells were abandoned as a cell model to study PAR4 and its downstream proteins.

4.4.3 MEG-01 cells as a model expressing physiological levels of PAR4

MEG-01 cells are cells of a megakaryocyte lineage taken from a CML patient in blast crisis. They are Philadelphia chromosome positive (Ogura M et al., 1985). The theory for using this cell line to study PAR4 and its downstream proteins comes from the fact that being primitive megakaryocyte cells, they will have begun to express the machinery and proteins of megakaryocytes during differentiation. The only caveat is that given they are still in a blast state, they may not express (on the surface) or respond like their mature counterparts. Therefore, we first aimed to identify whether MEG-01 cells expressed PAR4; this was shown successfully in IF images. However, the pattern shown appeared diffuse through the cells which contrasted to the overexpression systems in HEK293. The HEK293 cells transfected to over-express wt-PAR4 show a classic honeycomb-like appearance on the surface of cells expressing the tagged protein, whereas, in MEGs, PAR4 signal is detected in high degree right throughout the cell. The concern would be that the receptor is intracellularly retained; however, given megakaryocytes role to produce platelets, there is a requirement to produce enormous amounts of protein, therefore, detecting intracellular PAR4 is not surprising.

4.4.4 Treating MEG-01 cells with phorbol 12-myristate 13-acetate (PMA) incudes differentiation

It has previously been established that treatment of MEG-01 cells with PMA induces megakaryocytic leukaemia cell differentiation via the activation of protein kinase C (PKC) isoforms, in particular PKCβII and PKCε, as well as PKD (Chen and Kan, 2015). Initially, we aimed at inducing the differentiation of MEG-01 cells with PMA on the theory that they may be more appropriate as a model for calcium assays. An interesting early observation was that unlike HEK293 cells transfected with PAR4, MEG-01 cells show a more diffuse expression. The theory was that, due to being blast cells, a lot of the functional protein may be retained, thus inducing differentiation may result in enhanced surface expression.

MEG-01 cells were initially trialled with the treatment of 10 nM and 25 nM of PMA, as these are the concentrations commonly used in other published studies. Early assessment of changes induced by PMA was done via bright field imaging over 72 hours. Interestingly, signs of differentiation were observable even with brightfield, including nuclear ploidy, dense granule production, full maturation and proplatelet extensions (Figure 4.7). Interestingly, once treated with PMA, MEG-01 cells appear to cease division or slow considerably, as was seen when comparing the control vs. treatment cell numbers over the three days. The initial success resulted in imaging PMA-treated MEGs via IF imaging, capturing images of ploidy at various stages, including fully mature megakaryocytes which had increased in size to >70μm. What was equally interesting within these imaging experiments, was adhered platelets to the glass slide measuring around 2μm. This proved proof of concept that MEG-01 cells were a good model for studying PARs in a physiological context (Figure 4.8). A final study aimed to quantify the differentiation state of PMA-treated MEGs by comparing ploidy with untreated MEG-01 cells. The number of nuclei within the PMA-treated MEGs were

compared with those in the non-treatment group (Figure 4.9). This showed that PMA successfully induced MEG-01 differentiation by increasing the ploidy across all groups vs. the NT group.

Despite showing promise as a model of maturing megakaryocytes and potentially inducing a more physiologically relevant phenotype, these early experiments provided a proof of concept on previous work. Unfortunately, due to obtaining these results at the end of my experimental time, bringing this model forward to assess calcium response and Cofilin pathway signalling wasn't possible but would have provided an interesting avenue to explore further.

4.4.5 Cofilin-2 in MEG-01 cells

Given that bioinformatic analysis revealed Cofilin-2 as a high-impact hit across all three replicates, we first aimed to look at whether MEG-01 cells contained Cofilin-2. Initially, we aimed to validate the use of the Cofilin-2 antibody, using human cardiomyocytes cells (AC-16) as a positive control and successfully showing that MEG-01 cells express Cofilin-2, albeit at low levels. This was further validated via western blot, in which whole rat heart lysate was used as a positive control, along with increasing cell densities of MEG-01 cells (Figure 4.11C). The western blot showed positive bands in cell densities of 500,000 and 1M, providing additional evidence that MEG-01 cells did express Cofilin-2.

Having shown that MEG-01 cells expressed Cofilin-2, we then aimed to determine if stimulation with thrombin had any effect on the phosphorylation state of Cofilin-2 through IF analysis (Figure 4.12). What was surprising in these experiments was that stimulation of 1 U/mL of thrombin resulted in a significant reduction in Cofilin-2 expression compared to baseline. In contrast, stimulation with 3 U/mL of thrombin resulted in a significant increase of Cofilin-2 compared to baseline. What was also interesting for pCof-2 in these

experiments was that unlike what was shown in Cofilin-1, the phosphorylation of Cofilin-2 does not show dose dependence with thrombin. It was also shown that expression is considerably lower than that of Cofilin-1, making quantification with western blotting potentially difficult. The most surprising observation was the change in Cofilin-2 expression with thrombin, which did show dose dependency, showing a decrease in expression with 1 U/mL thrombin but an increase in expression with 3 U/mL thrombin when compared to baseline.

These initial experiments showed that MEG-01 cells expressed both Cofilin-2 and pCofilin-2 and that stimulation with thrombin affected the phosphorylation state in the same way as was shown with Cofilin-1. Unfortunately, due to delays in the delivery of the pCofilin-2 antibody, we were unable to obtain any further data in the context of TFLRRN or AYPGKF or using stimulation time points with western blotting due to the very short amount of time before lab work finished. However, it succeeded in proving an initial effect, and if more time had been available, experiments conducted in Cofilin-1 would have been undertaken in the context of Cofilin-2. Given the much lower expression level of Cofilin-2 seen in MEG-01 cells, the margin for error was too great in the reproducibility of results, and therefore, a focus on Cofilin-1 was pursued.

4.4.6 Validation of Cofilin-1 and pCofilin-1 in MEG-01 cells

Given that MEG-01 cells were a completely new cell line purchased, the first aim was to characterise these cells and validate optimal antibody concentrations to determine the best conditions for stimulation experiments. MEG-01 cells are shown to be extremely heterogeneous cells with variations in size, nuclear content, phenotypic state, etc. First, we showed that Cofilin and p-Cofilin expression was relatively abundant, with Cofilin reaching saturation on western blot at cell densities greater than 200K at an antibody concentration of (1:100K) (Figure 4.13A). At the same time, p-Cofilin showed a good band intensity at 200K cells at antibody concentrations of (1:15K)

(Figure 4.13B). These densities and concentrations seemed the best for further experiments based on the validation blots performed. In part, because at densities of less than 200K cells, the cell pellet was very difficult to see, which would have resulted in more significant protein variation in subsequent experiments or loss in protein if the cell pellet was dislodged. Greater than 200K cells produced very saturated bands, particularly in Cofilin, which would be difficult to quantify. These experiments at least provided a baseline for further work to be performed.

The initial validation experiments were carried out in MEG-01 cells within serum conditions; generally, cells tend to be serum starved to synchronise the cell cycle and down-regulate the cellular process. Therefore, we next looked at the effect that serum starvation had on MEG-01 cells; what was interesting is that observationally, no change in cell shape, size, or signs of stress occurred over 4 hours (Figure 4.14A). In addition, a western blot was performed over (0, 1, 2 and 4 hours), with expression levels of p-Cofilin showing no significant change from baseline (Figure 4.14B). The same was also shown in LIMK2 (Figure 4.14C). Despite this, in subsequent experiments, we did perform a 2-hour serum starve before stimulation, in part to ensure cell cycle synchronicity but also because other kinases (ERK and AKT) were to be looked at, which certainly in other cells like HEKs serum starvation does affect baseline pERK expression.

Chapter Five:

Interrogation of the Cofilin Signalling Pathways Downstream of PAR1 and PAR4 Activation

5. Results Chapter 3

5.1 Introduction

MEG-01 cells have been shown to express both PAR4 and Cofilin making it a suitable cell line model for exploring the PAR4/Cofilin axis within the context of a physiologically relevant in vitro model.

Understanding the interaction between PAR4 and the Cofilin pathway can reveal new therapeutic targets. Modulating Cofilin activity via PAR4 could offer a strategy to control platelet function and prevent excessive thrombus formation in ACS. Insights into the PAR4-Cofilin pathway could guide the development of novel antiplatelet agents that alter cytoskeletal dynamics, potentially reducing the risk of bleeding associated with current antiplatelet therapies.

5.2 Hypothesis and Aims

Given that PAR4 is widely accepted to couple to G12/13, which signals via RhoA, it was hypotheised that activation of PAR4 would affect the phosphorylation state and, therefore, the activity of cofilin. RhoA is known to phosphorylate and activate ROCK, which phosphorylates LIMK, which is the main phosphorylator of cofilin.

This chapter aims to:

- Determine if activating PAR1 and PAR4 has any effect on the phosphorylation state of Cofilin in MEG-01 cells
- Determine differential effects of PAR1 and PAR4 activation on cofilin activity in MEG-01 cells
- Interrogate the cofilin signalling pathway downstream of PAR1 and PAR4 activation

5.3 Cofilin Signalling Pathways Downstream of PAR1 and PAR4 Activation

5.3.1 Brightfield imaging of MEG-01 cells following treatment with Thrombin, PAR1-AP and PAR4-AP

Before conducting any experiments for downstream proteins of PAR4, we first conducted some imaging experiments on MEG-01 cells to see if treatment of MEG-01 cells with thrombin, PAR1-AP, or PAR4-AP induced any visual changes following stimulation. MEG-01 cells were initially serum starved for 2 hours before stimulation and imaged (Figure 5.1, top 4 images). MEG-01 cells were then stimulated with 1 U/mL thrombin, 100 μM PAR1-AP (TFLRRN) and 300 μM PAR4-AP (AYPGKF). Images were taken at 0 minutes (baseline) just before stimulation, 5 minutes, 1 hour, 2 hours and 4 hours.

The first images were taken at 5 minutes (top, middle), and overall, all cells were comparable to baseline; no obvious morphological changes were detectable at this stage. The next set of images was taken at 1 hour (middle). At this stage, morphological changes were detectable in the thrombin and AYPGKF-treated MEG-01 cells (black arrows). They showed a loss of spherical shape, with cells taking on a less uniform shape than the baseline. In the TFLRRN-treated group, shape change wasn't all that obvious and was comparable to untreated cells. The next set of images taken was at 2 hours (middle, bottom). At this stage, morphological changes detected in MEG-01 cells were still present in the thrombin and AYPGKF-treated groups. The TF-treated group was still comparable to those without treatment (NT). The final set of images taken was at 4 hours (bottom). All cells had visually returned to spherical shape at this stage and were mostly comparable to (NT).

This simple experiment showed visually that treatment of MEG-01 cells with thrombin and AYPGKF appears to induce morphological changes in the shape of MEG-01 cells. Interestingly, treatment of MEG-01 cells with TFLRRN, which activates solely PAR1, didn't induce any visual changes in cell morphology like

those seen in the thrombin and AYPGKF-treated groups. This seems to indicate that activation of PAR4 is more responsible for inducing shape changes in MEG-01 cells and not PAR1.

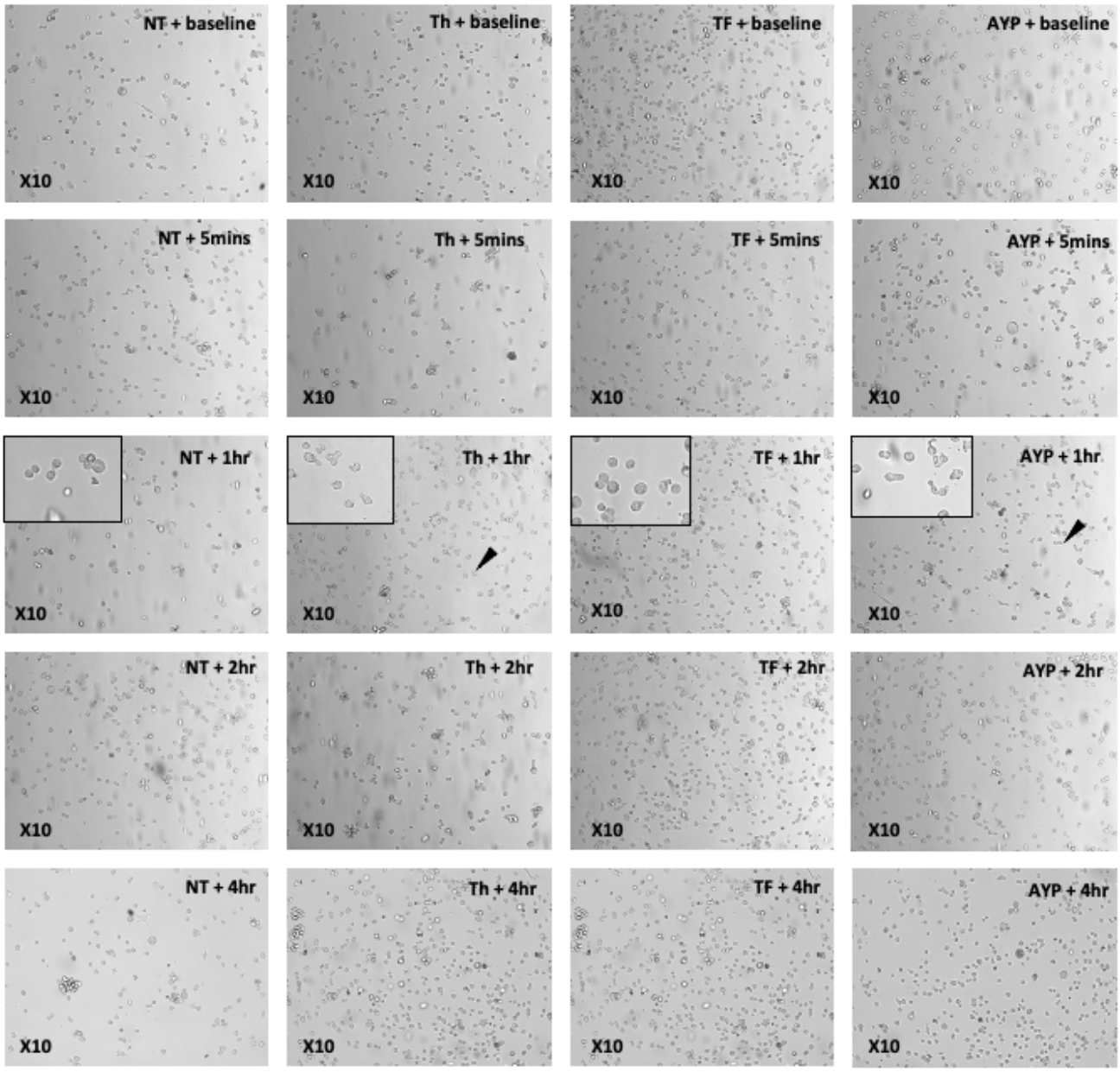

Figure 5.1 Brightfield imaging of MEG-01 cells following treatment with Thrombin, TF and AYP. Left shows brightfield images of MEG01 cells with no treatment (NT) (control) over the time course (0mins (baseline), 5 mins, 1 hour, 2 hour and 4 hour) from top to bottom. The (middle left) shows MEG-01 cells treated with 1 U/mL of thrombin over the time course (top to bottom). Observable changes in MEG-01 cell morphology can be seen from 1 hour post treatment with loss of spherical shape and protrusions seen (back arrows). The (middle right) shows MEG-01 cells treated with 100μM of TFLLR over the time course (top to bottom). The (right) shows MEG-01 cells treated with 300μM of AYPGKF over the time course (top to bottom). Observable changes in MEG-01 cell morphology can be seen from 1 hour post treatment with loss of spherical shape and protrusions seen (back arrows). Images are representative of five independent replicates (n=5).

5.3.2 Immunofluorescent analysis of phospho-Cofilin changes following stimulation of MEG-01 cells with thrombin

Given that thrombin was shown to have a significant effect on the phosphorylation of Cofilin-2 following stimualation of MEG-01 cells with 1 U/mL and 3 U/mL of thrombin when quantified via immunofluorescence at a timepoint of 15 minutes post-stimulation. Therefore, we next aimed at quantifying changes in the phosphorylation state of Cofilin-1 expression using immunofluorescence analysis to see if the results observed coincide with those seen in Cofilin-2.

MEG-01 cells were stimulated with either 1 U/mL or 3 U/mL of thrombin for 15 minutes before slides were prepared for IF imaging. Representative images are shown in (Figure 5.2A). The top four images (left to right) show MEG-01 cells in which a secondary labelled antibody was added to ensure that the signal detected wasn't due to non-specific binding of the secondary. As can be seen no green signal can be seen, meaning the secondary antibody is specific to its target, and the background signal is, therefore, minimal. The next shows MEG-01 cells treated with both primary and secondary antibodies, which are unstimulated (baseline); the green signal shows the presence of total-Cofilin. The next image shows an expression of total-Cofilin in MEG-01 cells stimulated with 1 U/mL of thrombin, and the final image shows an expression of total-Cofilin in MEG-01 cells stimulated with 3 U/mL of thrombin. Generally, the expression of total-Cofilin seems relatively unchanged between BL and stimulated MEG-01 cells, as expected.

The bottom four images (left to right) show MEG-01 cells in which a secondary labelled antibody was added to ensure the signal detected wasn't due to non-specific binding of the secondary. As can be seen no green signal can be seen, meaning the secondary antibody is specific to its target, and the background signal is, therefore, minimal. The next shows MEG-01 cells treated with both primary and secondary antibodies, which are unstimulated (baseline); the green signal shows the presence of phospho-Cofilin. The next image shows

an expression of phospho-cofilin in MEG-01 cells stimulated with 1 U/mL of thrombin, and the final image shows an expression of phospho-cofilin in MEG-01 cells stimulated with 3 U/mL of thrombin. The images show that phospho-cofilin expression increases proportionately to the amount of thrombin used. With 1 U/mL thrombin, there is an obvious increase in phospho-cofilin compared to the baseline. In addition, the degree of phospho-Cofilin expression in the 3 U/mL thrombin group appears greater than that of the 1 U/mL thrombin group. It should be noted that phospho-cofilin changes don't appear universal in MEG-01 cells, with some showing mass increase in phospho-cofilin. In contrast, others appear to express relatively low levels.

Quantification was performed in ImageJ, taking individual cells' mean fluorescence intensity (MFI) across three independent replicates (Figure 5.2B). The number of cells was analysed using grouped analysis. For total Cofilin, the number of values (n=42) for secondary only gave an (MFI of 6.016±0.07); for BL total-Cofilin, the number of values (n=49), which gave an (MFI of 45.08±2.334), for 1 U/mL of thrombin total Cofilin the number of values (n=39) which gave an (MFI of 47.16±2.393) and for 3 U/mL of thrombin the number of values (n=30) which gave an (MFI of 45.56±3.303). Groups were compared using the Mann-Whitney U-test, with the hypothetical mean being the unstimulated (BL) total-cofilin (MFI of 45.08±2.334). For 1 U/mL (45.08 vs 47.16, p=0.3913, ns) and 3 U/mL thrombin (45.08 vs 45.56, p=0.8852, ns). These results show that thrombin stimulation does not alter the expression of total Cofilin in MEG-01 cells with any significant effect.

For phospho-Cofilin, the number of values (n=42) for secondary only gave an (MFI of 6.016±0.07); for BL p-Cofilin, the number of values (n=44), which gave an (MFI of 9.993±0.48), for 1 U/mL of thrombin p-Cofilin the number of values (n=49) which gave a (MFI of 13.90±0.81) and for 3 U/mL of thrombin the number of values (n=56) which gave a (MFI of 22.71±2.305). Groups were compared using the Mann-Whitney U-test, with the hypothetical mean being the unstimulated (BL) p-Cofilin (MFI of 9.993±0.48). For 1 U/mL (9.993 vs

13.90, p<0.0001 ****, s) and 3 U/mL thrombin (9.993 vs 22.71, p<0.0001 ****, s). These results show that thrombin stimulation significantly increases the phosphorylation of Cofilin and that the concentration of thrombin used also affects levels of p-Cofilin (Figure 5.2C). It should also be noted from the spread of the data that p-Cofilin expression is not universal within MEG-01 cells, with some showing mass expression of p-Cofilin following stimulation. In contrast, others expressed levels similar to baseline.

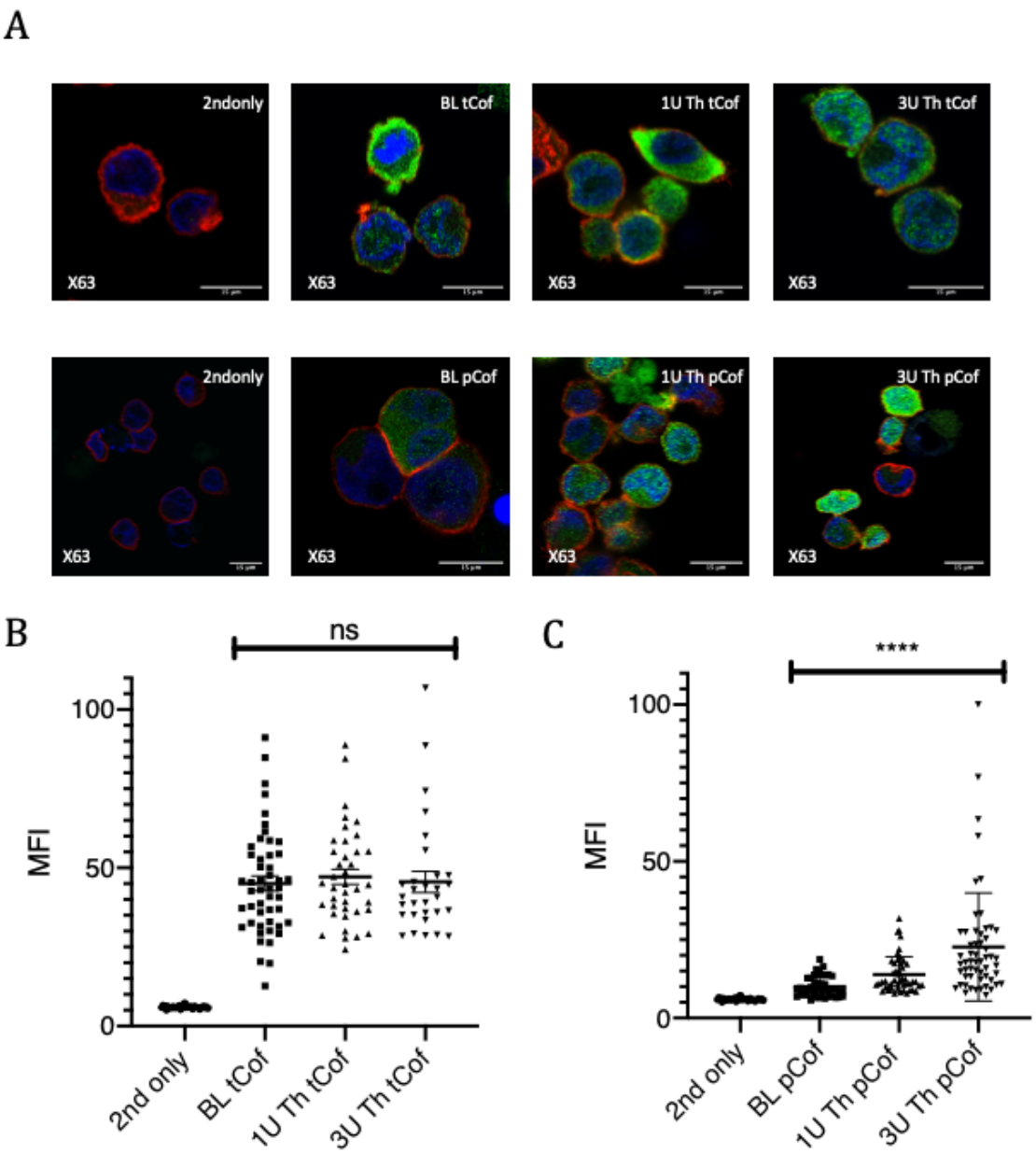

Figure 5.2 Immunofluorescent analysis of Cofilin phosphorylation following stimulation of MEG-01 cells with Thrombin. A) shows confocal microscopy imaging of MEG-01 cells using (X63 magnification), top four images are total-cofilin and bottom four images are p-cofilin. Antibody control shows no non-specific staining indicating green signal is positive for cofilin signal. B) shows total-cofilin expression changes upon stimulation with 1 U/mL and 3 U/mL at 15 mins post stimulation. Mean fluorescent intensity was compared to the MFI of BL tCof using Mann-Whitney U-test. The assumed theoretical mean used was that of BL tCof (45.05). C) shows phospho-cofilin expression changes upon stimulation with 1 U/mL and 3 U/mL at 15 mins post stimulation. Mean fluorescent intensity was compared to the MFI of BL pCof using Mann-Whitney U-test. The assumed theoretical mean used was that of BL pCof (9.993). Data are the mean ±SEM for the MFI from three independent replicates (n=3). The level of statistical significance is shown compared with the BL (Unstimulated) control (* $p<0.05$, ** $p<0.01$, *** $p<0.001$, **** $p<0.0001$ and ns (not significant).

5.3.3 Immunofluorescent analysis of phospho-Cofilin changes following stimulation of MEG-01 cells with TFLRRN or AYPGKF

Given that thrombin was shown to have a significant effect on the phosphorylation of Cofilin following stimulation of MEG-01 cells with 1 U/mL or 3 U/mL of thrombin when quantified in the previous experiment. Therefore, we next aimed at quantifying changes in phospho-Cofilin expression using immunofluorescence analysis in MEG-01 cells when stimulated with either TFLRRN (100 μM) or AYPGKF (300 μM).

MEG-01 cells were stimulated with either 100 μM of TFLRRN or 300 μM AYPGKF for 15 minutes before slides were prepared for IF imaging. Representative images are shown in (Figure 5.3A). The top four images (left to right) show MEG-01 cells in which a secondary labelled antibody was added to ensure that the signal detected wasn't due to non-specific binding of the secondary. As can be seen no green signal can be seen, meaning the secondary antibody is specific to its target, and the background signal is, therefore, minimal. The next shows MEG-01 cells treated with both primary and secondary antibodies, which are unstimulated (baseline); the green signal shows the presence of total-Cofilin. The next image shows expression of total-Cofilin in MEG-01 cells stimulated with 100 μM of TFLRRN, and the final image shows expression of total-Cofilin in MEG-01 cells stimulated with 300 μM of AYPGKF. Generally, total-Cofilin expression seems relatively unchanged between BL and stimulated MEG-01 cells, although the expression seems slightly higher in the stimulated cells.

The bottom four images (left to right) show MEG-01 cells in which a secondary labelled antibody was added to ensure the signal detected wasn't due to non-specific binding of the secondary. As can be seen no green signal can be seen, meaning the secondary antibody is specific to its target, and the background signal is, therefore, minimal. The next shows MEG-01 cells treated with both primary and secondary antibodies, which are unstimulated (baseline); the green signal shows the presence of phospho-Cofilin. The next image shows

an expression of phospho-cofilin in MEG-01 cells stimulated with 100 μM of TFLRRN, and the final image shows an expression of phospho-cofilin in MEG-01 cells stimulated with 300 μM of AYPGKF. From the images, phospho-Cofilin expression in MEG-01 cells stimulated with 100 μM of TFLRRN appears to show a phospho-Cofilin expression similar to that of unstimulated (BL) phospho-Cofilin. With 300 μM AYPGKF, there is an obvious increase in phospho-cofilin compared to the baseline. It should be noted that phospho-cofilin changes don't appear universal in MEG-01 cells, with some showing mass increase in phospho-cofilin. In contrast, others appear to express relatively low levels.

Quantification was performed in ImageJ, taking individual cells' mean fluorescence intensity (MFI) across three independent replicates (Figure 5.3B). The number of cells was analysed using grouped analysis. For total Cofilin, the number of values (n=96) for secondary only gave an (MFI of 4.315±0.07); for BL total-Cofilin, the number of values (n=85), which gave an (MFI of 44.26±1.481), for 100 μM of TFLRRN total Cofilin the number of values (n=123) which gave a (MFI of 61.47±2.171) and for 300 μM of AYPGKF the number of values (n=104) which gave a (MFI of 55.79±1.555). Groups were compared using the Mann-Whitney U-test, with the hypothetical mean being the unstimulated (BL) total-cofilin (MFI of 44.26±1.481). For 100 μM TFLRRN (44.26 vs 61.47, $p<0.0001$ ****, s) and for 300 μM AYPGKF (44.26 vs 55.79, $p<0.0001$ ****, s). These results show that TFLRRN and AYPGKF stimulation appear to alter the expression of total-Cofilin in MEG-01 cells, with the difference in baseline for both being significant.

For phospho-Cofilin, the number of values (n=96) for secondary only gave an (MFI of 4.315±0.07); for BL p-Cofilin, the number of values (n=96), which gave an (MFI of 8.151±0.36), for 100 μM of TFLRRN p-Cofilin the number of values (n=127) which gave a (MFI of 9.864±0.52) and for 300 μM of AYPGKF the number of values (n=102) which gave a (MFI of 14.25±0.67). Groups were compared using the Mann-Whitney U-test, with the hypothetical mean being

the unstimulated (BL) p-Cofilin (MFI of 8.151±0.36). For 100 μM TFLRRN (8.151 vs 9.993, $p<0.01$ **, s) and for 300 μM AYPGKF (8.151 vs 14.25, $p<0.0001$ ****, s) (Figure 5.3C). These results show that TFLRRN and AYPGKF stimulation significantly increase Cofilin's phosphorylation, with TFLRRN showing a lesser effect (8.151 vs 9.993). However, stimulation of MEG-01 cells with AYPGKF showed a significant change in the expression of p-Cofilin (8.151 vs 14.25). It should also be noted from the spread of the data that p-Cofilin expression is not universal within MEG-01 cells, with some showing mass expression of p-Cofilin following stimulation. In contrast, others expressed levels similar to baseline.

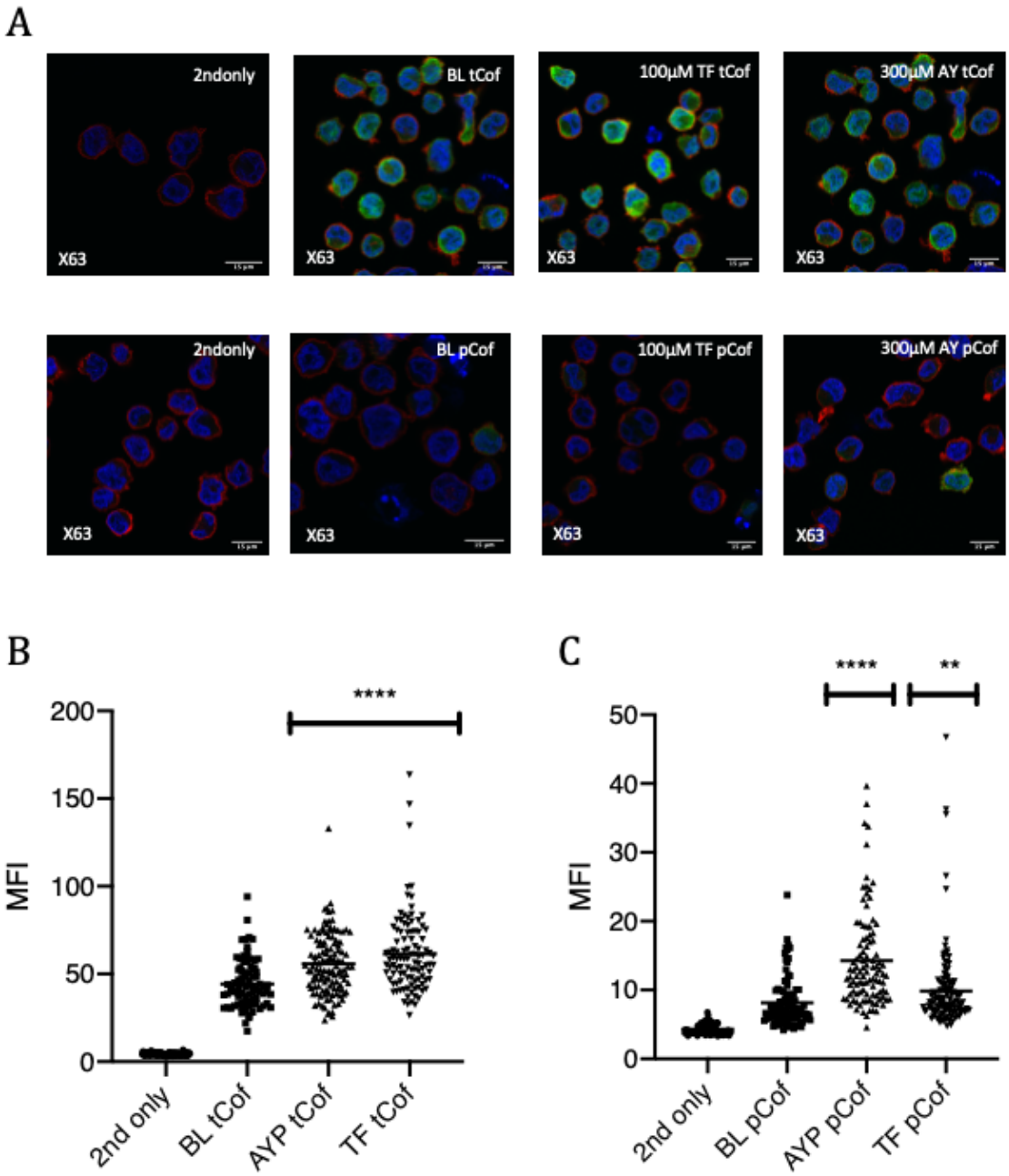

Figure 5.3 Immunofluorescent analysis of Cofilin phosphorylation following stimulation of MEG-01 cells with TFLLR and AYPGKF. A) shows confocal microscopy imaging of MEG-01 cells using (X63 magnification), top four images are total-cofilin and bottom four images are p-cofilin. Antibody control shows no non-specific staining indicating green signal is positive for cofilin signal. B) shows total-cofilin expression changes upon stimulation with 100 µM TFLLR and 300µM AYPGKF at 15 mins post stimulation. Mean fluorescent intensity was compared to the MFI of BL tCof using Mann-Whitney U-test. The assumed theoretical mean used was that of BL tCof (44.26). C) shows phospho-cofilin expression changes upon stimulation with 100 µM TFLRRN and 300µM AYPGKF at 15 mins post stimulation. Mean fluorescent intensity was compared to the MFI of BL pCof using Mann-Whitney U-test. The assumed theoretical mean used was that of BL pCof (8.151). Data are the mean ±SEM for the MFI from three independent replicates (n=3). The level of statistical significance is shown compared with the BL (Unstimulated) control (* $p<0.05$, ** $p<0.01$, *** $p<0.001$, **** $p<0.0001$ and ns (not significant).

5.3.4 Phospho-Cofilin changes following Stimulation of MEG-01 cells with Thrombin

Following the validation of the Cofilin antibodies, we next aimed to determine the effect that cleavage and stimulation of PAR1 and PAR4 receptors with thrombin had on the phosphorylation of Cofilin over a time course of (0 -120 mins). MEG-01 cells were stimulated with 1 U/mL of thrombin at the following timepoints (0, 1, 2, 5, 15, 30, 60, 120 mins).

Representative blots of the time course for p-Cof (top) and t-Cof (bottom) are shown in Figure 5.4A. The blots for pCof appear to show an increase in the density of phospho-cofilin starting at 5 mins and reaching a peak at 15 mins. Results were plotted and compared to the baseline (0mins), and statistical analysis was performed using the One-sample t-test, with the assumed hypothetical mean being 1, the same as the baseline. The time course showed 1 minute (1.393±0.13 fold over unstimulated, $p=0.0533$, ns) 2 minutes (1.444±0.11 fold over unstimulated, $p<0.05$ *, s), 5 minutes (1.553±0.15 fold over unstimulated, $p<0.05$ *, s), 15 minutes (1.615±0.09 fold over unstimulated, $p<0.01$ **, s), 30 minutes (1.182±0.08 fold over unstimulated, $p=0.1206$, ns), 60 minutes (1.350±0.10 fold over unstimulated, $p<0.05$ *, s) and 120 minutes (1.110±0.09 fold over unstimulated, $p=0.3071$, ns). The time course results from four independent replicates (n=4) (Figure 5.4A, Bottom). Overall, stimulation of PAR1 and PAR4 with thrombin in MEG-01 cells does show a significant effect on phosphorylation of Cofilin at 2, 5 15, and 60 mins with the greatest fold change to baseline being 1.615 at a time of 15 mins, with that timepoint also being the most significant over the time course.

To determine the success of stimulation conditions, phosphorylation of ERK was used. As a classical canonical signalling cascade downstream of receptor stimulation, including both PAR1 and PAR4, it was used as a positive control for testing stimulation conditions. Representative blots of the time course for p-ERK (top) and t-ERK (bottom) are shown in Figure 5.4B. Changes in band

intensity can be seen from the 1-minute mark and remain sustained up to 30 minutes before a decrease in band intensity at the 60 and 120-minute bands, which have returned to near baseline intensity. Results were plotted and compared to the baseline (0mins), and statistical analysis was performed using the One-sample t-test, with the assumed hypothetical mean being 1, the same as the baseline. The time course showed; 1 minute (1.628±0.17 fold over unstimulated, $p<0.05$ *, s) 2 minutes (1.538±0.15 fold over unstimulated, $p<0.05$ *, s), 5 minutes (1.599±0.29 fold over unstimulated, $p=0.1274$, ns), 15 minutes (1.681±0.37 fold over unstimulated, $p=0.1615$, ns), 30 minutes (1.904±0.43 fold over unstimulated, $p=0.1279$, ns), 60 minutes (1.371±0.35 fold over unstimulated, $p=0.3695$, ns) and 120 minutes (1.421±0.29 fold over unstimulated, $p=0.2380$, ns). The results are the average of four independent replicates ($n=4$) Figure 5.4B (bottom). Overall, stimulation of MEG-01 cells showed a significant increase in p-ERK at 1 min and 2 mins. The stimulation time course showed an initial rise in ERK phosphorylation at 1 minute, with a slight decline at 2 minutes before showing a steady rise to a second peak at 30 minutes, again declining but not reaching baseline over the time course of the experiment. Results showed that increases in p-ERK over the stimulation time course meant that thrombin successfully induced downstream signalling cascades of receptor activation. Therefore, it was confirmed that the results seen in p-Cof are reliable.

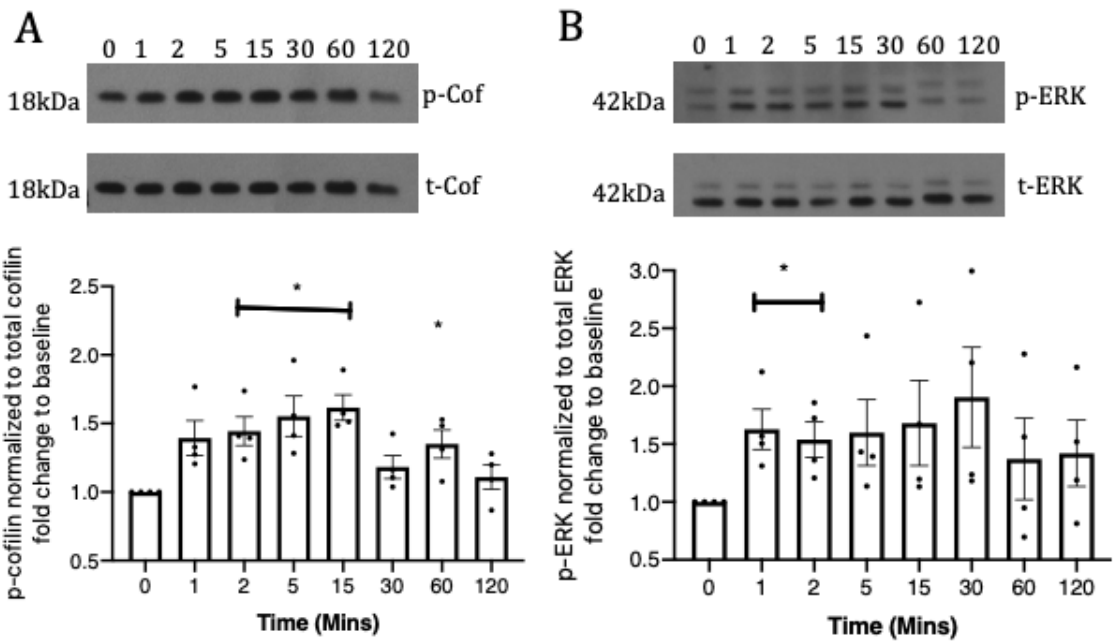

Figure 5.4 The effects on cofilin and ERK phosphorylation following stimulation of MEG-01 cells with 1 U/mL of Thrombin. A) shows representative western blot images of p-Cofilin (top) and loading control total-Cofilin (bottom) for the stimulation time course (0-120 minutes). Time points were compared with unstimulated (0 minutes) using one-sample t-test. B) shows representative western blot images of p-ERK (top) and loading control total-ERK (bottom) for the stimulation time course (0-120 minutes). Time points were compared with unstimulated (0 minutes) using One-sample t-test. Data are the mean ±SEM for the normalized signal from five independent replicates (n=5). The level of statistical significance is shown compared with the Unstimulated (0 minutes) control (* $p<0.05$, ** $p<0.01$, *** $p<0.001$, **** $p<0.0001$ and ns (not significant).

5.3.5 Phospho-Cofilin changes following Stimulation of MEG-01 cells with PAR1-AP TFLRRN

It was shown that thrombin stimulation of MEG-01 cells had a significant effect on the phosphorylation of Cofilin. Next, we aimed to determine whether the effect was driven by the activation of either PAR1 or PAR4 or a combination of both. Therefore, to determine if PAR1 was responsible for the effects observed during the stimulation of MEG-01 cells with thrombin. MEG-01 cells were stimulated with 100 μM of TFLRRN at the following timepoints (0, 1, 2, 5, 15, 30, 60, 120 mins).

Representative blots of the time course for p-Cof (top) and t-Cof (bottom) are shown in Figure 5.5A. The blots for pCof appear to show universal pCof density across the time points with no apparent visual increases in expression. Results were plotted and compared to the baseline (0mins), and statistical analysis was performed using the One-sample t-test, with the assumed hypothetical mean being 1, the same as the baseline. The time course showed; 1 minute (1.048±0.20 fold over unstimulated, p=0.6089, ns) 2 minutes (1.064±0.09 fold over unstimulated, p=0.2, ns), 5 minutes (1.009±0.2 fold over unstimulated, p=0.9250 ns), 15 minutes (1.015±0.12 fold over unstimulated, p=0.7921, ns), 30 minutes (0.9949±0.01 fold over unstimulated, p=0.9134, ns), 60 minutes (0.9988±0.13 fold over unstimulated, p=0.9837, ns) and 120 minutes (0.9639±0.15 fold over unstimulated, p=0.6092, ns). The time course results from five independent replicates (n=5) (Figure 5.5A, Bottom). Overall, stimulation of PAR1 with TFLRRN in MEG-01 cells does not show any significant effect on phosphorylation of Cofilin at any of the time points and virtually no change from baseline levels is observed.

To determine the success of stimulation conditions, phosphorylation of ERK was used. Representative blots of the time course for p-ERK (top) and t-ERK (bottom) are shown in Figure 5.5B. Changes in band intensity can be seen from the 1-minute mark, showing a rapid increase in pERK expression from

baseline and a peak at 2 minutes. Although the signal stays above baseline, a decline starts at 5 minutes, heading visually close to baseline by 30 minutes. This contrasts with the pERK signal observed in thrombin-stimulated MEG-01 cells, which maintain a much more sustained pERK signal. Results were plotted and compared to the baseline (0mins), and statistical analysis was performed using the One-sample t-test, with the assumed hypothetical mean being 1, the same as the baseline. The time course showed; 1 minute (2.098±0.68 fold over unstimulated, $p<0.05$ *, s) 2 minutes (2.115±0.55 fold over unstimulated, $p<0.05$ *, s), 5 minutes (1.726±0.83 fold over unstimulated, $p=0.1219$, ns), 15 minutes (1.364±0.68 fold over unstimulated, $p=0.2985$, ns), 30 minutes (1.127±0.44 fold over unstimulated, $p=0.5494$, ns), 60 minutes (1.228±0.62 fold over unstimulated, $p=0.4559$, ns) and 120 minutes (1.016±0.48 fold over unstimulated, $p=0.9454$, ns). The results are the average of five independent replicates (n=5) Figure 5.5B (bottom). Overall, stimulation of MEG-01 cells showed a significant increase in p-ERK at 1 min and 2 mins. The stimulation time course showed an initial rapid rise in ERK phosphorylation at 1 minute with a peak signal intensity at 2 minutes before slowly declining back to baseline throughout the time points. Results showed that increases in p-ERK over the stimulation time course meant that TFLRRN successfully induced downstream signalling cascades of PAR1 receptor activation and confirmed that results seen in p-Cof are reliable.

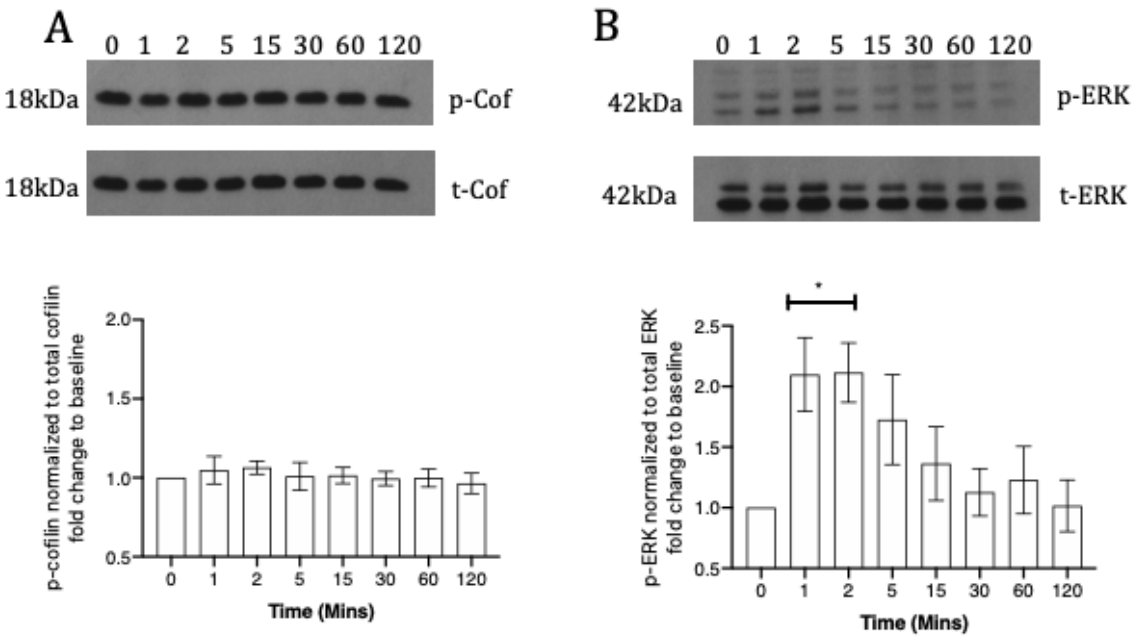

Figure 5.5 The effects on cofilin and ERK phosphorylation following stimulation of MEG-01 cells with 100 µM of PAR1-AP (TFLLR-NH$_2$). A) shows representative western blot images of p-Cofilin (top) and loading control total-Cofilin (bottom) for the stimulation time course (0-120 minutes). Time points were compared with unstimulated (0 minutes) using One-sample t-test. B) shows representative western blot images of p-ERK (top) and loading control total-ERK (bottom) for the stimulation time course (0-120 minutes). Time points were compared with unstimulated (0 minutes) using One-sample t-test. Data are the mean ±SEM for the normalized signal from five independent replicates (n=5). The level of statistical significance is shown compared with the Unstimulated (0 minutes) control (* $p<0.05$, ** $p<0.01$, *** $p<0.001$, **** $p<0.0001$ and ns (not significant).

5.3.6 Phospho-Cofilin changes following Stimulation of MEG-01 cells with PAR4-AP AYPGKF

It was shown that thrombin stimulation of MEG-01 cells had a significant effect on the phosphorylation of Cofilin. Next, we aimed to determine whether the effect was driven by the activation of either PAR1 or PAR4 or a combination of both. Therefore, to determine if PAR4 was responsible for the effects observed during the stimulation of MEG-01 cells with thrombin. MEG-01 cells were stimulated with 300 μM of AYPGKF at the following timepoints (0, 2, 5, 15, 30, 60, 120 mins). The 1-minute time point was excluded because the peak phospho-cofilin increase was noted at 15 minutes in the thrombin stimulation experiments. However, for pERK, the 1-minute time point was included due to the fast increases in pERK observed in the previous two ligands.

Representative blots of the time course for p-Cof (top) and t-Cof (bottom) are shown in Figure 5.6A. The blots for pCof appear to show increases in phosphor-Cofilin over time to a peak at 15 minutes, the same observed in the thrombin-stimulated experiments. Results were plotted and compared to the baseline (0mins), and statistical analysis was performed using the One-sample t-test, with the assumed hypothetical mean being 1, the same as the baseline. The time course showed; 2 minutes (1.263±0.12 fold over unstimulated, p=0.1237, ns), 5 minutes (1.307±0.21 fold over unstimulated, p=0.2470, ns), 15 minutes (1.560±0.21 fold over unstimulated, p=0.0856, ns), 30 minutes (1.316±0.22 fold over unstimulated, p=0.2385, ns), 60 minutes (1.350±0.24 fold over unstimulated, p=0.2365, ns) and 120 minutes (1.296±0.13 fold over unstimulated, p=0.1152, ns). The time course results from five independent replicates (n=5) (Figure 5.6A, Bottom). Overall, stimulation of PAR4 with AYPGKF in MEG-01 cells does affect Cofilin's phosphorylation, although, due to variation within the data, it fails to achieve significance within these replicate experiments. However, it should be noted that at the peak of pCof at 15 minutes, the data fails to achieve significance with a p-value of 0.0896.

To determine the success of stimulation conditions, phosphorylation of ERK was used. Representative blots of the time course for p-ERK (top) and t-ERK (bottom) are shown in Figure 5.6B. Changes in band intensity can be seen from the 1-minute mark, showing an increase in pERK expression from baseline and sustaining the signal to 5 minutes before the decrease in signal is observable from 15 minutes until it reaches close to baseline at the 120-minute time point. Results were plotted and compared to the baseline (0mins), and statistical analysis was performed using the One-sample t-test, with the assumed hypothetical mean being 1, the same as the baseline. The time course showed 1 minute (2.781±0.34 fold over unstimulated, $p<0.05$ *, s) 2 minutes (2.577±0.56 fold over unstimulated, $p<0.05$ *, s), 5 minutes (2.317±0.48 fold over unstimulated, $p<0.05$ *, s), 15 minutes (1.518±0.23 fold over unstimulated, $p=0.0775$, ns), 30 minutes (1.476±0.15 fold over unstimulated, $p<0.05$ *, s), 60 minutes (1.325±0.14 fold over unstimulated, $p=0.0671$, ns) and 120 minutes (1.070±0.16 fold over unstimulated, $p=0.6814$, ns). The results are the average of five independent replicates (n=5) Figure 5.6B (bottom). Overall, stimulation of MEG-01 cells showed a significant increase in p-ERK at 1 min, 2 mins, 5 mins and 30 mins. The stimulation time course showed an initial rise in ERK phosphorylation at 1 minute with its peak signal intensity. From 2 minutes onwards, signal intensity declines to baseline throughout the time points. Results showed that increases in p-ERK over the stimulation time course meant that AYPGKF successfully induced downstream signalling cascades of PAR4 receptor activation and confirmed that results seen in p-Cof are reliable.

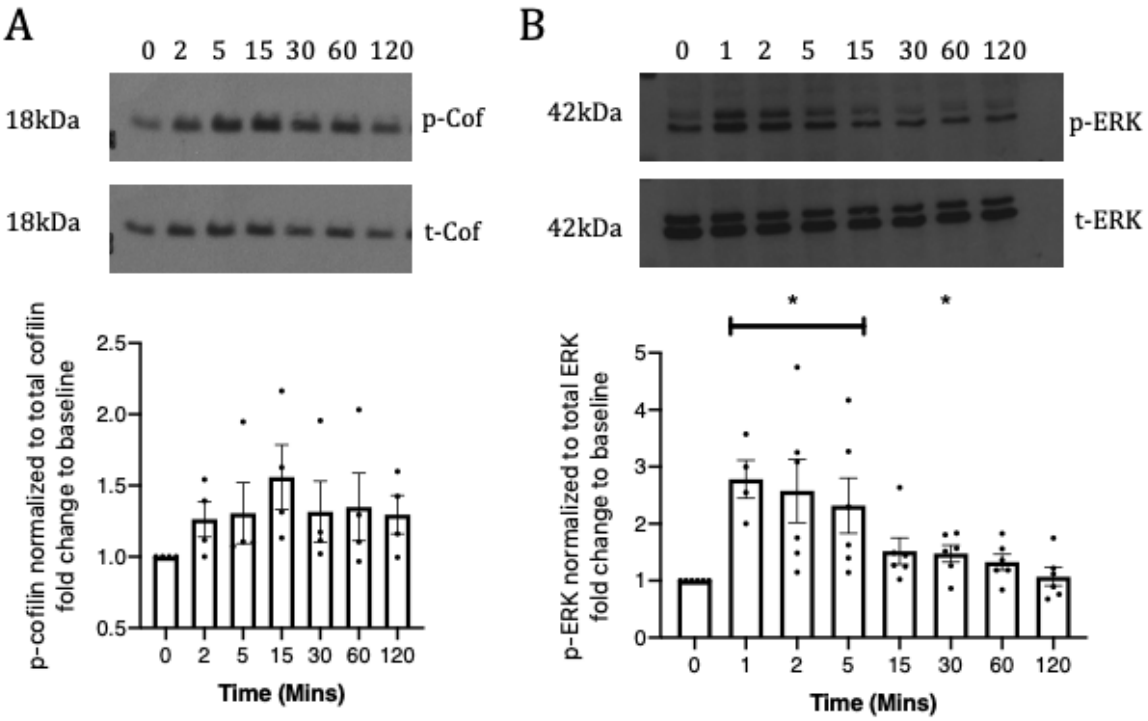

Figure 5.6 The effects on cofilin and ERK phosphorylation following stimulation of MEG-01 cells with 300 µM of PAR4-AP (AYPGKF-NH_2). A) shows representative western blot images of p-Cofilin (top) and loading control total-Cofilin (bottom) for the stimulation time course (0-120 minutes). Time points were compared with unstimulated (0 minutes) using One-sample t-test. B) shows representative western blot images of p-ERK (top) and loading control total-ERK (bottom) for the stimulation time course (0-120 minutes). Time points were compared with unstimulated (0 minutes) using One-sample t-test. Data are the mean ±SEM for the normalized signal from five independent replicates (n=5). The level of statistical significance is shown compared with the Unstimulated (0 minutes) control (* $p<0.05$, ** $p<0.01$, *** $p<0.001$, **** $p<0.0001$ and ns (not significant).

5.3.7 Stimulation of MEG-01 cells with thrombin or AYPGKF induces differing patterns of AKT phosphorylation.

Another canonical downstream signalling pathway of PAR activation is the phosphorylation of AKT. Having already shown that thrombin and AYPGKF show significant effects in the upregulation of pERK following stimulation of MEG-01 cells. We therefore looked to see the effect that stimulation of MEG-01 cells with either 1 U/mL of thrombin or 300 μM of AYPGKF had on phosphorylation of AKT over the time course of (0,1, 2, 5, 15, 30, 60 and 120 mins).

Representative blots of the thrombin-stimulated time course for pAKT (top) and tAKT (bottom) are shown in Figure 5.7A. The blots for pAKT appear to show an increase in signal density starting at 1 min until 5 mins, where after that, signal intensity appears to decline back towards baseline. Results were plotted and compared to the baseline (0mins), and statistical analysis was performed using the One-sample t-test, with the assumed hypothetical mean being 1, the same as the baseline. The time course showed; 1 minute (1.568±0.11 fold over unstimulated, $p<0.05$ *, s) 2 minutes (1.660±0.55 fold over unstimulated, $p=0.3195$, ns), 5 minutes (1.392±0.25 fold over unstimulated, $p=0.2170$, ns), 15 minutes (1.174±0.41 fold over unstimulated, $p=0.700$, ns), 30 minutes (1.020±0.27 fold over unstimulated, $p=0.9443$, ns), 60 minutes (0.7375±0.24 fold over unstimulated, $p=0.1127$, ns) and 120 minutes (0.8077±0.1 fold over unstimulated, $p=0.1524$, ns). The time course results from four independent replicates (n=4) (Figure 5.7A, left).

Representative blots of the AYPGKF stimulated time course for pAKT (top) and tAKT (bottom) are shown in Figure 5.7B (bottom, left). The blots for pAKT appear to show an increase in density much later than that of thrombin, with signal increases starting at 30 minutes and continuing until 120 minutes, where signal intensity remains higher than baseline. Results were plotted and compared to the baseline (0mins), and statistical analysis was performed using the One-sample t-test, with the assumed hypothetical mean being 1, the same

as the baseline. The time course showed; 1 minute (1.060±0.19 fold over unstimulated, p=0.7775, ns), 2 minutes (1.224±0.26 fold over unstimulated, p=0.4536, ns), 5 minutes (1.146±0.17 fold over unstimulated, p=0.4619, ns), 15 minutes (1.127±0.16 fold over unstimulated, p=0.4845, ns), 30 minutes (1.724±0.52 fold over unstimulated, p=0.2544, ns), 60 minutes (1.956±0.60 fold over unstimulated, p=0.2079, ns) and 120 minutes (1.774±0.46 fold over unstimulated, p=0.1930, ns). The time course results from four independent replicates (n=4) (Figure 5.7B, left).

These experiments showed that stimulation of MEG-01 cells affects the phosphorylation of AKT with a rapid decline back to baseline; what is interesting, however, is that stimulation of MEG-01 cells with AYPGKF showed a starkly different effect, with a very slow on for AKT phosphorylation beginning at 30 minutes post-stimulation. However, it was not a significant effect due to extensive variations in the data for AYPGKF-stimulated MEGs.

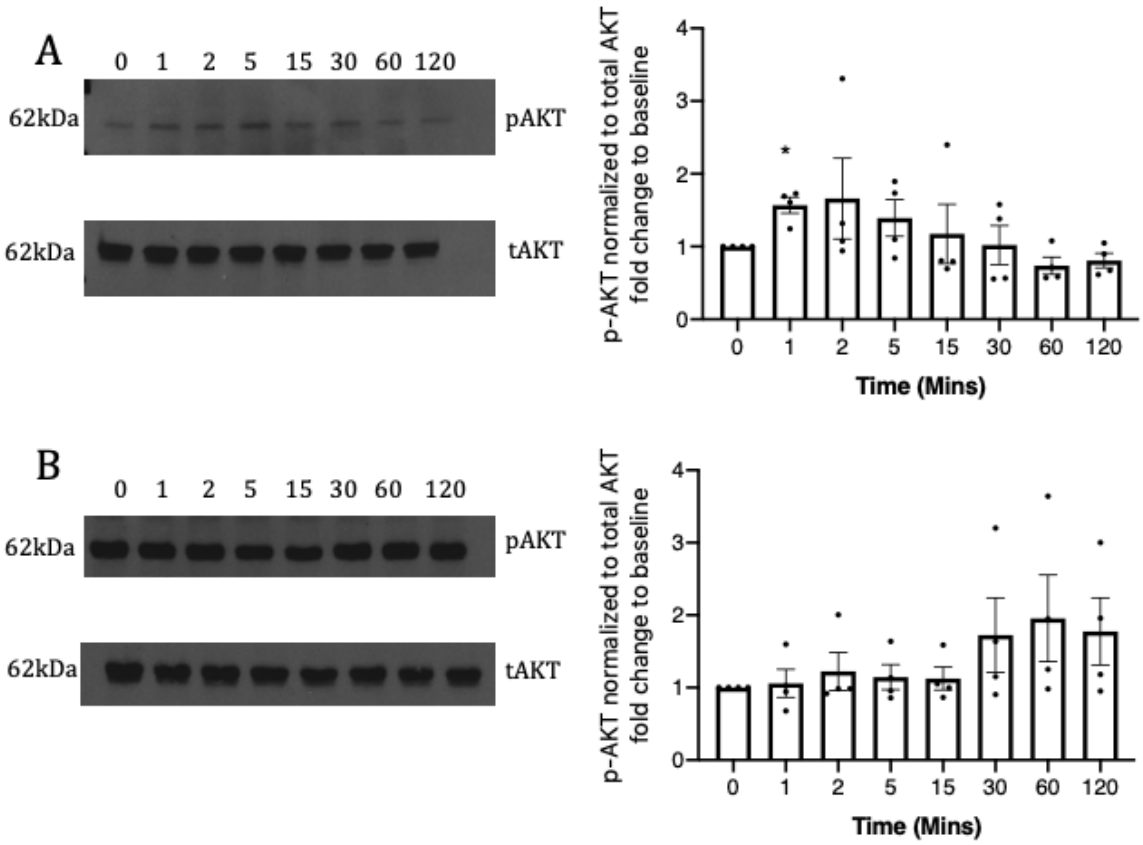

Figure 5.7 The effects on AKT phosphorylation following stimulation of MEG-01 cells with Thrombin or AYPGKF. A) shows representative western blot images of pAKT (top) and loading control tAKT (bottom) for the stimulation time course (0-120 minutes) with 1 U/mL of thrombin. Time points were compared with unstimulated (0 minutes) using One-sample t-test. B) shows representative western blot images of pAKT (top) and loading control tAKT (bottom) for the stimulation time course (0-120 minutes) with 300μM AYPGKF. Time points were compared with unstimulated (0 minutes) using One-sample t-test. Data are the mean ±SEM for the normalized signal from four independent replicates (n=4). The level of statistical significance is shown compared with the Unstimulated (0 minutes) control (* $p<0.05$, ** $p<0.01$, *** $p<0.001$, **** $p<0.0001$ and ns (not significant).

5.3.8 The effect varying concentrations of thrombin has on the phospho-regulation of Cofilin

As the previous experiments showed, the stimulation of MEG-01 cells with 1 U/mL of thrombin with the greatest quantifiable changes detected at the 5- and 15-minute time points. Therefore, we next aimed to determine if the concentration of thrombin used for the stimulation has a variance on the effect it exerts on MEG-01 cells. The stimulation time course used was (0mins (BL), 5 mins and 15 mins) across three concentrations of thrombin (0.3 U/mL, 1 U/mL and 3 U/mL).

Representative blots of the concentration-time course for p-Cof (top) and t-Cof (bottom) are shown in Figure 5.8 (left). The blots for pCof appear to show an increase in the density of phospho-Cofilin (0.3 U/mL, left), (1 U/mL, middle) and (3 U/mL, right) starting at 5 mins and reaching a peak at 15 mins across all three of the thrombin concentrations used. Results were plotted and compared to the baseline (0mins), and statistical analysis was performed using the One-sample t-test, with the assumed hypothetical mean being 1, the same as the baseline. The time course of 0.3 U/mL of thrombin showed for 5 minutes (1.738±0.25 fold over unstimulated, $p<0.05$ *, s) and 15 minutes (2.048±0.29 fold over unstimulated, $p<0.05$ *, s). The time course for 1 U/mL of thrombin showed for 5 minutes (1.317±0.068 fold over unstimulated, $p<0.05$ *, s) and 15 minutes (1.787±0.16 fold over unstimulated, $p<0.05$ *, s). The time course for 3 U/mL of thrombin showed for 5 minutes (1.512±0.07 fold over unstimulated, $p<0.05$ *, s) and 15 minutes (1.765±0.39 fold over unstimulated, $p=0.1893$, ns). The data is the result of five independent replicates (n=5) for 0.3 U/mL and 1 U/mL thrombin and three independent replicates (n=3) for 3 U/mL thrombin Figure 5.8 (right). Loss of replicate data for 3 U/mL resulted from the washed signal at the end of developed blots, resulting in blots that were hard to quantify.

These experiments showed that the effect thrombin excerpts on the phosphorylation of Cofilin is achieved at a variety of concentrations including

very low levels of ligand (0.3 U/mL). Interestingly, the greatest fold change in pCof levels was achieved at 0.3 U/mL (2.048±0.29 fold) at 15 minutes. These experiments confirm those seen previously that stimulation of MEG-01 cells with thrombin increases pCof levels to a peak at 15 minutes across a time course but also shows that the same effect can be achieved at a variety of thrombin concentrations, including low levels of thrombin.

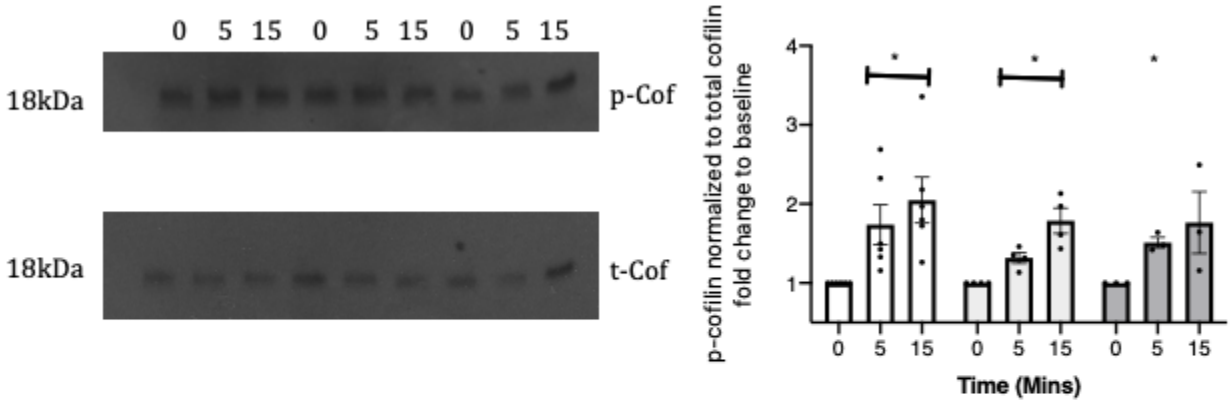

Figure 5.8 The effects on cofilin phosphorylation following stimulation of MEG-01 cells with increasing concentrations of Thrombin (0.3, 1, 3UmL). Left shows representative western blot images of p-Cofilin (top) and loading control total-Cofilin (bottom) for the stimulation time course (0, 5 and 15 minutes). Concentrations of thrombin used (0.3 U/mL, left three), (1 U/mL, middle three) and (3 U/mL, right three). Time points were compared with unstimulated (0 minutes) using One-sample t-test (right). Data are the mean ±SEM for the normalized signal from five independent replicates (n=5) for 0.3 U/mL and 1 U/mL thrombin and three independent replicates (n=3) for 3 U/mL thrombin. The level of statistical significance is shown compared with the Unstimulated (0 minutes) control (* $p<0.05$, ** $p<0.01$, *** $p<0.001$, **** $p<0.0001$ and ns (not significant).

5.3.9 The effect varying concentrations of PAR1-AP (TFLRRN) and PAR4-AP (AYPGKF) has on the phospho-regulation of Cofilin

As was shown in the previous experiment, stimulation of MEG-01 cells with PAR1-AP TFLRRN at a concentration of 100 μM showed no increase in the phosphorylation of Cofilin over the entirety of the time course. However, given the potency of TFLRRN, it was hypothesised that there was the potential for saturation at 100 μM. Therefore, we tested three additional concentrations of TFLRRN (1 μM, 10 μM, 30 μM and 100 μM) over the time course of (0mins (BL), 5 mins and 15 mins).

Representative blots of the concentration-time course for p-Cof (top) and t-Cof (bottom) are shown in Figure 5.9A (left). The blots for pCof appear to show no apparent increase in the density of phospho-Cofilin bands at (1 μM, left), (10 μM, left middle), (30 μM, right middle) and (100 μM, right). Results were plotted and compared to the baseline (0mins), and statistical analysis was performed using the One-sample t-test, with the assumed hypothetical mean being 1, the same as the baseline. The time course of 1 μM of TFLRRN showed for 5 minutes (1.066±0.04 fold over unstimulated, p=0.1565, ns) and 15 minutes (0.9429±0.11 fold over unstimulated, p=0.6438, ns). The time course of 10 μM of TFLRRN showed for 5 minutes (1.020±0.15 fold over unstimulated, p=0.8954, ns) and 15 minutes (0.9639±0.14 fold over unstimulated, p=0.8070, ns). The time course of 30 μM of TFLRRN showed for 5 minutes (0.9285±0.09 fold over unstimulated, p=0.4700, ns) and 15 minutes (0.9109±0.07 fold over unstimulated, p=0.2558, ns). The time course of 100 μM of TFLRRN showed for 5 minutes (0.9268±0.09 fold over unstimulated, p=0.4437, ns) and 15 minutes (0.8895±0.12 fold over unstimulated, p=0.3958, ns). The data results from five independent replicates (n=5) (Figure 5.9A, right).

The previous stimulation time course of MEG-01 cells with PAR4-AP (AYPGKF) showed a similar Cofilin phosphorylation trajectory observed in thrombin-stimulated MEGs. However, it failed to achieve significance due to greater variation in the data as opposed to thrombin. Therefore, we aimed at

testing different concentrations of AYPGKF (100 μM, 300 μM and 500 μM) to see if the concentration of AYPGKF had differing effects on Cofilin phosphorylation across the time points where pCof levels showed the greatest change to baseline. The time points used were (0 (BL), 5 and 15 mins) across the three concentrations of AYPGKF used.

Representative blots of the concentration-time course for p-Cof (top) and t-Cof (bottom) are shown in Figure 5.9B (left). The blots for pCof appear to show an increase in the density of the bands for phospho-Cofilin (100 μM, left), (300 μM, middle) and (500 μM, right) starting at 5 mins and reaching a peak at 15 mins across all three of the AYPGKF concentrations used. Results were plotted and compared to the baseline (0mins), and statistical analysis was performed using the One-sample t-test, with the assumed hypothetical mean being 1, the same as the baseline. The time course of 100 μM of AYPGKF showed for 5 minutes (1.312±0.04 fold over unstimulated, $p<0.001$ ***, s) and 15 minutes (1.379±0.07 fold over unstimulated, $p<0.01$ **, s). The time course of 300 μM of AYPGKF showed for 5 minutes (1.230±0.01 fold over unstimulated, $p<0.0001$ ****, s) and 15 minutes (1.343±0.06 fold over unstimulated, $p<0.01$ **, s). The time course of 500 μM of AYPGKF showed for 5 minutes (1.137±0.04 fold over unstimulated, $p<0.05$ *, s) and 15 minutes (1.251±0.07 fold over unstimulated, $p<0.05$ *, s). The data results from five independent replicates (n=5) (Figure 5.9B, right).

Despite using various concentrations of TFLRRN, it failed to induce any detectable change in the phosphorylation state of Cofilin across any of the concentrations used for the 5-minute and 15-minute time points. Although generally, some actual declines from baseline on average weren't significant and could more signify human error than genuine decreases in pCof expression induced by TFLRRN. In addition, these experiments added a further level of robustness to the assumptions that PAR1 doesn't excerpt its effect on Cofilin proteins, and, therefore, the results seen in the thrombin-stimulated time course are most likely driven by the activation of PAR4.

The original stimulation time course of MEG-01 cells with AYPGKF showed increased pCof expression to a peak at 15 minutes, the same as thrombin. However, due to variations in the data, it failed to achieve significance. This experiment showed an increase in pCof expression across all concentrations of AYPGKF used achieving a peak at 15 mins. However, interestingly, all three concentrations used achieved a significant increase in the time points analysed, with the 300 μM achieving the most significant degree of significance. This experiment confirmed that changes in pCof expression seen in thrombin-stimulated MEGs are most likely driven by the activation of PAR4 and that modulation of actin dynamics through PARs is mediated predominantly by PAR4.

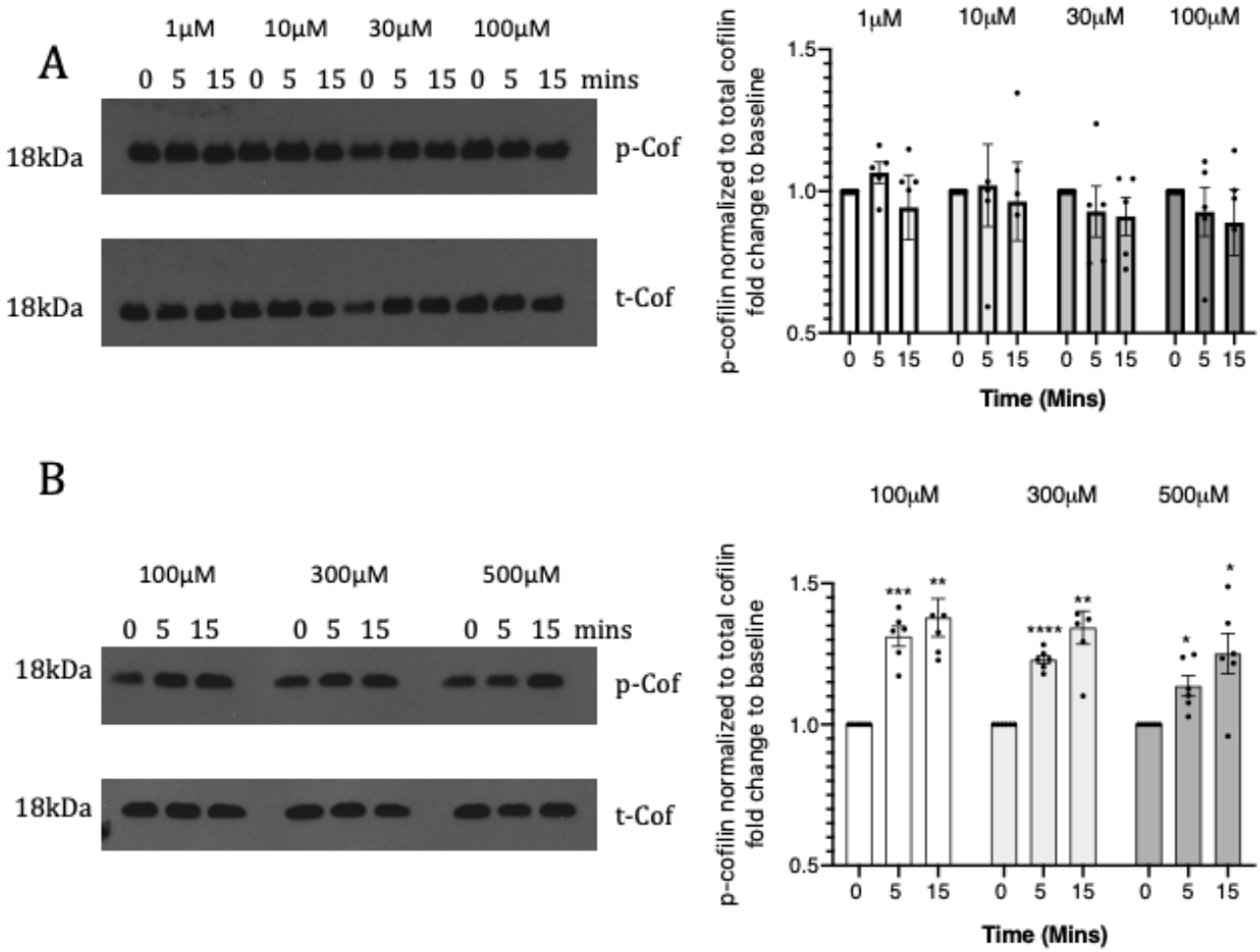

Figure 5.9. The effects on cofilin phosphorylation following stimulation of MEG-01 cells with increasing concentrations of PAR1-AP (1μM, 10μM, 30μM and 100 μM) and PAR4-AP (100 μM, 300μM and 500μM). A) Left shows representative western blot images of p-Cofilin (top) and loading control total-Cofilin (bottom) for the stimulation time course (0, 5 and 15 minutes). Concentrations of PAR1-AP used (1μM, 10μM, 30μM and 100 μM), (1μM, left three), (10μM, left middle three), (30μM, right middle three) and (100 μM, left three). Time points were compared with unstimulated (0 minutes) using One-sample t-test (right). B) Left shows representative western blot images of p-Cofilin (top) and loading control total-Cofilin (bottom) for the stimulation time course (0, 5, 15 minutes). Concentrations of PAR4-AP used (100 μM, 300μM and 500μM), (100 μM left three), (300μM middle three) and (500μM right three). Time points were compared with unstimulated (0 minutes) using One-sample t-test (right). Data are the mean ±SEM for the normalized signal from five independent replicates (n=5). The level of statistical significance is shown compared with the Unstimulated (0 minutes) control (* $p<0.05$, ** $p<0.01$, *** $p<0.001$, **** $p<0.0001$ and ns (not significant).

5.3.10 The effect of thrombin stimulation of MEG-01 cells on upstream phosphorylators of Cofilin (LIMK2 and ROCK1)

Given that stimulation of MEG-01 cells with thrombin was shown to significantly affect the phosphorylation of Cofilin over a time course, with significance also shown in the thrombin concentration gradient experiment, we next aimed at looking at the effect that thrombin would have on Cofilin phosphorylating proteins (LIMK2 and ROCK1) over a time course of (0 – 120 mins). MEG-01 cells were stimulated with 1 U/mL of thrombin at the following timepoints (0, 1, 2, 5, 15, 30, 60, 120 mins).

The first of the Cofilin phosphorylators we looked at was LIMK2. Representative blots of the time course are shown in (Figure 5.10A). The blots show an increase in LIMK2 from baseline beginning at 1 minute and reaching a peak in expression at 15 minutes before the signal decreases at 30 minutes back towards baseline over the remainder of the time course. Results were plotted and compared to the baseline (0mins), and statistical analysis was performed using the One-sample t-test, with the assumed hypothetical mean being 1, the same as the baseline. The time course showed; 1 minute (1.279±0.16 fold over unstimulated, p=0.1613, ns), 2 minutes (1.069±0.18 fold over unstimulated, p=0.7213, ns), 5 minutes (1.090±0.20 fold over unstimulated, p=0.6772, ns), 15 minutes (1.323±0.23 fold over unstimulated, p=0.2400, ns), 30 minutes (1.088±0.14 fold over unstimulated, p=0.5739, ns), 60 minutes (0.9637±0.11 fold over unstimulated, p=0.7642, ns) and 120 minutes (1.119±0.07 fold over unstimulated, p=0.1563, ns). The time course results from four independent replicates (n=4) (Figure 5.10A, Bottom).

We also looked at the effect thrombin stimulation had on ROCK1, which is the protein directly upstream of LIMK2 and is responsible for phosphorylating LIMK, allowing it to excerpt its effects on Cofilin. Representative blots of the time course are shown in (Figure 5.10B). The blots show an initial increase of ROCK1 from baseline beginning at 1 min before declining again at 2 mins; band intensity increases again at 5 mins with a peak at 15 mins before

declining again back towards baseline over the remainder of the time course. Results were plotted and compared to the baseline (0mins), and statistical analysis was performed using the One-sample t-test, with the assumed hypothetical mean being 1, the same as the baseline. The time course showed; 1 minute (1.555±0.36 fold over unstimulated, p=0.2007, ns), 2 minutes (1.148±0.21 fold over unstimulated, p=0.5200, ns), 5 minutes (1.446±0.23 fold over unstimulated, p=0.1221, ns), 15 minutes (1.404±0.13 fold over unstimulated, p<0.05 *, s), 30 minutes (1.289±0.15 fold over unstimulated, p=0.1225, ns), 60 minutes (1.195±0.14 fold over unstimulated, p=0.2395, ns) and 120 minutes (1.605±0.51 fold over unstimulated, p=0.2993, ns). The time course results from four independent replicates (n=4) (Figure 5.10B, Bottom).

This experiment showed that stimulation of MEG-01 cells with thrombin does affect the main Cofilin phosphorylator LIMK; however, due to variation in the data, none of the time points achieved significance. The pattern of increased protein expression follows the same pattern as that of Cofilin phosphorylation, reaching a peak at 15 minutes before declining back to baseline. The 15-minute time point showed the greatest increase in LIMK expression, further suggesting that stimulation of the PAR4 receptor in MEG-01 cells has downstream effects on the Cofilin pathway and actin dynamics. However, ROCK1 showed a similar pattern of increased expression as LIMK, although the increase in expression at 15 minutes was significant in this case.

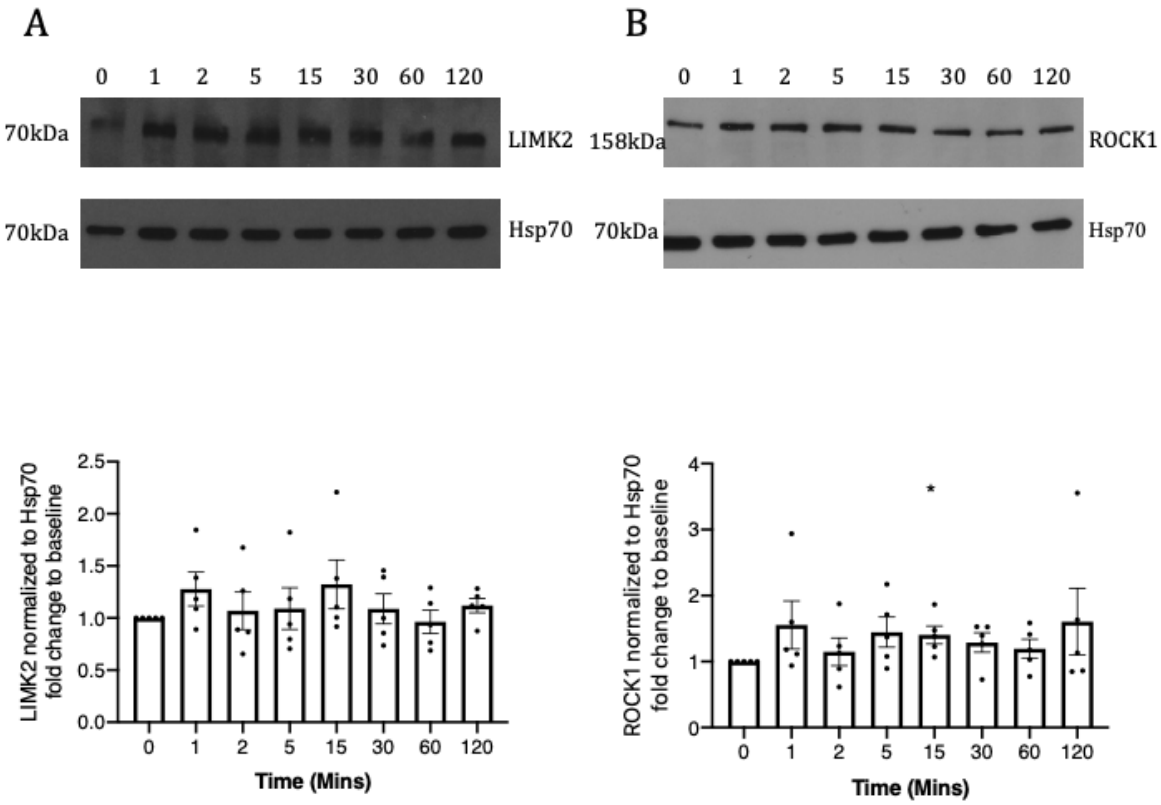

Figure 5.10 The effects on Cofilin phosphorylating proteins (LIMK and ROCK) following stimulation of MEG-01 cells with Thrombin. A) shows representative western blot images of LIMK2 (top) and loading control Hsp70 (bottom) for the stimulation time course (0-120 minutes) with 1 U/mL of Thrombin. Time points were compared with unstimulated (0 minutes) using One-sample t-test. B) shows representative western blot images of ROCK1 (top) and loading control Hsp70 (bottom) for the stimulation time course (0-120 minutes) with 1 U/mL Thrombin. Time points were compared with unstimulated (0 minutes) using One-sample t-test. Data are the mean ±SEM for the normalized signal from four independent replicates (n=4). The level of statistical significance is shown compared with the Unstimulated (0 minutes) control (* $p<0.05$, ** $p<0.01$, *** $p<0.001$, **** $p<0.0001$ and ns (not significant).

5.3.11 The effect of Thrombin stimulation of MEG-01 cells on upstream phosphorylator of Cofilin (TESK)

Given that the previous experiment showed that stimulation of MEG-01 cells with thrombin has a significant effect on ROCK1 and did change the expression of LIMK2 (although not significant), we next looked at the other Cofilin phosphorylator TESK1 over a time course of (0 – 120 mins). MEG-01 cells were stimulated with 1 U/mL of thrombin at the following timepoints (0, 1, 2, 5, 15, 30, 60, 120 mins).

Representative blots of the time course are shown in (Figure 5.11A) TESK1 shows a double band pattern (top) with Hsp70 used as a loading control (bottom). The blots for the upper band appear to show an initial increase in expression, starting at 1 minute to 2 minutes compared to baseline before returning to baseline signal at 5 minutes and then declining to below baseline for the remainder of the time course. In comparison, the lower band shows an initial increase in expression until 5 minutes before beginning to decline at 15 minutes below baseline by the end of the time course. The upper band Results were plotted and compared to the baseline (0mins), and statistical analysis was performed using the One-sample t-test, with the assumed hypothetical mean being 1, the same as the baseline. The time course showed; 1 minute (1.012±0.18 fold over unstimulated, p=0.9508, ns), 2 minutes (1.200±0.25 fold over unstimulated, p=0.4862, ns), 5 minutes (1.058±0.25 fold over unstimulated, p=0.8297, ns), 15 minutes (0.9653±0.21 fold over unstimulated, p=0.8801, ns), 30 minutes (0.8839±0.18 fold over unstimulated, p=0.5692, s), 60 minutes (0.6122±0.07 fold over unstimulated, p<0.05 *, s) and 120 minutes (0.7902±0.18 fold over unstimulated, p=0.1074, ns). The time course results from four independent replicates (n=4) (Figure 5.11B).

The lower band Results were plotted and compared to the baseline (0mins), and statistical analysis was performed using the One-sample t-test, with the assumed hypothetical mean being 1, the same as the baseline. The time course showed; 1 minute (0.9616±0.25 fold over unstimulated, p=0.8896, ns),

2 minutes (1.288±0.27 fold over unstimulated, p=0.3671, ns), 5 minutes (1.712±0.58 fold over unstimulated, p=0.3039, ns), 15 minutes (1.104±0.36 fold over unstimulated, p=0.7944, ns), 30 minutes (1.142±0.15 fold over unstimulated, p=0.4126, s), 60 minutes (1.024±0.33 fold over unstimulated, p=0.9451, ns) and 120 minutes (0.6729±0.23 fold over unstimulated, p=0.2580, ns). The time course results from four independent replicates (n=4) (Figure 5.11B).

This experiment showed that stimulation of MEG-01 cells with AYPGKF affects the other Cofilin phosphorylator TESK1; interestingly these were the result of a decrease in expression of TESK1 on the upper band at 60 mins. However, the signal begins to drop below baseline at 15 mins, which coincides with peak phosphorylation of Cofilin and for the lower band at 30 mins post-stimulation.

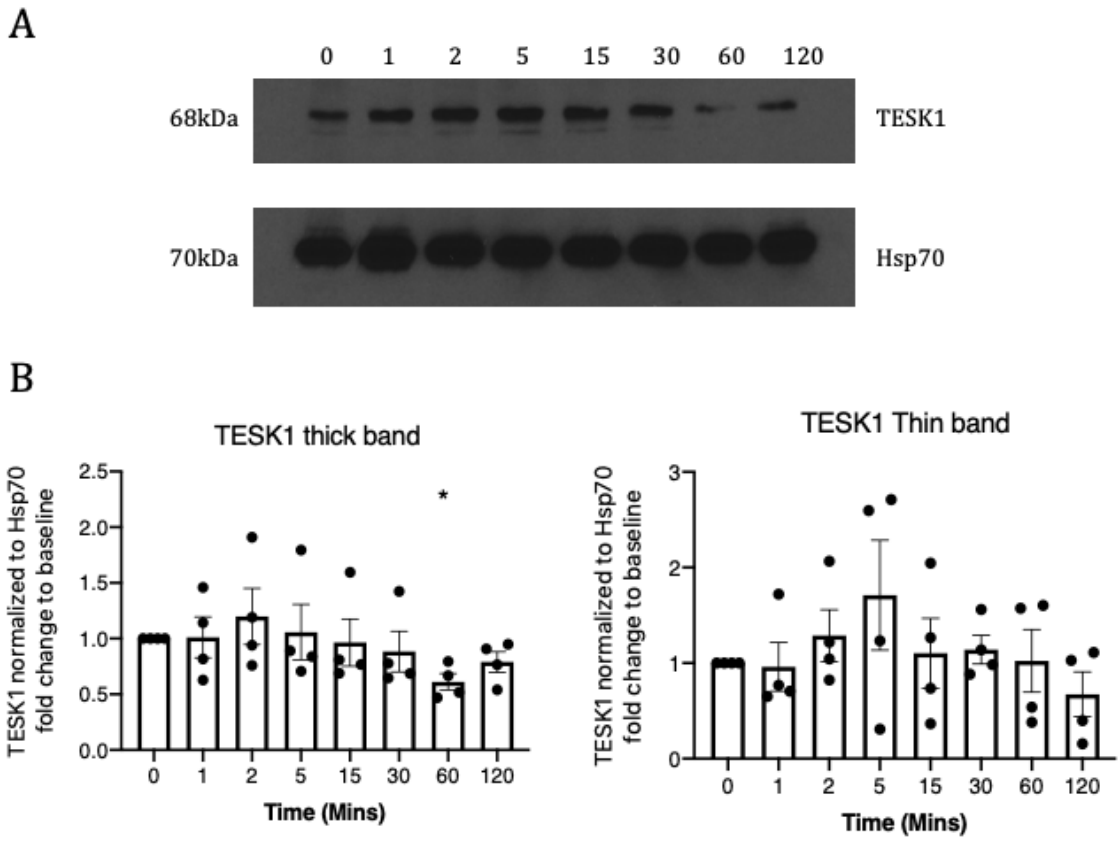

Figure 5.11 The effects on Cofilin inactivator (TESK1) following stimulation of MEG-01 cells with Thrombin. A) shows representative western blot images of TESK1 (top) and loading control Hsp70 (bottom) for the stimulation time course (0-120 minutes) with 1 U/mL of Thrombin. B) Time points were compared with unstimulated (0 minutes) using One-sample t-test, first the top thick band (left) and time points were compared with unstimulated (0 minutes) using One-sample t-test, the bottom thin band (right). Data are the mean ±SEM for the normalized signal from four independent replicates (n=4). The level of statistical significance is shown compared with the Unstimulated (0 minutes) control (* $p<0.05$, ** $p<0.01$, *** $p<0.001$, **** $p<0.0001$ and ns (not significant).

5.3.12 The effects on Cofilin phosphatases (activators) following stimulation of MEG-01 cells with Thrombin.

Given that stimulation of MEG-01 cells with thrombin was shown to have a significant effect on the phosphorylation of Cofilin over a time course, with significance also shown in the thrombin concentration gradient experiment. We next looked at the effect that thrombin would have on Cofilin phosphatases (SSH1 and PDXP) over a time of (0 – 120 minutes). MEG-01 cells were stimulated with 1 U/mL of thrombin at the following timepoints (0, 1, 2, 5, 15, 30, 60, 120 mins).

The first of the Cofilin phosphatases we looked at was SSH1. Representative blots of the time course are shown in (Figure 5.12A). The blots show a slight decline in expression at 1 and 2 minutes before expression increases above baseline at 5 minutes before declining to less than baseline at 30 minutes and 60 minutes before returning to baseline at 120 minutes. Results were plotted and compared to the baseline (0mins), and statistical analysis was performed using the One-sample t-test, with the assumed hypothetical mean being 1, the same as the baseline. The time course showed; 1 minute (0.9673±0.11 fold over unstimulated, p=0.8014, ns), 2 minutes (0.9026±0.29 fold over unstimulated, p=0.7678, ns), 5 minutes (1.152±0.37 fold over unstimulated, p=0.7168, ns), 15 minutes (0.8372±0.17 fold over unstimulated, p=0.4462, ns), 30 minutes (0.8141±0.08 fold over unstimulated, p=0.1490, ns), 60 minutes (0.8549±0.19 fold over unstimulated, p=0.5252, ns) and 120 minutes (1.058±0.18 fold over unstimulated, p=0.7771, ns). The time course results from three independent replicates (n=3) (Figure 5.12A, Bottom).

The other of the Cofilin phosphatases we looked at was PDXP. Representative blots of the time course are shown in (Figure 5.12B). The blots show an initial drop in expression at 1 and 2 mins before steadily raising to 5 mins and remaining relatively stable below baseline for the remainder of the time course. Results were plotted and compared to the baseline (0mins), and statistical analysis was performed using the One-sample t-test, with the assumed

hypothetical mean being 1, the same as the baseline. The time course showed; 1 minute (0.9086±0.04 fold over unstimulated, p=0.0837, ns) 2 minutes (0.6938±0.1 fold over unstimulated, p<0.05 *, s), 5 minutes (0.8043±0.09 fold over unstimulated, p=0.1077, ns), 15 minutes (0.7775±0.06 fold over unstimulated, p<0.05 *, s), 30 minutes (0.7472±0.05 fold over unstimulated, p<0.05 *, s), 60 minutes (0.7516±0.06 fold over unstimulated, p<0.05 *, s) and 120 minutes (0.7678±0.08 fold over unstimulated, p=0.0580, ns). The time course results from four independent replicates (n=4) (Figure 5.12B, Bottom).

This experiment showed that stimulation of MEG-01 cells with thrombin affects Cofilin activators. There was a decrease in the expression of SSH at 30 minutes, although, due to variation in the data, it failed to achieve significance. Interestingly, PDXP also showed decreases in expression throughout the stimulation time course, with several time points showing significant decreases in expression. Most significant decreases in protein expression occurred at (2 mins, 15 mins, 30 mins and 60 mins). From 15 mins onwards, when Cofilin phosphorylation began to return to baseline after the 15 mins mark, the decrease in SSH and PDXP expression beyond this could be the result of protein degradation following its dephosphorylation of Cofilin.

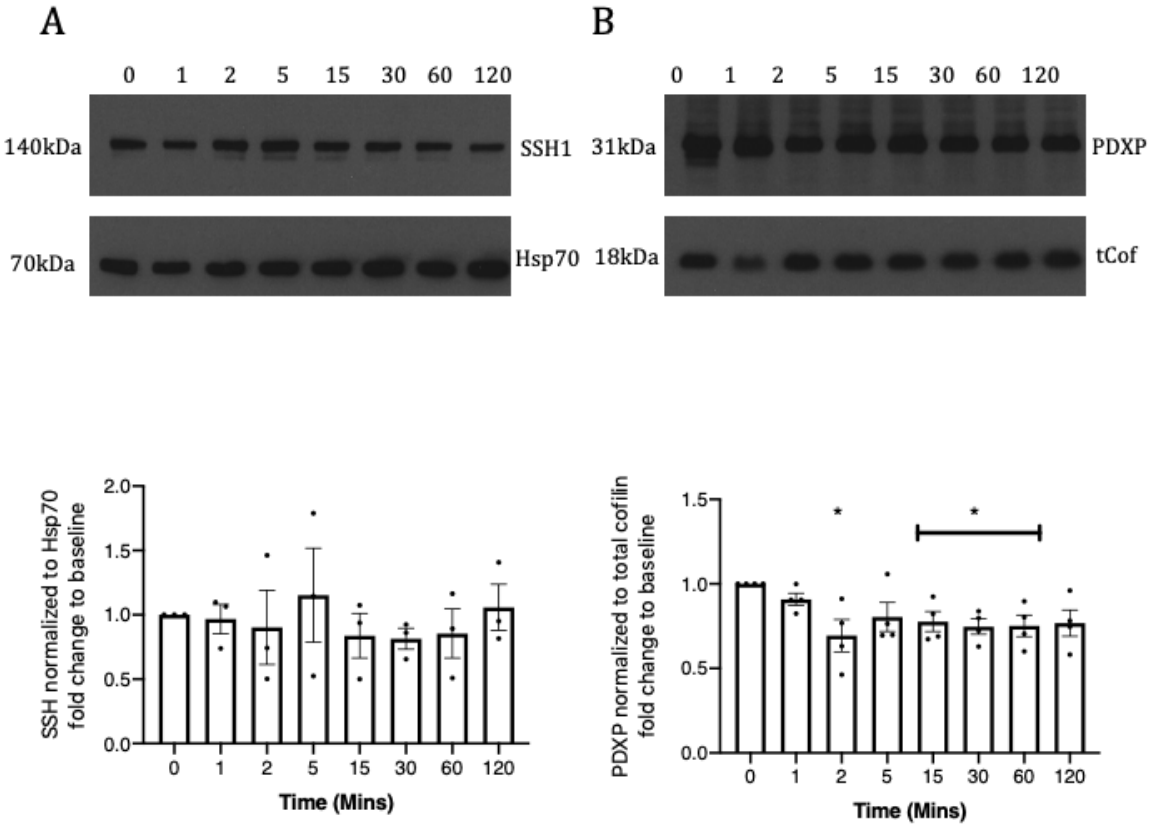

Figure 5.12. The effects on Cofilin phosphatases (SSH and PDXP) following stimulation of MEG-01 cells with Thrombin. A) shows representative western blot images of SSH (top) and loading control Hsp70 (bottom) for the stimulation time course (0-120 minutes) with 1 U/mL of Thrombin. Time points were compared with unstimulated (0 minutes) using One-sample t-test. B) shows representative western blot images of PDXP (top) and loading control tCof (bottom) for the stimulation time course (0-120 minutes) with 1 U/mL Thrombin. Time points were compared with unstimulated (0 minutes) using One-sample t-test. Data are the mean ±SEM for the normalized signal from three independent replicates (n=3) for SHH and from four independent replicates (n=4) for PDXP. The level of statistical significance is shown compared with the Unstimulated (0 minutes) control (* $p<0.05$, ** $p<0.01$, *** $p<0.001$, **** $p<0.0001$ and ns (not significant).

5.3.13 The effect of AYPGKF stimulation of MEG-01 cells on upstream phosphorylates of Cofilin (LIMK2 and ROCK1)

Given that stimulation of MEG-01 cells with AYPGKF was shown to affect Cofilin's phosphorylation over a time course (although not significant), significance was shown in the AYPGKF concentration gradient experiment. We next aimed to look at the effect that stimulation of MEG-01 cells with AYPGKF had on upstream negative regulators of Cofilin activity (LIMK2 and ROCK1) over a time course of (0 – 120 mins). MEG-01 cells were stimulated with 300 μM of AYPGKF at the following timepoints (0, 1, 2, 5, 15, 30, 60, 120 mins).

The first of the Cofilin phosphorylators we looked at was LIMK2. Representative blots of the time course are shown in (Figure 5.13A). The blots show an increase in LIMK2 from baseline beginning at 1 minute and reaching a peak in expression at 15 minutes before the signal decreases at 30 minutes back towards baseline over the remainder of the time course. Results were plotted and compared to the baseline (0mins), and statistical analysis was performed using the One-sample t-test, with the assumed hypothetical mean being 1, the same as the baseline. The time course showed; 1 minute (1.198±0.06 fold over unstimulated, $p<0.05$ *, s), 2 minutes (1.262±0.19 fold over unstimulated, $p=0.2648$, ns), 5 minutes (1.202±0.17 fold over unstimulated, $p=0.3294$, ns), 15 minutes (1.353±0.06 fold over unstimulated, $p<0.01$ **, s), 30 minutes (1.260±0.15 fold over unstimulated, $p=0.1886$, ns), 60 minutes (1.345±0.23 fold over unstimulated, $p=0.2273$, ns) and 120 minutes (1.224±0.26 fold over unstimulated, $p=0.4592$, ns). The time course results from four independent replicates (n=4) (Figure 5.13A, Bottom).

We also looked at the effect AYPGKF stimulation had on ROCK1, which is the protein directly upstream of LIMK2 and is responsible for phosphorylating LIMK, allowing it to excerpt its effects on Cofilin. Representative blots of the time course are shown in (Figure 5.13B). The blots show an initial increase of ROCK1 from baseline beginning at 1 min before declining again at 2 mins;

band intensity increases again at 5 mins with a peak at 15 mins before declining again back towards baseline over the remainder of the time course. Results were plotted and compared to the baseline (0mins), and statistical analysis was performed using the One-sample t-test, with the assumed hypothetical mean being 1, the same as the baseline. The time course showed; 1 minute (1.394±0.29 fold over unstimulated, p=0.2739, ns), 2 minutes (1.008±0.24 fold over unstimulated, p=0.9496, ns), 5 minutes (1.190±0.23 fold over unstimulated, p=0.4712, ns), 15 minutes (1.468±0.29 fold over unstimulated, p=0.4053, s), 30 minutes (1.284±0.32 fold over unstimulated, p=0.4426, ns), 60 minutes (1.111±0.25 fold over unstimulated, p=0.6892, ns) and 120 minutes (1.020±0.20 fold over unstimulated, p=0.9262, ns). The time course results from four independent replicates (n=4) (Figure 5.13B, Bottom). This experiment showed that stimulation of MEG-01 cells with AYPGKF significantly affects the main Cofilin phosphorylator LIMK. The pattern of increased protein expression follows the same pattern as that of Cofilin phosphorylation, reaching a peak at 15 minutes before declining back to baseline. The 15-minute time point showed the most significant increase in LIMK expression, which further suggests that stimulation of the PAR4 receptor in MEG-01 cells has downstream effects on the Cofilin pathway and actin dynamics. However, in the case of ROCK1, although it showed a similar pattern of increased expression as LIMK, as would be expected, none of the time points achieved significance in these experiments.

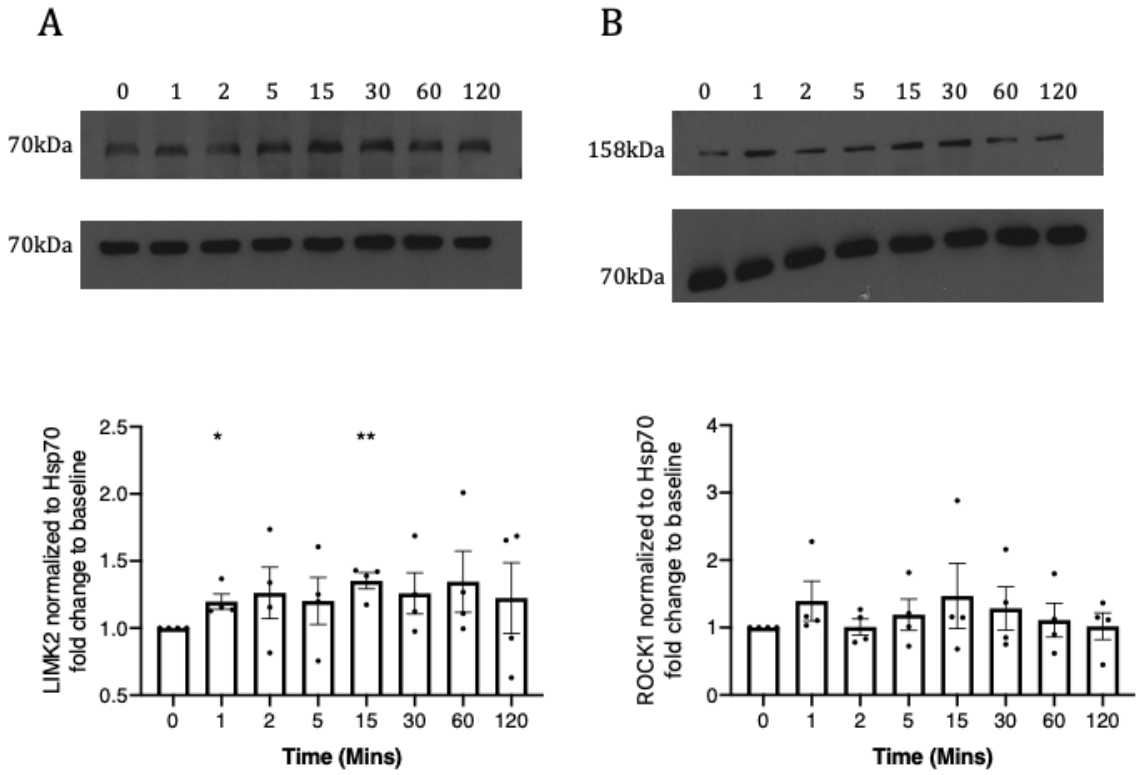

Figure 5.13. The effects on Cofilin phosphorylating proteins (LIMK and ROCK) following stimulation of MEG-01 cells with AYPGKF. A) shows representative western blot images of LIMK2 (top) and loading control Hsp70 (bottom) for the stimulation time course (0-120 minutes) with 300μM of AYPGKF. Time points were compared with unstimulated (0 minutes) using One-sample t-test. B) shows representative western blot images of ROCK1 (top) and loading control Hsp70 (bottom) for the stimulation time course (0-120 minutes) with 300μM AYPGKF. Time points were compared with unstimulated (0 minutes) using One-sample t-test. Data are the mean ±SEM for the normalized signal from four independent replicates (n=4). The level of statistical significance is shown compared with the Unstimulated (0 minutes) control (* $p<0.05$, ** $p<0.01$, *** $p<0.001$, **** $p<0.0001$ and ns (not significant).

5.3.14 The effect of AYPGKF stimulation of MEG-01 cells on upstream phosphorylator of Cofilin (TESK)

Given that the previous experiment showed that stimulation of MEG-01 cells with AYPGKF has a significant effect on LIMK2, we next looked at the other Cofilin phosphorylator TESK1 over a time course of (0 – 120 mins). MEG-01 cells were stimulated with 300 μM of AYPGKF at the following timepoints (0, 1, 2, 5, 15, 30, 60, 120 mins).

Representative blots of the time course are shown in (Figure 5.14A) TESK1 shows a double band pattern (top) with Hsp70 used as a loading control (bottom). The blots for the upper band appear to show a decrease in expression starting at 1 minute to 30 minutes compared to baseline before returning to baseline signal at 60 minutes for the remainder of the time course. At the same time, the lower band appears to remain steady at the beginning of the time course before showing a significant decrease in expression from 15 minutes for the remainder of the time course. The upper band Results were plotted and compared to the baseline (0mins), and statistical analysis was performed using the One-sample t-test, with the assumed hypothetical mean being 1, the same as the baseline. The time course showed; 1 minute (0.7633±0.10 fold over unstimulated, p=0.1169, ns), 2 minutes (0.6894±0.14 fold over unstimulated, p=0.1042, ns), 5 minutes (0.7241±0.10 fold over unstimulated, p=0.0756, ns), 15 minutes (0.6614±0.07 fold over unstimulated, p<0.05 *, s), 30 minutes (0.6809±0.08 fold over unstimulated, p<0.05 *, s), 60 minutes (0.9009±0.11 fold over unstimulated, p=0.4506, ns) and 120 minutes (0.9113±0.06 fold over unstimulated, p=0.2337, ns). The time course results from four independent replicates (n=4) (Figure 5.14B).

The lower band Results were plotted and compared to the baseline (0mins), and statistical analysis was performed using the One-sample t-test, with the assumed hypothetical mean being 1, the same as the baseline. The time course showed; 1 minute (1.099±0.5 fold over unstimulated, p=0.8556, ns), 2 minutes (1.116±0.46 fold over unstimulated, p=0.8197, ns), 5 minutes

(1.061±0.32 fold over unstimulated, p=0.8612, ns), 15 minutes (0.5889±0.13 fold over unstimulated, p=0.0538, ns), 30 minutes (0.6194±0.16 fold over unstimulated, p=0.1043, s), 60 minutes (0.5281±0.08 fold over unstimulated, p<0.05 *, s) and 120 minutes (0.7629±0.16 fold over unstimulated, p=0.2396, ns). The time course results from four independent replicates (n=4) (Figure 5.14B).

This experiment showed that stimulation of MEG-01 cells with AYPGKF affects the other Cofilin phosphorylator TESK1. Interestingly, these were the result of a decrease in expression of TESK1 at both bands (at different times), with the upper band showing significant decreases at 15 mins and 30 mins, which coincides with peak phosphorylation of Cofilin and for the lower band at 60 mins post-stimulation.

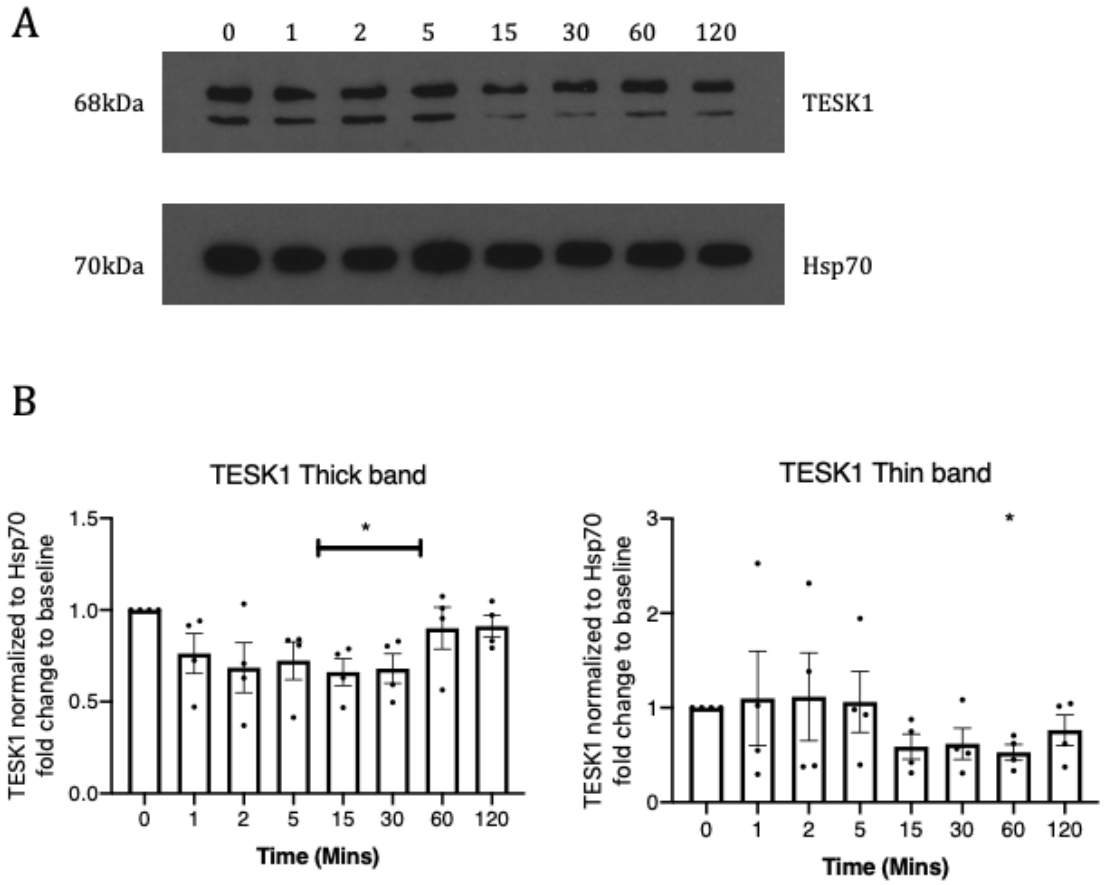

Figure 5.14. The effects on Cofilin inactivator (TESK1) following stimulation of MEG-01 cells with AYPGKF. A) shows representative western blot images of TESK1 (top) and loading control Hsp70 (bottom) for the stimulation time course (0-120 minutes) with 300μM of AYPGKF. B) Time points were compared with unstimulated (0 minutes) using One-sample t-test the time points were compared with unstimulated (0 minutes) using One-sample t-test, the bottom thin band (right). Data are the mean ±SEM for the normalized signal from four independent replicates (n=4). The level of statistical significance is shown compared with the Unstimulated (0 minutes) control (* $p<0.05$, ** $p<0.01$, *** $p<0.001$, **** $p<0.0001$ and ns (not significant).

5.3.15 The effects on Cofilin phosphatases (activators) following stimulation of MEG-01 cells with AYPGKF.

Given that stimulation of MEG-01 cells with AYPGKF was shown to affect Cofilin's phosphorylation over a time course (although not significant), significance was shown in the AYPGKF concentration gradient experiment. We next looked at the effect that AYPGKF would have on Cofilin phosphatases (SSH1 and PDXP) over a time of (0 – 120 minutes). MEG-01 cells were stimulated with 300 μM of AYPGKF at the following timepoints (0, 1, 2, 5, 15, 30, 60, 120 mins).

The first of the Cofilin phosphatases we looked at was SSH1. Representative blots of the time course are shown in (Figure 5.15A). The blots show a steady state of expression before expression levels drop to 30 minutes, remaining below baseline expression until the end of the experiment. Results were plotted and compared to the baseline (0mins), and statistical analysis was performed using the One-sample t-test, with the assumed hypothetical mean being 1, the same as the baseline. The time course showed; 1 minute (0.9696±0.10 fold over unstimulated, p=0.7926, ns) 2 minutes (0.9313±0.12 fold over unstimulated, p=0.6114, ns), 5 minutes (0.9617±0.07 fold over unstimulated, p=0.6395, ns), 15 minutes (1.023±0.22 fold over unstimulated, p=0.8699, ns), 30 minutes (0.7775±0.05 fold over unstimulated, p<0.05 *, s), 60 minutes (0.8028±0.29 fold over unstimulated, p=0.5700, ns) and 120 minutes (0.7074±0.29 fold over unstimulated, p=0.4217, ns). The time course results from four independent replicates (n=4) (Figure 5.15A, Bottom).

The other of the Cofilin phosphatases we looked at was PDXP. Representative blots of the time course are shown in (Figure 5.15B). The blots show an initial drop in expression at 1 and 2 minutes before steadily increasing to 30 minutes before again showing a drop at 60 and 120 minutes. Results were plotted and compared to the baseline (0mins), and statistical analysis was performed using the One-sample t-test, with the assumed hypothetical mean being 1, the same as the baseline. The time course showed; 1 minute (0.7154±0.06 fold over

unstimulated, p<0.05 *, s) 2 minutes (0.7267±0.1 fold over unstimulated, p=0.1134, ns), 5 minutes (0.9029±0.14 fold over unstimulated, p=0.5560, ns), 15 minutes (0.8849±0.05 fold over unstimulated, p=0.1701, ns), 30 minutes (0.9789±0.04 fold over unstimulated, p=0.6711, ns), 60 minutes (0.9317±0.01 fold over unstimulated, p<0.05 *, s) and 120 minutes (0.7454±0.04 fold over unstimulated, p<0.05 *, s). The time course results from four independent replicates (n=4) (Figure 5.15B, Bottom).

This experiment showed that stimulation of MEG-01 cells with AYPGKF affects Cofilin activators. Interestingly, there was a decrease in expression of SSH at 30 mins and PDXP at (1 min, 60 mins and 120 mins) being significant. Most of the significant decreases in protein expression occurred at 30 mins onwards; this was when Cofilin phosphorylation began to return to baseline after the 15min mark, and therefore, the decrease in SSH and PDXP expression beyond the 30min mark could be the result of degradation of protein following its dephosphorylation of Cofilin.

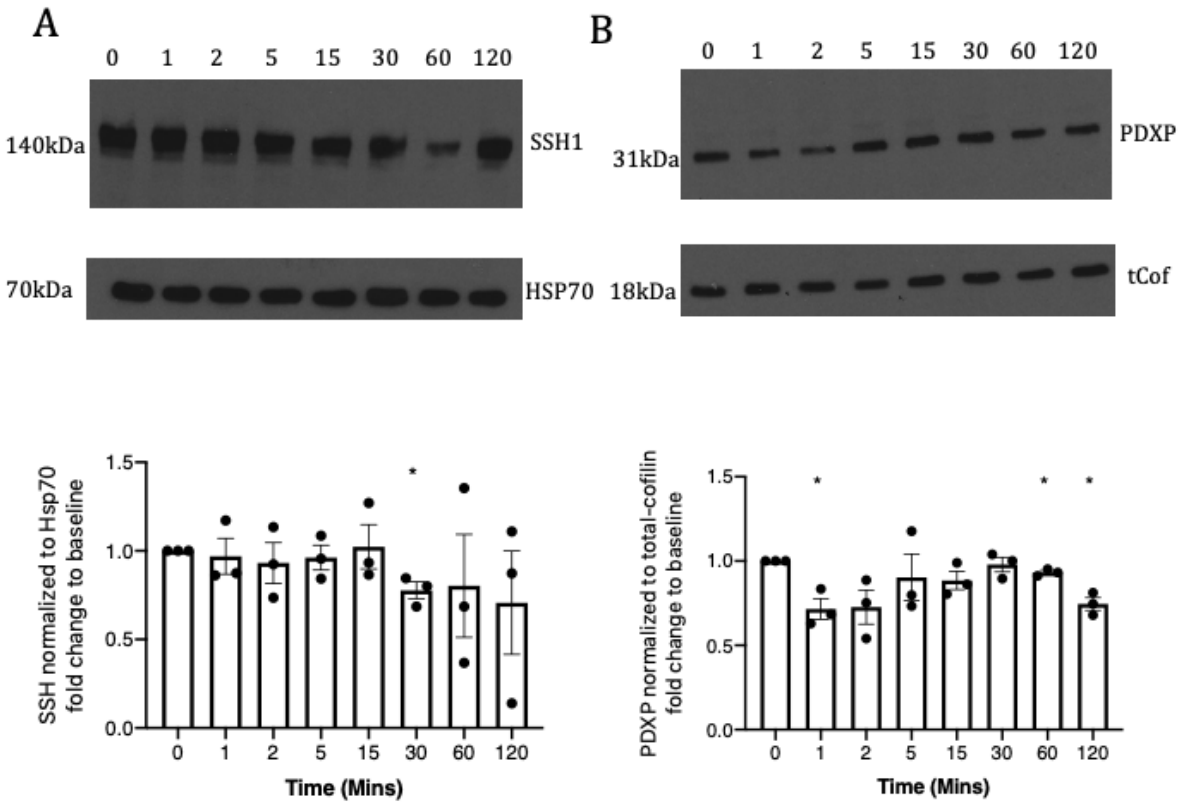

Figure 5.15. The effects on Cofilin phosphatases (SSH and PDXP) following stimulation of MEG-01 cells with AYPGKF. A) shows representative western blot images of SSH (top) and loading control Hsp70 (bottom) for the stimulation time course (0-120 minutes) with 300μM of AYPGKF. Time points were compared with unstimulated (0 minutes) using One-sample t-test. B) shows representative western blot images of PDXP (top) and loading control tCof (bottom) for the stimulation time course (0-120 minutes) with 300μM AYPGKF. Time points were compared with unstimulated (0 minutes) using One-sample t-test. Data are the mean ±SEM for the normalized signal from four independent replicates (n=4). The level of statistical significance is shown compared with the Unstimulated (0 minutes) control (* $p<0.05$, ** $p<0.01$, *** $p<0.001$, **** $p<0.0001$ and ns (not significant).

5.4 Discussion

5.4.1 Results summary

MEG-01 cells showed significant increases in the phosphorylation of Cofilin following stimulation with thrombin and AYPGKF. Peak phosphorylation was reached at 15 minutes post stimulation. Phosphorylation increased at varying concentrations of both thrombin and AYPGKF all achieving significance at the 5 minute and 15-minute time points with 15 minutes being the peak level. Results were confirmed using immunofluorescence analysis.

Stimulation of MEG-01 cells with TFLRRN showed no significant increases in Cofilin phosphorylation over a time course or with varying concentrations of TFLRRN. Changes in Cofilin phosphorylation are PAR-4 mediated in MEG-01 cells.

Stimulation of MEG-01 cells with thrombin or AYPGKF showed significant changes in expression levels of upstream regulators of Cofilin activity in particular LIMK at 15 minutes and ROCK at 5 minutes. However, changes in expression levels of all proteins were detected at various points over the time course for (LIMK2, ROCK1, TESK1, PDXP and SSHL1). PAR4 mediates Cofilin phosphorylation state via modulation of upstream regulators of Cofilin activity in MEG-01 cells.

5.4.2 Cofilin pathway is mediated via PAR4 activation in MEG-01 cells

After confirming through immunofluorescence imaging that MEG-01 cells indeed express PAR4 at the protein level, our focus shifted to exploring the effects stimulation of PARs would have on these cells. We employed thrombin, which activates both PAR1 and PAR4, as well as the selective agonists TFLRRN (PAR1) and AYPGKF (PAR4), to observe if stimulation resulted in cellular changes. The use of bright-field imaging was employed in these initial

studies, the rationale being that release of granular contents and signs of membrane budding would be observable. A time course experiment was set up at various intervals (0 minutes (baseline); 5 minutes; 1 hour; 2 hours; and 4 hours) (Figure 5.1).

Interestingly, at the 5-minute mark, all treatment groups, visually resembled the baseline state. However, by the 1-hour point, significant morphological changes were observed specifically in the groups treated with thrombin and AYPGKF, both of which activate PAR4. These morphological changes were noteably absent in both the baseline and TFLRRN-treated groups, the latter selectively activating only PAR1. These morphological changes persisted at the 2-hour time point before returning to the baseline state by the 4-hour timepoint.

These early observations were particularly compelling in light of the broader objectives of this thesis, which was focussed on characterising the effects of PAR4 stimulation on the Cofilin pathways in MEG-01 cells. These initial observations provided a good foundation for validating the conclusions from the previous chapter, where it was concluded that Cofilin was a high-impact interactor downstream of PAR4. Cofilins strong association with actin dynamics appears to be supported by these morphological shifts. The fact that these changes were exclusively observed in groups where PAR4 was activated, and not in those where only PAR1 was involved, supports the notion that PAR4 plays a unique and distinct role in regulating MEG-01 cell morphology, through its downstream effects on actin pathways.

5.4.3 Phosphorylation of Cofilin is driven by PAR4 activation and not PAR1

The effects of PAR4 activation on Cofilin phosphorylation were investigated in MEG-01 cells through western blotting time-course analysis. Initially, we examined Cofilin activity following stimulation with 1 U/mL thrombin. This revealed an increase in the phosphorylation state of Cofilin as early as 1-

minute, with levels continuing to rise and peaking at 15 minutes post-stimulation (Figure 5.4A). Concurrently, pERK levels were assessed, as ERK phosphorylation occurs downstream of both PAR1 and PAR4 activation, serving as a positive control to confirm effective receptor stimulation. Thrombin stimulation led to a rapid increase in pERK, which sustained until 30 minutes post-stimulation before gradually declining. Despite this decrease, pERK levels remained elevated throughout the time course, peaking at 30 minutes, although the variation in the data meant the 30-minute timepoint failed to achieve significance (Figure 5.4B). The sustained pERK signalling confirmed that both PAR1 and PAR4 were activated, driving downstream signalling cascades and that changes in pCofilin expression was driven by PAR1, PAR4 or both.

This data suggests that Cofilin phosphorylation was indeed a result of thrombin-activated PAR1 and PAR4, as evidenced by the canonical signalling differences between these two receptors. PAR1 is known for its rapid on/off signalling, whereas PAR4 elicits a slower, more sustained response (Covic et al., 2000). One particularly interesting observation in these experiments was the prolonged pERK signalling, which suggested co-activation of PAR1 and PAR4. Although this did not definitively identify which receptor was responsible for the changes in pCofilin expression, it provided insights into the synergistic relationship between PAR1 and PAR4. Previous studies suggest that co-expression of PARs may enable more efficient PAR4 activation, either through dimerization or proximity, allowing thrombin to cleave PAR4 more efficiently at lower concentrations. (Lin et al., 2013).

Further validation of the effects of PAR1 and PAR4 activation on downstream signalling in the Cofilin pathway came from experiments using varying concentrations of thrombin. Since peak pCofilin levels were observed at 15 minutes post-stimulation, this time point was used to assess responses to different thrombin concentrations (Figure 5.8). Interestingly despite varying thrombin concentrations levels, the phosphorylation of Cofilin followed a similar pattern across all conditions, reinforcing the observations from the initial

time course. These independent replicates, with five experiments in each set, confirmed the significance of the date. However, the effect of 3 U/mL thrombin at 15 minutes was less significant due to high variability, possibly because the corresponding blot bands appeared fainter, making quantification difficult.

Initially, we hypothesised that different thrombin concentrations would allow us to distinguish the relative contributions of PAR1 and PAR4 to Cofilin phosphorylation. Previous studies have shown that low thrombin concentrations (0.3 U/mL arm) predominantly activate PAR1, while higher concentrations (3 U/mL arm) activate PAR4. Surprisingly, the results revealed increases in pCofilin across all concentration arms, with the greatest fold change observed at the lowest thrombin concentration (0.3 U/mL). This suggested that PAR1 might play a more prominent role in driving these changes than initially expected. However, considering the MEG-1 cells physiologically express both PAR1 and PAR4, this hypothesis was complicated by the potential for heterodimerisation between PARs, which could allow PAR4 activation at lower thrombin concentrations. Thus, determining which receptor primarily drove Cofilin phosphorylation was not possible at this stage (Arachiche et al., 2013).

Further investigation into thrombin's effects on Cofilin phosphorylation was conducted using immunofluorescence analysis at the 15-minutes post-stimulation time point. This experiment employed two thrombin concentrations (1 U/mL and 3 U/mL) to account for the previously observed non-significant result in the thrombin concentration gradient experiments (Figure 5.2) The higher concentration of thrombin (3 U/mL) led to greater phosphorylation of Cofilin, demonstrating dose-dependent effects. Interestingly, pCofilin expression varied among cells, with some showing marked increases post-stimulation, while others remained similar to baseline. This heterogeneity may reflect biased signalling, where specific G-protein coupling following receptor activation (e.g., G12/13 for RhoA or Gq for PLC) determines the downstream pathway (Lynch and Wang, 2016). Given that RhoA-ROCK pathway is a

known regulator of Cofilin (Deng et al., 2019), it is likely that PAR4, signalling through this cascade, exerts the dominant effect on pCofilin expression. These findings indicated that thrombin stimulation of MEG-01 cells significantly regulated the Cofilin pathway but leaves unresolved which PAR is the master regulator of this process.

To clarify the roles of PAR1 and Par4 in Cofilin phosphorylation, we utilised PAR-specific ligands that activate each receptor independently, bypassing the need for thrombin cleavage. For PAR1 the commonly used ligand is TFLRRH-NH_2, while PAR4 is targeted by AYPGKF-NH_2. The development of a more potent peptide for PAR4 has been developed A-Phe(4-F)-PGWLVKNG, although was not available for this study due to delays in delivery (Yang et al., 2022).

When MEG-01 cells were stimulated with TFLRRN, surprisingly, no significant change in Cofilin phosphorylation was observed at any time point, suggesting that PAR1 activation does not directly impact the Cofilin pathway (Figure 5.5A). However, pERK was run in parallel, confirming that TFLRRN successfully activated PAR1, as indicated by the significant and robust increase in ERK phosphorylation at 1 and 2 minutes post stimulation (Figure 5.5B). The rapid on/off pERK signalling seen in TFLRRN was markedly different from the more sustained pERK response observed with thrombin, further supporting the notion that thrombin's effects on Cofilin are mediated by PAR4 rather than PAR1.

Given the potency of TFLRRN as a PAR1 agonist, we hypothesised that the lack of Cofilin response might be due to receptor saturation at the 100 uM concentration. To test this, we lowered TFLRRN concentrations (1 uM, 10 uM, 30 uM, and 100 uM) and assessed the time course again as was done with thrombin. However, even with varying concentrations, no significant effect on Cofilin phosphorylation was detected (Figure 5.9A). Repeated experiments with additional replicates confirmed that PAR1 activation does not influence Cofilin phosphorylation in MEG-01 cells.

In contrast, when MEG-01 cells were stimulated with PAR4-specific ligand AYPGKF, Cofilin phosphorylation followed a similar pattern to that observed with thrombin, although variation in replicates prevented statistical significance (Figure 5.6A). The parallel pERK analysis showed a rapid and sustained increase in ERK phosphorylation, again contrasting with the rapid decline observed in the PAR1 stimulation (Figure 5.6B). These results further indicated that PAR4 is the receptor driving Cofilin phosphorylation in response to thrombin.

To further confirm these findings, we conducted experiments using varying concentrations of AYPGKF (lower and higher than the initial 300 uM). This time, all concentrations showed significant increases in Cofilin phosphorylation, with the greatest fold change observed at the lower concentration (Figure 5.9B). These results suggested that receptor saturation at higher ligand concentrations may blunt the response, with these results also further supporting the role of PAR4 in regulating the Cofilin pathway.

Finally, IF analysis at the 15-minute time point was carried out post-stimulation with AYPGKF confirmed that PAR4 activation significantly affects Cofilin phosphorylation in MEG-01 cells. The IF data closely mirrored the results from western blot analysis, further corroborating the role of PAR4 in this pathway (Figure 5.3). Together these findings provided compelling evidence that PPAR4, rather than PAR1, is the primary regulator of the Cofilin pathway in MEG-01 cells, highlighting the distinct downstream signalling roles of these receptors (Han and Nieman, 2018a).

5.4.4 Activation of PAR1 and PAR4 show distinct AKT signalling kinetics in MEG-01 cells

Given that stimulation of MEG-01 cells with thrombin, TFLRRN, and AYPGKF elicited a robust and significant response with differing signalling kinetics in ERK. We further aimed to investigate kinase signalling in MEG-01 cells

stimulated with thrombin and AYPGK, this time in the context of AKT phosphorylation. AKT phosphorylation, is an important kinase of downstream GPCR activation including both PAR1 and PAR4. AKT is an intracellular signalling kinase activated by PI3K and PKD1, both of which are known downstream effectors of these pathways.

When stimulated with thrombin, MEG-01 cells exhibited a rapid increase in pAKT levels, peaking at 2 minutes before declining to baseline by 30 minutes (Figure 5.7). In contrast stimulation with AYPGKF resulted in a slower rise in pAKT, starting at 2 minutes, remaining stable until a significant peak at 60 minutes, followed by a gradual decrease.

The contrasting signalling kinetics between thrombin and AYPGKF is noteworthy. The rapid rise and fall in pAKT with thrombin aligns with typical PAR1 activation patterns, while the slower, prolonged response seen in AYPGKF is unexpected and deviates from previous stimulation outcomes. One possible explanation for this difference is the role of ROCK, which can inhibit PI3K activity and, consequently, AKT phosphorylation. Since PAR4 activation influences ROCK expression, the delayed rise in pAKT during AYPGKF stimulation may reflect a reduction in ROCK activity over time (New et al., 2007). Conversely, the dual activation of PAR1 and PAR in thrombin-stimulated MEG-01 cells leads to distinct and rapid signalling kinetics.

5.4.5 PAR4 influences Cofilin activity and phosphorylation status via influencing the activity of its upstream regulators

Having shown that PAR4 regulates the activity and phosphorylation state downstream of activation, we then looked at exploring the upstream regulators of Cofilin phosphorylation and dephosphorylation following stimulation with thrombin (1 U/mL) and AYPGKF (300 μM). We first looked at the proteins which phosphorylate Cofilin (LIMK2, ROCK1 and TESK1). When stimulated with thrombin MEG-01 cells show an increase in LIMK2 expression at 15 mins which was similar for ROCK1, which showed a peak at 5 mins and sustained until 15 mins (Figure 5.10). Whereas MEG-01 cells stimulated with AYPGKF

showed a similar increase in LIMK2 to a peak at 15 mins; however, they achieved significance at 1 min and at the 15min peak (Figure 5.13).

Again, with ROCK1, the data shows a similar pattern of expression over the time course as thrombin by reaching peak levels around the 5min and 15 mins (Figure 5.10). When looking at the context of the process of Cofilin phosphorylation, which was observed in the original experiments, the pattern that we see follows the expected pattern that explains the process of what is happening; ROCK1 is the furthest upstream in the proteins looked at in the context of the Cofilin pathway what was observed is a peak in expression at 5 mins post-stimulation, this then phosphorylates LIMK2 which reached its peak at the next time point 15 mins which then phosphorylates Cofilin whose peak phosphorylation occurred at 15 mins the same time point that LIMK2 expression was shown. The same observations are also seen in AYPGKF-stimulated MEG-01 cells, although with slight variations, particularly in ROCK, in which the peak was reached at 15 mins and increased at 5 mins, which is in contrast to that observed in thrombin (Figure 5.13). This is most likely explained by the lack of significance in the data seen in AYPGKF stimulated ROCK1 time course, which resulted in variation that differed from that of thrombin; therefore, full conclusion and comparability are difficult to make when looking at the two. However, in the context of LIMK2, significance was seen at the 1-minute mark, showing an increase to a highly significant peak at 15 minutes, the same trajectory that the thrombin arm took. This data adds further value to PAR4 influence on the Cofilin pathway by influencing the activity of LIMK2, which phosphorylates Cofilin.

In addition, we also looked at another phosphorylator of Cofilin, which is TESK1; an initial strange observation within MEG-01 cells is that TESK1 blots with a distinct double band pattern. Literature searching and the website from which the antibody was purchased show TESK1 as a single band at 68kDa. We looked at changes that occurred post-stimulation with thrombin and AYPGKF in the context of both the bands being separate entities (i.e. if the

protein exists in two separate states within MEG-01 cells), then stimulation could affect the banding patterns in different ways. When stimulated with thrombin, the upper thick band shows an initial rise in expression at 2 mins before showing a drop in expression to below baseline reaching a low at 60 mins before expression begins to recover. The lower thin band shows a different trajectory with increases in expression to a peak at 5 mins before declining to well below baseline at 120 mins (Figure 5.11). The data for the thin band showed wide variation with large errors and, therefore, didn't achieve significance across any time-course points.

When stimulated with AYPGKF, the upper thick band showed a widely different degree of expression than that seen in the thrombin-stimulated arm; the pattern showed a rapid decline in expression at 1 min post-stimulation which continued down to a peak at 15 mins before recovering to near baseline at 60 mins. The lower thin band was similar to thrombin stimulate MEGs in that there was a rise in expression observed at 2 mins; however then showed a rapid reduction in expression from 15 mins before showing a slight recovery in expression at 120 mins (Figure 5.14). Stimulation of PAR4 with either thrombin or AYPGKF appears to alter the expression of TESK1. Using the more significant data obtained in the AYPGKF arm appears to reduce expression. Oddly enough, it does this with the dual bands at different points in time. For the upper thick band, a reduction in expression occurs from 1 minute to 30 minutes; for the lower thin band, a decrease in expression occurs from 15 minutes to 120 minutes. The exact role the two bands play is unclear, as mentioned above. However, some literature does elucidate that two transcripts of TESK1 exist: a 3.6kb transcript (upper band) expressed predominantly in testis and a 2.5kb transcript (lower thin band), expressed ubiquitously but at lower levels (Toshima et al., 1999). It has been shown at least that MEG-01 cells express both of these transcript variants in easily detectable amounts, which was an interesting observation as general literature shows TESK1 as a single band on western blots.

We then looked at proteins that dephosphorylate Cofilin (activation) to see if either thrombin or AYPGKF influenced this arm of the Cofilin pathway. We did this by looking at two proteins, which are key to the activation of Cofilin by dephosphorylating it at ser3: Slingshot homolog (SSHL1) and PDXP (also known as Chronophin). When stimulated with thrombin, MEG-01 cells show a slight increase in SSH expression at 5 mins before declining to less than baseline expression at 15 mins before returning to baseline signal at 120 mins (Figure 5.12A). As previously mentioned, SSHL1 exists in the cytoplasm bound to 14-3-3 and in a generally inactive state. The decline in expression starting at 15 mins until 60 mins is the time point in which peak phosphorylation occurs. Therefore, the drop in expression of SSHL1 could be explained by the fact that SSHL1 binds to f-actin and becomes 1200 times more active in dephosphorylating Cofilin (Kurita et al., 2008). The drop in expression could be explained by SSHL1 being bound to f-actin and, therefore, not being detected within the gel due to the size of the protein in combination with F-actin. If this were the case, this would explain the decline in expression at the peak time, SSHL1 would be excreting its effect, and pCof levels would begin to return to baseline. Meanwhile, for MEG-01, cells stimulated with AYPGKF SSHL1 showed a slight decline in expression at 1 min and 2 mins before returning to baseline levels at 5 mins and 15 mins.

Interestingly like with thrombin expression dropped below baseline for 30 mins and 60 mins with expression remaining low at 120 mins in the AYPGKF stimulated arm in contrast to thrombin (Figure 5.15A). It should be noted that the error at the 60min and 120min time points was relatively wide in the AYPGKF stimulated experiments. However, the 30-minute time point was consistent in its expression pattern across the thrombin and AYPGKF arms. Although not significant in thrombin, it was in the AYPGKF arm, showing a consistent expression pattern change when PAR4 is activated in MEGs.

In the context of PDXP, when MEG-01 cells were stimulated with thrombin, they showed a drop in expression from the 1-minute mark until the end of the time course; the expression of PDXP never returned to baseline following

thrombin stimulation. In addition, four of the time points showed significance for the decline in expression (Figure 5.12B). Meanwhile, MEG-01 cells stimulated with AYPGKF showed a similar overall expression pattern in that PDXP expression dropped below baseline for the entirety of the time course. However, it showed a more varied pattern than in thrombin. It did, however, achieve significance for drop in expression for three of the time points (Figure 5.15B). Despite very little information on the activation or post-activity metabolism of PDXP, both thrombin and AYPGKF-stimulated MEGs showed a similar expression pattern from as early as the 1-minute mark. Unlike SSH, where inferences can be made to understand the expression pattern, expression remained lower than the baseline for the entire time course. For PDXP, it is more difficult as all that is known is that it is bound to and inactive in the cytoplasm when bound to Hsp90 and, upon activation of upstream regulators, detaches from Hsp90 to excerpt its effect (Huang et al., 2008). Given the instant drop and sustained decline in expression, what has happened so early on is hard to determine. However, given that the observations were seen in both the thrombin and AYPGKF arm, with significance seen in both, it can be concluded that the results are at least reliable.

5.4.6 Concluding remarks

Proteomic data showed a high association of actin remodelling proteins with PAR4, particularly the Cofilin pathway. The chapter aimed to assess whether the activation of PAR4 resulted in the activation of the Cofilin pathway. The data obtained showed that stimulation of MEG-01 cells does result in changes in the phosphorylation state of Cofilin-1 and Cofilin-2. In particular, Cofilin-1 stimulation of the PAR4 receptor was shown to be the main driver of Cofilin activity in MEG-01 cells, which was also demonstrated through the assessment of the upstream regulators of Cofilin. The data obtained in this chapter provided evidence to the previous chapter that PAR4 does associate and regulate Cofilin-1 (and potentially Cofilin-2) activity in MEG-01 cells.

Chapter Six:

General discussion

6.0 General Discussion

6.1 Introduction

From its original cloning in 1998, PAR4 was considered a redundant backup receptor to the primary thrombin receptor PAR1 (Xu et al., 1998; Coughlin, 2000). As our understanding of PAR4 has increased, it has become an important receptor in various tissue types and displays distinct signalling kinetics to PAR1. Despite this, its role in various processes, including platelet activation, inflammation, cancer progression and metastasis, has singled PAR4 out as a crucial receptor in physiological and pathological processes (Zhang et al., 2018).

This project aimed firstly to identify novel protein interactors of PAR4 through mass spectrometry proteomic data and secondly to validate and explore the effect (if any) that PAR4 activation had on this protein/pathway. The proteomic data showed high degrees of association with actin remodelling proteins, particularly high confidence hits across replicates of the actin-severing protein Cofilin. Many papers state PAR4 is responsible for platelet shape change and spreading but fail to fully elucidate this role, with no research directly seeking to find a correlation between PAR4 and Cofilin within a physiological context. Given that PAR4 is known to activate RhoA, the most upstream protein of the Cofilin pathway, the hypothesis was that PAR4 would influence Cofilin activity and identify a novel pathway downstream of PAR4 that is not currently explored (French and Hamilton, 2016).

6.2 Result Summary

Proteomic data was analysed to identify novel interacting proteins with PAR4; this consisted of filtering proteomic datasets from three independent replicates generated via LC-MS/MS from HEK293 cells stably expressing wt-PAR4 or mut-Y157C PAR4 or dual expression (Emmott and Goodfellow, 2014). Data showed a correlation intra-experimentally with interacting proteins with wt-PAR4 and mut-Y157C PAR4 receptor. However, no correlation was shown inter-experimentally when comparing replicates, showing that variation is present within mass spec data and the importance of obtaining replicates. Proteins that gave SILAC ratios above the determined threshold across two or more replicates across the three ratios (L, M, and H) gave 996 proteins as potential interactors. These were analysed for gene enrichment but provided vast networks from which it was difficult to extract meaningful data.

When comparing gene enrichment between wt-PAR4 and mut-Y157C PAR4, similarities in enrichment families were seen between them; however, as was expected, mut-Y157C PAR4 showed more simple gene ontology maps due to having fewer proteins than that of wt-PAR. This was expected as the mut-Y157C PAR4 receptor is retained within the ER and, therefore, would have reduced interaction with proteins than the wt-PAR4 receptor (Cunningham et al., 2012; Norman et al., 2016). Isolating the PAR4 receptor gene within the whole proteome and applying kmeans clustering to extract the closest interacting proteins allowed for identifying potential interacting partners. Gene enrichment analysis applied to this cluster revealed a strong association with actin-remodelling proteins responsible for maintaining and remodelling the actin cytoskeleton across all three analyses. In addition, proteins above the threshold across all three proteomic replicates revealed Cofilin-2 as a high-confidence interactor. Given its role in actin severing, it was chosen as the protein and pathway to explore the downstream of PAR4. Also, no previous research has investigated the link between PAR4 and Cofilin and its regulatory pathway (Bamburg et al., 1980; Bravo-Cordero et al., 2013).

MEG-01 cells were used to validate the role of PAR4 activation on the Cofilin pathway. It is the closest cell model to platelets and would express physiological levels of PAR1 and PAR4 and physiological levels relevant to normal human platelets (Ogura M et al., 1985; Heo et al., 2022). Techniques used in the assessment of this were primarily western blotting and immunofluorescence. Stimulating MEG-01 cells with thrombin showed significant effects on the phosphorylation of Cofilin, reaching a peak at 15 minutes; this was shown through western blotting and IF, even when varying the concentrations of thrombin. In addition, effects on other proteins of the Cofilin pathway were also shown, mainly in TESK1 and PDXP. Although effects on expression levels were noted in all markers, they failed to achieve significance. As thrombin cleaves and activates both PAR1 and PAR4, the use of PAR-specific peptides showed that stimulation of just PAR1 leads to no significant increase in Cofilin phosphorylation, including when varying the concentration of TFLRRN. However, the change in phosphorylation was significant in IF but was considerably lower than that of thrombin and PAR4-stimulated MEG-01 cells.

Stimulation of MEG-01 cells for just PAR4 showed a similar phosphorylation pattern as in thrombin, although it failed to achieve significance. Still, when varying the concentration, high significance was seen in all groups; this observation was also shown in IF, indicating that the observations seen in thrombin were PAR4 driven while confirming the finding of a PAR4/Cofilin interaction hypothesised in the first chapter. In addition, significant effects were observed in all proteins in the Cofilin pathway, particularly LIMK2, which showed high significance at 15 minutes when Cofilin phosphorylation peaked (Bravo-Cordero et al., 2013). Initial experiments were undertaken regarding Coflin-2. It was shown that MEG-01 cells contain Cofilin-2 and that stimulation of MEG-01 cells with thrombin shows a significant effect on the phosphorylation state as observed in the context of Coflin-1.

6.3 Interrogating the PAR4 proteome

6.3.1 Proteomic data confirms functional disparity between wt-PAR4 and Y157C

The first part of the thesis looked at analysing proteomic datasets generated through SILAC LC-MS/MS for novel interactors with PAR4 receptors (Emmott and Goodfellow, 2014). Analysis of the proteomic data showed replicate 1 identified 5626 proteins (2905 after filtering), replicate 2 found 6181 proteins (3213 after filtering) and replicate 3 identified only 3860 proteins (1768 after filtering). Of note, replicates 1 and 2 shared similarities in identified proteins, while replicate 3 showed significantly fewer. The discrepancy was particularly evident in the Gaussian distribution graphs, where replicates 1 and 2 shared similar distributions in SILAC ratios, but replicate three differs notably. This suggests variation within the data, and despite assessment to prove reproducibility, none of the replicates showed correlation, indicating potential inconsistencies but highlighting the importance of multiple replicates.

Given the variation, we assessed the correlation between wt-PAR4 and mut-Y157C, the theory being that they should at least show some correlation. It was shown that despite differences in protein expression levels, there was a strong positive correlation in interacting proteins between wt-PAR4 and mut-Y157C PAR4 within experimental replicates, indicating similar interactions between the two variants. However, wt-PAR4 exhibited more identified interacting proteins than mut-Y157C PAR4, most likely explained by the later intracellular retention and reduced expression on the plasma membrane (Cunningham et al., 2012; Norman et al., 2016).

Further analysis of this difference was examined by comparing gene enrichment differences between the two using PANTHER, BiNGO and Reactome. PANTHER showed that while there were similarities between the two in molecular function and cellular component categories between the two

variants, differences were observable in the biological process and protein class categories. In particular, functions related to adaptor, transducer, and transporter activities were enriched in wt-PAR4 but not in the mut-Y157C PAR4. The analysis via BiNGO further confirmed the differences in enriched functions between the two variants, interestingly highlighting distinct molecular activities and biological processes associated with each variant. Finally, Reactome showed similarities and differences in enriched functions, with variations observed in catalytic activity and cellular processes; overall, these findings shed additional light on the functional consequences of the Y157C mutation in PAR4, illustrating its effects on protein interactions, cellular processes, and molecular activates.

6.3.2 F2RL3 shows close proximity to actin dynamic proteins

The final piece of analysis aimed at homing in on a potential novel protein for further study through the extraction of a cluster close to the PAR4 gene; this analysis revealed a network of proteins associated with PAR4 activation, with a prominent focus being on proteins involved in actin dynamics and cytoskeleton reorganisation. Gene enrichment profiles showed that PAR4 was associated with proteins involved in cytoskeletal binding, actin filament organisation, and cellular localisation processes. Interestingly, the association of PAR4 with actin-related proteins was consistent across multiple analyses, underscoring the importance of PAR4 in regulating actin dynamics (Heo et al., 2022). Among these, a key protein emerged as a high confidence hit across all replicates: the actin-severing protein Cofilin, a crucial protein in actin filament turnover and actin dynamics (Gurniak et al., 2005). Therefore, understanding the interplay between PAR4 and the Cofilin pathway may lead to identifying novel therapeutic targets for conditions involving dysregulation of PAR4 signalling, such as thrombosis, inflammation and cancer progression. The data obtained highlighted the intricate relationship between PAR4 activation and actin dynamics, suggesting a novel avenue for further

exploration and potential therapeutic interventions in PAR4 dysregulation or overexpression.

6.3.3 Unstimulated vs stimulated – adding additional complexity

While the analysis provided valuable insights into the protein interactions and pathways associated with PAR4 activation, several limitations could be considered and improved on. The first is the sample size. Three replicates were analysed to determine a novel protein interactor, the minimum number of replicates to derive any significant data. However, three is the minimum, and it cannot be ignored that replicate 3 showed an obvious difference from the other two replicates; this could indicate an outlier. Therefore, a larger dataset of five would have enhanced the robustness of the findings. Bioinformatics tools for constructing protein networks and gene ontology analysis rely heavily on prediction and, therefore, are subject to limitations and potential biases; however, in this context, this limitation is mitigated through functional validation within biological systems. In addition, the findings observed may be specific to the experimental conditions used (HEK293 overexpression). Therefore, the observed interactions in a non-native system don't necessarily translate to different cellular contexts or disease models; therefore, what is observed won't necessarily translate to the physiological context. Finally, these experimental analyses were conducted in unstimulated PAR4. Therefore, changes in protein expression, which could have been observed when comparing interaction between unstimulated and stimulated, could have provided greater context and strength to potential interacting proteins while also allowing for the assessment of up or down-regulation expression changes between the two states.

6.4 Functional validation of PAR4/Cofilin axis in MEG-01 cells

6.4.1 Cofilin-1 phosphorylation is mediated by PAR4 and not PAR1

Having identified Cofilin as a potential interacting protein of PAR4 through proteomic data analysis, the next aim was to functionally validate this assumption by using MEG-01 as a cell model of physiological PAR4 expression (Ogura M et al., 1985; Heo et al., 2022). Initial microscopic observations showed that stimulation of MEG-01 cells with thrombin and AYPGKF induced morphological changes, whereas TFLRRN did not. Stimulation of MEG-01 cells with thrombin led to a significant increase in Cofilin phosphorylation, with peak phosphorylation observed 15 minutes post-stimulation. Varying concentrations of thrombin showed a concentration-dependent effect on Cofilin phosphorylation, even with low concentrations inducing significant phosphorylation.

The immunofluorescent analysis confirmed the dose-dependent increase in phosphorylation of Cofilin with heterogeneity observed in cellular responses, confirming it wasn't a global upregulation. Delineation of PAR-specific activation was undertaken using TFLRRN (PAR1) and AYPGKF (PAR4), showing that PAR1 activation did not significantly affect Cofilin phosphorylation, indicating it was not responsible for the observed changes seen in the thrombin-stimulated cells. Although immunofluorescent analysis did show minor changes in Cofilin phosphorylation with PAR1 activation enough to be significant, this change wasn't comparable to that observed in thrombin-stimulated MEG-01 cells. However, PAR4 activation led to significant increases in Cofilin phosphorylation, suggesting PAR4 is responsible for regulating the Cofilin pathway downstream of its activation, with Immunofluorescent analysis confirming the results seen in western blotting

experiments with PAR4 stimulation showing highly significant changes in the phosphorylation of Cofilin.

In addition, these studies showed distinct signalling kinetics through ERK phosphorylation, with rapid on/off observed in PAR1, whereas slower on and more sustained signalling was observed in PAR4. They also demonstrated distinct downstream effects of PAR1 and PAR4 activation, highlighting the individual roles of these receptors and showing that early assumptions of PAR4 are indeed incorrect (Han and Nieman, 2018a).

6.4.2 PAR4 activation influences upstream regulators of Cofilin activity

We also looked at the regulatory mechanisms of Cofilin phosphorylation and dephosphorylation pathways in response to PAR4 activation induced by thrombin and AYPGKF stimulation. Both thrombin and AYPGKF increased the expression of LIMK2 and ROCK1, two key regulators of Cofilin phosphorylation, suggesting their involvement in PAR4-mediated signalling (Bravo-Cordero et al., 2013). Additionally, TESK1 exhibited a distinct double-band pattern, which changed differential post-stimulation, indicating potential phosphoregulatory roles in Cofilin dynamics downstream of the PAR4 activation (Toshima et al., 1999).

Regarding proteins which dephosphorylate, Cofilin, thrombin, and AYPGKF led to changes in SSHL1 expression, which indicates Cofilin activation, whereas stimulation led to sustained reduction in PDXP expression. The implication of this reduction in expression is undetermined, and whether this prolonged reduction resulted from its dephosphorylation of Cofilin or subsequent proteolytic degradation is not determined. Despite this activation of the PAR4 receptor, it influences all arms of the Cofilin pathway.

While these results provided valuable insights into the regulatory mechanisms of Cofilin phosphorylation and dephosphorylation in response to PAR4 activation, the study has limitations that should be acknowledged. First, these studies were performed primarily in MEG-01 cells, which are megakaryoblastic leukaemia cells and may not fully recapitulate the physiological responses of primary cells or other cell types. Therefore, looking at these responses in different cell types or in vivo would add further robustness to the data.

Additionally, we looked at a subset of proteins involved in regulating Cofilin activity (ROCK1, LIMK2, TESK1, SSHL1, and PDXP). While these are the key regulators of Cofilin activity, other signalling molecules and pathways may contribute to the overall cellular response to PAR4 activation. Further exploration incorporating a broader range of signalling components and converging pathways would provide a more comprehensive understanding of the regulatory network governing Cofilin dynamics.

Moreover, the results relied heavily on western blotting and immunofluorescent analysis to assess the protein and phosphorylation levels. While western blotting is a gold standard for evaluating protein expression changes, it does have some inherent limitations, including variability in antibody specificity, detection sensitivity and quantification accuracy (Begum et al., 2022). While also an old method used within the lab, the margin for human error is quite large. Therefore, using the complementary approach in immunofluorescent analysis mitigates the limitations and provides robustness to the conclusions obtained. However, additional techniques such as proximity ligation assays, knockout models, and co-immunoprecipitation could have provided further evidence to draw more robust conclusions.

6.4.3 Thrombin influences on Cofilin-2

The final arm of the analysis assessed the effect of stimulation of MEG-01 cells on the phosphorylation state of Cofilin-2. The results showed that MEG-01 cells indeed express the Cofilin-2 isoform, as shown in western blotting and immunofluorescent imaging, although the expression levels were much lower than those of cardiac-derived cells (Xue and Robinson, 2013; Shishkin et al., 2017). Additionally, it was shown that thrombin-induced differential expression in Cofilin-2 levels when compared to Cofilin-1. This was shown by the fact that 1 U/mL of thrombin resulted in a significant reduction in Cofilin-2 expression, whereas 3 U/mL thrombin led to a significant increase. Equally, regarding Cofilin-1, phosphorylation showed a dose-dependent response, whereas Cofilin-2 phosphorylation, although significant, didn't show dose dependence, with 1 U/mL and 3 U/mL showing almost identical phosphorylation levels. These initial observations underscore the complexity of PAR1 and PAR4 signalling pathways in modulating Cofilin dynamics, suggesting distinct regulatory mechanisms for Cofilin isoforms.

Despite some initial observations, robust conclusions weren't technically possible due to limitations in the volume of data gathered, primarily due to delays in antibody delivery, which meant explorations with PAR-specific peptides were not possible within the time. Therefore, from the preliminary data, Thrombin does show a significant effect on the regulation of Cofilin-2 activity. Still, the restricted scope resulted in an incomplete understanding of the signalling dynamics in the context of Cofilin-2. In addition, due to the relatively low level of expression of Cofilin-2 in MEG-01 cells, particularly when compared to that of Cofilin-1, detection with western blot was very difficult, which, if applied to stimulation experiments would result in a greater level of variability due to difficulties that would have been presented in the quantification.

6.5 Conclusions from cell data

The investigation into the role of PAR4 on the Cofilin pathway, both Cofilin-1 and Cofilin-2, has provided valuable insights into the complex signalling mechanisms underlying cellular responses to thrombin and peptide agonists. Through the experiments above in MEG-01 cells, the study explored the phosphorylation dynamics of Cofilin-1 and Cofilin-2 in response to PAR1 and PAR4 activation, shedding light on the regulatory mechanisms involved in cytoskeletal dynamics and cellular function.

Firstly, the study confirmed the presence of Cofilin-1 in MEG-01 cells and demonstrated that stimulation with thrombin and PAR4 agonist (AYPGKF) led to a significant increase in phosphorylated Cofilin-1 levels, indicating activation of the Cofilin pathway downstream of PAR4 activation. These findings suggest that PAR4 (not PAR1) signalling plays a crucial role in modulating cytoskeletal dynamics by regulating Cofilin-1 phosphorylation.

Moreover, the study investigated the Cofilin pathway's upstream regulators and downstream effectors to elucidate the signalling cascades in PAR4-medicated modulation of cytoskeletal dynamics. Through analysis of proteins involved in Cofilin phosphorylation (LIMK2, ROCK1 and TESK1) and dephosphorylation (SSHL1 and PDXP), the study revealed intricate temporal dynamics in response to thrombin and AYPGKF.

Notably, PAR4 activation influenced the expression activity of upstream kinases (ROCK1, LIMK2 and TESK1) and phosphatases (SSHL1 and PDXP), providing mechanistic insights into the regulation of Cofilin phosphorylation and cellular responses to PAR4 activation.

Furthermore, the investigation expanded focus to examine the expression and phosphorylation of Cofilin-2 in response to thrombin stimulation. The study successfully validated the presence of Cofilin-2 in MEG-01 cells and

demonstrated that thrombin stimulation elicited significant changes in total Cofilin-2 expression and phosphorylation status. Interestingly, unlike Cofilin-1, phosphorylation of Cofilin-2 did not exhibit dose dependency with thrombin concentration, indicating potential differences in the signalling pathways regulating these two isoforms of Cofilin. These findings highlight the complexity of Cofilin regulation and suggest distinct roles for Cofilin-1 and Cofilin-2 in cellular responses to thrombin.

In conclusion, the investigation into the role of PAR1 and PAR4 in modulating Cofilin phosphorylation and cytoskeletal dynamics has provided valuable insights into the complex interplay between PAR signalling and cellular response. By elucidating the regulatory mechanisms underlying Cofilin phosphorylation and identifying isoform-specific effects of thrombin stimulation, this study has laid the foundation for further research exploring the therapeutic potential of targeting PARs.

6.6 Future Work

6.6.1 Additional techniques and methods

A combination of experimental approaches and techniques could be utilised to enhance the robustness of the data investigating the interaction between PAR4 and Cofilin. These would aim to validate physical interaction, elucidate the signalling pathways involved, and provide spatial and dynamic insights into the interaction dynamics within cells.

Co-immunoprecipitation assays represent the gold standard for confirmation of protein-protein interactions (Miernyk and Thelen, 2008). By immunoprecipitating one protein of interest and detecting the other through western blotting, the direct interaction between PAR4 and Cofilin could be confirmed. This technique would provide valuable insight and evidence of physical association between the two proteins. In addition, using mass

spectrometry on Co-IP PAR4 or Cofilin complexes could also help to identify potential binding partners and signalling pathways.

Another assay that would provide valuable information is the proximity ligation assay, which is a powerful tool for visualising protein-protein interaction in situ. This is done by utilising antibodies conjugated to oligonucleotides, followed by ligation and rolling circle amplification, which can provide evidence of interactions at a single molecule level (Sable et al., 2018). This technique could have provided spatial information about the PAR4-Cofilin interaction within cells, offering insights into their subcellular localisation and potential functional consequences.

Furthermore, fluorescence resonance energy transfer assays offer another approach to assess the proximity and interaction between PAR4 and Cofilin molecules within live cells. By labelling the proteins with suitable fluorophores and measuring their energy transfer, FRET can provide quantitative data on their interaction dynamics in real time (Margineanu et al., 2016). This technique would have been particularly useful in studying the dynamic changes in protein-protein interactions in response to PAR4 receptor stimulation.

Fluorescence recovery after photobleaching (FRAP) is another helpful tool that could have been utilised in live cells to provide insights into the dynamics of Cofilin in response to PAR4 activation. Monitoring Cofilin mobility and turnover rates before and after PAR4 activation can reveal changes in its activity and interaction with the cytoskeleton (Mueller et al., 2012).

Further studies that would have complimented the data presented could have been on the utility of gene silencing or knockout models on PAR4 and Cofilin within MEG-01 cells, which could elucidate their functional roles. Comparing the phosphorylation status of Cofilin in cells without PAR4 expression could confirm its involvement in Cofilin regulation. Equally, the knockout of Cofilin

could have provided insights into whether its presence was essential to actin dynamics or whether salvage pathways or Cofilin-2 could have compensated for its loss (Hearn et al., 2020).

Drug inhibition assays with pharmacological inhibitors of PAR1 and PAR4 could have been used to further dissect their roles in regulating Cofilin activity. Treatment of cells with specific inhibitors of PAR1 and PAR4 or inhibitors of downstream pathway proteins could help to construct further the signalling cascades leading to Cofilin activation and inhibition within MEG-01 cells.

6.6.2 Additional models of study

Having performed this study using the MEG-01 cell line which is a megakaryoblast cell-line. Another potential method to further explore PAR4 in the context of the cofilin signalling pathway would be using primary megakaryocytes. There are three possible sources of acquiring human primary megakaryocytes, including bone marrow aspirate. In this case, bone marrow is extracted from a patient, usually from the iliac crest. The mononuclear cell fraction would then be obtained through density-grade centrifugation and further sorted to obtain megakaryocytes through fluorescence-activated cell sorting (FACs) using the markers (CD41, CD61). Another source is from peripheral blood; this method would have various considerations that must be met because megakaryocytes are sequestered in the bone marrow and are extremely rare in peripheral blood. The final method would be using umbilical cord blood, which is a good source of haematopoietic stem cells and would be encouraged to differentiate into megakaryocytes by supplementing with megakaryocytic growth factors such as thrombopoietin.

Despite being a potential option, the reality is that obtaining primary megakaryocytes is, in fact, purely hypothetical due to the ethical considerations of obtaining them from human sources. Bone marrow is a highly precious sample; donations are usually only made during a bone

marrow transplant. Due to the pain and considerable infection risk associated with obtaining bone marrow. The likelihood of ethical approval and patient consent is virtually zero. In addition, obtaining megakaryocytes during initial studies like those performed in this thesis would be unethical. In reality, primary megakaryocyte harvest would only be viable if there was a clinical need for study with a benefit to the patient as the end goal. In the context of this thesis, results are in infancy and, therefore, wouldn't be viable at this stage.

However, there is the potential to study PAR4/cofilin signalling in the context of human platelets. A potential source of these would be the National Blood Transfusion Service. Platelets are viable for transfusion only five days after harvest. Vast amounts of platelets are disposed of, which are still viable but past the time for a patient transfusion. Again, ethical considerations need to be addressed when using any human products, which can be particularly difficult to do. In addition, platelets must be continually agitated; otherwise, they will begin to clot. The ability to coordinate collection and experimental work would be something that would have to be carefully considered to obtain meaningful data and avoid wasting human donations, which are precious samples and require full auditability as to their fate.

Another exciting area to explore is whether PAR4 is expressed on the surface of the mitochondria. As previously shown in Chapter 3, there was a high association of PAR4 with mitochondrial proteins. Various GPCRs have now been shown to be expressed in the mitochondria, including AT_1R, AT_2R, cannabinoid receptors, and $P2Y_1$ and $P2Y_2$ (Fasciani et al., 2022).
Study of this has been made possible due to the ability to isolate mitochondria from cells and study them as separate entities. Before the conclusion of this thesis, initial findings from this thesis resulted in funding for another student to explore this. It has been shown that PAR4 is expressed on the surface of the mitochondria. However, its role in mitochondrial signalling hasn't yet been determined.

6.7 Closing remarks - Has the research question been answered?

Based on the data presented, it is evident that PAR4 interacts with Cofilin and modulates its phosphorylation status, thereby influencing cytoskeletal dynamics. The study revealed that stimulation of MEG-01 cells with thrombin and a PAR4 agonist (AYPGKF) resulted in significant increases in phosphorylated Cofilin-1 levels, indicating activation of the Cofilin pathway downstream of PAR4 activation. This observation suggests that PAR4 signalling is crucial in regulating Cofilin phosphorylation and cytoskeletal dynamics.

Furthermore, the investigation demonstrated that PAR4 activation influenced the expression and activity of upstream regulators of Cofilin phosphorylation, including LIMK2, ROCK1, and TESK1 (Heo et al., 2022). The temporal dynamics of protein expression and phosphorylation observed in response to PAR4 activation provide mechanistic insights into the signalling cascades involved in PAR4-medicated modulation of cytoskeletal dynamics.

Moreover, the study extended its analysis to Cofilin-2. It revealed that thrombin stimulation elicited significant changes in both total Cofilin-2 expression and its phosphorylation state, further highlighting the interaction between PAR4 signalling and Cofilin regulation. The distinct effects of PAR4 activation on Cofilin-1 and Cofilin-2 phosphorylation suggest isoform-specific functions and signalling pathways, underscoring the complexity of Cofilin regulation in response to PAR4 activation.

In conclusion, the data strongly support the hypothesis that PAR4 interacts with Cofilin and regulates phosphorylation, thereby influencing cytoskeletal dynamics. These findings provide valuable insights into the molecular mechanisms underlying PAR4-mediated modulation of cellular responses and

highlight the potential therapeutic implications of targeting PAR4 signalling in diseases associated with dysregulated cytoskeletal dynamics.

Chapter Seven:

References

7.0 References

Agnew, B.J., Minamide, L.S., and Bamburg, J.R. (1995). Reactivation of phosphorylated actin depolymerizing factor and identification of the regulatory site. J. Biol. Chem. *270*: 17582–17587.

Agrawal, P.B., Greenleaf, R.S., Tomczak, K.K., Lehtokari, V.L., Wallgren-Pettersson, C., Wallefeld, W., et al. (2007). Nemaline myopathy with minicores caused by mutation of the CFL2 gene encoding the skeletal muscle actin-binding protein, cofilin-2. Am. J. Hum. Genet. *80*: 162–167.

Agrawal, P.B., Joshi, M., Savic, T., Chen, Z., and Beggs, A.H. (2012). Normal myofibrillar development followed by progressive sarcomeric disruption with actin accumulations in a mouse Cfl2 knockout demonstrates requirement of cofilin-2 for muscle maintenance. Hum. Mol. Genet. *21*: 2341–2356.

Algahtani, F. (2017). Clinical use of vorapaxar as an emerging antithrombin agent: A literature review of current evidence. J. Appl. Hematol. *8*: 127–134.
Andre, P., Morooka, T., Sim, D., Abe, K., Lowell, C., Nanda, N., et al. (2011). Critical role for Syk in responses to vascular injury. Blood *118*: 5000–5010.

Andrews, R.K., and Berndt, M.C. (2013). Bernard-Soulier syndrome: an update. Semin Thromb Hemost *39*: 656–662.

Arachiche, A., Mumaw, M.M., la Fuente, M. de, and Nieman, M.T. (2013). Protease-activated receptor 1 (PAR1) and PAR4 heterodimers are required for PAR1-enhanced cleavage of PAR4 by α-thrombin. J. Biol. Chem. *288*: 32553–32562.

Backliwal, G., Hildinger, M., Chenuet, S., Wulhfard, S., Jesus, M. De, and Wurm, F.M. (2008). Rational vector design and multi-pathway modulation of HEK 293E cells yield recombinant antibody titers exceeding 1 g/l by transient

transfection under serum-free conditions. Nucleic Acids Res. *36*:.

Bamburg, J.R. (1999). PROTEINS OF THE ADF/COFILIN FAMILY: Essential Regulators of Actin Dynamics. Annu Rev Cell Dev Biol *15*: 185–230.

Bamburg, J.R., Harris, H.., and Weeds, A.. (1980). Partial purification and characterization of an actin depolymerizing factor from brain. FEBS Lett. *121*: 178–182.

Begum, H., Murugesan, P., and Tangutur, A.D. (2022). Western blotting: A powerful staple in scientific and biomedical research. Biotechniques *73*: 59–69.

Bellenchi, G.C., Gurniak, C.B., Perlas, E., Middei, S., Ammassari-Teule, M., and Witke, W. (2007). N-cofilin is associated with neuronal migration disorders and cell cycle control in the cerebral cortex. Genes Dev. *21*: 2347–2357.

Belous, A., Wakata, A., Knox, C.D., Nicoud, I.B., Pierce, J., Anderson, C.D., et al. (2004). Mitochondrial P2Y-like receptors link cytosolic adenosine nucleotides to mitochondrial calcium uptake. J. Cell. Biochem. *92*: 1062–1073.

Bender, M., Thon, J.N., Ehrlicher, A.J., Wu, S., Mazutis, L., Deschmann, E., et al. (2015). Microtubule sliding drives proplatelet elongation and is dependent on cytoplasmic dynein. Blood *125*: 860–868.

Benezech, C., Nayar, S., Finney, B., Withers, D., Lowe, K., Desanti, G., et al. (2014). CLEC-2 is required for development and maintenance of lymph nodes. Blood *123*: 3200–3207.

Bennett, J.S., Berger, B.W., and Billings, P.C. (2009). The structure and function of platelet integrins. J. Thromb. Haemost. *7*: 200–205.

Bergmeier, W., and Lucia, S. (2013). Platelet ITAM signaling. Curr. Opin. Haematol. *20*: 445–450.

Berridge, M.J., Lipp, P., and Bootman, M.D. (2000). The versatility and universality of calcium signalling. Nat. Rev. Mol. Cell Biol. *1*: 11–21.

Bianchi, E., Norfo, R., Pennucci, V., Zini, R., and Manfredini, R. (2016). Genomic landscape of megakaryopoiesis and platelet function defects. Blood *127*: 1249–1259.

Bor, W.L., Zheng, K.L., Tavenier, A.H., Gibson, C.M., Granger, C.B., Bentur, O., et al. (2021). Pharmacokinetics, pharmacodynamics, and tolerability of subcutaneous administration of a novel glycoprotein IIb/IIIa inhibitor, RUC-4, in patients with ST-segment elevation myocardial infarction. EuroIntervention *17*: 401–410.

Boulaftali, Y., Hess, P.R., Kahn, M.L., and Bergmeier, W. (2014). Platelet Immunoreceptor Tyrosine-based Activation Motif (ITAM) signaling and vascular integrity. Circ. Res. *114*: 1174–1184.

Bravo-Cordero, J.J., Magalhaes, M.A.O., Eddy, R.J., Hodgson, L., and Condeelis, J. (2013). Functions of cofilin in cell locomotion and invasion. Nat. Rev. Mol. Cell Biol. *14*: 405–417.

Bury, L., Falcinelli, E., and Gresele, P. (2021). Learning the ropes of platelet count regulation: Inherited thrombocytopenias. J. Clin. Med. *10*: 1–24.

Bye, A.P., Unsworth, A.J., and Gibbins, J.M. (2016). Platelet signaling: A complex interplay between inhibitory and activatory networks. J. Thromb. Haemost. *14*: 918–930.

C., P. (1994). Aspirin as an antiplatelet drug. N Engl J Med. *330*: 1287–1294.

Carr, R., Koziol-White, C., Zhang, J., Lam, H., An, S.S., Tall, G.G., et al. (2016). Interdicting Gq activation in airway disease by receptor-dependent and receptor-independent mechanisms. Mol. Pharmacol. *89*: 94–104.

Chackalamannil, S., Wang, Y., Greenlee, W.J., Hu, Z., Xia, Y., Ahn, H.S., et al. (2008). Discovery of a novel, orally active himbacine-based thrombin receptor antagonist (SCH 530348) with potent antiplatelet activity. J. Med. Chem. *51*: 3061–3064.

Chang, Y.W., Hsieh, P.W., Chang, Y.T., Lu, M.H., Huang, T.F., Chong, K.Y., et al. (2015). Identification of a novel platelet antagonist that binds to CLEC-2 and suppresses podoplanin-induced platelet aggregation and cancer metastasis. Oncotarget *6*: 42733–42748.

Chen, X., Wei, S., Ji, Y., Guo, X., and Yang, F. (2015). Quantitative proteomics using SILAC: Principles, applications, and developments. Proteomics *15*: 3175–3192.

Chen, Y.-L., and Kan, W.-M. (2015). Down-regulation of superoxide dismutase 1 by PMA is involved in cell fate determination and mediated via protein kinase D2 in myeloid leukemia cells. Biochim. Biophys. Acta *1853*: 2662–2675.

COHEN, J.A., and LEEKSMA, C.H. (1956). Determination of the life span of human blood platelets using labelled diisopropylfluorophosphonate. J. Clin. Invest. *35*: 964–969.

Collins, D.R.J., Tompson, A.C., Onakpoya, I.J., Roberts, N., Ward, A.M., and Heneghan, C.J. (2017). Global cardiovascular risk assessment in the primary prevention of cardiovascular disease in adults: Systematic review of systematic reviews. BMJ Open *7*:.

Coughlin, S.R. (2000). Thrombin signalling and protease-activated receptors. Nature *407*: 258–264.

Covic, L., Gresser, A.L., and Kuliopulos, A. (2000). Biphasic kinetics of activation and signaling for PAR1 and PAR4 thrombin receptors in platelets. Biochemistry *39*: 5458–5467.

Covic, L., Misra, M., Badar, J., Singh, C., and Kuliopulos, A. (2002). Pepducin-based intervention of thrombin-receptor signaling and systemic platelet activation. Nat. Med. *8*: 1161–1165.

Cunningham, M., McIntosh, K., Bushell, T., Sloan, G., and Plevin, R. (2016). Proteinase-activated receptors (PARs) as targets for antiplatelet therapy. Biochem. Soc. Trans. *44*: 606–612.

Cunningham, M.R., McIntosh, K.A., Pediani, J.D., Robben, J., Cooke, A.E., Nilsson, M., et al. (2012). Novel role for proteinase-activated receptor 2 (PAR2) in membrane trafficking of proteinase-activated receptor 4 (PAR4). J. Biol. Chem. *287*: 16656–16669.

Deng, Z., Jia, Y., Liu, H., He, M., Yang, Y., Xiao, W., et al. (2019). RhoA/ROCK pathway: implication in osteoarthritis and therapeutic targets. Am. J. Transl. Res. *11*: 5324–5331.

Diener, H.C., Cunha, L., Forbes, C., Sivenius, J., Smets, P., and Lowenthal, A. (1996). European stroke prevention study 2. Dipyridamole and acetylsalicylic acid in the secondary prevention of stroke. J. Neurol. Sci. *143*: 1–13.

Dorsam, R.T., Kim, S., Jin, J., and Kunapuli, S.P. (2002). Coordinated signaling through both G12/13 and Gi pathways is sufficient to activate GPIIb/IIIa in human platelets. J. Biol. Chem. *277*: 47588–47595.

Ebbe, S., and Stohlman, F. (1965). Megakaryocytopoiesis in the Rat. Blood *26*: 20–35.

Edelstein, L.C., Simon, L.M., Lindsay, C.R., Kong, X., Teruel-Montoya, R., Tourdot, B.E., et al. (2014). Common variants in the human platelet PAR4 thrombin receptor alter platelet function and differ by race. Blood *124*: 3450–3458.

Eiseler, T., Döppler, H., Yan, I.K., Kitatani, K., Mizuno, K., and Storz, P. (2009). Protein kinase D1 regulates cofilin-mediated F-actin reorganization and cell motility through slingshot. Nat. Cell Biol. *11*: 545–556.

Emmott, E., and Goodfellow, I. (2014). Identification of protein interaction partners in mammalian cells using SILAC-immunoprecipitation quantitative proteomics. J. Vis. Exp. 1–8.

Fasciani, I., Carli, M., Petragnano, F., Colaianni, F., Aloisi, G., Maggio, R., et al. (2022). GPCRs in Intracellular Compartments: New Targets for Drug Discovery. Biomolecules *12*:.

French, S.L., Arthur, J.F., Lee, H., Nesbitt, W.S., Andrews, R.K., Gardiner, E.E., et al. (2016). Inhibition of protease-activated receptor 4 impairs platelet procoagulant activity during thrombus formation in human blood. J. Thromb. Haemost. *14*: 1642–1654.

French, S.L., and Hamilton, J.R. (2016). Protease-activated receptor 4: from structure to function and back again. Br. J. Pharmacol. *173*: 2952–2965.

French, S.L., and Hamilton, J.R. (2017). Drugs targeting protease-activated receptor-4 improve the anti-thrombotic therapeutic window. Ann. Transl. Med. *5*: 1–5.

Gao, Y., Smith, E., Ker, E., Campbell, P., Cheng, E. chun, Zou, S., et al. (2012). Role of RhoA-Specific Guanine Exchange Factors in Regulation of Endomitosis in Megakaryocytes. Dev. Cell *22*: 573–584.

George, J., Soares, C., Montersino, A., Beique, J.C., and Thomas, G.M. (2015). Palmitoylation of LIM Kinase-1 ensures Spine-Specific actin polymerization and morphological plasticity. Elife *2015*: 1–25.

Gibbs, C.R., and Lip, G.Y.H. (1998). Do we still need dipyridamole? Br. J. Clin. Pharmacol. *45*: 323–328.

Giles, C. (1981). The platelet count and mean platelet volume. Br. J. Haematol. *48*: 31–37.

Gillett, G.T., Fox, M.F., Rowe, P.S., Casimir, C.M., and Povey, S. (1996). Mapping of human non-muscle type cofilin (CFL1) to chromosome 11q13 and muscle-type cofilin (CFL2) to chromosome 14. Ann. Hum. Genet. *60*: 201–211.

Gobbi, G., Mirandola, P., Carubbi, C., Masselli, E., Sykes, S.M., Ferraro, F., et al. (2013). Proplatelet generation in the mouse requires PKCε-dependent RhoA inhibition. Blood *122*: 1305–1311.

Gohla, A., Birkenfeld, J., and Bokoch, G.M. (2005). Chronophin, a novel HAD-type serine protein phosphatase, regulates cofilin-dependent actin dynamics. Nat. Cell Biol. *7*: 21–29.

Gohla, A., and Bokoch, G.M. (2002). 14-3-3 Regulates Actin Dynamics by Stabilizing Phosphorylated Cofilin. Curr. Biol. *12*: 1704–1710.

Gragnano, F., Golia, E., Natale, F., Bianchi, R., Pariggiano, I., Crisci, M., et al. (2017). Von Willebrand Factor and Cardiovascular Disease: From a Biochemical Marker to an Attractive Therapeutic Target. Curr Vasc Pharmacol.

15: 404–415.

Gresele P, Deckmyn H, Nenci GG, V.J. (1991). Thromboxane synthase inhibitors, thromboxane receptor antagonists and dual blockers in thrombotic disorders. Trends Pharmacol Sci. *Apr;12 (4)*: 158–163.

Gresele, P. (2013). Antiplatelet agents in clinical practice and their haemorrhagic risk. Blood Transfus. *11*: 349–356.

Gurniak, C.B., Perlas, E., and Witke, W. (2005). The actin depolymerizing factor n-cofilin is essential for neural tube morphogenesis and neural crest cell migration. Dev. Biol. *278*: 231–241.

Hakanishi-Matsui, M., Zheng, Y.W., Sulciner, D.J., Welss, E.J., Ludeman, M.J., and Coughlin, S.R. (2000). PAR3 is a cofactor for PAR4 activation by thrombin. Nature *404*: 609–613.

Halkes, P., Gijn, L.. van, Kappelle, P.., Koudstaal, A., and Algra, A. (2006). Aspirin plus dipyridamole versus aspirin alone after cerebral ischaemia of arterial origin (ESPRIT): randomised controlled trial. Lancet *367*: 1665–1673.

Han, X., Hofmann, L., la Fuente, M. de, Alexander, N., Palczewski, K., and Neiman, M. (2020). PAR4 activation involves extracellular loop-3 and transmembrane residue Thr 153. Blood *136*: 2217–2228.

Han, X., and Nieman, M.T. (2018a). PAR4 (Protease-Activated Receptor 4): PARticularly Important 4 Antiplatelet Therapy. Arterioscler. Thromb. Vasc. Biol. *38*: 287–289.

Han, X., and Nieman, M.T. (2018b). Protease activated receptor 4: a backup receptor or a dark horse as a target in antiplatelet therapy? Ann. Transl. Med. *6*: 56–56.

Han, X., and Nieman, M.T. (2020). The domino effect triggered by the tethered ligand of the protease activated receptors. Thromb. Res. *196*: 87–98.

Hearn, J.I., Green, T.N., Chopra, M., Nursalim, Y.N.S., Ladvanszky, L., Knowlton, N., et al. (2020). N-Methyl-D-Aspartate Receptor Hypofunction in Meg-01 Cells Reveals a Role for Intracellular Calcium Homeostasis in Balancing Megakaryocytic-Erythroid Differentiation. Thromb. Haemost. *120*: 671–686.

Hechler, B., Nonne, C., Eun, J.R., Cattaneo, M., Cazenave, J.P., Lanza, F., et al. (2006). MRS2500 [2-iodo-N6-methyl-(N)-methanocarba-2′-deoxyadenosine-3′,5′-bisphosphate], a potent, selective, and stable antagonist of the platelet P2y1 receptor with strong antithrombotic activity in mice. J. Pharmacol. Exp. Ther. *316*: 556–563.

Heo, Y., Jeon, H., and Namkung, W. (2022). PAR4-Mediated PI3K/Akt and RhoA/ROCK Signaling Pathways Are Essential for Thrombin-Induced Morphological Changes in MEG-01 Cells. Int. J. Mol. Sci. *23*: 1–15.

Herrington, W., Lacey, B., Sherliker, P., Armitage, J., and Lewington, S. (2016). Epidemiology of Atherosclerosis and the Potential to Reduce the Global Burden of Atherothrombotic Disease. Circ. Res. *118*: 535–546.

Herzog, B.H., Fu, J., Wilson, S.J., Hess, P.R., Sen, A., McDaniel, J.M., et al. (2013). Podoplanin maintains high endothelial venule integrity by interacting with platelet CLEC-2. Nature *502*: 105–109.

Heuberger, D.M., and Schuepbach, R.A. (2019). Correction to: Protease-activated receptors (PARs): Mechanisms of action and potential therapeutic modulators in PAR-driven inflammatory diseases (Thrombosis Journal (2019) 17: 4 DOI: 10.1186/s12959-019-0194-8). Thromb. J. *17*: 1–24.

Hidaka, H., and Asano, T. (1976). Human blood platelet 3′:5′-cyclic nucleotide phosphodiesterase: Isolation of low-Km and high-Km phosphodiesterase. Biochim. Biophys. Acta - Enzymol. *429*: 485–497.

Hoxie, J.A., Ahuja, M., Belmonte, E., Pizarro, S., Parton, R., and Brass, L.F. (1993). Internalization and recycling of activated thrombin receptors. J. Biol. Chem. *268*: 13756–13763.

Huang, T.Y., Minamide, L.S., Bamburg, J.R., and Bokoch, G.M. (2008). Chronophin mediates an ATP-sensing mechanism for cofilin dephosphorylation and neuronal cofilin-actin rod formation. Dev. Cell *15*: 691–703.

Husted, S., Emanuelsson, H., Heptinstall, S., Sandset, P.M., Wickens, M., and Peters, G. (2006). Pharmacodynamics, pharmacokinetics, and safety of the oral reversible P2Y12 antagonist AZD6140 with aspirin in patients with atherosclerosis: A double-blind comparison to clopidogrel with aspirin. Eur. Heart J. *27*: 1038–1047.

Ikeda, S., Cunningham, L.A., Boggess, D., Hobson, C.D., Sundberg, J.P., Naggert, J.K., et al. (2003). Aberrant actin cytoskeleton leads to accelerated proliferation of corneal epithelial cells in mice deficient for destrin (actin depolymerizing factor). Hum. Mol. Genet. *12*: 1029–1036.

Italiano, J.E., Lecine, P., Shivdasani, R.A., and Hartwig, J.H. (1999). Blood platelets are assembled principally at the ends of proplatelet processes produced by differentiated megakaryocytes. J. Cell Biol. *147*: 1299–1312.

Jadoui, S., Chapelain, O. Le, Ollivier, V., Mostefa-Kara, A., Meglio, L. Di, Dupont, S., et al. (2021). Glenzocimab does not impact glycoprotein VI-dependent inflammatory hemostasis. Haematologica *106*: 2000–2003.

Joo, S. Mechanisms of Platelet Activation and Integrin α II β 3 Mediators of Platelet Activation Adenosine diphosphate Platelet Integrins Integrins are a widely expressed family of heterodimeric transmembrane receptors linking extracellular ligands to intracellul. 1–8.

Jung, S.K., Dae, G.J., Yoon, T.S., Jae, H.K., Seong, E.R., and Seung, J.K. (2007). Crystal structure of human slingshot phosphatase 2. Proteins Struct. Funct. Genet. *68*: 408–412.

Kaikita, K., Ogawa, H., Yasue, H., Takeya, M., Takahashi, K., Saito, T., et al. (1997). Tissue factor expression on macrophages in coronary plaques in patients with unstable angina. Arterioscler. Thromb. Vasc. Biol. *17*: 2232–2237.

Kanellos, G., and Frame, M.C. (2016). Cellular functions of the ADF/cofilin family at a glance. J. Cell Sci. *129*: 3211–3218.

Kanellos, G., Zhou, J., Patel, H., Ridgway, R.A., Huels, D., Gurniak, C.B., et al. (2015). ADF and Cofilin1 Control Actin Stress Fibers, Nuclear Integrity, and Cell Survival. Cell Rep. *13*: 1949–1964.

Kanke, T., Macfarlane, S.R., Seatter, M.J., Davenport, E., Paul, A., McKenzie, R.C., et al. (2001). Proteinase-activated Receptor-2-mediated Activation of Stress-activated Protein Kinases and Inhibitory κB Kinases in NCTC 2544 Keratinocytes. J. Biol. Chem. *276*: 31657–31666.

Kereiakes, D.J., Henry, T.D., Demaria, A.N., Bentur, O., Carlson, M., Yue, C.S., et al. (2020). First human use of ruc-4: A nonactivating second-generation small-molecule platelet glycoprotein iib/iiia (integrin αiibβ3) inhibitor designed for subcutaneous point-of-care treatment of st-segment–elevation myocardial infarction. J. Am. Heart Assoc. *9*:.

Khan, A., Li, D., Ibrahim, S., Smyth, E., and Woulfe, D.S. (2014). The physical association of the P2Y12 receptor with PAR4 regulates arrestin-mediated akt activation. Mol. Pharmacol. *86*: 1–11.

Kim, B.J., Kwon, S.U., Park, J.H., Kim, Y.J., Hong, K.S., Wong, L.K.S., et al. (2020). Cilostazol Versus Aspirin in Ischemic Stroke Patients With High-Risk Cerebral Hemorrhage: Subgroup Analysis of the PICASSO Trial. Stroke *51*: 931–937.

Kim, H.H., and Liao, J.K. (2008). Translational therapeutics of dipyridamole. Arterioscler. Thromb. Vasc. Biol. *28*:.

Kovacsovics, T.J., and Hartwig, J.H. (1996). Thrombin-induced GPIb-IX centralization on the platelet surface requires actin assembly and myosin II activation. Blood *87*: 618–629.

Kühn, S., and Geyer, M. (2014). Formins as effector proteins of rho GTPases. Small GTPases *5*: 1–16.

Kurita, S., Watanabe, Y., Gunji, E., Ohashi, K., and Mizuno, K. (2008). Molecular dissection of the mechanisms of substrate recognition and F-actin-mediated activation of cofilin-phosphatase slingshot-1. J. Biol. Chem. *283*: 32542–32552.

La Fuente, M. De, Noble, D.N., Verma, S., and Nieman, M.T. (2012). Mapping human Protease-activated Receptor 4 (PAR4) homodimer interface to transmembrane helix 4. J. Biol. Chem. *287*: 10414–10423.

Lawler, S. (1999). Regulation of actin dynamics: The LIM kinase connection. Curr. Biol. *9*: 800–802.

Le, F.Y., Lien, J.C., Huang, L.J., Huang, T.M., Tsai, S.C., Teng, C.M., et al.

(2001). Synthesis of 1-benzyl-3-(5′-hydroxymethyl-2′-furyl)indazole analogues as novel antiplatelet agents. J. Med. Chem. *44*: 3746–3749.

Lebozec, K., Jandrot-Perrus, M., Avenard, G., Favre-Bulle, O., and Billiald, P. (2017). Design, development and characterization of ACT017, a humanized Fab that blocks platelet's glycoprotein VI function without causing bleeding risks. MAbs *9*: 945–958.

Lecut, C., Feeney, L.A., Kingsbury, G., Hopkins, J., Lanza, F., Gachet, C., et al. (2003). Human platelet glycoprotein VI function is antagonized by monoclonal antibody-derived fab fragments. J. Thromb. Haemost. *1*: 2653–2662.

Leeksma, C.H.., and Cohen, J.. (1955). Determination of the life of Human blood platelets using labelled Diisopropylfluorophosphonate. Nature *175*: 552–553.

Leger, A.J., Jacques, S.L., Badar, J., Kaneider, N.C., Derian, C.K., Andrade-Gordon, P., et al. (2006). Blocking the protease-activated receptor 1-4 heterodimer in platelet-mediated thrombosis. Circulation *113*: 1244–1254.

Lei Adili; Hou, Yan; Zhou, Hui; Wang, Yiming; Marshall, Alexandra H.; Liang, Chaofan; Dai, Xiangrong; Li, Benjamin Xiaoyi; Vanhoorelbeke, Karen; Ni, Heyu, X.R. (2014). Anfibatide, a novel GPIb complex antagonist, inhibits platelet adhesion and thrombus formation in vitro and in vivo in murine models of thrombosis. Thromb Haemost *112*: 279–289.

Léon, C., Freund, M., Ravanat, C., Baurand, A., Cazenave, J.P., and Gachet, C. (2001). Key role of the P2Y1 receptor in tissue factor-induced thrombin-dependent acute thromboembolism: Studies in P2Y1-knockout mice and mice treated with a P2Y1 antagonist. Circulation *103*: 718–723.

Li, B.X., Dai, X., Xu, X.R., Adili, R., Neves, M.A.D., Lei, X., et al. (2021). In vitro

assessment and phase I randomized clinical trial of anfibatide a snake venom derived anti-thrombotic agent targeting human platelet GPIbα. Sci. Rep. *11*: 1–17.

Li, J., Vootukuri, S., Shang, Y., Negri, A., Jiang, J.-K., Nedelman, M., et al. (2014). RUC-4: A Novel αIIbβ3 Antagonist for Pre-hospital Therapy of Myocardial Infarction. Arter. Thromb Vasc Biol. *34*: 2321–2329.

Li, T.T., Fan, M.L., Hou, S.X., Li, X.Y., Barry, D.M., Jin, H., et al. (2015). A novel snake venom-derived GPIb antagonist, anfibatide, protects mice from acute experimental ischaemic stroke and reperfusion injury. Br. J. Pharmacol. *172*: 3904–3916.

Li, Z., Delaney, M.K., O'Brien, K.A., and Du, X. (2010). Signaling during platelet adhesion and activation. Arterioscler. Thromb. Vasc. Biol. *30*: 2341–2349.

Libby, P., Buring, J.E., Badimon, L., Hansson, G.K., Deanfield, J., Bittencourt, M.S., et al. (2019). Atherosclerosis. Nat. Rev. Dis. Prim. *5*: 1–18.

Lin, H., Liu, A.P., Smith, T.H., and Trejo, J. (2013). Cofactoring and dimerization of proteinase-activated receptors. Pharmacol. Rev. *65*: 1198–1213.

Lin, Y.C., Boone, M., Meuris, L., Lemmens, I., Roy, N. Van, Soete, A., et al. (2014). Genome dynamics of the human embryonic kidney 293 lineage in response to cell biology manipulations. Nat. Commun. *5*:.

Lin, Y.C., Ko, Y.C., Hung, S.C., Lin, Y.T., Lee, J.H., Tsai, J.Y., et al. (2019). Selective Inhibition of PAR4 (Protease-Activated Receptor 4)-Mediated Platelet Activation by a Synthetic Nonanticoagulant Heparin Analog. Arterioscler. Thromb. Vasc. Biol. *39*: 694–703.

Lind, S., Dahlgren, C., and Forsman, H. (2019). The putative G α q-inhibiting pepducin P4Pal 10 distinctly modulates function of the G α i- coupled receptors FPR2 and FFA2R in neutrophils Short title : A Gαq-inhibiting pepducin modulates neutrophil functions.

Lindström, S., Wang, L., Smith, E.N., Gordon, W., Hylckama Vlieg, A. Van, Andrade, M. De, et al. (2019). Genomic and transcriptomic association studies identify 16 novel susceptibility loci for venous thromboembolism. Blood *134*: 1645–1657.

Liu, L.W., Vu, T.K.H., Esmon, C.T., and Coughlin, S.R. (1991). The region of the thrombin receptor resembling hirudin binds to thrombin and alters enzyme specificity. J. Biol. Chem. *266*: 16977–16980.

Lynch, J.R., and Wang, J.Y. (2016). G protein-coupled receptor signaling in stem cells and cancer. Int. J. Mol. Sci. *17*:.
Macfarlane, S.R., Seatter, M.J., Kanke, T., Hunter, G.D., and Plevin, R. (2001). Proteinase-Activated Receptors. *53*: 245–282.

Machlus, K.R., and Italiano, J.E. (2013). The incredible journey: From megakaryocyte development to platelet formation. J. Cell Biol. *201*: 785–796.
Maciver, S.K., and Hussey, P.J. (2002). Protein family review The ADF / cofilin family : actin-remodeling proteins. Genome Biol. 1–12.

Maekawa, M., Ishizaki, T., Boku, S., Watanabe, N., Fujita, A., Iwamatsu, A., et al. (1999). Signaling from Rho to the actin cytoskeleton through protein kinases ROCK and LIM-kinase. Science (80-.). *285*: 895–898.

Mangin, P.H., Tang, C.J., Bourdon, C., Loyau, S., Freund, M., Hechler, B., et al. (2012). A humanized glycoprotein VI (GPVI) mouse model to assess the antithrombotic efficacies of anti-GPVI agents. J. Pharmacol. Exp. Ther. *341*: 156–163.

Mann, M. (2006). Functional and quantitative proteomics using SILAC. Nat. Rev. Mol. Cell Biol. *7*: 952–958.

Margineanu, A., Chan, J.J., Kelly, D.J., Warren, S.C., Flatters, D., Kumar, S., et al. (2016). Screening for protein-protein interactions using Förster resonance energy transfer (FRET) and fluorescence lifetime imaging microscopy (FLIM). Sci. Rep. *6*:.

Massberg, S., Konrad, I., Bültmann, A., Schulz, C., Münch, G., Peluso, M., et al. (2004). Soluble glycoprotein VI dimer inhibits platelet adhesion and aggregation to the injured vessel wall in vivo. FASEB J. *18*: 397–399.

Mayer, K., Hein-Rothweiler, R., Schupke, S., Janisch, M., and Bernlochner, I. (2021). Efficacy and Safety of Revacept, a Novel Lesion-Directed Competitive Antagonist to Platelet Glycoprotein VI, in Patients Undergoing Elective Percutaneous Coronary Intervention for Stable Ischemic Heart Disease: The Randomized, Double-blind, Placebo-Contro. JAMA Cardiol *6*: 753–761.

Mazighi, M., Kohrmann, M., Lemmens, R., Lyrer, P., Molina, C., Richard, S., et al. (2023). THERAPEUTIC INHIBITION OF PLATELET GLYCOPROTEIN VI IN ACUTE ISCHEMIC STROKE. Lancet 1–56.

McCudden, C.R., Hains, M.D., Kimple, R.J., Siderovski, D.P., and Willard, F.S. (2005). G-protein signaling: Back to the future. Cell. Mol. Life Sci. *62*: 551–577.

McFadyen, J.D., Schaff, M., and Peter, K. (2018). Current and future antiplatelet therapies: Emphasis on preserving haemostasis. Nat. Rev.

Cardiol. *15*: 181–191.

Meijden, P.E.J. van der, and Heemskerk, J.W.M. (2019). Platelet biology and functions: new concepts and clinical perspectives. Nat. Rev. Cardiol. *16*: 166–179.

Meng, D., Luo, M., and Liu, B. (2021). The Role of CLEC-2 and Its Ligands in Thromboinflammation. Front. Immunol. *12*: 688643.

Merali, S., Wang, Z., Frost, C., Meadows-Shropshire, S., Hawthorne, D., Yang, J., et al. (2023). First-in-human study to assess the safety, pharmacokinetics, and pharmacodynamics of BMS-986141, a novel, reversible, small-molecule, PAR4 agonist in non-Japanese and Japanese healthy participants. Platelets *34*:.

Mi, H., and Thomas, P. (2019). PANTHER Pathway: an ontology-based pathway dtabase coupled With Data Analysis Tools. *563*: 123–140.

Miernyk, J.A., and Thelen, J.J. (2008). Biochemical approaches for discovering protein-protein interactions. Plant J. *53*: 597–609.

Miki, H., Suetsugu, S., and Takenawa, T. (1998). WAVE, a novel WASP-family protein involved in actin reorganization induced by Rac. EMBO J. *17*: 6932–6941.

Mizuno, K., Okano, I., Ohashi, K., Nunoue, K., Kuma, K.I., Miyata, T., et al. (1994). Identification of a human cDNA encoding a novel protein kinase with two repeats of the LIM/double zinc finger motif. Oncogene *9*: 1605–1612.

Mohri, K., Takano-Ohmuro, H., Nakashima, K., Hayakawa, K., Endo, T., Hanaoka, K., et al. (2000). Expression of cofilin isoforms during development

of mouse striated muscles. J. Muscle Res. Cell Motil. *21*: 49–57.

Morgan, T.E., Lockerbie, R.O., Minamide, L.S., Browning, M.D., and Bamburg, J.R. (1993). Isolation and characterization of a regulated form of actin depolymerizing factor. J. Cell Biol. *122*: 623–633.

Moriyama, K., Iida, K., and Yahara, I. (1996). Phosphorylation of Ser-3 of cofilin regulates its essential function on actin. Genes to Cells *1*: 73–86.

Mueller, F., Morisaki, T., Mazza, D., and McNally, J.G. (2012). Minimizing the impact of photoswitching of fluorescent proteins on FRAP analysis. Biophys. J. *102*: 1656–1665.

Mumaw, M.M., la Fuente, M. de, Noble, D.N., and Nieman, M.T. (2014). Targeting the anionic region of human protease-activated receptor 4 inhibits platelet aggregation and thrombosis without interfering with hemostasis. J. Thromb. Haemost. *12*: 1331–1341.

Munoz, A.-K., Jamasbi, J., Uhland, K., Degen, H., Munch, G., Ungerer, M., et al. (2017). Recombinant GPVI-Fc added to single or dual antiplatelet therapy in vitro prevents plaque-induced platelet thrombus formation. Thromb. Haemost. *117*: 1651–1659.

Nagata-Ohashi, K., Ohta, Y., Goto, K., Chiba, S., Mori, R., Nishita, M., et al. (2004). A pathway of neuregulin-induced activation of cofilin-phosphatase Slingshot and cofilin in lamellipodia. J. Cell Biol. *165*: 465–471.

Nakano, K., Kanai-Azuma, M., Kanai, Y., Moriyama, K., Yazaki, K., Hayashi, Y., et al. (2003). Cofilin phosphorylation and actin polymerization by NRK/NESK, a member of the germinal center kinase family. Exp. Cell Res. *287*: 219–227.

Nash, J., Meah, M.N., Whittington, B., Debono, S., Raftis, J., Miller, M.R., et al. (2024). PAR4 Antagonism in Patients with Coronary Artery Disease Receiving Antiplatelet Therapies. Arterioscler. Thromb. Vasc. Biol. *44*: 987–996.

New, D.C., Wu, K., Kwok, A.W.S., and Wong, Y.H. (2007). G protein-coupled receptor-induced Akt activity in cellular proliferation and apoptosis. FEBS J. *274*: 6025–6036.

Nieswandt, B., Varga-Szabo, D., and Elvers, M. (2009). Integrins in platelet activation. J. Thromb. Haemost. *7*: 206–209.

Nilsson, M.. (2010). Characterisation of proteinase-activated receptor-4 (PAR-4) signalling in NCTC-2544 cells stably expressing PAR-4 (Clone 10H9) and PAR-4 expressing cells, EAhy-926.

Nishita, M., Tomizawa, C., Yamamoto, M., Horita, Y., Ohashi, K., and Mizuno, K. (2005). Spatial and temporal regulation of cofilin activity by LIM kinase and Slingshot is critical for directional cell migration. J. Cell Biol. *171*: 349–359.

Niwa, R., Nagata-Ohashi, K., Takeichi, M., Mizuno, K., and Uemura, T. (2002). Control of actin reorganization by slingshot, a family of phosphatases that dephosphorylate ADF/cofilin. Cell *108*: 233–246.

Norman, J.E., Cunningham, M.R., Jones, M.L., Walker, M.E., Westbury, S.K., Sessions, R.B., et al. (2016). Protease-activated receptor 4 variant p.Tyr157Cys reduces platelet functional responses and alters receptor trafficking. Arterioscler. Thromb. Vasc. Biol. *36*: 952–960.

Nunoue, K., Ohashi, K., Okano, I., and Mizuno, K. (1995). LIMK-1 and LIMK-2, two members of a LIM motif-containing protein kinase family. Oncogene *11*:

701–710.

Nunthanasup, N., Ketprasit, N., Noulsri, E., Palasuwan, A., Combes, V., Kulkeaw, K., et al. (2023). Thrombopoietin-independent generation of platelet-like particles from megakaryoblastic cells. Sci. Rep. *13*: 1–15.

Nurden, A.T. (2006). Glanzmann thrombasthenia. Orphanet J. Rare Dis. *1*: 1–8.

Ockeloen, C.W., Gilhuis, H.J., Pfundt, R., Kamsteeg, E.J., Agrawal, P.B., Beggs, A.H., et al. (2012). Congenital myopathy caused by a novel missense mutation in the CFL2 gene. Neuromuscul. Disord. *22*: 632–639.

Odell, T.T., and Jackson, C.W. (1968). Polyploidy and maturation of rat megakaryocytes. Blood *32*: 102–110.

Odell, T.T., and Macdonald, T.P. (1961). Life Span of Mouse Blood Platelets. Exp. Biol. Med. *106*: 107–108.

Offermanns, S. (2006). Activation of platelet function through G protein-coupled receptors. Circ. Res. *99*: 1293–1304.

Ogura M, M.Y., R, O., and Al., E. (1985). Establishment of a novel human megakaryoblastic leukemia cell line, MEG-01, with positive Philadelphia chromosome. Blood *66*: 1384–1392.

Ohashi, K., Nagata, K., Maekawa, M., Ishizaki, T., Narumiya, S., and Mizuno, K. (2000). Rho-associated kinase ROCK activates LIM-kinase 1 by phosphorylation at threonine 508 within the activation loop. J. Biol. Chem. *275*: 3577–3582.

Ohta, Y., Kousaka, K., Nagata-Ohashi, K., Ohashi, K., Muramoto, A., Shima,

Y., et al. (2003). Differential activities, subcellular distribution and tissue expression patterns of three members of Slingshot family phosphatases that dephosphorylate cofilin. Genes to Cells *8*: 811–824.

Okano, I., Hiraoka, J., Otera, H., Nunoue, K., Ohashi, K., Iwashita, S., et al. (1995). Identification and characterization of a novel family of serine/threonine kinases containing two N-terminal LIM motifs. J. Biol. Chem. *270*: 31321–31330.

Paolo Gresele, Gustav V.R. Born, Carlo Patrono, C.P.P. (2012). Handbook of Experimental Pharmacology: Antiplatelet Agents.

Patel, S.R., Richardson, J.L., Schulze, H., Kahle, E., Galjart, N., Drabek, K., et al. (2005). Differential roles of microtubule assembly and sliding in proplatelet formation by megakaryocytes. Blood *106*: 4076–4085.

Patrignani, P., and Patrono, C. (2018). Aspirin, platelet inhibition and cancer prevention. Platelets *29*: 779–785.

Patrono, C., and Rocca, B. (2017). Type 2 Diabetes, Obesity, and Aspirin Responsiveness. J. Am. Coll. Cardiol. *69*: 613–615.

Patterson, K.I., Brummer, T., O'Brien, P.M., and Daly, R.J. (2009). Dual-specificity phosphatases: Critical regulators with diverse cellular targets. Biochem. J. *418*: 475–489.

Pecci Valeria; Panza, Emanuele; Barozzi, Serena; Gruppi, Cristian; Seri, Marco; Balduini, Carlo L., A.B. (2011). Mutations responsible for MYH9-related thrombocytopenia impair SDF-1-driven migration of megakaryoblastic cells. Thromb Haemost *106*: 693–704.

Pedersen AK, F.G. (1984). Dose-related kinetics of aspirin. Presystemic

acetylation of platelet cyclooxygenase. N Engl J Med. *311*: 1206–1211.

Peterburs, P., Heering, J., Link, G., Pfizenmaier, K., Olayioye, M.A., and Hausser, A. (2009). Protein kinase D regulates cell migration by direct phosphorylation of the cofilin phosphatase slingshot 1 like. Cancer Res. *69*: 5634–5638.

Pleines, I., Dütting, S., Cherpokova, D., Eckly, A., Meyer, I., Morowski, M., et al. (2013). Defective tubulin organization and proplatelet formation in murine megakaryocytes lacking Rac1 and Cdc42. Blood *122*: 3178–3187.

Pleines, I., Eckly, A., Elvers, M., Hagedorn, I., Eliautou, S., Bender, M., et al. (2010). Multiple alterations of platelet functions dominated by increased secretion in mice lacking Cdc42 in platelets. Blood *115*: 3364–3373.

Pleines, I., Hagedorn, I., Gupta, S., May, F., Chakarova, L., Hengel, J. Van, et al. (2012). Megakaryocyte-specific RhoA deficiency causes macrothrombocytopenia and defective platelet activation in hemostasis and thrombosis. Blood *119*: 1054–1063.

Poulter, N.S., and Thomas, S.G. (2015). Cytoskeletal regulation of platelet formation: Coordination of F-actin and microtubules. Int. J. Biochem. Cell Biol. *66*: 69–74.

Prudent, R., Demoncheaux, N., Diemer, H., Collin-Faure, V., Kapur, R., Paublant, F., et al. (2018). A quantitative proteomic analysis of cofilin phosphorylation in myeloid cells and its modulation using the LIM kinase inhibitor Pyr1. PLoS One *13*: 1–17.

R Rohatgi, L Ma, H Miki, M Lopez, T Kirchhausen, T Takenawa, et al. (1999). The Interaction between N-WASP and the Arp2/3 Complex Links Cdc42-

Dependent Signals to Actin Assembly. Cell *97*: 221–231.

Richardson, J.L., Shivdasani, R.A., Boers, C., Hartwig, J.H., and Italiano, J.E. (2005). Mechanisms of organelle transport and capture along proplatelets during platelet production. Blood *106*: 4066–4075.

Rigg, R.A., Healy, L.D., Chu, T.T., Ngo, A.T.P., Mitrugno, A., Zilberman-rudenko, J., et al. (2020). Protease-activated receptor 4 (PAR4) activity promotes platelet granule release and platelet-leukocyte interactions. Platelets *30*: 126–135.

Rikken, S.A.O.F., Selvarajah, A., Hermanides, R.S., Coller, B.S., Gibson, C.M., Granger, C.B., et al. (2023). Prehospital treatment with zalunfiban (RUC-4) in patients with ST- elevation myocardial infarction undergoing primary percutaneous coronary intervention: Rationale and design of the CELEBRATE trial. Am. Heart J. *258*: 119–128.

Rodríguez, L.A.G., Martín-Pérez, M., Hennekens, C.H., Rothwell, P.M., and Lanas, A. (2016). Bleeding risk with long-term low-dose aspirin: A systematic review of observational studies. PLoS One *11*: 1–20.

Roth, G.A., Johnson, C., Abajobir, A., Abd-Allah, F., Abera, S.F., Abyu, G., et al. (2017). Global, Regional, and National Burden of Cardiovascular Diseases for 10 Causes, 1990 to 2015. J. Am. Coll. Cardiol. *70*: 1–25.

Rudinga, G.R., Khan, G.J., and Kong, Y. (2018). Protease-activated receptor 4 (PAR4): A promising target for antiplatelet therapy. Int. J. Mol. Sci. *19*:.

Sable, R., Jambunathan, N., Singh, S., Pallerla, S., Kousoulas, K.G., and Jois, S. (2018). Proximity ligation assay to study protein-protein interactions of proteins on two different cells. Biotechniques *65*: 150–157.

Sakuma, M., Shirai, Y., Yoshino, K.I., Kuramasu, M., Nakamura, T., Yanagita, T., et al. (2012). Novel PKCα-mediated phosphorylation site(s) on cofilin and their potential role in terminating histamine release. Mol. Biol. Cell *23*: 3707–3721.

Sandmann, R., and Köster, S. (2016). Topographic Cues Reveal Two Distinct Spreading Mechanisms in Blood Platelets. Sci. Rep. *6*: 1–11.

Sasaki, T., Shirai, T., Tsukiji, N., Otake, S., Tamura, S., Ichikawa, J., et al. (2018). Functional characterization of recombinant snake venom rhodocytin: rhodocytin mutant blocks CLEC-2/podoplanin-dependent platelet aggregation and lung metastasis. J. Thromb. Haemost. *16*: 960–972.

Schachtner, H., Calaminus, S.D.J., Sinclair, A., Monypenny, J., Blundell, M.P., Leon, C., et al. (2013). Megakaryocytes assemble podosomes that degrade matrix and protrude through basement membrane. Blood *121*: 2542–2552.

Schecter, A.D., Giesen, P.L.A., Taby, O., Rosenfield, C.L., Rossikhina, M., Fyfe, B.S., et al. (1997). Tissue factor expression in human arterial smooth muscle cells: TF is present in three cellular pools after growth factor stimulation. J. Clin. Invest. *100*: 2276–2285.

Schilling Jasper; Dobrow, Michael; Baumann, Martine; Riederer, Markus A.; Juif, Pierre-Eric; Ufer, Mike, U.D. (2021). Insights from In Vitro and Clinical Data to Guide Transition from the Novel P2Y12 Antagonist Selatogrel to Clopidogrel, Prasugrel, and Ticagrelor. Thromb Haemost *121*: 755–766.

Scirica, B.M., Bonaca, M.P., Braunwald, E., Ferrari, G.M. De, Isaza, D., Lewis, B.S., et al. (2012). Vorapaxar for secondary prevention of thrombotic events for patients with previous myocardial infarction: A prespecified subgroup analysis of the TRA 2°P-TIMI 50 trial. Lancet *380*: 1317–1324.

Serebruany, V.L., Malinin, A.I., Eisert, R.M., and Sane, D.C. (2004). Risk of Bleeding Complications with Antiplatelet Agents: Meta-Analysis of 338,191 Patients Enrolled in 50 Randomized Controlled Trials. Am. J. Hematol. *75*: 40–47.

Shao, B., Hoover, C., Shi, H., Kondo, Y., Lee, R.H., Chen, J., et al. (2022). Deletion of platelet CLEC-2 decreases GPIbα-mediated integrin αIIbβ3 activation and decreases thrombosis in TTP. Blood *139*: 2523–2533.

Shapiro, M.J., Weiss, E.J., Faruqi, T.R., and Coughlin, S.R. (2000). Protease-activated receptors 1 and 4 are shut off with distinct kinetics after activation by thrombin. J. Biol. Chem. *275*: 25216–25221.

Shishkin, S., Eremina, L., Pashintseva, N., Kovalev, L., and Kovaleva, M. (2017). Cofilin-1 and other ADF/cofilin superfamily members in human malignant cells. Int. J. Mol. Sci. *18*: 1–27.

Simon, M.I., Strathmann, M.P., and Gautam, N. (1991). Diversity of g proteins. Science *252*: 802–808.

Sinnaeve, P., Fahrni, G., Schelfaut, D., Spirito, A., Mueller, C., Frenoux, J.M., et al. (2020). Subcutaneous Selatogrel Inhibits Platelet Aggregation in Patients With Acute Myocardial Infarction. J. Am. Coll. Cardiol. *75*: 2588–2597.

Smith, T.H., Coronel, L.J., Li, J.G., Dores, M.R., Nieman, M.T., and Trejo, J. (2016). Protease-activated Receptor-4 Signaling and Trafficking Is Regulated by the Clathrin Adaptor Protein Complex-2 Independent of β-Arrestins. J. Biol. Chem. *291*: 18453–18464.

Smyth, S.S., Whiteheart, S., Italiano, J.E., Bray, P., and Coller, B.S. (2015). Platelet Morphology, Biochemistry, and Function. In Williams Hematology, 9e, K. Kaushansky, M.A. Lichtman, J.T. Prchal, M.M. Levi, O.W. Press, L.J. Burns,

et al., eds. (New York, NY: McGraw-Hill Education), p.

Soosairajah, J., Maiti, S., Wiggan, O., Sarmiere, P., Moussi, N., Sarcevic, B., et al. (2005). Interplay between components of a novel LIM kinase-slingshot phosphatase complex regulates cofilin. EMBO J. *24*: 473–486.

Spratley, S.J., Bastea, L.I., Döppler, H., Mizuno, K., and Storz, P. (2011). Protein kinase D regulates cofilin activity through p21-activated kinase 4. J. Biol. Chem. *286*: 34254–34261.

Springer, T.A., Zhu, J., and Xiao, T. (2008). Structural basis for distinctive recognition of fibrinogen γC peptide by the platelet integrin αIIbβ3. J. Cell Biol. *182*: 791–800.

Stewart, J., Manmathan, G., and Wilkinson, P. (2017). Primary prevention of cardiovascular disease: A review of contemporary guidance and literature. JRSM Cardiovasc. Dis. *6*: 204800401668721.

Storey, R.F., Gurbel, P.A., Berg, J. ten, Bernaud, C., Dangas, G.D., Frenoux, J.M., et al. (2020). Pharmacodynamics, pharmacokinetics, and safety of single-dose subcutaneous administration of selatogrel, a novel P2Y12 receptor antagonist, in patients with chronic coronary syndromes. Eur. Heart J. *41*: 3132–3140.

Sumi, T., Matsumoto, K., and Nakamura, T. (2001). Specific activation of LIM kinase 2 via phosphorylation of threonine 505, by ROCK, a Rho-dependent protein kinase. J. Biol. Chem. *276*: 670–676.

Sun, B., Li, H., Shakur, Y., Hensley, J., Hockman, S., Kambayashi, J., et al. (2007). Role of phosphodiesterase type 3A and 3B in regulating platelet and cardiac function using subtype-selective knockout mice. Cell. Signal. *19*: 1765–1771.

Sun, Y., Liang, L., Dong, M., Li, C., Liu, Z., and Gao, H. (2019). Cofilin 2 in Serum as a Novel Biomarker for Alzheimer's Disease in Han Chinese. Front. Aging Neurosci. *11*: 1–11.

Suzuki, A., Shin, J.W., Wang, Y., Min, S.H., Poncz, M., Choi, J.K., et al. (2013). RhoA Is Essential for Maintaining Normal Megakaryocyte Ploidy and Platelet Generation. PLoS One *8*:.

T, G., IB, Y., MI, Y., GE, W., J, W., VV, U., et al. (2017). Synergistic inhibition of both P2Y1 and P2Y12 adenosine diphosphate receptors as novel approach to rapidly attenuate platelet-mediated thrombosis. Physiol. Behav. *176*: 139–148.

Thirion, C., Stucka, R., Mendel, B., Gruhler, A., Jaksch, M., Nowak, K.J., et al. (2001). Characterization of human muscle type cofilin (CFL2) in normal and regenerating muscle. Eur. J. Biochem. *268*: 3473–3482.

Thomas, P., and Smart, T.G. (2005). HEK293 cell line: A vehicle for the expression of recombinant proteins. J. Pharmacol. Toxicol. Methods *51*: 187–200.

Thon, J.N., Montalvo, A., Patel-Hett, S., Devine, M.T., Richardson, J.L., Ehrlicher, A., et al. (2010). Cytoskeletal mechanics of proplatelet maturation and platelet release. J. Cell Biol. *191*: 861–874.

Tijssen, M.R., Cvejic, A., Joshi, A., Hannah, R.L., Ferreira, R., Forrai, A., et al. (2011). Genome-wide analysis of simultaneous GATA1/2, RUNX1, FLI1, and SCL binding in megakaryocytes identifies hematopoietic regulators. Dev. Cell *20*: 597–609.

Toshima, J., Ohashi, K., Okano, I., Nunoue, K., Kishioka, M., Kuma, K.I., et al. (1995). Identification and characterization of a novel protein kinase, TESK1,

specifically expressed in testicular germ cells. J. Biol. Chem. *270*: 31331–31337.

Toshima, J., Tanaka, T., and Mizuno, K. (1999). Dual specificity protein kinase activity of testis-specific protein kinase 1 and its regulation by autophosphorylation of serine-215 within the activation loop. J. Biol. Chem. *274*: 12171–12176.

Toshima, J., Toshima, J.Y., Takeuchi, K., Mori, R., and Mizuno, K. (2001). Cofilin Phosphorylation and Actin Reorganization Activities of Testicular Protein Kinase 2 and Its Predominant Expression in Testicular Sertoli Cells. J. Biol. Chem. *276*: 31449–31458.

Tourdot, B.E., Stoveken, H., Trumbo, D., Yeung, J., Kanthi, Y., Edelstein, L.C., et al. (2018). Genetic variant in human PAR (Protease-Activated Receptor) 4 enhances thrombus formation resulting in resistance to antiplatelet therapeutics. Arterioscler. Thromb. Vasc. Biol. *38*: 1632–1643.

Toyoda, K., Uchiyama, S., Yamaguchi, T., Easton, J.D., Kimura, K., Hoshino, H., et al. (2019). Dual antiplatelet therapy using cilostazol for secondary prevention in patients with high-risk ischaemic stroke in Japan: a multicentre, open-label, randomised controlled trial. Lancet Neurol. *18*: 539–548.

Tricoci, P., Huang, Z., Held, C., Moliterno, D.J., Armstrong, P.W., Werf, F. Van De, et al. (2012). Thrombin-receptor antagonist vorapaxar in acute coronary syndromes. N. Engl. J. Med. *366*: 20–33.

Ungerer, M., Li, Z., Baumgartner, C., Goebel, S., Vogelmann, J., Holthoff, H.P., et al. (2013). The GPVI - Fc Fusion Protein Revacept Reduces Thrombus Formation and Improves Vascular Dysfunction in Atherosclerosis without Any Impact on Bleeding Times. PLoS One *8*: 1–14.

Ungerer, M., Rosport, K., Bültmann, A., Piechatzek, R., Uhland, K., Schlieper, P., et al. (2011). Novel antiplatelet drug revacept (dimeric glycoprotein VI-Fc) specifically and efficiently inhibited collagen-induced platelet aggregation without affecting general hemostasis in humans. Circulation *123*: 1891–1899.

Uphaus, T., Richards, T., Weimar, C., Neugebauer, H., Poli, S., Weissenborn, K., et al. (2022). Revacept, an Inhibitor of Platelet Adhesion in Symptomatic Carotid Stenosis: A Multicenter Randomized Phase II Trial. Stroke *53*: 2718–2729.

Vandendries, E.R., Hamilton, J.R., Coughlin, S.R., Furie, B., and Furie, B.C. (2007). Par4 is required for platelet thrombus propagation but not fibrin generation in a mouse model of thrombosis. Proc. Natl. Acad. Sci. U. S. A. *104*: 288–292.

Venkatachalan, S.P., Bushman, J.D., Mercado, J.L., Sancar, F., Christopherson, K.R., and Boileau, A.J. (2007). Optimized expression vector for ion channel studies in Xenopus oocytes and mammalian cells using alfalfa mosaic virus. Pflugers Arch. *454*: 155–163.

Venkatakrishnan, A.J., Deupi, X., Lebon, G., Tate, C.G., Schertler, G.F., and Madan Babu, M. (2013). Molecular signatures of G-protein-coupled receptors. Nature *494*: 185–194.

Verdoni, A.M., Aoyama, N., Ikeda, A., and Ikeda, S. (2008). Effect of destrin mutations on the gene expression profile in vivo. Physiol. Genomics *34*: 9–21.
Vezza, R., Roberti, R., Nenci, G.G., and Gresele, P. (1993). Prostaglandin E2 potentiates platelet aggregation by priming protein kinase C. Blood *82*: 2704–2713.

Voors-Pette, C., Lebozec, K., Dogterom, P., Jullien, L., Billiald, P., Ferlan, P., et al. (2019). Safety and Tolerability, Pharmacokinetics, and

Pharmacodynamics of ACT017, an Antiplatelet GPVI (Glycoprotein VI) Fab: First-in-Human Healthy Volunteer Trial. Arterioscler. Thromb. Vasc. Biol. *39*: 956–964.

Vu, T.K.H., Hung, D.T., Wheaton, V.I., and Coughlin, S.R. (1991a). Molecular cloning of a functional thrombin receptor reveals a novel proteolytic mechanism of receptor activation. Cell *64*: 1057–1068.

Vu, T.K.H., Wheaton, V.I., Hung, D.T., Charo, I., and Coughlin, S.R. (1991b). Domains specifying thrombin-receptor interaction. Nature *353*: 674–677.

Wallentin, L., Varenhorst, C., James, S., Erlinge, D., Braun, O.Ö., Jakubowski, J.A., et al. (2008). Prasugrel achieves greater and faster P2Y12receptor-mediated platelet inhibition than clopidogrel due to more efficient generation of its active metabolite in aspirin-treated patients with coronary artery disease. Eur. Heart J. *29*: 21–30.

Welsh, R.C., Rao, S. V., Zeymer, U., Thompson, V.P., Huber, K., Kochman, J., et al. (2012). A randomized, double-blind, active-controlled phase 2 trial to evaluate a novel selective and reversible intravenous and oral P2Y 12 inhibitor elinogrel versus clopidogrel in patients undergoing nonurgent percutaneous coronary intervention: The INNOVATE-P. Circ. Cardiovasc. Interv. *5*: 336–346.

Whitley, M.J., Henke, D.M., Ghazi, A., Neiman, M., Stoller, M., Simon, L.M., et al. (2018). The Protease-Activated Receptor 4 Ala120Thr Variant Alters Platelet Responsiveness to Low-Dose Thrombin, Protease- Activated Receptor 4 Desensitization and Is Blocked by Noncompetitive P2Y12 Inhibition. J Thromb Haemost. *16*: 2501–2514.

Wilson, S.J., Ismat, F.A., Wang, Z., Cerra, M., Narayan, H., Raftis, J., et al. (2018). PAR4 (Protease-Activated Receptor 4) Antagonism with BMS-986120 Inhibits Human Ex Vivo Thrombus Formation. Arterioscler. Thromb. Vasc. Biol.

38: 448–456.

Witt, S.M. De, Swieringa, F., Cavill, R., Lamers, M.M.E., Kruchten, R. Van, Mastenbroek, T., et al. (2014). Identification of platelet function defects by multi-parameter assessment of thrombus formation. Nat. Commun. *5*:.

Wong, P.C., Seiffert, D., Bird, J.E., Watson, C.A., Bostwick, J.S., Giancarli, M., et al. (2017). Blockade of protease-activated receptor- 4(PAR4) provides robust antithrombotic activity with low bleeding. Sci. Transl. Med. *9*:.

Wong, P.C., Watson, C., and Crain, E.J. (2016). The P2Y1 receptor antagonist MRS2500 prevents carotid artery thrombosis in cynomolgus monkeys. J. Thromb. Thrombolysis *41*: 514–521.

Wu, C., Hwang, T., and Liao, C. (2002a). Selective inhibition of Protease-Activated Receptor 4-dependant platelet activation by YD-3. Thromb. Haemost. *87*: 1026–1033.

Wu, C.C., Hwang, T.L., Liao, C.H., Kuo, S.C., Lee, F.Y., Lee, C.Y., et al. (2002b). Selective inhibition of protease-activated receptor 4-dependent platelet activation by YD-3. Thromb. Haemost. *87*: 1026–1033.

Wu, C.C., Hwang, T.L., Liao, C.H., Kuo, S.C., Lee, F.Y., and Teng, C.M. (2003). The role of PAR4 in thrombin-induced thromboxane production in human platelets. Thromb. Haemost. *90*: 299–308.

Wurm, F.M. (2004). Production of recombinant protein therapeutics in cultivated mammalian cells. Nat. Biotechnol. *22*: 1393–1398.

Xia, T., Takagi, J., Coller, B.S., Wang, J.H., and Springer, T.A. (2004). Structural basis for allostery in integrins and binding to fibrinogen-mimetic therapeutics. Nature *432*: 59–67.

Xu, W.F., Andersen, H., Whitmore, T.E., Presnell, S.R., Yee, D.P., Ching, A., et al. (1998). Cloning and characterization of human protease-activated receptor 4. Proc. Natl. Acad. Sci. U. S. A. *95*: 6642–6646.

Xue, B., and Robinson, R.C. (2013). Guardians of the actin monomer. Eur. J. Cell Biol. *92*: 316–332.

Yamamoto, M., Nagata-Ohashi, K., Ohta, Y., Ohashi, K., and Mizuno, K. (2006). Identification of multiple actin-binding sites in cofilin-phosphatase Slingshot-1L. FEBS Lett. *580*: 1789–1794.

Yang, J., Mapelli, C., Wang, Z., Sum, C.S., Hua, J., Lawrence, R.M., et al. (2022). An optimized agonist peptide of protease-activated receptor 4 and its use in a validated platelet-aggregation assay. Platelets *33*: 979–986.

Yoo, Y., Ho, H.J., Wang, C., and Guan, J.L. (2010). Tyrosine phosphorylation of cofilin at Y68 by v-Src leads to its degradation through ubiquitin-proteasome pathway. Oncogene *29*: 263–272.

Zhang, H., Jiang, P., Zhang, C., Lee, S., Wang, W., and Zou, H. (2018). PAR4 overexpression promotes colorectal cancer cell proliferation and migration. Oncol. Lett. *16*: 5745–5752.

Zhao, P., Metcalf, M., and Bunnett, N.W. (2014). Biased signaling of protease-activated receptors. Front. Endocrinol. (Lausanne). *5*: 67.

Zheng, B., Li, J., Jiang, J., Xiang, D., Chen, Y., Yu, Z., et al. (2021). Safety and efficacy of a platelet glycoprotein Ib inhibitor for patients with non-ST segment elevation myocardial infarction: A phase Ib/IIa study. Pharmacotherapy *41*: 828–836.

Zheng, Y., Adams, T., Zhi, H., Yu, M., Wen, R., Newman, P.J., et al. (2015). Restoration of responsiveness of phospholipase Cγ2-deficient platelets by enforced expression of phospholipase Cγ1. PLoS One *10*: 1–20.

Zhu, H., Yang, H., Zhao, S., Zhang, J., Liu, D., Tian, Y., et al. (2018). Role of the cofilin 2 gene in regulating the myosin heavy chain genes in mouse myoblast C2C12 cells. Int. J. Mol. Med. *41*: 1096–1102.

Zhu, J., Choi, W., Mccoy, J.G., Negri, A., Zhu, J., Naini, S., et al. (2012). Structur-guided design of a high-affinity platelet integrin αIIbβ3 receptor antagonist that disrupts Mg(2)+ binding to the MIDAS. *4*: 1–23.

Chapter Eight:

Supplementary

S1 Cell systems used to study PAR4

The Human Embryonic Kidney 293 (HEK293) cell line was generated in 1973 by obtaining cells from an aborted foetus transformed by exposing the cells to sheared fragments of DNA from the human adenovirus type 5 (Lin et al., 2014). They are incredibly effective at being successfully transfected with plasmid vectors which contain CMV promotors to express recombinant proteins for study (Thomas and Smart, 2005). They are a good cell line for the study of overexpression of non-native proteins due to their ease of growth (DMEM, 10% FCS, 5% CO_2 incubator at 37°C) and a fast-doubling time of approx. 36hours allowing for rapid generation of recombinant protein studies and generation of data. HEK293 cells are used extensively as an overexpression system including the study of PAR4, its mutants and in the determination of novel protein/protein interactions using proteomics. These cells are ideal as they do not possess endogenous PAR4, therefore over-expression of PAR4 and the relevant variants can be characterized with ease.

S1.1 Optimising transfection conditions for recombinant cell systems using tagged PAR4 plasmids

The Human embryonic kidney cell line HEK293 and HEK293T (TSA201) have been previously shown to be a widely used tool for expressing proteins of interest due to their efficiency in up taking DNA and production of correctly folded proteins in high volumes (Wurm, 2004; Backliwal et al., 2008). HEK293 cells were originally tested for transfectability of PAR4-mCherry plasmid DNA (Figure S.1A) but were found to be sensitive with a high percentage of cell lifting and rounded cells which made cell imaging difficult. It was therefore decided to test transfection of PAR4-mCherry plasmid DNA in TSA201 cells (HEK293 stably expression SV40 T-antigen). It was found that these cells grew more effectively with less lifting. TSA201 cells of differing seeding densities (30, 40 and 50% confluence) were transfected with 1μg DNA: 5.7μl PEI with PEI:no DNA as a control (Figure S.1B). Control untransfected and PAR4-mCherry Transfected cells were lysed and processed for analysis of protein expression using Western blotting. Increase of cell density was noted in the control tubulin blots (Figure S.1C, bottom panel). Overexpression of PAR4-mCherry resulted in the appearance of two notable bands resolving between 55-100kDa (Figure S.1C, top panel) when probed for mCherry using a highly selective α-Red anti-RFP antibody (Chromotek). Based on quantification of the positive signal, it was clear that transfection of cells at 50% confluence offered maximal protein expression. The results showed that TSA201 cells could be used as a successful model to transiently express PAR4. This would be a suitable model as would allow for the expression of both PAR1 and PAR4 together which would better capitulate receptor co-expression in platelets.

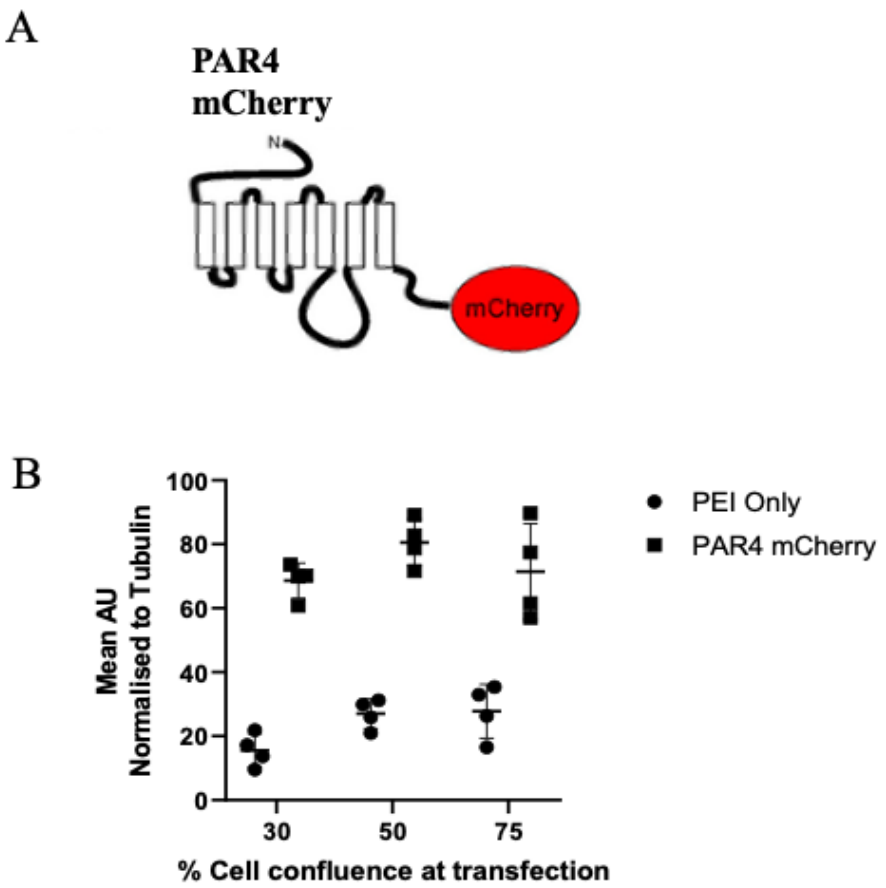

Figure S.1 Transient transfection of PAR4-mCherry plasmid DNA in TSA201 cells. A) Shows the structure of the wt-PAR4 protein conjugated to the mCherry RFP. B+C) Shows western blot results for mCherry for varying seeding concentration of TSA201 cells at densities of 30, 50 and 75% confluence (Left to right). PEI only with no DNA was used as a negative control. All seeding densities shows positive staining for mCherry indicating successful transfection, with 50% confluent cells showing highest transfection efficiency. Tubulin was used as a housekeeping gene. Data shown is representative of four independent repeats.

S1.2 PAR4 patient mutation Y157C results in ER retention due to incorrect protein folding and reduced surface expression

As was shown in the previous Figure TSA201 cells were used to successfully express wt-PAR4 with success, this was shown by the 2-band pattern seen in Western blotting (Unfolded immature protein (intracellular) and mature folded glycosylated protein (surface expressed)) (Cunningham et al., 2012), The mutation Y157C which was proposed as the targetable allosteric site by AtomWise and which the small molecule Hits delivered by AtomWise will be based on (Figure S.2A). It has previously been shown that this mutation results in ER retention due incorrect folding, with greatly reduced surface expression (Norman et al., 2016). Wt-PAR4 and Y157C were compared by Immunofluorescent imaging (Figure S.2A+B) clear differences were observed with receptor localization between wild-type and mutant. In these experiments it was clear that the previous published data could be reproduced with ease. As shown in the Western blot, expression of WT yielded two clear bands (55-100kDa), however only the lower protein band was observed which coincided with intracellular retention of PAR4 in Y157C expressing cells (Figure S.3B).

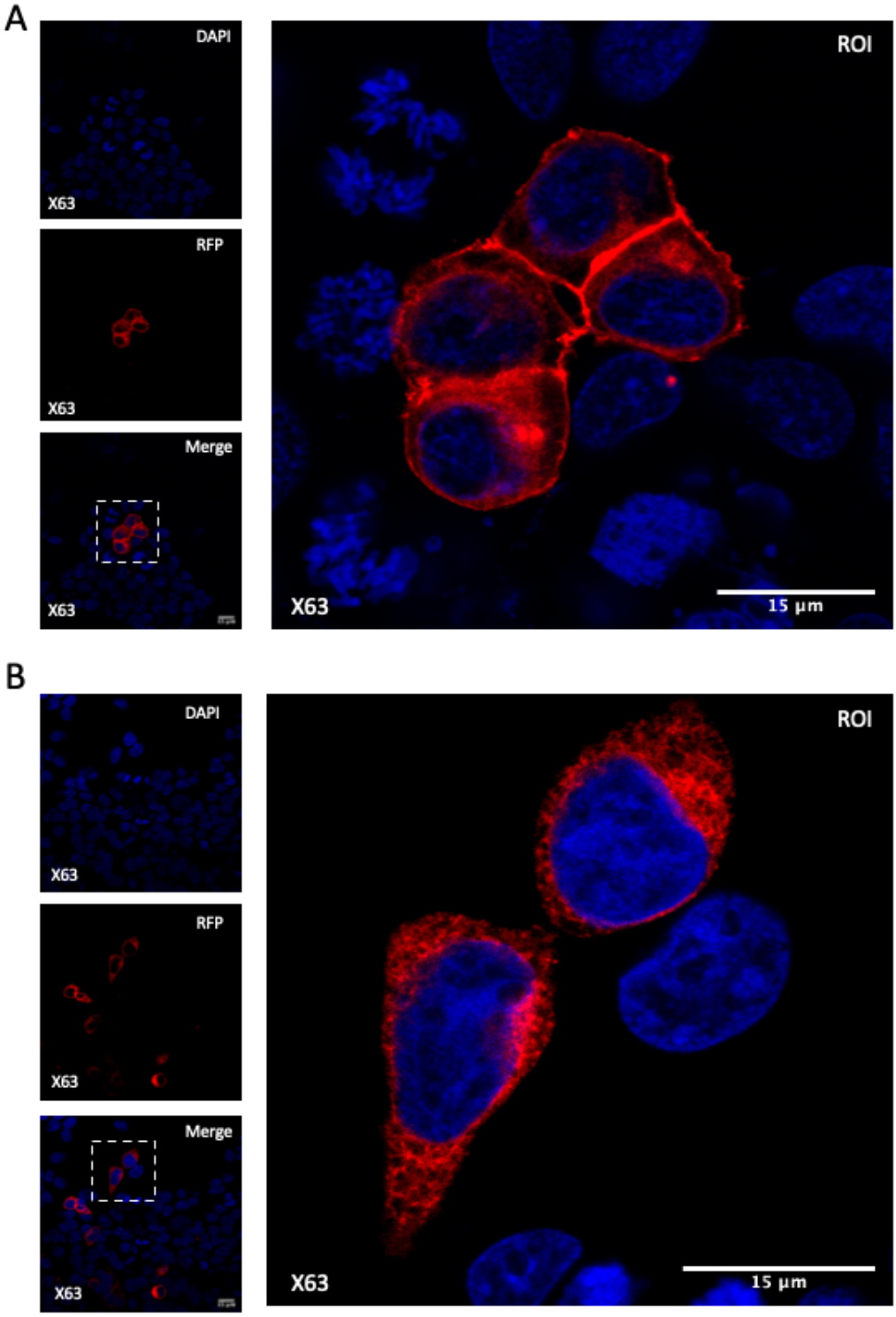

Figure S.2 Transient transfection of HEK293 cells with mCherry tagged PAR4 plasmids. A) Shows Immunofluorescence results for wt-PAR4 which shows staining throughout the cell with enhanced signal around the edge of the cell which coincides with the majority of receptor being surface expressed. B) Shows Immunofluorescence results for mut-Y157C which shows staining throughout the cell with no signal concentrated on the surface which coincides with the majority of receptor being intracellularly retained. DAPI was used as a counterstain. Scale bar = 15μm.

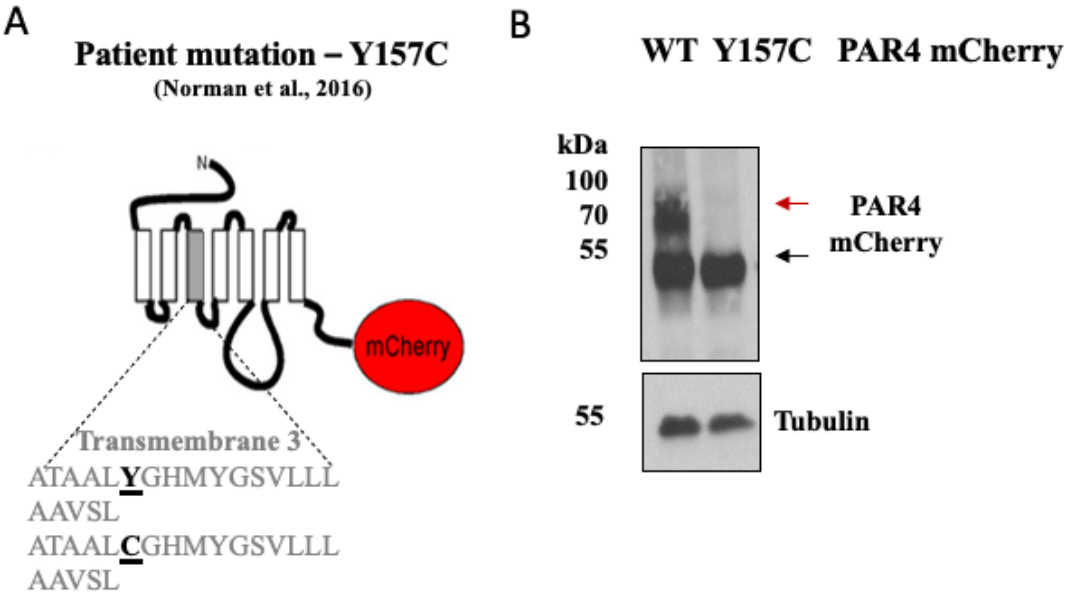

Figure S.3 Transient transfection of PAR4-mCherry and Y157C-mCherry plasmid DNA in TSA201 cells. A) Shows the structure of the Y157C protein conjugated to the mCherry RFP. B) Shows western blot results for wt-PAR4 and Y157C mutant, the mutant protein shows loss of the dual band pattern of wt-PAR4 indicating retention in the ER and loss of surface expression. Tubulin was used as a housekeeping gene.

S1.3 Transfection of YFP tagged PAR4 plasmids in HEK293 cells

To further test the intracellular retention of mut-Y157C, a new wt-PAR4 construct tagged with YFP was assessed for suitability for co-transfection with mut Y157C mCherry. HEK293 cells were seeded into a 12-well plate at a density of $0.1x10^6$ and transfected with pcDNA3.1 wt-PAR4 YFP initially at 1μg and 3μg DNA and 5.7μl PEI, PEI only was used as a control. Cells were also transfected with pcDNA3.1 mut-Y157C mCherry at 0.5μg and 1μg DNA and 5.7μl PEI, PEI only was used as a control. Reduction of 3μg to 0.5μg and 1μg for all further immunofluorescence microscopy was due to overloading of microscope in the 3μg DNA imaging, pcDNA3.1 wt-PAR4 YFP showed successful transfection (Figure S.4A).

In addition, Control PEI:no DNA and wt-PAR4 YFP (1μg and 3μg) transfected HEK293 cells were lysed and processed for analysis of protein expression using Western blotting. Overexpression of PAR4-YFP resulted in the appearance of two notable bands resolving between 55-100kDa (Figure S.4B) when probed for YFP using a highly selective anti-GFP antibody (Chromotek). Based on quantification of the positive signal, it was clear that transfection of cells at higher DNA concentration offered increased protein expression in a concentration dependent manner (Figure S.4B, bottom right panel).

HEK293 cells were successfully transfected to express wt-PAR4 YFP and mut-Y157C PAR4 mCherry as was assessed by IF confocal microscopy and western blotting. In order to quantify the transfection efficiency of these PAR4 plasmids in HEK293 cells confocal images taken were assessed for wt-PAR4 YFP (n=4) and mut-Y157C PAR4 mCherry (n=3). It was shown that wt-PAR4 YFP gave an average transfection efficiency of 29.77% and mut-Y157C PAR4 mCherry gave an average transfection efficiency of 11.51% (Figure S.4C).

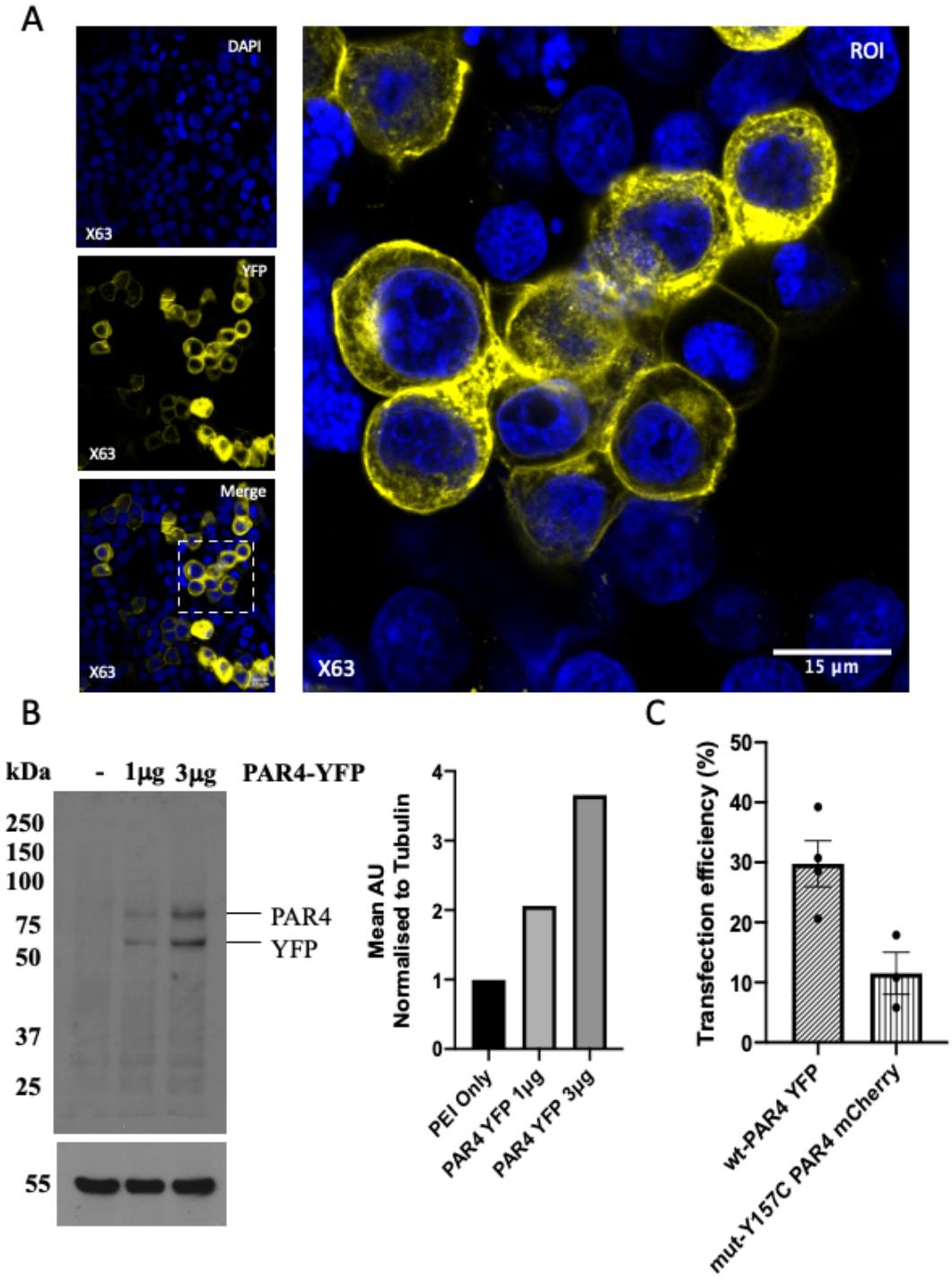

Figure S.4 Transient transfection of HEK293 cells with YFP tagged PAR4 plasmids. A) Shows IF images under oil immersion at 63X magnification. wt-PAR4 YFP showed positive expression in the appropriate channel indicating successful transfection. B) Shows expression of wt-PAR4 in transfected HEK293 cells detected by western blot (left) expression of wt-PAR4 shows protein expression is concentration dependent on DNA concentration transfected (right). C) Shows transfection efficiency plotted as an average of YFP (n=4), mean=29.77%. Y157C mCherry (n=3), mean 11.51%.

S1.4 Co-transfection of HEK293 cells with tagged PAR4 plasmids

HEK293 cells were transfected with 1μg wt-PAR YFP DNA + 1μg mut-Y157C mCherry DNA: 5.7μl PEI or 1μg wt-PAR YFP DNA + 1μg wt-PAR4 mCherry DNA: 5.7μl PEI in 12-well dishes and processed for IF as previously described. HEK293 cells were successfully transfected with both tagged proteins as shown by IF images obtained (Figure S.5A+C).
In order to determine the colocalization of wild-type and mutant IF images were analysed using FIJI ImageJ using the JACoP plugin for colocalization. As expected, co-expression of wt-PAR4 YFP and wt-PAR4 mCherry showed almost near perfect colocalization with a Pearson's coefficient of 0.957 with scatterplot shown in Figure (S.5B).

Colocalization analysis of HEK293 cells expressing wt-PAR YFP and mut-Y157C mCherry gave a Pearson's coefficient of 0.64, which indicates some degree of colocalization along the biosynthetic pathway, scatter plot shown in Figure (S.4D). The results provide further evidence for the PAR4 mutant Y157C being retained intracellularly with in the ER. These results are in line with expectation as the majority of wild-type protein would be expressed on the surface but would colocalize with the mutant along the biosynthetic pathway before being expressed on the surface.

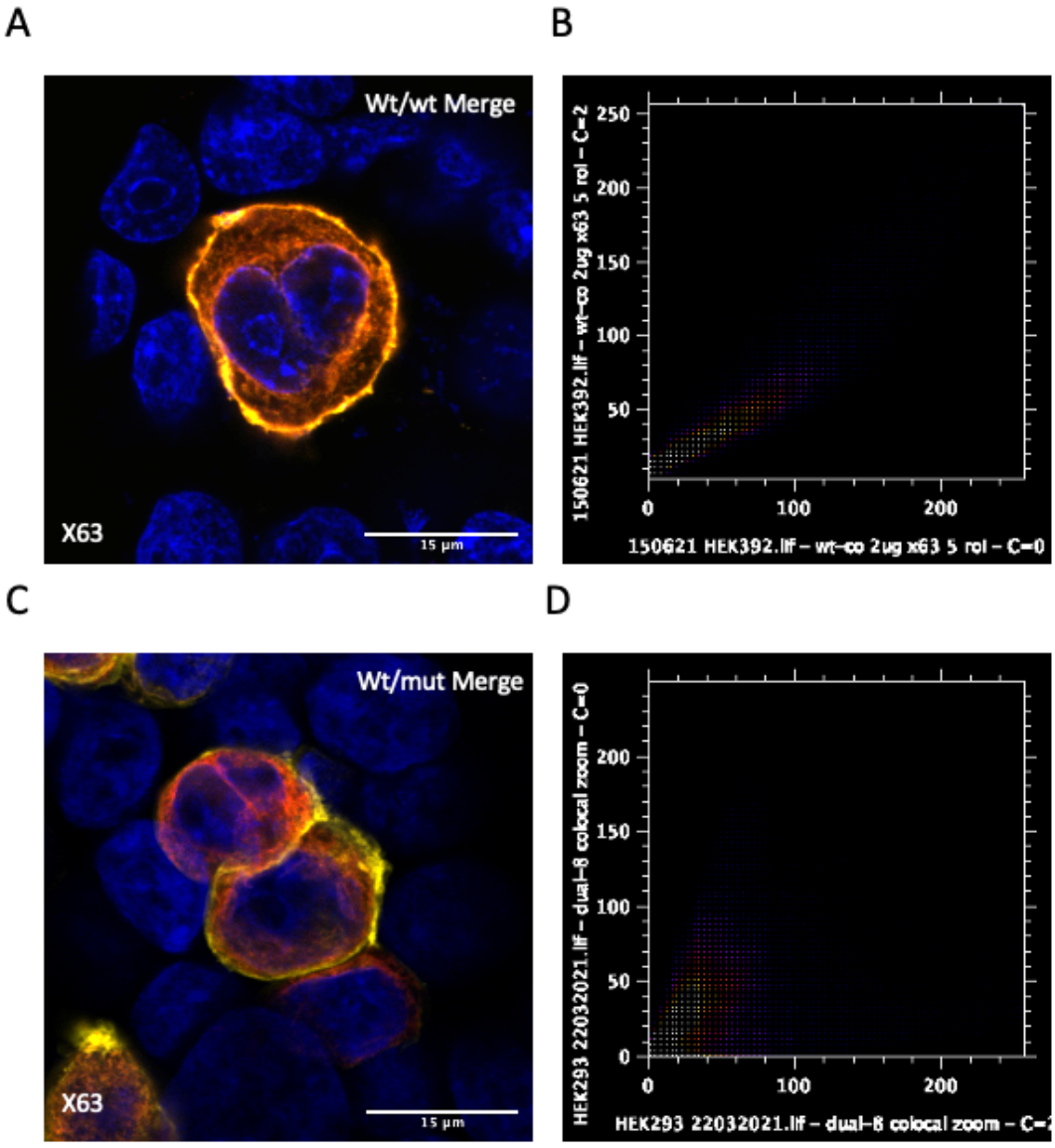

Figure S.5 Co-expression of tagged PAR4 plasmids in HEK293 cells. A) shows a representative image of co-expression of wt-PAR4 YFP and wt-PAR4 mCherry in HEK293 cells. B) Shows scatterplot of tagged receptor colocalization, Pearson's coefficient was 0.957 indicating near perfect colocalization. C) shows a representative image of co-expression of wt-PAR YFP and mut-Y157C mCherry in HEK293 cells. D) Shows scatterplot of tagged receptor colocalization, Pearson's coefficient was 0.64 indicating some degree of colocalization. DAPI was used as a counter stain. Scale bar = 15μm.

S1.5 Calcium mobilization in 10h9 (wt-PAR4) cells following treatment with AYPGFK

Previous studies have shown that the keratinocyte cell line NCTC-2544 does not express endogenous PARs (Kanke et al., 2001). Therefore, it is a suitable cell line to test calcium response in PAR4 without any other endogenous PARs. The cell line 10h9 is NCTC-2544 transfected to stably express wt-PAR4 and it was therefore used to test calcium mobilization responses when treated with increasing concentrations of PAR4 activating peptide AYPGFK (0-500μM). Raw calcium traces are shown in Figure S.6A. This resulted in a concentration-dependent increase in intracellular calcium as measured by a well-established Fluo-4 calcium flux assay (EC50 – 125.9μM). Representative trace data is shown in Figure S.6A across all concentrations tested, with a full concentration response curve of peak data plotted in Figure S.6B.

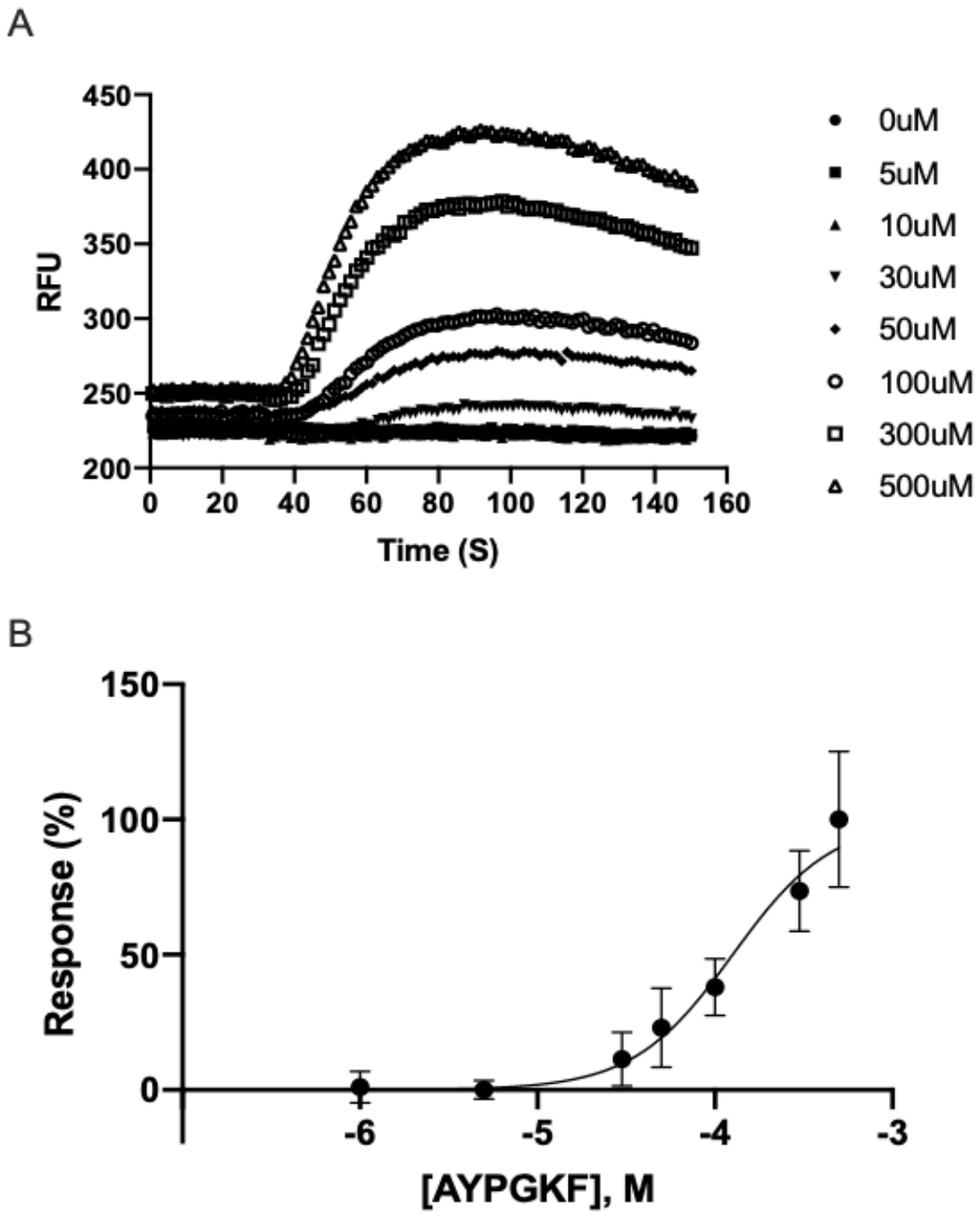

Figure S.6 Fluo-4 calcium mobilization in 10h9 cells following treatment with AYPGKF. A) Shows raw traces of changes in relative fluorescent units (RFU) following addition of increasing concentrations (0-500μM) of AYPGKF to 10h9 cells. AYPGKF ligand was added at ~30 seconds. Raw calcium traces are the mean of N=3 replicates. B) Shows a dose response curve generated from results of A, each point is the average of N=3. EC50 of AYPGKF is 125.9μM (95% CI 95.12μM to 167.6μM).

S1.6 Calcium mobilization in 10h9 (wt-PAR4) cells following treatment with Thrombin

The same 10h9 NCTC-2544 transfected to stably express wt-PAR4 was used to test calcium mobilization responses when treated with increasing concentrations of thrombin (0-10.0IU/mL). PAR4 calcium responses to thrombin in this cell line were notably low as PAR4 is a low affinity thrombin receptor which lacks the hirudin-like domain (Xu et al., 1998). In addition, as previous studies have hypothesized PAR4 activation by thrombin is enhanced by formation of heterodimers with PAR1 which contains the high-affinity hirudin-like domain and therefore bring thrombin into close contact with PAR4 allowing for enhanced activation (Leger et al., 2006). As 10h9 cells do not express PAR1, activation of PAR4 does not occur as efficiently as it would in endogenous cell systems which express both receptors. However, this system is effective in evaluating the effects of PAR4 inhibition during a small molecule screen as these cells lack PAR1 but stably over-express PAR4 and therefore negate potential off-target effects on the drug on PAR1. Raw calcium traces are shown in Figure S.7A. The resultant concentration dependent rise in intracellular calcium to thrombin (EC50 – 1.427IU/mL) was plotted and shown in the concentration response curve in Figure S.7B.

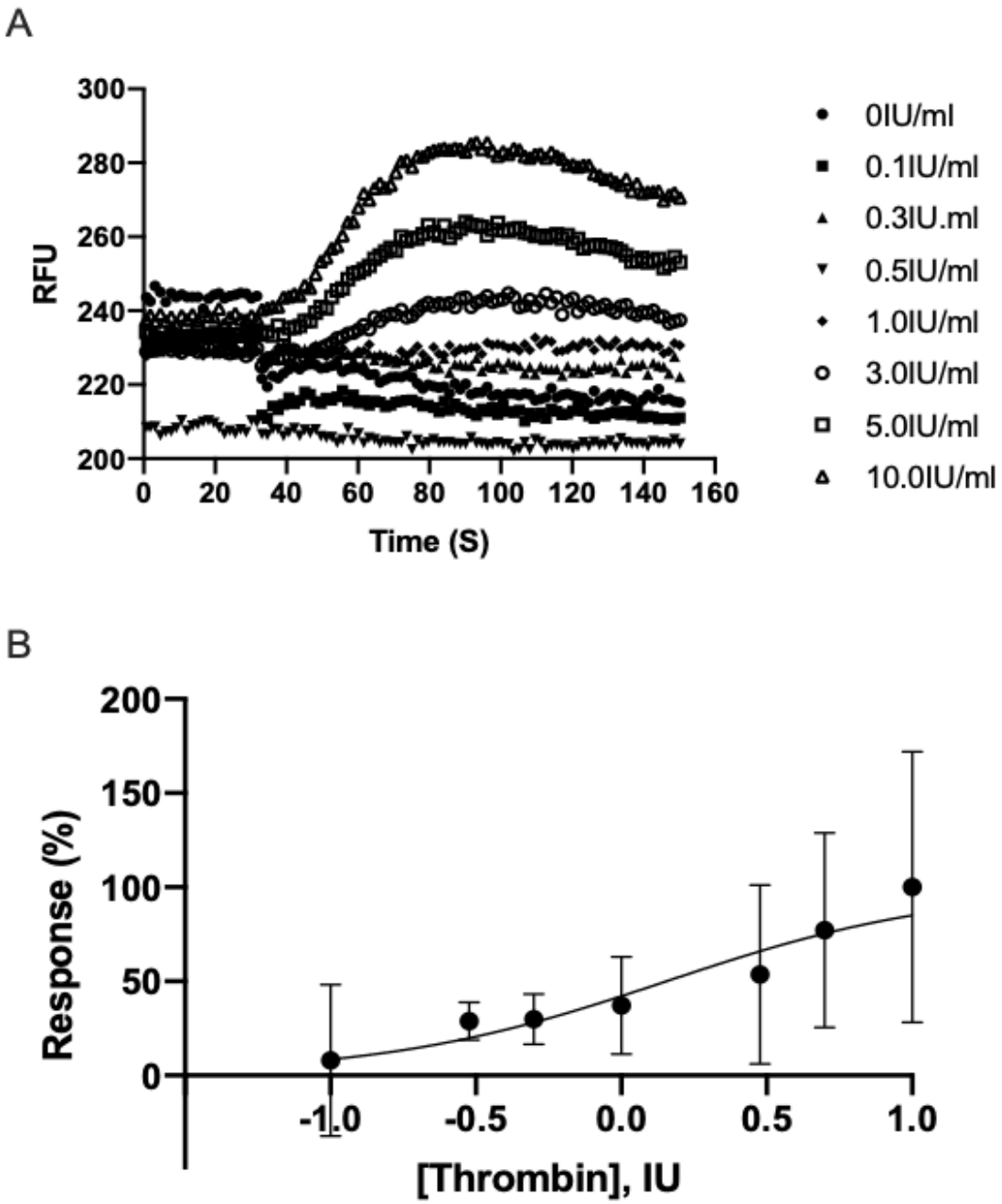

Figure S.7 Fluo-4 calcium mobilization in 10h9 cells following treatment with Thrombin. A) Shows raw traces of changes in relative fluorescent units (RFU) following addition of increasing concentrations (0-10.0μIU/mL) of Thrombin to 10h9 cells. Thrombin was added at ~30 seconds. Raw calcium traces are the mean of N=3 replicates. B) Shows a dose response curve generated from results of A, each point is the average of N=3. EC50 of Thrombin is 1.427IU/mL (95% CI 0.4262 to 4.619IU/mL).

S1.7 Detection of PAR4 receptor in MEG-01 cells

Although in theory a useful model for studying physiological downstream signalling of PAR4, we first aimed at proving proof of principal that MEG-01 cells did actually express PAR4.

MEG-01 cells were incubated with PAR4 antibody in suspension and adherent phenotypes and imaged using IF with confocal microscopy. Representative images of MEG-01 cells in suspension are shown in (Figure S.8A). From left, image shows MEG-01 cells incubated with only secondary labelled antibody which shows no fluorescence and proves that any signal detected is the result of antibody binding to target. Middle and right shows MEG-01 which have been incubated with PAR4 antibody and shows positive signal in all cells as was expected. Scale bars 15μm.

In addition, as expression pattern of PAR4 didn't follow that seen in HEK293 overexpression with the honeycomb appearance, adherent MEG-01 cells were also incubated with PAR4 antibody are shown in (Figure S.8B). Again, diffuse expression of PAR4 antibody is noted. Scale bars 30μm.

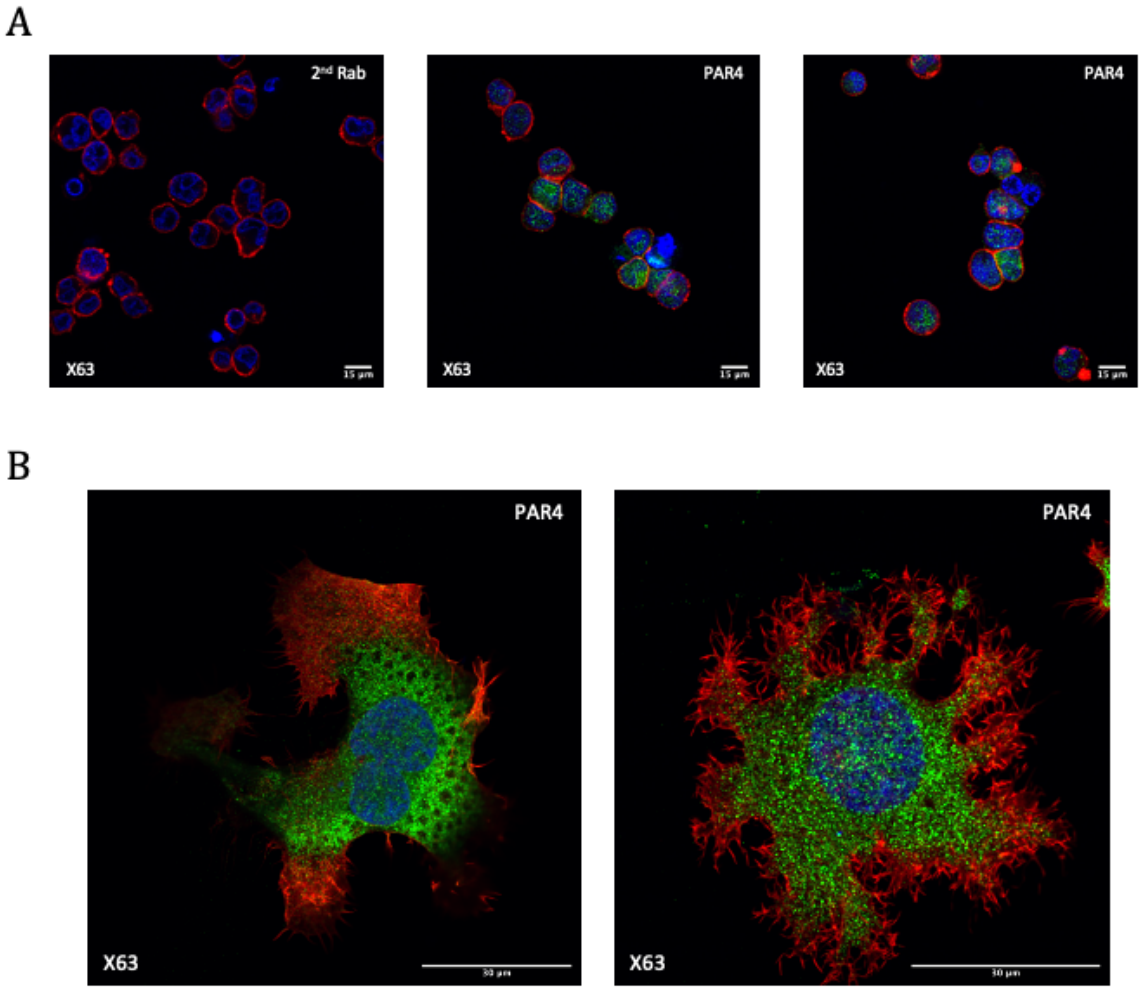

Figure S.8 PAR4 expression in MEG-01 cells using IF. A) shows representative images of suspension MEG-01 cells for PAR4 expression. From left to right, first image shows MEG-01 cells incubated with secondary only antibody, no fluorescence in green channel confirms absence of non-specific binding. Middle and right image shows PAR4 expression in MEG-01 cells (green), pattern shown is not like that of HEK293 overexpression. B) shows representative images of adherent MEG-01 cells expression of PAR4, similar diffuse expression of PAR4 receptor throughout the cell is shown. A) scale bars are 15μm and B) scale bars 30μm.

S2 Supplementary References

Backliwal, G., Hildinger, M., Chenuet, S., Wulhfard, S., Jesus, M. De, and Wurm, F.M. (2008). Rational vector design and multi-pathway modulation of HEK 293E cells yield recombinant antibody titers exceeding 1 g/l by transient transfection under serum-free conditions. Nucleic Acids Res. *36*:.

Cunningham, M.R., McIntosh, K.A., Pediani, J.D., Robben, J., Cooke, A.E., Nilsson, M., et al. (2012). Novel role for proteinase-activated receptor 2 (PAR2) in membrane trafficking of proteinase-activated receptor 4 (PAR4). J. Biol. Chem. *287*: 16656–16669.

Kanke, T., Macfarlane, S.R., Seatter, M.J., Davenport, E., Paul, A., McKenzie, R.C., et al. (2001). Proteinase-activated Receptor-2-mediated Activation of Stress-activated Protein Kinases and Inhibitory κB Kinases in NCTC 2544 Keratinocytes. J. Biol. Chem. *276*: 31657–31666.

Leger, A.J., Jacques, S.L., Badar, J., Kaneider, N.C., Derian, C.K., Andrade-Gordon, P., et al. (2006). Blocking the protease-activated receptor 1-4 heterodimer in platelet-mediated thrombosis. Circulation *113*: 1244–1254.

Lin, Y.C., Boone, M., Meuris, L., Lemmens, I., Roy, N. Van, Soete, A., et al. (2014). Genome dynamics of the human embryonic kidney 293 lineage in response to cell biology manipulations. Nat. Commun. *5*:.

Norman, J.E., Cunningham, M.R., Jones, M.L., Walker, M.E., Westbury, S.K., Sessions, R.B., et al. (2016). Protease-activated receptor 4 variant p.Tyr157Cys reduces platelet functional responses and alters receptor trafficking. Arterioscler. Thromb. Vasc. Biol. *36*: 952–960.

Thomas, P., and Smart, T.G. (2005). HEK293 cell line: A vehicle for the expression of recombinant proteins. J. Pharmacol. Toxicol. Methods *51*: 187–200.

Wurm, F.M. (2004). Production of recombinant protein therapeutics in cultivated mammalian cells. Nat. Biotechnol. *22*: 1393–1398.

Xu, W.F., Andersen, H., Whitmore, T.E., Presnell, S.R., Yee, D.P., Ching, A., et al. (1998). Cloning and characterization of human protease-activated receptor 4. Proc. Natl. Acad. Sci. U. S. A. *95*: 6642–6646.